APPLIED COMPUTATIONAL ELECTROMAGNETICS SOCIETY JOURNAL

October 2025
Vol. 40 No. 10
ISSN 1054-4887

The ACES Journal is abstracted in INSPEC, in Engineering Index, DTIC, Science Citation Index Expanded, the Research Alert, and to Current Contents/Engineering, Computing & Technology.

The illustrations on the front cover have been obtained from the ARC research group at the Department of Electrical Engineering, Colorado School of Mines

Published, sold and distributed by: River Publishers, Alsbjergvej 10, 9260 Gistrup, Denmark

OCTOBER 2025 REVIEWERS

Ghulam Ahmad
Esraa Mousa Ali
Zaheer Ahmed Dayo
Junbing Duan
Nasr H. Gad
Muyu Hou
Srilakshmi Inuganti
Ulrich Jakobus
Mehmet Onur Kok
Lida Kouhalvandi
Vinoth M.
Raja Mchaalia
Anton Menshov
Alfredo Gomes Neto
Andrew Peterson
Giovanni Maria Sardi
Sayidmarie
Manthan Shah
Somchat Sonasang
Halil Topozlu
Zhengyong Yu

THE APPLIED COMPUTATIONAL ELECTROMAGNETICS SOCIETY JOURNAL

Vol. 40 No. 10 October 2025

TABLE OF CONTENTS

Quantitative Analysis of Confidence Interval for Electromagnetic Characteristics of Hypersonic Targets

Yupeng Zhu[1], Dina Chen[2], Huaguang Bao[2], and Min Han[1,*]

[1]Institute of Systems Engineering
Academy of Military Sciences, People's Liberation Army of China, Beijing 100082, China
nudtyp@163.com, hanminchina@163.com
*Corresponding Author

[2]Nanjing University of Science and Technology
Nanjing 210094, China
1390737464@qq.com, hgbao@njust.edu.cn

Abstract – In response to the current lack of rapid and efficient techniques for uncertainty analysis in electromagnetic problems, this paper proposes an efficient uncertainty quantification method based on the finite-difference time-domain (FDTD) method. A conformal FDTD formulation integrated with polynomial chaos expansion (PCE) is comprehensively derived. For random input variables exhibiting Gaussian distribution characteristics, Hermite polynomial expansion and Galerkin testing are employed. Furthermore, by incorporating the Runge-Kutta time-stepping scheme, the method efficiently quantifies electromagnetic scattering characteristics considering stochastic variations in plasma electron density of hypersonic targets. Numerical experiments demonstrate that the proposed approach provides a reliable framework for uncertainty analysis in complex electromagnetic environments.

Index Terms – Electromagnetic characteristics, hypersonic target, polynomial chaos expansion, uncertainty.

I. INTRODUCTION

Near-space refers to the region between 20 km and 100 km altitude, which includes most of the stratosphere, the entire mesosphere, and parts of the thermosphere. When hypersonic targets reach near-space regions during high-speed flight, they encounter a highly complex high-temperature plasma sheath [1]. As radio signals propagate through the plasma sheath, they experience absorption and scattering effects that alter the electromagnetic characteristics of the vehicle, posing significant challenges for communication and radar detection of hypersonic vehicles [2, 3]. The hypersonic flow environment is further complicated by high-temperature non-equilibrium flows, chemical reactions, and thermodynamic non-equilibrium. Regarding confidence intervals in radar detection, the primary question is it the target or just noise. The decision is based on comparing the received signal power to a threshold. The significance of confidence intervals in radar tracking is accurate estimation of the tracked motion state of the target. Although environmental parameters can be measured on the ground, it is prohibitively expensive. Thus, numerical simulation techniques are crucial for analyzing the electromagnetic properties of hypersonic targets [4, 5]. Despite the high accuracy of numerical methods, real-world problems often introduce numerous uncertainty factors. This has led to a strong interest in studying the effects of these stochastic fluctuations to enhance the precision and reliability of engineering analyses.

Considering the actual environment, manufacturing processes, and other factors, practical electromagnetic systems are susceptible to uncertainties such as electromagnetic interference (EMI) and electromagnetic compatibility (EMC) [6–8]. It is crucial to consider and quantify the impact of these uncertainties through methods like electromagnetic compatibility analysis and bioelectromagnetic analysis [9]. There are primarily two types of numerical quantification methods. One type is statistical methods based on sampling theory, with the most famous being the Monte Carlo (MC) method [10]. Hastings et al. used the MC-FDTD method to analyze the electromagnetic scattering characteristics of random rough surfaces [11]. While the Monte Carlo method is simple to implement, it suffers from low convergence rates, resulting in significant computational time. The other type is stochastic methods based on probability theory, which include several techniques. Smith proposed the Stochastic FDTD (SFDTD) method using Taylor series expansion and applied it to bioelectromagnetic simulations, achieving an analysis of the electromagnetic properties of multilayer skin tissues considering uncertainties in dielectric parameters and conductivity [12–14]. Nguyen et al. employed the

Submitted On: July 29, 2025
Accepted On: October 07, 2025

https://doi.org/10.13052/2025.ACES.J.401001

SFDTD method to study the electromagnetic characteristics of magnetized plasma with random electron and ion concentrations in the atmosphere [15]. Silly-Carette et al. used the Stochastic Collocation (SC) method, combined with FDTD simulation, to analyze the uncertainty of the impact of plane waves with random incident angles on human head radiation [16]. Edwards et al. combined the PCE technique with the FDTD method to analyze EMC problems, quantifying uncertainties in scenarios involving uniformly distributed reflection coefficients of shielding plates and the random variation of dielectric sphere radii, dielectric parameters, and magnetic permeability [17]. Austin and Sarris utilized the FDTD method based on PCE technology to conduct efficient analysis of integrated circuits with geometrically varying dimensions [18]. Pyrialakos et al. used the FDTD method, based on PCE technology and the Karhunen-Loeve (KL) expansion method, for spatially inhomogeneous materials with stochastic exponential gradients. This allowed for rapid analysis of the electromagnetic characteristics of uncertain problems by decoupling multi-input variable random processes and reducing the polynomial order describing random output variables [19]. Lin et al. proposed a framework for uncertainty quantification based on the isogeometric boundary element method and PCE method in the acoustic field and robust shape optimization for sound barriers [20]. Jiang et al. proposed a novel and comprehensive computational framework based on intrusive polynomial chaos approach to effectively analyze the uncertainty problem of thermomagnetic convection caused by random temperature fluctuations [21]. In comparison to Monte Carlo methods, probabilistic-based stochastic methods are operationally intricate but exhibit enhanced convergence characteristics.

Yang et al. introduced the Monte Carlo method to streamline the uncertainty analysis in the measurement of electromagnetic parameters for absorbing materials using the transmission/reflection method and investigated the key factors influencing system uncertainty [22]. In electromagnetic compatibility analysis, the quantification of uncertainty frequently encounters challenges caused by the curse of dimensionality, Jiang et al. proposes an enhanced sparse polynomial chaos expansion method that combines hyperbolic truncation, E-optimality criterion, and the subspace pursuit algorithm to improve both computational efficiency and model accuracy [23].

Given the absence of fast and efficient analysis techniques for uncertain electromagnetic problems in the time-domain differential equation method, this paper explores an efficient uncertainty analysis technique based on the time-domain differential equation method. Specifically, we investigate the conformal finite-difference time-domain (FDTD) method augmented with polynomial chaos expansion (PCE) technology. In this study, we focus on employing the Hermite polynomial expansion and Galerkin test to address random problems characterized by Gaussian distribution of input variables. Additionally, we integrate the Runge-Kutta exponential time-history difference technique into the analysis. Through these combined approaches, we achieve quantitative analysis of the uncertain electromagnetic scattering characteristics of hypersonic target plasma, specifically considering the random variation of electron concentration. The proposed methodology allows for a thorough examination of the uncertainties associated with the scattering behavior of hypersonic target plasma. By effectively incorporating the PCE technology and specialized numerical techniques within the conformal FDTD framework, we can analyze the electromagnetic response of the system in the presence of random variations in electron concentration. This research significantly contributes to advancing our understanding of the uncertain electromagnetic properties of hypersonic targets, enabling more accurate characterization and prediction of their scattering characteristics.

II. POLYNOMIAL CHAOS EXPANSION TECHNIQUES

The Monte Carlo method is a classical sampling statistical method that offers clear principles and easy implementation. However, it is often time-consuming due to the need for repeated sampling calculations. In contrast, PCE technology, as a probabilistic statistical method, conducts an orthogonal polynomial expansion on random input variables and their corresponding response variables. This approach transforms uncertainty quantification into solving expansion coefficients, allowing us to obtain statistical characteristics of uncertainty problems through a single simulation. In deterministic time-domain electromagnetic simulations, the computational dimension typically consists of the time dimension (t) and spatial dimensions (x, y, z). When uncertain variables are present in the electromagnetic system, an additional dimension ξ is introduced to capture the randomness of electromagnetic waves. For conventional time-domain differential equation methods, basis functions or direct difference methods are employed for spatial expansions, while difference methods are used for time expansions. Therefore, when dealing with the newly introduced dimension, suitable methods must be employed for expansion. In this paper, we adopt the polynomial chaos expansion method on the additional dimension. This involves using orthogonal polynomials to expand random variables. The selection of orthogonal polynomials should consider

the probabilistic statistical distribution of the random input variables. If the random input variable follows a Gaussian probability distribution, Hermite polynomials can be chosen. If the random input variables follow a uniform distribution, Legendre polynomials can be selected. These choices are made based on the statistical properties of the random variables to ensure accurate representation and analysis of the uncertainties in the electromagnetic system.

A. Gaussian probability distribution

Assuming that the random input variable $In(\xi)$ satisfies the Gaussian probability distribution, then the input variable can be described as:

$$In(\xi) = \mu_{In} + \sigma_{In}\xi. \tag{1}$$

Here μ_{In} is the average value,σ_{In} is the standard deviation, and ξ is a random quantity satisfying the standard normal distribution. Using Hermite polynomial to expand the uncertain response variable $f(r,t,\xi)$:

$$f(r,t,\xi) = \sum_{k=0}^{k=p} \psi_k(\xi) f^k(r,t). \tag{2}$$

Here $\psi_k(\xi)$ is Hermite polynomial and p is polynomial order. The Hermite polynomial of order k is defined as:

$$\psi_k(\xi) = (-1)^k e^{\xi^2/2} \frac{d^k}{d\xi^k} e^{-\xi^2/2}. \tag{3}$$

Hermite polynomials satisfy the following recursion relation and orthogonality:

$$\begin{gathered} \psi_0(\xi) = 1, \quad \psi_1(\xi) = \xi, \\ \psi_{k+1}(\xi) = \xi\psi_k(\xi) - k\psi_{k-1}(\xi), \quad k > 1, \end{gathered} \tag{4}$$

$$\begin{aligned} \langle \psi_m(\xi), \psi_n(\xi) \rangle &= \int_{-\infty}^{+\infty} \psi_m(\xi)\psi_n(\xi) e^{-\xi^2/2} d\xi \\ &= n!\sqrt{2\pi}\delta_{mn}. \end{aligned} \tag{5}$$

Here δ_{mn} is the Kronecker impulse function.

B. Uniform distribution

If the random input variable $In(\xi)$ follows the uniform distribution of [a,b], then the input variable can be described as:

$$In(\xi) = \frac{b-a}{2}\xi + \frac{a+b}{2}. \tag{6}$$

Here ξ follows the uniform distribution of $[-1,1]$. The Legendre polynomial is used to expand the uncertain response variable $f(r,t,\xi)$:

$$f(r,t,\xi) = \sum_{k=0}^{k=p} P_k(\xi) f^k(r,t). \tag{7}$$

Here $P_k(\xi)$ represents the Legendre polynomial and p is the polynomial order. The Hermite polynomial of order k is defined as:

$$P_k(\xi) = \frac{1}{2^k k!} \frac{d^k}{d\xi^k} [(\xi^2 - 1)^k]. \tag{8}$$

The Legendre polynomial satisfies the following recursion relation and orthogonality:

$$\begin{gathered} P_0(\xi) = 1, P_1(\xi) = \xi, \\ (k+1)P_{k+1}(\xi) = (2k+1)\xi P_k(\xi) - kP_{k-1}(\xi), \quad k > 1, \end{gathered} \tag{9}$$

$$\langle P_m(\xi), P_n(\xi) \rangle = \int_{-1}^{1} P_m(\xi)P_n(\xi)d\xi = \frac{2}{2n+1}\delta_{mn}. \tag{10}$$

III. UNCERTAINTY ELECTROMAGNETIC ANALYSIS

Plasma is a unique state of matter consisting of ions, electrons, and non-ionized neutral particles. It is characterized by its collective behavior and is primarily influenced by electromagnetic forces. Plasma exists in a neutral state overall, despite the presence of charged particles. Plasma finds a wide range of applications across various fields, including biomedical, electronic, and military domains. In the realm of electronics, plasma is utilized in microelectronics for processes like plasma etching and deposition, which are crucial in the fabrication of integrated circuits and other electronic devices. Plasma displays, such as plasma TVs, rely on the ionization of gas to produce light. High-power microwave devices also employ plasma to generate and control electromagnetic radiation. Plasma-based techniques can be used to reduce radar cross-section and improve the stealth capabilities of military equipment. Additionally, plasmas can be harnessed to enhance the aerodynamic properties of aircraft by controlling the boundary layer flow around the surface. The electromagnetic analysis of plasma needs to correctly extract the equivalent electromagnetic parameters of plasma, where plasma frequency ω_p and plasma collision frequency v_c are the two main parameters.

The oscillation frequency of electrons and ions in plasma under the combined action of external disturbance and coulomb force is called the oscillation angular frequency of plasma, also known as the cut-off frequency of plasma. The plasma frequency ω_p is the sum of the angular frequency of electron oscillation ω_{pe} and the angular frequency of ion oscillation ω_{pi}, namely $\omega_p = \omega_{pe} + \omega_{pi}$. The angular frequency of electron oscillation and the angular frequency of ion oscillation

have the following forms:

$$\omega_{pe} = \sqrt{\frac{n_e q_e^2}{m_e \varepsilon_0}}, \quad \omega_{pi} = \sqrt{\frac{n_i q_e^2}{m_i \varepsilon_0}}, \tag{11}$$

where n_e is the number of electrons per unit volume, n_i is the number of ions per unit volume, q_e is the electron charge, m_e is the electron mass, m_i is the ion mass, and ε_0 is the dielectric constant of free space. Under normal aerodynamic conditions, m_i is much greater than m_e. Correspondingly, ω_{pi} is much smaller than ω_{pe}. The angular frequency of ion oscillation is negligible, so it can be approximated $\omega_p \approx \omega_{pe}$. The angular frequency of plasma oscillation is expressed as:

$$\omega_p \approx \sqrt{\frac{n_e q_e^2}{m_e \varepsilon_0}}. \tag{12}$$

Plasma collision frequency v_c is also a necessary parameter in the dielectric constant of the plasma, in which the electron collision frequency dominates. There are many kinds of collisions between particles in plasma, the most important part is the collision between electrons and ions and the collision between electrons and neutral particles.

The collision frequency between electrons and neutral particles is:

$$v_{em} = 6.3 \times 10^{-9} n_m \sqrt{\frac{T}{300}}. \tag{13}$$

The collision frequency of electrons and ions is:

$$v_{ei} = \frac{5.5 n_i}{T_e^{3/2}} \left[\ln\left(\frac{280 T_e}{n_i^{1/3}} \right) + \frac{1}{3} \ln\left(\frac{T}{T_e} \right) \right]. \tag{14}$$

Normally,$v_{em} \gg v_{ei}$. Therefore, it can be approximated $v_c \approx v_{em}$. The expression of plasma collision frequency is:

$$v_c \approx v_{em} = 6.3 \times 10^{-9} n_m \sqrt{\frac{T}{300}}, \tag{15}$$

where n_m is the density of neutral particles in the gas.

The electromagnetic parameters of unmagnetized plasma can be described by the Drude model in the following form:

$$\varepsilon = \varepsilon_0 \left(1 + \frac{\omega_p^2}{j\omega(j\omega + v_c)} \right). \tag{16}$$

Substituting the above equation into the frequency-domain Maxwell curl equations, we get:

$$j\omega\varepsilon_0 \left(1 + \frac{\omega_p^2}{j\omega(j\omega + v_c)} \right) \boldsymbol{E} = \nabla \times \boldsymbol{H}, \tag{17}$$

$$j\omega\mu \boldsymbol{H} = -\nabla \times \boldsymbol{E}. \tag{18}$$

By introducing the polarization current density $\boldsymbol{J}$ and converting the above equation into the time-domain, the following expression can be obtained:

$$\varepsilon_0 \frac{\partial \boldsymbol{E}}{\partial t} + \boldsymbol{J} = \nabla \times \boldsymbol{H}. \tag{19}$$

$$\mu \frac{\partial \boldsymbol{H}}{\partial t} = -\nabla \times \boldsymbol{E}. \tag{20}$$

$$\frac{\partial \boldsymbol{J}}{\partial t} + v_c \boldsymbol{J} = \varepsilon_0 \omega_p^2 \boldsymbol{E}. \tag{21}$$

In a rectangular coordinate system, the component of polarization current density in the $\frac{dJ_x}{dt} + vJ_x = \varepsilon_0 \omega_p^2 E_x$ direction is expressed as:

$$\frac{\partial \boldsymbol{J}_x}{\partial t} + v_c \boldsymbol{J}_x = \varepsilon_0 \omega_p^2 \boldsymbol{E}_x. \tag{22}$$

We multiply both sides of equation (22) by the factor $e^{v_c t}$ and simplify to get:

$$\frac{\partial (\boldsymbol{J}_x e^{v_c t})}{\partial t} = \varepsilon_0 \omega_p^2 \boldsymbol{E}_x. \tag{23}$$

Using second-order Runge-Kutta time difference and simplifying the above equation, the following recurrence relationship can be obtained:

$$\begin{aligned} J_x^{n+1} = {} & e^{-v_c \Delta t} J_x^n + \frac{1 - e^{-v_c \Delta t}}{v_c} \varepsilon_0 \omega_p^2 E_x^n \\ & + \frac{(e^{-v_c \Delta t} - 1 + v_c \Delta t)}{v_c^2 \Delta t} [\varepsilon_0 \omega_p^2 E_x^{n+1} - \varepsilon_0 \omega_p^2 E_x^n]. \end{aligned} \tag{24}$$

Equation (19) can be discretized by using central difference in time as:

$$E_x^{n+1} = E_x^n + \frac{\Delta t}{\varepsilon_0} (\nabla \times \boldsymbol{H})_x - \frac{\Delta t}{2\varepsilon_0} (J_x^{n+1} + J_x^n). \tag{25}$$

By substituting equation (24) into equation (25) and simplifying, we get:

$$\begin{aligned} E_x^{n+1} = {} & \frac{1}{1 + \frac{\omega_p^2}{2v_c^2}(e^{-v_c \Delta t} - 1 + v_c \Delta t)} \\ & \times \left\{ \left[1 - \frac{\Delta t \omega_p^2}{2v_c} (1 - e^{-v_c \Delta t}) \right. \right. \\ & \left. + \frac{\omega_p^2}{2v_c^2} (e^{-v_c \Delta t} - 1 + v_c \Delta t) \right] E_x^n \\ & \left. + \frac{\Delta t}{\varepsilon_0} (\nabla \times \boldsymbol{H})_x - \frac{\Delta t}{2\varepsilon_0} (1 + e^{-v_c \Delta t}) J_i^n \right\}. \end{aligned} \tag{26}$$

Similar treatment is done in the other directions, and the iterative formula of the magnetic field is the same as

that of the ordinary FDTD, which means that the plasma can still be treated with traditional metal conformal treatment when it is located at the metal interface. From equations (24) and (26), the iterative formula of Runge-Kutta in the discretized three-dimensional unmagnetized plasma can be obtained. The following is a concrete expression for J_x and E_x in the x direction at the coordinates $(i+1/2,j,k)$. The form of the y and z direction components is similar, so those expressions are omitted.

$$\begin{aligned}
&J_x^n\left(i+\frac{1}{2},j,k\right)\\
&\quad=e^{-\nu_c\Delta t}J_x^{n-1}\left(i+\frac{1}{2},j,k\right)\\
&\qquad+\frac{1-e^{-\nu_c\Delta t}}{\nu_c}\varepsilon_0\omega_p^2E_x^{n-1}\left(i+\frac{1}{2},j,k\right)\\
&\qquad+\frac{(e^{-\nu_c\Delta t}-1+\nu\Delta t)}{\nu_c^2\Delta t}\\
&\qquad\times\left[\varepsilon_0\omega_p^2E_x^n\left(i+\frac{1}{2},j,k\right)\right.\\
&\qquad\left.-\varepsilon_0\omega_p^2E_x^{n-1}\left(i+\frac{1}{2},j,k\right)\right]. \qquad (27)\\
&E_x^{n+1}\left(i+\frac{1}{2},j,k\right)\\
&\quad=\frac{1}{1+\frac{\omega_p^2}{2\nu_c^2}(e^{-\nu_c\Delta t}-1+\nu_c\Delta t)}\\
&\qquad\times\left\{\left[1-\frac{\Delta t\omega_p^2}{2\nu_c}(1-e^{-\nu_c\Delta t})\right.\right.\\
&\qquad\left.\left.+\frac{\omega_p^2}{2\nu_c^2}(e^{-\nu\Delta t}-1+\nu_c\Delta t)\right]\right.\\
&\qquad\times E_x^n\left(i+\frac{1}{2},j,k\right)\\
&\qquad+\frac{\Delta t}{\varepsilon_0}\left[\frac{1}{\Delta y}\left(H_z^{n+1/2}\left(i+\frac{1}{2},j+\frac{1}{2},k\right)\right.\right.\\
&\qquad\left.-H_z^{n+1/2}\left(i+\frac{1}{2},j-\frac{1}{2},k\right)\right)\\
&\qquad-\frac{1}{\Delta z}\left(H_y^{n+1/2}\left(i+\frac{1}{2},j,k+\frac{1}{2}\right)\right.\\
&\qquad\left.\left.-H_y^{n+1/2}\left(i+\frac{1}{2},j,k-\frac{1}{2}\right)\right)\right]\\
&\qquad\left.-\frac{\Delta t}{2\varepsilon_0}(1+e^{-\nu_c\Delta t})J_x^n\right\}. \qquad (28)
\end{aligned}$$

Here, the electron concentration in the plasma is considered as a random variable satisfying certain statistical characteristics. Assuming that the electron concentration satisfies the Gaussian probability distribution, then the electron concentration can be described as:

$$n_e(\xi)=\mu_{n_e}+\sigma_{n_e}\xi, \qquad (29)$$

where μ_{n_e} represents the average electron concentration, σ_{n_e} is its standard deviation, and ξ is the random quantity satisfying the standard normal distribution. Because the random change of electron concentration leads to the corresponding random change of electric field, magnetic field, and current density, these variables are expanded by Hermite polynomial and expressed as:

$$\begin{aligned}
&E(i+1/2,j,k,\xi)\\
&\quad=\sum_{m=0}^{p}\psi_m(\xi)e(i+1/2,j,k,m). \qquad (30)\\
&H(i+1/2,j+1/2,k,\xi)\\
&\quad=\sum_{m=0}^{p}\psi_m(\xi)h(i+1/2,j+1/2,k,m). \qquad (31)\\
&J(i+1/2,j,k,\xi)\\
&\quad=\sum_{m=0}^{p}\psi_m(\xi)J(i+1/2,j,k,m). \qquad (32)
\end{aligned}$$

By substituting equation (12) and equations (29–32) into equation (28), we get:

$$\begin{aligned}
&[1+An_e(\xi)]\sum_{m=0}^{p}\psi_m(\xi)e_x^{n+1}(i+1/2,j,k,m)\\
&\quad=[1-Bn_e(\xi)+An_e(\xi)]\\
&\qquad\times\sum_{m=0}^{p}\psi_m(\xi)e_x^n(i+1/2,j,k,m)\\
&\qquad+\frac{\Delta t}{\varepsilon_0}\left[\frac{1}{\Delta y}\left(\sum_{m=0}^{p}\psi_m\right.\right.\\
&\qquad\times(\xi)h_z^{n+1/2}(i+1/2,j+1/2,k,m)\\
&\qquad\left.-\sum_{m=0}^{p}\psi_m(\xi)h_z^{n+1/2}(i+1/2,j-1/2,k,m)\right)\\
&\qquad-\frac{1}{\Delta z}\left(\sum_{m=0}^{p}\psi_m(\xi)h_y^{n+1/2}(i+1/2,j,k+1/2,m)\right.\\
&\qquad\left.\left.-\sum_{m=0}^{p}\psi_m(\xi)h_y^{n+1/2}(i+1/2,j,k-1/2,m)\right)\right]\\
&\qquad-\frac{\Delta t}{2\varepsilon_0}(1+e^{-\nu_c\Delta t})\sum_{m=0}^{p}\psi_m\\
&\qquad\times(\xi)J_x^n(i+1/2,j+1/2,k,m). \qquad (33)
\end{aligned}$$

The coefficients A and B satisfy the following relation:

$$A = \frac{q_e^2}{2\nu_c^2 m_e \varepsilon_0}(e^{-\nu_c \Delta t} - 1 + \nu_c \Delta t). \quad (34)$$

$$B = \frac{\Delta t q_e^2}{2\nu_c m_e \varepsilon_0}(1 - e^{-\nu_c \Delta t}). \quad (35)$$

Equation (36) is tested by using Hermite polynomial and simplified by using Hermite polynomial recurrence relation and orthogonal property:

$$\begin{aligned}
&A\sigma_{n_e} e_x^{n+1}(i+1/2,j,k,l-1) \\
&\quad + (1+A\mu_{n_e}) e_x^{n+1}(i+1/2,j,k,l) \\
&\quad + (l+1)A\sigma_{n_e} e_x^{n+1}(i+1/2,j,k,l+1) \\
&= (A-B)\sigma_{n_e} e_x^{n}(i+1/2,j,k,l-1) \\
&\quad + [1+(A-B)\mu_{n_e}] e_x^{n}(i+1/2,j,k,l) \\
&\quad + (l+1)(A-B)\sigma_{n_e} e_x^{n}(i+1/2,j,k,l+1) \\
&\quad + \frac{\Delta t}{\varepsilon_0}\left[\frac{1}{\Delta y}(h_z^{n+1/2}(i+1/2,j+1/2,k,l)\right. \\
&\quad - h_z^{n+1/2}(i+1/2,j-1/2,k,l)) \\
&\quad - \frac{1}{\Delta z}(h_y^{n+1/2}(i+1/2,j,k+1/2,l) \\
&\quad \left. - h_y^{n+1/2}(i+1/2,j,k-1/2,l))\right] \\
&\quad - \frac{\Delta t}{2\varepsilon_0}(1+e^{-\nu_c \Delta t}) J_x^n(i+1/2,j+1/2,k,l). \quad (36)
\end{aligned}$$

It can be seen from the observation of equation (36) that when uncertainty electromagnetic analysis is carried out using p-order polynomial chaos expansion method, the updates of the unknowns of the electric field at different edges are independent of each other, but the updates of the unknown electric field at the same edge $p+1$ need to be synchronized. Its iterative matrix equation satisfies the tridiagonal property and can be quickly solved by the catch-up method. The updated formulas for the remaining field quantities are similarly derived and are not listed here.

IV. NUMERICAL EXAMPLES

In order to verify the correctness and effectiveness of the proposed conformal FDTD uncertainty analysis method based on PCE technology, the electromagnetic scattering analysis of the AGARD HB-2 calibration model is carried out. As shown in Fig. 1(a), the total length of the target is 1.4932 m When this target flies at a high speed, plasma will be generated on the surface, and its plasma parameters n_e and T can be obtained through the fluid dynamics simulation software CFD-FASTRAN. Here, the flight height of the target is set at 30 km. The flight speed is set to Mach 10, and the generated plasma flow field has a radius of 0.8 m and a total length of 2.8 m. The distribution of n_e and T is shown in Figs. 1(b) and 1(c). Incident plane wave is against the light, incidence parameter is set to $\theta = 90^\circ, \varphi = 0^\circ$, $\alpha = 0^\circ$, and viewing angle is set to $\phi = 0^\circ, \theta = 0^\circ \sim 360^\circ$. The computing platform comprises a DELL server equipped with an Intel(R) Xeon(R) E7-4850 CPU running at 2.0 GHz, along with 512 GB of memory.

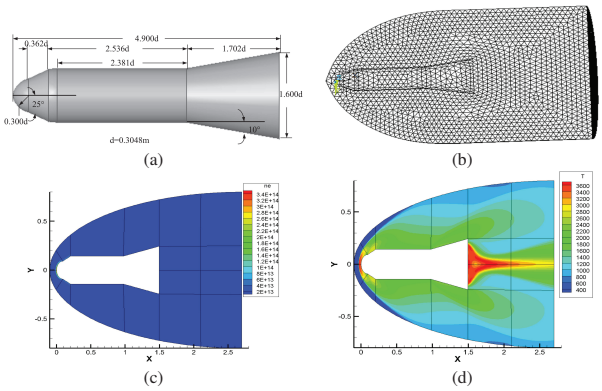

Fig. 1. The AGARD HB-2 calibration model at 30 km/10 Ma. (a) Geometric diagram, (b) grid diagram, (c) electron concentration, and (d) temperature.

First, the observation frequency is set to 300 MHz the spatial dispersion size is $\Delta x = \Delta y = \Delta z = 0.025$ m, and the time step is set to $\Delta t = 0.7\Delta x/\sqrt{3}c$, where c represents the propagation speed of electromagnetic waves in free space, the total number of time steps is set to 4000, and the electric field observation point is set at the discrete grid (16, 92, 92). Here, the randomness of electron concentration is considered, assuming that it satisfies the Gaussian probability distribution and the mean value satisfies the spatial distribution shown in Fig. 1. The mean value and standard deviation of electron concentration at different spatial locations are different, their ratio is assumed to be the same, and the standard deviation/mean value equals 2%. Monte Carlo method and CFDTD method based on PCE technology (PCE-CFDTD) were used for uncertainty analysis. The sampling times of Monte Carlo method was 100 times, and the polynomial order of PCE technology was set as $p = 1$. Figure 2 shows the expected and standard deviation of the electric field at the observation points of the two methods, which are in good agreement, indicating the correctness of the proposed PCE-CFDTD. Figure 3 shows the comparison diagram of the bistatic RCS mean

value of the target at 300 MHz. In order to further prove the effectiveness of PCE technology, the calculation time of the two methods is listed in Table 1. The Monte Carlo method with 100 samples takes 114,698 s, while the proposed PCE-CFDTD method takes only 5,901 s, which greatly saves calculation time. Results show the high efficiency of the proposed PCE-CFDTD method.

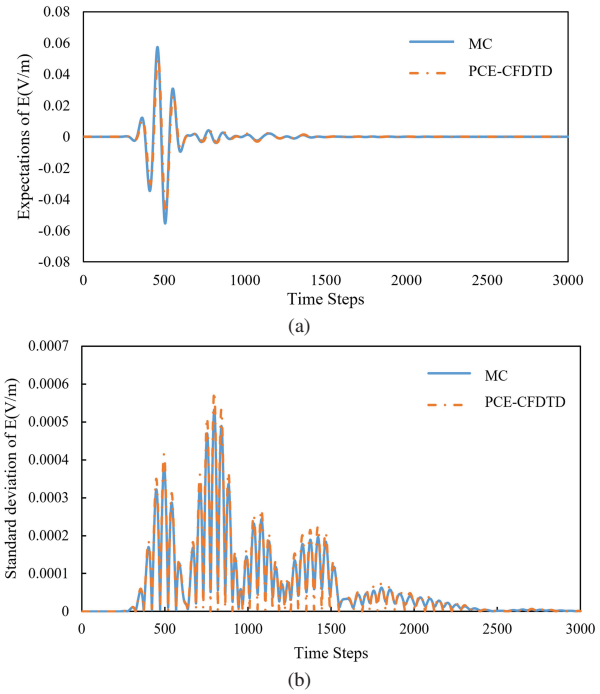

Fig. 2. Comparison of electric field results at the observation point of different methods. (a) Expectations and (b) standard deviation.

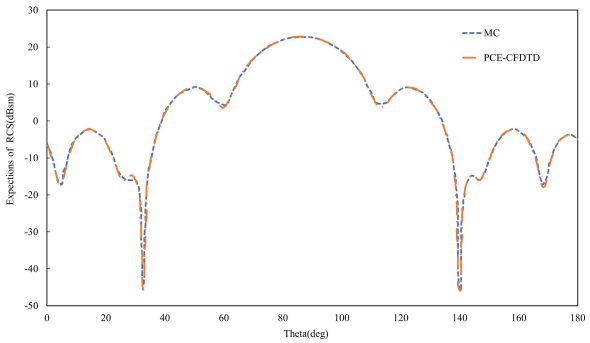

Fig. 3. Expectations of RCS at 300 MHz.

Table 1: CPU time comparison

Method	MC	PCE-CFDTD
CPU time(s)	114,698	5,901

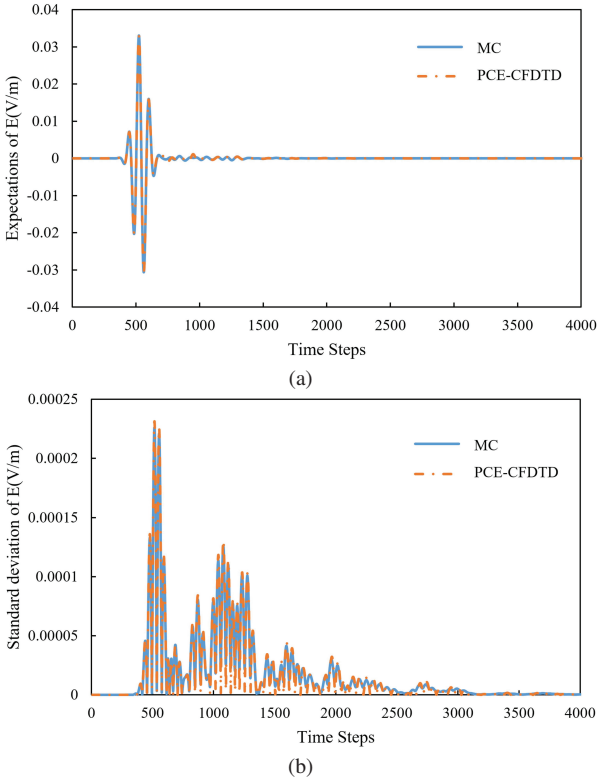

Fig. 4. Comparison of electric field results at the observation point of different methods. (a) Expectations and (b) standard deviation.

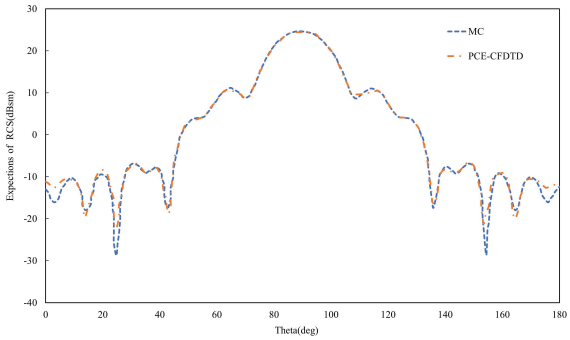

Fig. 5. Expectation comparison of RCS at 600 MHz.

Table 2: CPU time comparison

Method	MC	PCE-CFDTD
CPU time(s)	307,315	7583

Next, the observation frequency is set to 600 MHz, the spatial dispersion size is $\Delta x = \Delta y = \Delta z = 0.0125$ m, the time step is set to $\Delta t = 0.7\Delta x/\sqrt{3}c$, and the total number of time steps is set to 3000. The electric field observation point is set at the discrete grid (16, 92, 92), and the randomness of electron concentration is consistent with the above. Figure 4 shows the standard

deviation of the electric field at the observation point of the two methods, which is in good agreement. Figure 5 shows a comparison of the mean value of the bistatic RCS of the hypersonic HB-2 model at 600 MHz. Due to the limitation of computer resources and time, the calculation accuracy achieved by Monte Carlo sampling 100 times is not high enough. The calculation time of the two methods is listed in Table 2. The Monte Carlo method with 100 samples takes 307,315 s, while the proposed PCE-CFDTD method only takes 7,583 s, which greatly saves calculation time. Results show the high efficiency of the proposed PCE-CFDTD method.

V. CONCLUSIONS

In this paper, an efficient algorithm for hypersonic target uncertainty electromagnetic analysis is studied, and the conformal FDTD uncertainty electromagnetic analysis technique based on polynomial chaos expansion is proposed. Firstly, the iterative method of polynomial chaos expansion conformal FDTD method is derived and combined with metal/medium conformal technique and polynomial chaos expansion technique, an efficient electromagnetic analysis of the uncertainty problem of the electron concentration of the plasma generated on the hypersonic target surface is achieved. Currently, this method is limited to solving Maxwell's equations and has not yet been extended to other equations or to handling the coupling between multiphysics equations.in the future, it could be applied to solve heat conduction equations and address random thermal field problems with uncertain parameters.

REFERENCES

[1] Y. Zheng, I. Jun, and W. Tu, "Overview, progress and next steps for our understanding of the near-earth space radiation and plasma environment: Science and applications," *Advances in Space Research*, 2024.

[2] J. Cheng, K. Jin, Y. Kou, R. Hu, and X. Zheng, "An electromagnetic method for removing the communication blackout with a space vehicle upon re-entry into the atmosphere," *J. Appl. Phys.*, vol. 121, p. 093301, 2017.

[3] N. Mehra, R. K. Singh, and S. C. Bera, "Mitigation of communication blackout during re-entry using static magnetic field," *Prog. Electromag. Res. B,* vol. 63, pp. 161–172, 2015.

[4] Y. Hu, Z. Fan, D. Ding, and R. Chen, "Hybrid MLFMA/MLACA for analysis of electromagnetic scattering from inhomogeneous high-contrast objects," *Applied Computational Electromagnetics Society (ACES) Journal*, vol. 26, no. 10, pp. 765–772, 2011.

[5] Z. Cong, R. Chen, and Z. He, "Numerical modeling of EM scattering from plasma sheath: A review," *Engineering Analysis with Boundary Elements*, vol. 135, pp. 73–92, 2022.

[6] J. Bai, L. Zhang, L. Wang, and T. Wang, "Uncertainty analysis in EMC simulation based on improved method of moments," *Applied Computational Electromagnetics Society (ACES) Journal*, vol. 31, no. 1, pp. 66–71, 2016.

[7] A. Drandiæ and B. Trkulja, "Computation of electric field inside substations with boundary element methods and adaptive cross approximation," *Engineering Analysis with Boundary Elements*, vol. 91, pp. 1–6, 2018.

[8] J. Bai, B. Hu, and A. Duffy, "Uncertainty analysis for EMC simulation based on Bayesian optimization," *IEEE Transactions on Electromagnetic Compatibility*, vol. 67, no. 2, pp. 587–597, Apr. 2025.

[9] E. Garcia, "Electromagnetic compatibility uncertainty, risk, and margin management," *IEEE Transactions on Electromagnetic Compatibility*, vol. 52, no. 1, pp. 3–10, Feb. 2010.

[10] G. S. Fishman, *Monte Carlo. Concepts, Algorithms, and Applications*. New York, NY, USA: Springer, 1996.

[11] F. D. Hastings, J. B. Schneider, and S. L. Broschat, "A Monte-Carlo FDTD technique for rough surface scattering," *IEEE Transactions on Antennas and Propagation*, vol. 43, no. 11, pp. 1183–1191, Nov. 1995.

[12] K. M. Bisheh, B. Zakeri, and S. M. H. Andargoli, "Correlation coefficient estimation for stochastic FDTD method," *International Symposium on Telecommunications*, pp. 234–238, 2014.

[13] S. M. Smith and C. Furse, "Stochastic FDTD for analysis of statistical variation in electromagnetic fields," *IEEE Transactions on Antennas and Propagation*, vol. 60, no. 7, pp. 3343–3350, July 2012.

[14] S. M. Smith, "Stochastic finite-difference time-domain," Ph.D. dissertation, Dept. Elect. Eng, Univ. Utah, Salt Lake City, UT, USA, 2011.

[15] B. T. Nguyen, C. Furse, and J. J. Simpson, "A 3-D stochastic FDTD model of electromagnetic wave propagation in magnetized ionosphere plasma," *IEEE Transactions on Antennas and Propagation*, vol. 63, no. 1, pp. 304–313, Jan. 2015.

[16] J. Silly-Carette, D. Lautru, M. F. Wong, A. Gati, J. Wiart, and V. F. Hanna, "Variability on the propagation of a plane wave using stochastic collocation methods in a bio electromagnetic application," *IEEE Microwave and Wireless Components Letters*, vol. 19, no. 4, pp. 185–187, Apr. 2009.

[17] R. S. Edwards, A. C. Marvin, and S. J. Porter, "Uncertainty analyses in the finite-difference time-domain method," *IEEE Transactions on Electromagnetic Compatibility*, vol. 52, no. 1, pp. 155–163, Feb. 2010.

[18] A. C. M. Austin and C. D. Sarris, "Efficient analysis of geometrical uncertainty in the FDTD

method using polynomial chaos with application to microwave circuits," *IEEE Transactions on Microwave Theory and Techniques*, vol. 61, no. 12, pp. 4293-4301, 2013.

[19] G. G. Pyrialakos, T. T. Zygiridis, and N. V. Kantartzis, "A 3-D polynomial-chaos FDTD technique for complex inhomogeneous media with arbitrary stochastically-varying index gradients," *Applied Computational Electromagnetics Society (ACES) Journal*, vol. 1, no. 3, pp. 109–112, 2016.

[20] X. Lin, W. Zheng, and F. Huang, "Uncertainty quantification and robust shape optimization of acoustic structures based on IGA BEM and polynomial chaos expansion," *Engineering Analysis with Boundary Elements*, vol. 165, p. 105770, 2024.

[21] C. Jiang, Y. Qi, and E. Shi, "Combination of Karhunen-Loève and intrusive polynomial chaos for uncertainty quantification of thermomagnetic convection problem with stochastic boundary condition," *Engineering Analysis with Boundary Elements*, vol. 159, pp. 452–465, 2024.

[22] H. Yang, G. Wu, and P. Lyu, "Uncertainty analysis for electromagnetic parameter measurement method of absorbing materials based on waveguide device," *Journal of Electronic Measurement and Instrument*, vol. 39, no. 2, pp. 169–176, 2025.

[23] H. Jiang, F. Ferranti, and G. Antonini, "Enhanced sparse polynomial chaos expansion for electromagnetic compatibility uncertainty quantification problems," *IEEE Transactions on Electromagnetic Compatibility*, vol. 99, pp. 1–10, Aug. 2025.

Yupeng Zhu received the B.S. degree from the Department of Electronic Science, National University of Defense Technology, Changsha, China, in 2003, and the Ph.D. degree in 2009. He is currently a Research Fellow with the Academy of Military Sciences. He has published over 20 papers. His current research interests include radar signal processing, electromagnetic scattering and intelligent sensing technologies.

Dina Chen was born in Taizhou, Jiangsu, China. She received the B.S. degree from the Yancheng Institute of Technology, Yancheng, in 2022. She is currently pursuing the Ph.D. degree in the School of Microelectronics, Nanjing University of Science and Technology (NJUST), Nanjing. Her research interests include computational electromagnetics and microwave power component field-circuit coordination.

Huaguang Bao received the B.S. and Ph.D. degrees in communication engineering from the School of Electrical Engineering and Optical Technique, Nanjing University of Science and Technology, Nanjing, China, in 2011 and 2017, respectively. From 2017 to 2019, he was a Postdoctoral Fellow in the Computational Electromagnetics and Antennas Research Laboratory, Department of Electrical Engineering, The Pennsylvania State University, USA. He is currently a Professor with the Department of Integrated Circuit Engineering, Nanjing University of Science and Technology. His research interests include semiconductor simulation, RF-integrated circuits, and computational electromagnetics.

Min Han received the M.S. degree in information and communication engineering from the Nanjing University of Science and Technology, Nanjing, China, in 2013, and the Ph.D. degree in electromagnetic field and microwave engineering from Southeast University, Nanjing, in 2020. She is currently an Associate Researcher at the Academy of Military Sciences. Her research interests include electromagnetic scattering, millimeter wave circuits, and radar signal processing.

An Adaptive Multi-Objective Particle Swarm Optimization Algorithm for Excitation of Focused Phased Array in Microwave Hyperthermia Treatment Planning

Si Li[1], Yifan Shen[1], Atef Z. Elsherbeni[2], Yunlong Mao[1], and Cheng Lyu[3]

[1]Ocean College
Jiangsu University of Science and Technology, Jiangsu, 212134, China
lisi0511@just.edu.cn, shenyifan@stu.just.edu.cn, maoyunlong0511@just.edu.cn

[2]Electrical Engineering Department
Colorado School of Mines, Colorado, 80401, USA
aelsherb@mines.edu

[3]Information Engineering Department
Heilongjiang Agricultural Engineering Vocational College, Heilongjiang, 150006, China
cheng666@hrbeu.edu.cn

Abstract – A novel adaptive multi-objective particle swarm optimization (AMOPSO) is proposed to address the focus shift and redundant hotspots issues prevalent in current microwave hyperthermia treatment planning for breast cancer. By optimizing the excitation of phased array elements, more accurate beam focusing effect is achieved and the redundant hotspots are reduced, which significantly improves the treatment of breast cancer. The algorithm uses the difference between the optimized and target results as a feedback to self-constrain the algorithm, and introduces ratio of the peak power absorption (pPA) between the redundant hotspots and the target hotspot as a key objective function to reduce the number of redundant hotspots. Compared with the existing hyperthermia treatment planning (HTP) optimization algorithms, the proposed algorithm is capable of achieving precise focusing and a more substantial reduction in the number of redundant hotspots in a shorter computation time. Furthermore, the introduction of the pPA is capable of more effectively reducing the number of redundant hotspots and achieving a lower damage rate to healthy tissues.

Index Terms – Hyperthermia treatment planning (HTP), particle swarm optimization (PSO), phased arrays, specific absorption rate (SAR).

I. INTRODUCTION

Breast cancer poses a serious risk to women's health and life as it is one of the most common malignant tumors in the female population [1]. Among the available technologies, microwave hyperthermia treatment (MHT) has garnered significant attention due to its distinctive advantages [2]. This technology employs phased arrays to generate focused microwaves [3], offering merits such as rapid ablation, accurate localization, ease of use, lower risk of postoperative complications, and inexpensive medical costs [4, 5].

However, the practical application of MHT remains challenging, with the most significant hurdle being the precise focalization of microwave energy on tumor tissues while avoiding damage to surrounding healthy tissues [6]. Time-reversal (TR) technique is frequently employed in the optimization of hyperthermia treatment planning (HTP). However, the focused energy usually is shifted away from the target due to the attenuation and dispersion of microwaves in biological tissues, which negatively impacts the effectiveness of the treatment. To overcome these challenges, researchers usually optimize the excitation of the phased array elements to improve the focusing performance. In order to concentrate energy in a particular area within a semicircular breast model, Curto et al. [7] used the Nelder-Mead Simplex (NMS) method to study and adjust the phase of a 4-element phased array. In another study, Elkayal et al. [8] optimized a 4-element phased array to minimize focus shift using particle swarm optimization (PSO). Although the previously described studies were successful in focusing on the tumor, the focus range was far wider than the actual tumor area, causing greater damage to the surrounding healthy tissues, and the focusing resolution was obviously insufficient.

In order to increase the resolution, increasing the number of elements of the phased array becomes an intuitive solution [9]. For example, Nguyen et al. [10]

Submitted On: June 09, 2025
Accepted On: September 18, 2025

https://doi.org/10.13052/2025.ACES.J.401002

optimized the excitation of a 24-element phased array using PSO and Lyu et al. [11] optimized an 36-element phased array using differential evolution (DE). However, while these studies improved focusing accuracy to some extent, the optimization results inevitably led to the emergence of excess hotspots in the superficial region of healthy tissues. The specific absorption rates reached 90% [10] and 115% [11] at the tumor. Although it is possible to mitigate the effects of hotspots in this part of the region using physical techniques such as cooling liquids [12], this inevitably makes the therapy procedure more complicated and expensive.

Although it is theoretically impossible to eliminate redundant hotspots due to their inherent nature in the phased array, their effects can be suppressed through optimization [13]. Traditional single-objective optimization algorithms can be limited in their effectiveness at reducing redundant hotspots. Therefore, Baskaran et al. [14] employed a multi-objective genetic algorithm (MOGA) to optimize the excitation of an 18-element phased array , achieving greater tumor coverage and fewer redundant hotspots. However, the tumor selected in this study was in the superficial layer of breast tissue, which may restrict the general applicability of the results. Moreover, MOGA suffers from slow convergence and focus shift, making it difficult to meet clinical needs.

Recent studies have indicated that prevailing optimization algorithms continue to encounter significant obstacles in attaining accurate focusing effects and effectively reducing redundant hotspots. Traditional quantitative indicators such as hotspot to target quotient (HTQ), average power absorption ratio (aPA), and specific absorption rate (SAR) are inadequate for providing a comprehensive characterization of hotspots distribution. Moreover, extant algorithms evince suboptimal efficiency and adaptability.

In this paper, an adaptive multi-objective particle swarm optimization (AMOPSO) algorithm is proposed to address these issues. First, it innovatively introduces the peak power absorption ratio (pPA) as a quantitative indicator, which provides a more comprehensive assessment of hotspot distribution features. Secondly, an adaptive feedback mechanism is designed. This mechanism adjusts key parameters, such as inertia weight and learning factor, based on the discrepancy between the optimized and target results.

The proposed AMOPSO algorithm has been demonstrated to enhance global search efficiency and environmental adaptability of the algorithm through an error feedback-based dynamic parameter adjustment strategy. The incorporation of random perturbation terms and nonlinear fitness functions serves to effectively suppress the premature convergence phenomenon of particle swarm and enhance the robustness of the algorithm. The pPA indicator, when utilized in conjunction with conventional evaluation metrics, fosters a synergistic effect, thereby facilitating the establishment of a multifaceted hotspot control evaluation system. The findings from experiments suggest that, in comparison to conventional optimization algorithms, AMOPSO demonstrates superior performance in critical metrics.

The rest of the paper is organized as follows. Section II describes the research principles of HTP, including quantitative indicators of treatment quality, the optimization algorithm, the breast model and the device. Section III presents a comparative analysis of the optimization results of this algorithm, before concluding with a summary in section IV.

II. THE PROPOSED ALGORITHM

A. Quantitative indicators of treatment quality

The aim of HTP is to accurately concentrate electromagnetic wave energy within the tumor, while preventing the formation of redundant hotspots in healthy tissue. If total thermal damage to the tumor tissue can be accomplished and thermal damage to the surrounding healthy tissue is kept to less than 5%, the HTP is usually regarded as safe and successful [15].

The energy density deposition $Q(r)$ in the breast tissue is expressed as

$$Q(r) = 0.5\sigma(r)|\vec{E}(r)|^2, \tag{1}$$

where $r = (x, y, z)$ are spatial coordinates, $\sigma(r)$ is the conductivity of the tissue and $\vec{E}(r)$ is the total electric field inside the tissue, which is given by

$$\vec{E}(r) = \sum_{i=0}^{N-1} A_I e^{-i\varphi_i} \vec{E}_i(r), \tag{2}$$

where A_i and φ_i are the amplitude and phase delays of the ith antenna element, $\vec{E}_i(r)$ is the electric field provided by the ith antenna, and N ($N = 16$ in this work) is the number of antenna elements in the phased array. Normally, we use SAR as a measure of absorbed electromagnetic energy per unit time per unit mass of a biological tissue [16], in units of W/kg. $SAR(r)$ is expressed as

$$SAR(r) = \frac{Q(r)}{2\rho(r)} = \frac{\sigma(r)|\vec{E}(r)|^2}{2\rho(r)}, \tag{3}$$

where $\rho(r)$ is the density of the tissue. Since the physical properties of breast tissue are incorporated into the SAR calculation, the absorption of electromagnetic wave energy by breast tissue can be accurately observed through the SAR distribution.

When building the HTP optimization model, the focus shift and the number of hotspots are usually taken as the main optimization targets to ensure the precision and safety of the treatment effect, weighing up treatment accuracy and energy distribution uniformity. At the same time, the model must consider several key indicators comprehensively: HTQ, aPA, tumor coverage n% (TC_n) and damaged healthy tissue rate (DHTR) to enhance the therapeutic effect and minimize damage to normal tissues [17].

The focal shift is the spatial distance between the center of the region of strongest energy focus and the center of the target tumor, which is given by

$$FS = \|r_c - r_t\|_2, \tag{4}$$

where $r_t = (x_t, y_t, z_t)$ is the center coordinates of the tumor, $r_c = (x_c, y_c, z_c)$ is the center coordinates of the strongest hotspot, obtained by

$$r_c = \frac{1}{n(H_c)} \sum_{r \in H_c} r, \tag{5}$$

where

$$H_c = \{r \in H_{\max} \mid SAR(r) \geq 0.9 \times \max(SAR(r))\}, \tag{6}$$

$n(H_c)$ is the total number of points belonging to the center area H_c of the strongest hotspot $H_{\max}$, which is expressed as

$$H_{\max} = \arg\max_{H_i} \left(\max_{r \in H_i} SAR(r) \right), \tag{7}$$

$$H_i = \left\{ r \mid SAR(r) \geq \frac{1}{\sqrt{2}} \times \max(SAR(r)) \right\}, \tag{8}$$

H_i is the region of hotspots, and the strongest one is $H_{\max}$. The total number of H_i is the number of hotspots N.

HTQ assesses the relationship between the region of highest energy intensity and the average energy of the tumor. It is expressed as the ratio of average SAR values between in the top 1% healthy tissues and in the tumor, which is

$$HTQ = \overline{SAR}_{V_1} / \overline{SAR}_t, \tag{9}$$

where V_1 is the volume of the top 1% of healthy tissues with SAR values ranking from the highest to the lowest, $\overline{SAR}_{V_1}$ and $\overline{SAR}_t$ are the average SAR value in V_1 and in the tumor.

aPA assesses the relative energy absorbed by tumors. It is calculated by expressing the average energy difference between tumor tissue and healthy tissue, which is

$$aPA = \frac{(\sum P_t)/V_t}{(\sum P_h)/V_h}, \tag{10}$$

where P_t and P_h denote the power absorbed by the tumor and healthy tissue, respectively, V_t and V_h are the volumes of the tumor and healthy tissue, respectively.

TC_n is expressed as

$$TC_n = V_i(SAR > \max(SAR) \times n\%)/V_i, \tag{11}$$

TC_n represents the percentage of tumor volume in which the SAR value exceeds n% of the highest SAR observed within the tumor.

DHTR was calculated using the formula

$$DHTR = V_d / V_n, \tag{12}$$

where V_n is the volume of healthy tissue within 15 mm from the tumor edge, V_d is the volume of damaged healthy tissues.

However, the assessment of HTQ and aPA can vary significantly for different array sizes and breast models. This variability poses challenges in standardizing evaluation criteria and identifying redundant hotspots. When these indicators are used as the objective functions in algorithms, they often fail to effectively reduce redundant hotspots, thereby increasing computational complexity and optimization difficulty. To address these limitations, this study proposes a novel indicator, the pPA, which enables a comprehensive analysis of SAR distribution characteristics and hotspot distribution, particularly the relationship between the strongest absorption region and other high-absorption areas.

The pPA can be obtained through an analytical method based on the correlation of SAR values with their respective domains. The fundamental aspect of the method is the identification and determination of local peaks and locations of SAR values within the tissue by establishing a link between a specific point of interest and its corresponding domain. Subsequently, the strongest peak among these identified peaks is taken to be the main hotspot, whose SAR value is $SAR_{peakmax}$. The maximum value after comparing the SAR value $SAR_{peak}(i)$ at the remaining peak points with the SAR value $SAR_{peakmax}$ at the main hotspot is defined as the pPA, which is expressed as

$$pPA = \max\left(\frac{SAR_{peak}(i)}{SAR_{peakmax}} \right). \tag{13}$$

In comparison with existing indicators, pPA directly quantifies the relative strength of secondary hotspots compared to main hotspot, thereby providing higher accuracy in hotspot characterization. Furthermore, it possesses a discernible threshold for hotspot redundancy: when pPA is less than $1/\sqrt{2}$, SAR distribution guarantees that there is only one valid hotspot [18, 19], accurately quantifying the optimization objective.

B. The proposed algorithm

In the PSO, a population of N particles searches in a space of dimension D. At the tth iteration, the vectors of position $X_{i,t}$ and velocity $V_{i,t}$ of each individual $i(1 \le i \le N)$ in the population are represented by $X_{i,t}^j = (X_{i,t}^1, X_{i,t}^2, \ldots, X_{i,t}^D)$ and $V_{i,t}^j = (V_{i,t}^1, V_{i,t}^2, \ldots, V_{i,t}^D)$, respectively. Each iteration updates the velocity and position of each particle in each dimensional component on the basis of the found locally optimal solution and the globally optimal solution , which is updated as

$$V_{i,t+1}^j = wV_{i,t}^j + c_1 \mathrm{r}_{i,n}^j (P_{i,t}^j - X_{i,t}^j) + c_2 \mathrm{R}_{i,t}^l (G_{i,t}^j - X_{i,t}^j), \tag{14}$$

$$X_{i,t+1}^j = X_{i,t}^j + V_{i,t+1}^j, \tag{15}$$

where $i = 1,2,\ldots,N$, $j = 1,2,\ldots,D$, w is the inertia weight, c_1 and c_2 are the learning factors, $\mathrm{r}_{i,n}^j$ and $\mathrm{R}_{i,n}^j$ are two random numbers uniformly distributed in the range [0,1].

In the context of multi-objective optimization scenarios, existing multi-objective PSO algorithms encounter several limitations when they are extended [20–23]. Firstly, their adaptive strategies are devoid of a robust theoretical foundation, exhibiting an inadequate examination of particle movement characteristics and predominantly relying on a singular search strategy for updating particle states. Secondly, these algorithms neglect to consider the disparities in the optimization capabilities of individual particles, which hinders the achievement of a balance between algorithm convergence and solution diversity when confronted with complex optimization problems. Finally, the switching mechanism between global exploration and local exploitation remains imperfect, causing the algorithms to easily fall into local optimal solutions or suffer from insufficient convergence accuracy.

In order to enable the algorithm to dynamically adjust the balance between local and global searches according to the optimization effect, this paper proposes an adaptive search method combining a feedback adjustment mechanism and a random perturbation strategy. This method uses the discrepancy between the optimized and targeted results as a feedback signal to adaptively adjust the inertia weights and learning factors. The complete flowchart of the algorithm is shown in Fig. 1.

The adaptive functions of each parameter are

$$w(x) = 0.65 + 0.5 \times \cos\left(\frac{\pi}{2\sqrt{x}} + \frac{\pi}{3}\right) + \left(0.5 - 0.1 \times \cos\left(\frac{\pi}{2x}\right)\right) \times r, \tag{16}$$

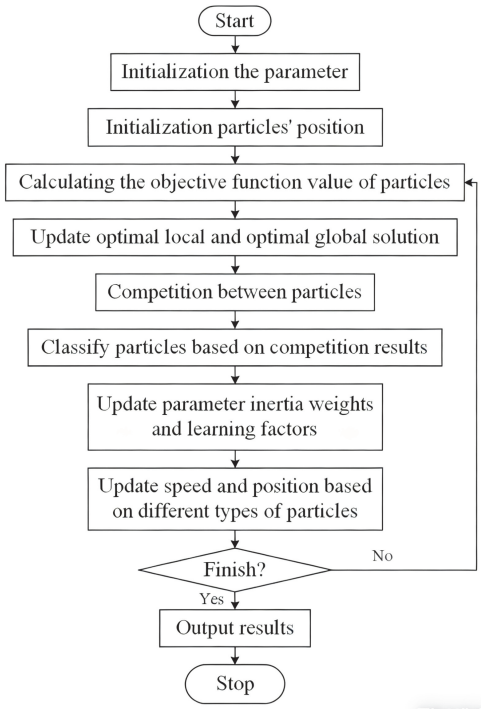

Fig. 1. Flowchart of the AMOPSO algorithm.

$$c_1(x) = 1.6 - 0.4 \times \sin\left(\frac{\pi}{2x}\right) + \left(0.4 - 0.2 \times \cos\left(\frac{\pi}{2x}\right)\right) \times r, \tag{17}$$

$$c_2(x) = 1.4 + 0.4 \times \sin\left(\frac{\pi}{2x}\right) + \left(0.4 - 0.2 \times \cos\left(\frac{\pi}{2x}\right)\right) \times r, \tag{18}$$

where $x = \sum a_i \cdot (opt_i - tar_i)(x > 0)$ is the fitness function related to the target parameters tar_i of the optimization process, a_i is defined as the weight corresponding to the optimized results opt_i, which is influenced by the importance of the ith target result, the range of variation and the optimization process.

The configuration of the parameters is illustrated in Fig. 2. As shown in the figure, it depicts the corresponding values of parameters w, c_1, and c_2 when the fitness function x takes values within the range of [0,20]. Considering the presence of random functions in (16), (17) and (18), the simulation interval is set to 0.01.

The formula is composed of three primary components: a constant term, a trigonometric term, and a random perturbation term. The constant term is established in accordance with the empirical ranges of the inertia weight and learning factor from traditional PSO [20, 21], thereby ensuring that the algorithm maintains its optimization capability during local exploitation. In contrast to the parameter changes observed in conventional

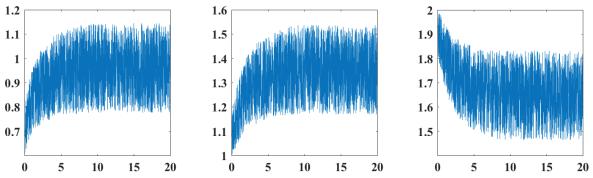

(a) (b) (c)

Fig. 2. Parameter configuration simulation diagram. (a) w, (b) c_1, (c) c_2.

AMOPSO, the trigonometric function term establishes a dynamic adjustment mechanism based on a nonlinear function. It considers the parameter intervals and transition criteria for the global exploration and local exploitation phases, accurately reflecting the dynamic changes in optimization. This nonlinear adaptation enhances global search, thereby preventing premature convergence and ensuring a balance between exploration and exploitation. The random perturbation term employs the random variable r to augment the algorithm's robustness, thereby substantially enhancing population diversity while preserving convergence efficiency. Compared to existing mainstream AMOPSO algorithm, this method demonstrates superior problem adaptability and maintains stable and reliable optimization performance in complex noisy environments and dynamic scenarios.

Furthermore, in order to optimize the utilization of the resources of each individual particle, the velocity is reassigned to those particles that have been identified as outliers over an extended period of time. This enables them to rapidly exit the outlier state. The particle velocity reset function V_r is

$$V_r^j = \frac{a_{FS}}{1+\exp\left(-\left(\Delta FS-5\right)/1.5\right)} + \frac{a_{pPA}}{1+\exp\left(-2\times\Delta pPA\right)} - a, \tag{19}$$

where a_{FS}, a_{pPA} and a are constants. $\Delta FS = FS_{best} - FS_{target}$, FS_{best} and FS_{target} are the optimal and target values of the focus shift. $\Delta pPA = pPA_{best} - pPA_{target}$, pPA_{best} and pPA_{target} are the optimal and target values of pPA, V_r^j is the velocity vector of the newborn particle, which decreases gradually with the optimization process, allowing the search range to shrink gradually to improve accuracy. In comparison with the rudimentary approach employed in existing AMOPSO algorithms [20, 24], the velocity reset strategy, which takes into account the discrepancies between optimized and targeted results, demonstrates superior performance. The system has been demonstrated to adaptively reset velocities for outliers, thereby boosting swarm activity and guiding them back to the search path. This, in turn, accelerates optimization and enhances accuracy.

C. Breast model and phased array device

The phased array model for MTP by the global optimization algorithm is shown in Figs. 3 (a) and (b).

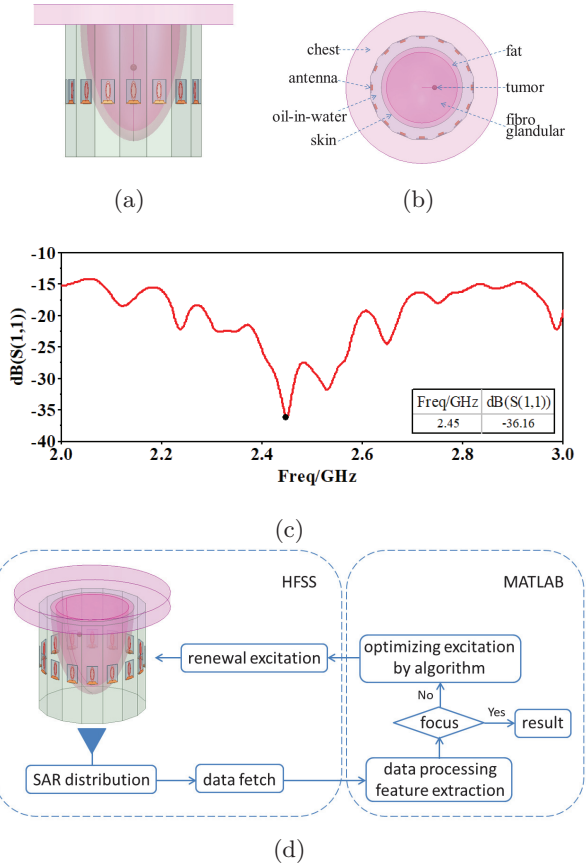

(a) (b) (c) (d)

Fig. 3. Optimization process of phased array excitation in HTP: (a) side view, (b) top view, (c) S_{11} parameters of the phased array element, (d) flowchart of HTP.

The simplified breast model is placed in a circular phased array formed by 16 antenna elements uniformly aligned with a radius of 100 mm and a height of 200 mm. The size of the phased array element is 31.25 mm $\times$ 21.4 mm, and it is made of Rogers RT5880 with dielectric constant of 2.2, loss angle tangent of 0.009, and thickness of 1.575 mm. S_{11} parameter is shown in Fig. 3 (c), which is in working condition with $S_{11} < -10$ dB at 2–3 GHz and achieves a good performance of -36 dB at the operating frequency of 2.45 GHz. The phased array and breast model were immersed in a coupling fluid (oil-in-water) with a relative dielectric constant of 22.9 and a conductivity of 0.07. The breast model consisted of skin, fat, breast fibers, and tumor [25].The HTP optimization process is shown in Fig. 3 (d). SAR distribution data can be obtained by HFSS simulation and then processed and analyzed to obtain the previously mentioned indicators in Matlab. The excitation of

the phased array is iteratively optimized and adjusted according to these indicators until it meets the predefined objectives. Finally, we can obtain the appropriate excitations of elements.

III. RESULTS AND ANALYSIS

A. Experimental results of different optimization algorithms

In order to demonstrate the performance advantages of the proposed AMOPSO algorithm, we compare it with linearly decreasing weights PSO (LDW-PSO) [26], GA [14], DE [11] and an adaptive MOPSO with multi-strategy based on energy conversion and explosive mutation (ecemAMOPSO) [20]. In the course of the comparison experiments, the algorithms were configured to utilize the same population size, objective function, number of iterations, and initial values. The simulations and optimization procedures were applied to tumors located at (0, 35, 35) mm.

The normalized SAR distributions of the optimization effects of different optimization algorithms focusing are shown in Fig. 4. The experimental simulation results are shown in the breast model to observe the SAR distribution more clearly. The red object represents the tumor, and the rectangle represents the simplified antenna structure. The axial and coronal planes are selected based on the location of the tumor center. The normalized SAR distribution is shown in the plan view, and the positions corresponding to the 3D map are marked. It can also be observed that the AMOPSO algorithm achieved accurate focusing and effectively reduced redundant hotspots, and there were no redundant hotspots in the region outside the focal plane of interest.

Table 1 shows the optimization results of each algorithm. As observed, the LDW-PSO algorithm still has difficulty in finding a desirable balance in multi-objective optimization despite its improved weighting strategy. The DE algorithm is unable to achieve synergistic optimization among multiple objectives despite its strong global search capability, thus affecting the overall performance.

Table 1: Quantitative indicators of treatment quality with different algorithms

	FS	**n**	**pPA**	**aPA**	**HTQ**	**TC_{70}**	**DHTR**
DE	1.90	13	0.86	4.22	0.86	96.13%	18.48%
LDW-PSO	1.91	3	0.78	4.62	0.70	94.36%	12.50%
GA	0.36	4	0.71	5.28	0.75	98.91%	9.94%
ecem-AMO-PSO	0.30	3	0.75	5.90	0.75	99.80%	7.77%
AMO-PSO	0.32	1	0.46	5.95	0.64	99.97%	4.53%

While both the GA and ecemAMOPSO algorithms have been demonstrated to achieve high precision in identifying the optimization target, the GA algorithm's capacity for local development is comparatively deficient. This limitation impedes the effective removal of redundant hotspots. The adjustment process of the parameter in ecemAMOPSO is closely coupled with the duration of the iteration, which makes it difficult for the algorithm to achieve stable convergence in a limited time, resulting in redundant hotspots remaining outside the target observation plane. In contrast, the AMOPSO algorithm is significantly superior to other algorithms in all indicators of pPA, HTQ, aPA and DHTR, which proves the excellent comprehensive optimization ability of AMOPSO high precision and multiple objectives.

The excitation results of the phased array obtained after optimization using the AMOPSO algorithm are presented in Table 2. The phase is defined as the relative phase difference with respect to element 1, with a range of $[-180^\circ, 180^\circ]$, and the amplitude is the feeding coefficient, with a range of [0, 1].

Table 2: Excitation of phased array elements

Element Number	**1**	**2**	**3**	**4**
phase(°)	0	39.57	−163.06	38.11
amplitude	1	1	0.78	0.80
Element Number	**5**	**6**	**7**	**8**
phase(°)	−75.19	−157.14	−91.41	−101.58
amplitude	0.59	1	0.82	1
Element Number	**9**	**10**	**11**	**12**
phase(°)	172.56	45.34	−48.15	−160.15
amplitude	0.34	1	1	1
Element Number	**13**	**14**	**15**	**16**
phase(°)	−64.71	49.60	−150.99	42.44
amplitude	0.37	0.97	0.82	1

In the context of microwave hyperthermia treatment plans, the presence of phased array phase errors has been observed to exert an influence on the performance indicators associated with treatment outcomes. A systematic investigation was conducted to evaluate the performance of phased array MHT under specific phase error conditions. To this end, 50 independent replicate experiments were performed, with phase differences fluctuating within a range of $\pm 10^\circ$ [27]. The maximum (Max), minimum (Min), average (Ave), and standard deviation (SD) of the experimental results are shown in Table 3.

The experimental results show that changes in phase difference parameters significantly affect the accuracy of focus positioning. This results in the FS and DHTR exceeding the established limit. While certain indicators may exceed the established limits, statistical analysis reveals that such deviations are not pervasive, and the results persist within acceptable ranges. The majority

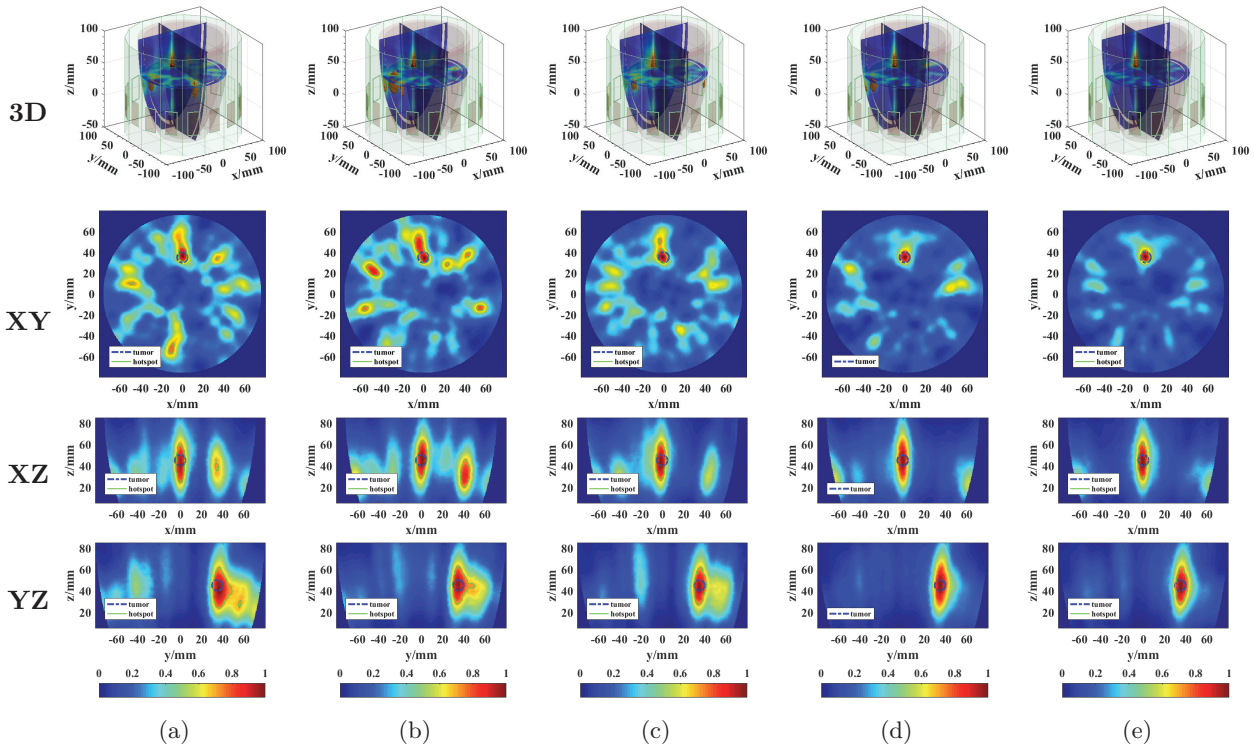

Fig. 4. Normalized SAR distribution with different algorithms. (a) DE, (b) LDW-PSO, (c) GA, (d) ecemAMOPSO, (e) AMOPSO.

Table 3: The impact of phase error on optimization results

	FS	n	pPA	aPA	HTQ	TC_{70}	DHTR
Max	0.526	1	0.653	6.071	0.675	99.951%	5.153%
Min	0.311	1	0.421	5.854	0.639	98.594%	4.297%
Ave	0.373	1	0.522	5.537	0.642	99.873%	4.581%
SD	0.081	1	0.053	0.056	0.006	0.419	0.249

of indicators meet the specified requirements, thereby demonstrating that the phased array system in MHTP exhibits a certain degree of stability and reliability under most conditions.

In consideration of the correlation between the diversity of breast tissues and the efficacy of MHT, this study employs the dielectric constant of breast tissues as the primary variable for experimental analysis [28]. This study systematically investigated the impact of dielectric constant fluctuations within a range of $\pm 10\%$ on key quantitative indicators for thermotherapy. The experimental results are shown in Table 3.

The experimental data demonstrate that alterations in the dielectric constant of the tissue result in variability among all performance indicators of the system. However, it is observed that all indicators meet the established requirements, and the impact is deemed to be within acceptable limits.

Table 4: The impact of dielectric constant fluctuations on optimization results

	FS	n	pPA	aPA	HTQ	TC_{70}	DHTR
Max	0.450	1	0.618	5,962	0.697	99.841%	4.893%
Min	0.320	1	0.445	5.642	0.640	96.714%	4.531%

B. Experimental results of algorithms optimized for tumors at different locations

Due to the intricate distribution of dielectric properties, the difficulty of performing HTP varies for tumors at different locations and depths. To verify that the algorithm proposed can achieve optimal treatment for a wide range of tumors, we performed focused experiments using the AMOPSO algorithm for tumors located at (0, 25, 50) mm, (0, 35, 35) mm, (0, 45, 45) mm and (0, 55, 30) mm, respectively.

The normalized SAR distributions of tumors at different positions are shown in Fig. 5.

As the location of the tumor deepens, electromagnetic waves are more scattered and absorbed when penetrating tissues, which causes the electromagnetic wave energy to be more dispersed and decay more rapidly. It can be observed from Fig. 5 that, as the tumor approaches the mid-axis of the breast tissue, the focal length progressively increases. Simultaneously,

the energy peak outside the focal region slightly rises, and the focal area gradually elongates. This phenomenon can be attributed to the scattering effect experienced by the electromagnetic waves as they penetrate the tissue, leading to a more dispersed energy distribution and thus an elongated focal region. Additionally, the absorption of electromagnetic wave energy by the breast tissue accelerates the attenuation of the waves, causing the focal region to become narrower. This attenuation not only alters the shape of the hotspot but also impacts on the overall efficacy of the treatment.

The results of the focus optimization process for tumors at different locations are presented in Table 5. The DHTR value was found to be less than 5% for all locations that were examined, suggesting that there was minimal damage to healthy tissues. The lowest pPA was observed at the focal position (0,45,40) mm. It is important to note that the aPA exhibited a gradual decrease in trend as the position of the tumor progressed deeper into the breast tissue. This finding suggests a strong correlation between the energy absorption efficiency and the spatial distribution of the focal point.

Table 5: Quantitative indicators of treatment quality optimized at different locations using AMOPSO

	FS	**n**	**pPA**	**aPA**	**HTQ**	**TC_{70}**	**DHTR**
(0,25,50)	0.48	1	0.64	5.08	0.71	96.20%	3.78%
(0,35,35)	0.32	1	0.46	5.95	0.64	99.30%	4.54%
(0,45,45)	0.46	1	0.36	7.88	0.69	99.70%	4.75%
(0,55,30)	0.33	1	0.45	8.46	0.62	100%	4.80%

C. Experimental results for different objective functions in AMOPSO

The AMOPSO algorithm is a system that guides the movement of an individual based on the discrepancy between optimized and target results. The objective function affects the optimization performance of the algorithm. In order to verify the applicability and superiority of the proposed objective function in HTP applications, an experimental comparative analysis was conducted to explore the optimization effect of different objective functions. The minimization objectives that have been selected for the optimization of the treatment of tumors located at (0, 35, 35) mm are as follows

$$\min(FS, 1/aPA), \tag{20}$$

$$\min(FS, HTQ), \tag{21}$$

$$\min(FS, pPA, 1/aPA, HTQ). \tag{22}$$

The optimized normalized SAR distribution is shown in Fig.6. It is evident from Fig. 6 that the outcomes obtained using the three optimization objectives are devoid of focus shift and redundant hotspot problems, thereby substantiating the AMOPSO algorithm's robust generalization capability.

The optimization results for each objective are displayed in Table 6. In the instance of objective (20) being utilized as the optimization objective, the value of aPA was determined to be 33.35% and 33.01% higher compared to objective (21) and (22), respectively. This optimization objective intuitively reflects the difference in energy absorption levels in the region of tumor and healthy tissues, achieved by decreasing the mean energy of the healthy tissue and increasing the mean energy of the tumor tissue. This results in an optimization that exhibits enhanced energy coverage within the region of tumor, though concomitantly results in elevated levels of healthy tissue damage.

Table 6: Quantitative indicators of treatment quality using AMOPSO with different objectives

	FS	**n**	**pPA**	**aPA**	**HTQ**	**TC_{70}**	**DHTR**
Obj.(20)	0.33	1	0.63	0.68	7.91	100%	5.08%
Obj.(21)	0.33	1	0.49	0.66	5.93	99.70%	5.30%
Obj.(22)	0.32	1	0.46	5.95	0.64	99.30%	4.54%

In the instance of objective (21) being utilized as the optimization objective, the value of HTQ was found to be 3.36% lower in comparison to objective (20), yet 3.15% higher than objective (22). The function of objective (21) is to reduce the average energy of healthy tissue, thereby reducing the energy in the tumor. This results in an enhancement of the contrast between the average energy of the tumor and the energy of the region of highest energy intensity within the healthy tissue. However, this adjustment resulted in the facile dispersion of energy to other regions of the tissue, giving rise to aPA values that were 35.01% and 0.23% lower than the values observed for the other two objectives. This resulted in a reduction in energy utilization and an increase in TC_{70}, as well as a decrease in DHTR, in comparison to the other two objectives.

In the instance of objective (22) being utilized as the optimization objective, the indicator of pPA effectively evaluates the distribution of the strongest hotspot and other important hotspots, thus demonstrating the most comprehensive optimization effect. The value of pPA is reduced by 25.8% and 6.1%, and the value of DHTR is reduced by 10.8% and 14.6%, respectively, compared with the other two objectives. It is evident that this has led to a substantial enhancement in the degree of optimization, which has consequently resulted in a notable reduction in the damage caused to healthy tissue, alongside a significant increase in the concentration of microwave energy. This finding suggests that the AOMPSO algorithm, utilizing objective (22) as the

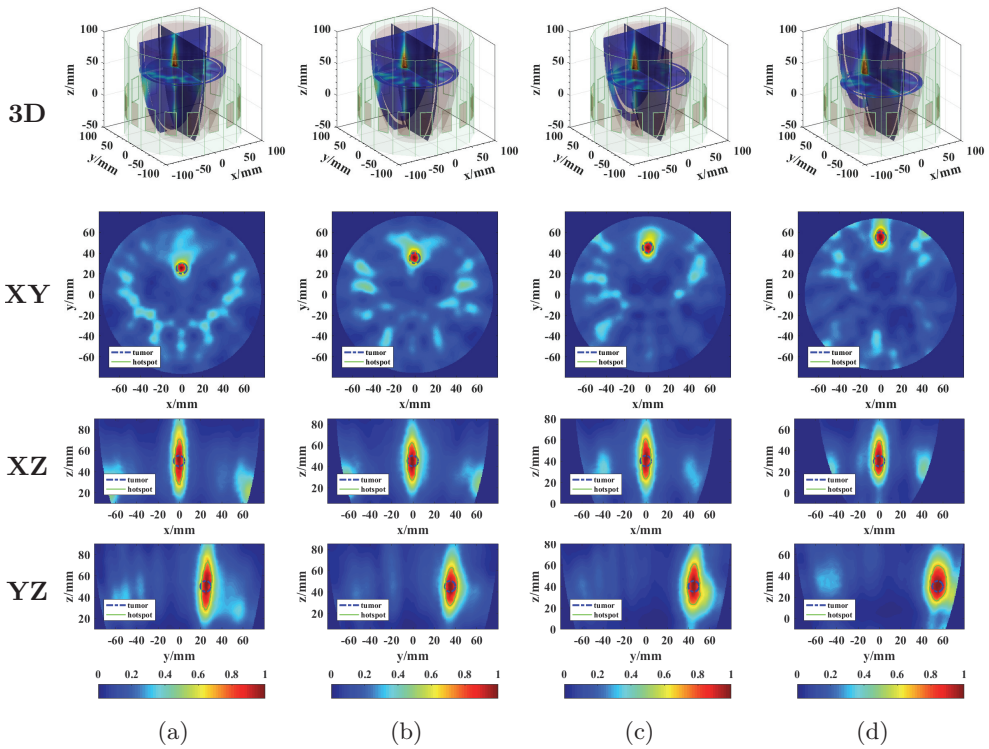

Fig. 5. Normalized SAR distribution with tumors at different locations using AMOPSO. (a) (0,25,50) mm, (b) (0,35,35) mm, (c) (0,45,45) mm, (d) (0,55,30) mm.

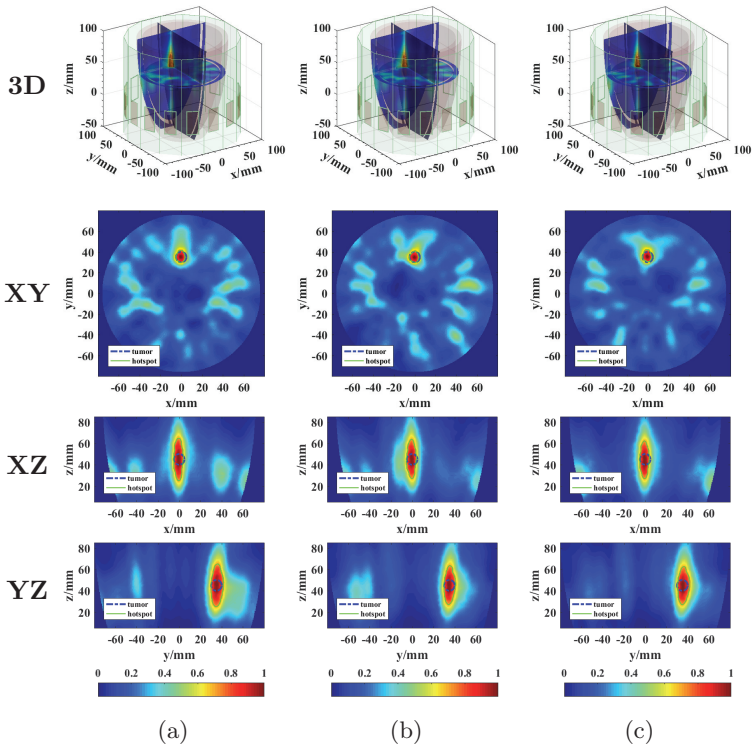

Fig. 6. Normalized SAR distribution with different objectives. (a) Obj.(20), (b) Obj.(21), (c) Obj.(22).

objective, is most effective in the context of phased array microwave hyperthermia treatment for breast cancer. This not only enhances the efficacy of treatment but also ensures the minimization of energy distribution and tissue damage in healthy tissues.

IV. CONCLUSION

In this paper, an AMOPSO algorithm is introduced as a groundbreaking solution to address the problems of focus shift and redundant hotspots in the HTP process of breast cancer. What sets the AMOPSO algorithm apart is its unparalleled superiority, as evidenced by comprehensive comparative analyses against other optimization algorithms. It not only outperforms its counterparts in terms of optimization efficacy but also stands out with its remarkable efficiency. This rapid convergence enables the algorithm to achieve pinpoint focusing accuracy while drastically reducing the number of redundant hotspots, resulting in a significantly enhanced treatment outcome for tumors.

One of the AMOPSO algorithm's most distinctive features is its exceptional adaptability to different tumor locations. An exhaustive investigation into its focalizing aptitudes reveals that the algorithm reliably attains predetermined objectives with exactitude, notwithstanding the intensifying complexity associated with more profound tumor locations. This showcases its remarkable ability to maintain accurate focusing over a wide range of scenarios, highlighting its broad applicability and versatility, which far surpasses that of many existing algorithms.

Additionally, the paper meticulously compares different SAR-based objective functions and uncovers a unique advantage of the AMOPSO algorithm. By incorporating pPA as an objective function, the algorithm substantially improves treatment effectiveness, outperforming traditional objective functions commonly used in HTP. This innovative approach represents a significant advancement in the field and demonstrates the AMOPSO algorithm's potential to redefine microwave thermal therapy optimization standards.

REFERENCES

[1] Y. Xu, M. Gong, Y. Wang, Y. Yang, S. Liu, and Q. Zeng, "Global trends and forecasts of breast cancer incidence and deaths," *Scientific Data*, vol. 10, no. 1, p. 334, May 2023.

[2] W. Zhu, S. Pan, J. Zhang, J. Xu, R. Zhang, Y. Zhang, Z. Fu, Y. Wang, C. Hu, and Z. Xu, "The role of hyperthermia in the treatment of tumor," *Critical Reviews in Oncology/Hematology*, vol. 204, p. 104541, Dec. 2024.

[3] A. Westra and W. Dewey, "Variation in sensitivity to heat shock during the cell-cycle of Chinese hamster cells in vitro," *International Journal of Radiation Biology and Related Studies in Physics, Chemistry and Medicine*, vol. 19, no. 5, pp. 467–477, Jan. 1971.

[4] X. Chen, L. Tan, T. Liu, and X. Meng, "Micro-nanomaterials for tumor microwave hyperthermia: Design, preparation, and application," *Current Drug Delivery*, vol. 14, no. 3, pp. 307–322, Apr. 2017.

[5] C. G. Pang, Z. F. Huang, S. L. Ji, H. Zhang, Y. L. Zhao, and Y. C. Hu, "Microwave-induced hyperthermia in situ in the treatment of tumors of proximal humerus: Long-term results with functionary sparing surgery," *Journal of Orthopaedic Surgery and Research*, vol. 18, no. 1, p. 433, June 2023.

[6] M. T. Bevacqua, R. Gaffoglio, G. G. Bellizzi, M. Righero, G. Giordanengo, L. Crocco, G. Vecchi, and T. Isernia, "Field and temperature shaping for microwave hyperthermia: Recent treatment planning tools to enhance SAR-based procedures," *Cancers*, vol. 15, no. 5, p. 1560, Mar. 2023.

[7] S. Curto, A. Garcia-Miquel, M. Suh, N. Vidal, J. M. Lopez-Villegas, and P. Prakash, "Design and characterisation of a phased antenna array for intact breast hyperthermia," *International Journal of Hyperthermia*, vol. 34, no. 3, pp. 250–260, Apr. 2018.

[8] H. A. Elkayal and N. E. Ismail, "Efficient focusing of microwave hyperthermia for small deep-seated breast tumors treatment using particle swarm optimization," *Computer Methods in Biomechanics and Biomedical Engineering*, vol. 24, no. 9, pp. 985–994, July 2021.

[9] X. Tang, X. Qing, N. Nasimuddin, Y. Zhou, B. Luo, W. Wang, and F. Chin, "Beam steering resolution for large antenna array," in *2021 IEEE International Symposium on Antennas and Propagation and USNC-URSI Radio Science Meeting (APS/URSI)*, pp. 273–274, IEEE, Singapore, Singapore, Dec. 2021.

[10] P. T. Nguyen, A. Abbosh, and S. Crozier, "Three-dimensional microwave hyperthermia for breast cancer treatment in a realistic environment using particle swarm optimization," *IEEE Transactions on Biomedical Engineering*, vol. 64, no. 6, pp. 1335–1344, June 2017.

[11] C. Lyu, W. Li, and B. Yang, "Differential evolution optimization of microwave focused hyperthermia phased array excitation for targeted breast cancer heating," *Sensors*, vol. 23, no. 8, p. 3799, Apr. 2023.

[12] M. Converse, E. Bond, B. Veen, and C. Hagness, "A computational study of ultra-wideband versus narrowband microwave hyperthermia for breast cancer treatment," *IEEE Transactions on Microwave Theory and Techniques*, vol. 54, no. 5, pp. 2169–2180, May 2006.

[13] Y. Zhang, Z. Han, S. Tang, S. Shen, C.-Y. Chiu, and R. Murch, "A highly pattern-reconfigurable

planar antenna with 360Â° single- and multi-beam steering," *IEEE Transactions on Antennas and Propagation*, vol. 70, no. 8, pp. 6490–6504, Aug. 2022.

[14] D. Baskaran and K. Arunachalam, "Multiobjective optimization of microwave phased array excitation for targeted tissue heating with reduced channel power in hyperthermia treatment planning," *IEEE Transactions on Microwave Theory and Techniques*, vol. 70, no. 1, pp. 622–630, Jan. 2022.

[15] O. Kivekäs, T. Lehtiniemi, and P. Vainikainen, "On the general energy-absorption mechanism in the human tissue," *Microwave and Optical Technology Letters*, vol. 43, no. 3, pp. 195–201, Nov. 2004.

[16] H. P. Kok, G. Schooneveldt, A. Bakker, R. De Kroon-Oldenhof, L. Korshuize-van Straten, C. E. De Jong, E. Steggerda-Carvalho, E. D. Geijsen, L. J. A. Stalpers, and J. Crezee, "Predictive value of simulated SAR and temperature for changes in measured temperature after phase-amplitude steering during locoregional hyperthermia treatments," *International Journal of Hyperthermia*, vol. 35, no. 1, pp. 330–339, Dec. 2018.

[17] Z. Xi, X. Wang, K. Ye, and X. Wang, "Performance evaluation of focused microwave brain hyperthermia guided by microwave-induced thermoacoustic tomography," *IEEE Journal of Electromagnetics, RF and Microwaves in Medicine and Biology*, vol. 7, no. 4, pp. 383–391, Dec. 2023.

[18] A. Buffi, P. Nepa, and G. Manara, "Design criteria for near-field-focused planar arrays," *IEEE Antennas and Propagation Magazine*, vol. 54, no. 1, pp. 40–50, Feb. 2012.

[19] Q. Liang, B. Chen, H. Wu, C. Ma, and S. Li, "A novel modified sparrow search algorithm with application in side lobe level reduction of linear antenna array," *Wireless Communications and Mobile Computing*, vol. 2021, no. 1, p. 9915420, Jan. 2021.

[20] W. Huang and W. Zhang, "Adaptive multi-objective particle swarm optimization with multi-strategy based on energy conversion and explosive mutation," *Applied Soft Computing*, vol. 113, p. 107937, Dec. 2021.

[21] Q. Gu, M. Jiang, S. Jiang, and L. Chen, "Multi-objective particle swarm optimization with R2 indicator and adaptive method," *Complex & Intelligent Systems*, vol. 7, no. 5, pp. 2697–2710, Oct. 2021.

[22] M. Mansouri, H. R. Safavi, and F. Rezaei, "An improved MOPSO algorithm for multi-objective optimization of reservoir operation under climate change," *Environmental Monitoring and Assessment*, vol. 194, no. 4, p. 261, Mar. 2022.

[23] J. Gong, H. Li, H. Yu, L. Shu, Z. Zhang, X. Han, and W. Lun, "Optimization of multi-pass coating for magnetic-thermal-assisted laser cladding based on data-enhanced WOA-DE-TELM and LHS-AMOPSO algorithm," *Surface and Coatings Technology*, vol. 497, p. 131765, Feb. 2025.

[24] G. Y. Yi, M. J. Kim, H. I. Kim, J. Park, and S. H. Baek, "Hyperthermia treatment as a promising anti-cancer strategy: Therapeutic targets, perspective mechanisms and synergistic combinations in experimental approaches," *Antioxidants*, vol. 11, no. 4, p. 625, Mar. 2022.

[25] C. Lyu, W. Li, S. Li, Y. Mao, and B. Yang, "Design of ultra-wideband phased array applicator for breast cancer hyperthermia therapy," *Sensors*, vol. 23, no. 3, p. 1051, Jan. 2023.

[26] H. Liu, X.-W. Zhang, and L.-P. Tu, "A modified particle swarm optimization using adaptive strategy," *Expert Systems with Applications*, vol. 152, p. 113353, Aug. 2020.

[27] G. He, X. Gao, and R. Zhang, "Impact analysis and calibration methods of excitation errors for phased array antennas," *IEEE Access*, vol. 9, pp. 59010–59026, 2021.

[28] A. Martellosio, M. Pasian, M. Bozzi, L. Perregrini, A. Mazzanti, F. Svelto, P. E. Summers, G. Renne, L. Preda, and M. Bellomi, "Dielectric properties characterization from 0.5 to 50 GHz of breast cancer tissues," *IEEE Transactions on Microwave Theory and Techniques*, vol. 65, no. 3, pp. 998–1011, Mar. 2017.

Si Li was born in Harbin, Heilongjiang, China, in 1987. She received the B.S. degree in electrical information engineering from the Jiangsu University of Science and Technology, Zhenjiang, China, in 2011, and the Ph.D. degree in information and communication engineering from Harbin Engineering University, Harbin, in 2018. She is now an Assistant Professor with the School of Oceanology, Jiangsu University of Science and Technology. Her research interests include metamaterials and antenna designs.

Yifan Shen was born in Wuxi, Jiangsu Province, China, in 2000. She received her B.S. degree in electronic information science and technology from Ocean College, Jiangsu University of Science and Technology in 2019. She is currently a graduate student at Ocean College, Jiangsu University of Science and Technology. Her research focuses on the cross-application of microwave technology, especially microwave hyperthermia treatment, including antenna design and optimization, phased array systems, and adaptive beamforming algorithms.

Atef Z. Elsherbeni is a renowned expert in electromagnetism, currently a professor at the Colorado School of Mines, and an IEEE Fellow and ACES Fellow. He received his Ph.D. in electrical engineering from the University of Manitoba in 1987 and subsequently taught at the University of Mississippi, where he held several academic and administrative positions. Elsherbeni's research has focused on computational electromagnetics, particularly in the application of finite-difference time-domain (FDTD) and finite-element methods (FEM). He has published a large number of academic papers and has given keynote speeches at several international conferences to share his research results and experience.

Yunlong Mao was born in Taizhou, Jiangsu, in 1989. He received the B.S. degree in electrical information engineering from the Jiangsu University of Science and Technology, Zhenjiang, China, in 2011, and the Ph.D. degree in information and communication engineering from Harbin Engineering University, Harbin, in 2018. He is now an Assistant Professor with the School of Oceanology, Jiangsu University of Science and Technology. His research interests include antennas and finite-difference time-domain method.

Cheng Lyu received her Bachelor's degree from Harbin Institute of Technology (HIT) in 2014 and earned his Doctor of Engineering degree in Information and Communication Engineering from Harbin Engineering University (HEU) in 2023. She currently serves as a Professor at Heilongjiang Agricultural Engineering Vocational College. Her research focuses on the intersection of microwave technology, particularly microwave thermotherapy for breast cancer, where she investigates non-invasive treatment systems. In the field of wireless communications, her expertise encompasses antenna design and optimization, phased array systems, and adaptive beamforming algorithms. Her work aims to advance both therapeutic technologiesand enhance the performance of intelligent antenna arrays for breast cancer hyperthermia therapy systems, bridging engineering innovation with potential clinical impact.

Application of Ground-Clump Method to Verification of Half-Space Dyadic Green's Matrices

Nikola Basta[1] and Branko Kolundžija[1,2]

[1]Department of General Electrical Engineering
University of Belgrade – School of Electrical Engineering, Belgrade 11120, Serbia
nbasta@etf.rs

[2]WIPL-D d.o.o.
Belgrade 11070, Serbia
kol@etf.rs

Abstract – A simple, robust, and easy-to-implement method is considered for verification of homogenous half-space dyadic Green's matrices (DGMs) that relate electric and magnetic fields to elementary current sources placed near an infinite ground plane. The DGMs, as a rule, are calculated using either the Sommerfeld integrals or their approximations. The verification is based on an alternative method for evaluation of DGMs, in which elementary current sources are modeled by electrically small antennas and the infinite ground plane is modeled by a finite-sized piece of ground, i.e. the ground clump. The method is demonstrated by using a typical 3-D EM solver based on the method-of-moments (MoM) solution of surface integral equations (SIEs). The single-antenna scenario is proved effective for obtaining results with controllable accuracy, with relative error going from 10^{-2} to 10^{-5}, which is demonstrated for ground clumps up to 20λ in diameter. A set of three electric and three magnetic dipoles is recommended for fast verification of DGMs.

Index Terms – Dyadic Green's matrix, Hertzian dipole, method of moments, Sommerfeld integrals, surface integral equation.

I. INTRODUCTION

For the past 100 years, there has been continuous interest in simulating antenna and scattering scenarios above and inside real ground (the half-space problem) [1–3]. This interest has risen with the recent development of space, aerial, and land systems for applications such as microwave remote sensing, ground-penetrating radar, and propagation of radio waves [4–8].

In order to compute the electromagnetic (EM) field of a realistic antenna near the half-space interface, one must first find the field responses to elementary electric and magnetic current sources in the same environment. These responses constitute the so-called dyadic Green's matrices (DGMs), the elements of which are either Sommerfeld integrals (SIs) or their linear combinations. There are many proposed solutions to SIs, i.e. the elements of DGMs, both approximate analytical and numerical. In this study, we consider solutions that are appropriate for large-scale homogenous half-space problems [9–13], and verifiable in terms of accuracy. The interest for such scenarios is high within the scientific and industrial community, e.g. in automotive [14], which motivates this study.

There are few reliable verification methods for DGMs that are available in the open literature. One straight-forward and direct method would be comparison of the obtained numerical results of individual SIs to the proven numerical values from previously published work [15]. In other methods, the authors refer to the integrals of Sommerfeld type (not necessarily the original SIs), the solution of which is known in closed form, thus verifying their numerical algorithms with *exact* error calculation [10, 16]. Most of the published approaches are, actually, *indirect* methods. For instance, when computing particular matrix elements of SIs one can observe their convergence, while increasing the computational resources [13, 17], but there is no easy way to check if an SI is converging to a wrong solution. Other methods rely on representative observables (e.g. input impedance of antenna, magnitude of electric or magnetic near and far field, radiation pattern) that are verified via results obtained from simulations of complex, yet approximate half-space scenarios, using 3-D EM simulation tools [18–22]. The major downside of all these approaches is the lack of a thorough verification process and of guidelines for accuracy evaluation of arbitrary SI.

Therefore, a more general approach for verification of half-space DGMs is required. It is desirable that

Submitted On: June 11, 2025
Accepted On: September 12, 2025

https://doi.org/10.13052/2025.ACES.J.401003

such a verification method can evaluate the EM field with various accuracy levels, and that the evaluation can be performed by the computational resources available. One such method is to model the infinite ground half-space by a finite sized piece of ground, i.e. the ground clump [23]. Although the ground-clump method is not the most efficient one, it is robust, reliable, and easy to implement in any frequency-domain general-purpose 3-D EM solver that can (a) model arbitrary composite metal and dielectric structures of finite size and (b) control the accuracy of the simulation by increasing the computational resources (number of unknowns, memory, and CPU time) [24–26].

In order to achieve the postulated objective, we propose a method based on simulation of two scenario projects in a commercial tool. In the first scenario, the elementary electric and magnetic dipoles are modeled as short dipole antennas and small loop antennas, respectively, in free space. In the second scenario, these antennas are placed in the vicinity of infinite ground plane, approximated by a specifically designed model of finite-sized piece of ground, i.e. a ground clump.

The desired DGMs are obtained by processing the two simulation results of input antenna impedances, and electric and magnetic fields in a selected grid of spatial points. Furthermore, we propose the following novelties: (a) rapid-verification set made of three orthogonal dipole antennas and three orthogonal loop antennas with minimal coupling, (b) optimal truncated ground-clump model for modeling of infinite ground boundary with respect to computational resources, (c) strategies for rapid verification of DGMs and strategies for assessment of high accuracy, and (d) rules for adjusting the geometry of the antennas and of the truncated ground clump (TGC), as well as simulation parameters, that allow for desirable accuracy with as low computer resources as possible.

In this paper, we address only the homogenous half-space problems, with particular interest in electrically large scenarios, whereas the multilayered or grounded-slab problems [11, 27, 28] are out of scope of this work. The implemented EM field is computed using all of the near-field terms, making the method valid for arbitrary source-observer distances. However, since the far field can be easily obtained using the reciprocity theorem and Fresnel reflection coefficients, the scope of this work is the near and intermediate radiation zone.

The basic concept is roughly presented in [29], while the details are elaborated in Section II. Application of the verification method by using a typical 3-D EM solver based on surface integral equations (SIEs) is described in Section III. Numerical examples are given in Section IV and the conclusions in Section V.

II. GENERAL CONCEPT OF THE VERIFICATION METHOD

Let us consider x, y, and z-oriented elementary Hertzian electric dipoles of length Δl and electric-current intensities I_x^{e}, I_y^{e}, and I_z^{e}, respectively. The dipoles are placed at source point A, on z-axis at height z' above lossy homogeneous half-space (real ground) of permittivity $\varepsilon = \varepsilon_0\varepsilon_r$ and permeability $\mu = \mu_0\mu_r$, as shown in Fig. 1. (Alternatively, we will consider x, y, and z-directed Hertzian magnetic dipoles of length Δl and magnetic current intensities I_x^{m},I_y^{m}, and I_z^{m}.)

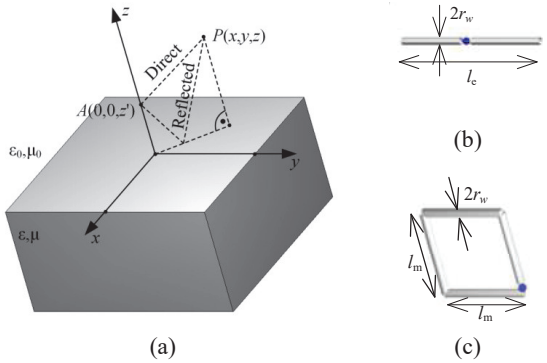

Fig. 1. Scenario in general purpose 3-D EM solver. (a) Finite-sized-body approximation of infinite half-space. (b) Model of y-oriented Hertzian electric dipole. (c) Model of x-oriented Hertzian magnetic dipoles.

The total electric field vector at an arbitrary observation point P, which is placed above the half-space, represents the sum of the direct field due to the dipoles and their field reflected from the boundary surface of the half-space. Cartesian components of the reflected electric field vector, $\mathbf{E}^{\mathrm{e}}$, are related to the set of Hertzian dipoles by DGM as:

$$\begin{bmatrix} E_x^{\mathrm{e}} \\ E_y^{\mathrm{e}} \\ E_z^{\mathrm{e}} \end{bmatrix} = \begin{bmatrix} G_{xx}^{\mathrm{ee}} & G_{xy}^{\mathrm{ee}} & G_{xz}^{\mathrm{ee}} \\ G_{yx}^{\mathrm{ee}} & G_{yy}^{\mathrm{ee}} & G_{yz}^{\mathrm{ee}} \\ G_{zx}^{\mathrm{ee}} & G_{zy}^{\mathrm{ee}} & G_{zz}^{\mathrm{ee}} \end{bmatrix} \begin{bmatrix} I_x^{\mathrm{e}} \\ I_y^{\mathrm{e}} \\ I_z^{\mathrm{e}} \end{bmatrix} \Delta l. \qquad (1)$$

Formally, the same relations can be written for Cartesian components of reflected magnetic field, $\mathbf{H}^{\mathrm{e}}$, due to Hertzian electric dipoles, as well as for Cartesian components of reflected electric and magnetic fields, $\mathbf{E}^{\mathrm{m}}$ and $\mathbf{H}^{\mathrm{m}}$, due to Hertzian magnetic dipoles. (In these cases, the superscripts for DGM elements are "me", "em", and "mm".) The total number of DGM elements to be evaluated in one point is 36. Usually, the high-accuracy evaluations of these matrix elements are performed by numerically computing the individual SIs, which is also the path taken here, in which we followed [12, 13, 15]. Final expressions are given in [30]. The

total number of integrals to be evaluated is 28. Obviously, it is a challenging task not only to develop a code that performs this numerical evaluation, but also to verify the accuracy of the results in the broad range of parameters of interest.

In this paper, we will illustrate verification of DGMs using a general-purpose 3-D EM solver in frequency domain in which we consider the reflected field at observation point P above ground, due to x, y and z-oriented Hertzian dipoles at the source point A (Fig. 1). Since the reflected field is mainly due to the nearby piece of the ground, for an approximate evaluation of reflected field at this point, it suffices to take into account only a finite part of this scenario. This finite size scenario can be modeled in any general-purpose 3-D EM solver. The ground is modeled as a body of finite size (ground clump), in the shape of a vertical cylinder of arbitrary cross-section, made of lossy homogeneous material of complex relative permittivity ε_{r}. The cylindrical body of square cross-section is shown in Fig. 1 (a).

Elementary Hertzian dipoles are modeled as equivalent thin-wire antennas. "Equivalent" means that thin-wire antennas produce approximately the same electric and magnetic fields as elementary Hertzian dipoles, at least for distances between source and observation points much greater than the antenna dimensions. In particular, the elementary Hertzian *electric* dipole is modeled as electrically short symmetrical linear dipole antenna of length l_{e} ($l_{\mathrm{e}} \ll \lambda$) as shown in Fig. 1 (b). Note that the total current along one arm of such antenna decreases linearly from input current I_0 to zero. Hence, in order for such an antenna to produce approximately the same electric and magnetic field as Hertzian electric dipole, it is necessary that:

$$I^{\mathrm{e}}\Delta l = \frac{I_0 l_{\mathrm{e}}}{2}. \tag{2}$$

The elementary Hertzian *magnetic* dipole is modeled as electrically small, square-loop antenna of side length l_{m} ($l_{\mathrm{m}}^2 \ll \lambda^2$), as shown in Fig. 1 (c). In order for such an antenna to produce approximately the same electric and magnetic field as Hertzian magnetic dipole, it is necessary that:

$$I^{\mathrm{m}}\Delta l = \mathrm{j}\omega\mu_0 I_0 l_{\mathrm{m}}^2. \tag{3}$$

The general verification procedure is performed in several steps:

1. One by one, equivalent wire antennas, shown in Figs. 1 (b) and 1 (c), are placed in the source point A, above ground clump, as depicted in Fig. 1 (a).
2. For each such project, the simulation is performed with and without the ground clump, resulting in total and direct field at observation point P.
3. Difference of these two fields gives the reflected field at observation point P.
4. Once the reflected field is known, one column of the DGM elements can be determined from equation of type (1).

For instance, let us consider the first project, in which the wire antenna equivalent to x-directed elementary Hertzian electrical dipole is placed above the ground clump. After the third step, the reflected field $\mathbf{E}^{\mathrm{e}}$ is determined. Since in these simulations I_y^{e} and I_z^{e} are equal to zero, the 1st column of DGM can be determined from (1) as:

$$G_{xx}^{\mathrm{ee}} = \frac{E_x^{\mathrm{e}}}{I_x^{\mathrm{e}}\Delta l}, \quad G_{yx}^{\mathrm{ee}} = \frac{E_y^{\mathrm{e}}}{I_x^{\mathrm{e}}\Delta l}, \quad G_{zx}^{\mathrm{ee}} = \frac{E_z^{\mathrm{e}}}{I_x^{\mathrm{e}}\Delta l}, \tag{4}$$

where $I_x^{\mathrm{e}}\Delta l = I_0 l_{\mathrm{e}}/2$ according to (2) and I_0 is the current intensity of ideal current generator used for excitation of the wire antenna. In particular, by setting unit value for $I^{\mathrm{e}}\Delta l$, DGM elements in (4) become equal to electric field components. (Alternatively, the wire antenna can be excited by an ideal voltage generator. In that case its voltage should be adjusted to give the same input current I_0 in two scenarios used in the second step.)

The accuracy of DGM elements evaluated in this way depends on two factors: (1) the accuracy of the finite size scenario simulation and (2) the size of the ground clump, intended to emulate the infinite ground. In the first case, the accuracy can be improved by increasing the resources used for the simulation (e.g. number of unknowns, memory, and CPU time). In the second case, the ground clump can be enlarged, which also increases the resources used for the simulation. In this way, the accuracy of DGM elements can be systematically increased up to desired level.

The verification method described above can be easily adjusted for the field transmitted into the ground, or for elementary Hertzian dipoles placed inside the ground.

III. IMPLEMENTATION OF THE VERIFICATION METHOD USING TYPICAL 3-D EM SOLVER BASED ON SURFACE INTEGRAL EQUATIONS

The proposed verification method is applied using WIPL-D Pro [26], a typical general-purpose frequency-domain 3-D EM solver based on method-of-moments solution of surface integral equations (MoM/SIE). In the case of MoM/SIE methods, the finite size material body is taken into account by equivalent electric and magnetic currents, placed over its surface. These currents are directly related to the components of the electric and magnetic field that are tangential to the surface. Note that in the case of lossy ground, electric and magnetic

field weaken rapidly with the distance from the Hertzian dipoles, so that for a large enough ground clump, the equivalent currents on the sides and bottom of the ground clump are negligible compared to those on the top. Consequently, the side and bottom surfaces can be omitted from the ground-clump model without effect on accuracy of simulation [23]. In the case of lossless ground, even though the decline of the field is somewhat slower, the same approximation can be applied. In the remainder of the text, such finite-sized model of ground will be referred to as TGC.

In this application, we started with a ground clump in the form of a vertical cylinder of height $h = 2a$, of circular cross-section of radius a, as shown in Fig. 2 (a). The total surface area of such clump is $S = 6a^2\pi$. In the MoM/SIE solvers, the number of unknowns and related simulation time depends on surface area in wavelengths squared. This number can be reduced using higher order basis functions (up to 7^{th} order) over quadrilateral patches, whose sides have maximum dimension of two wavelengths in air, i.e. $d_{\max} = 2\lambda$. In this case, the number of unknowns needed per wavelength squared of the clump surface for typical real ground and default simulation parameters is about 64, so that the total number of unknowns approximately amounts to $N = 1200\ (a/\lambda)^2$. Generally, all problems up to 120,000 unknowns can be easily solved on a standard desktop machine. It means that radius of the ground clump can be easily increased up to $a = 10\lambda$. By omitting the side and bottom surfaces, the cylindrical ground clump is reduced to a circular ground surface, as shown in Fig. 2 (b). In this way, the active surface for simulation, as well as the number of unknowns, is reduced approximately six times. Accordingly, the radius of such TGC can be easily increased to $a = 25\lambda$. In addition, diffraction effects at the sharp edge of circular TGC can be mitigated by adding a rounded rim, as shown in Fig. 2 (c). It is found that the optimal value for rim radius is half of a wavelength, $r_a = \lambda/2$, since its further increase does not further mitigate the diffraction effects, but increases the number of unknowns.

One way to improve the accuracy of simulation is to increase the number of patches, while keeping more or less the same maximum order of basis functions per patch. To enable such functionality, the initial model is created using the patches whose sides have maximum dimension much greater than $d_{\max}$, while internal meshing routine is automatically used to subdivide the initial mesh into minimal number of patches whose sides have maximum dimension not exceeding $d_{\max}$. In this case, by keeping more or less the same maximum order of basis functions per patch, the number of patches can be increased by decreasing $d_{\max}$. It is found that high accuracy of simulation is achieved by setting $d_{\max} = 0.8\lambda$ all over the model, and $d_{\max} = 0.4\lambda$ over the inner circle of radius $b = \lambda$, as shown in Fig. 2 (d). In this way the number of unknowns is increased approximately six times.

Antennas are modeled using WIPL-D Pro's built in thin-wire approximation, in which the wire segments are modeled as cylinders, as previously shown in Fig. 1. Dimensions of antennas are set to $l_{\text{e}} = \lambda/500$, $l_{\text{m}} = \lambda/250$, and $r_{\text{w}} = \lambda/30{,}000$. The number of unknowns used for antennas is negligible, being that $N = 1$ for the dipole antenna and $N = 4$ for the loop antenna. The antennas are excited by ideal voltage generators.

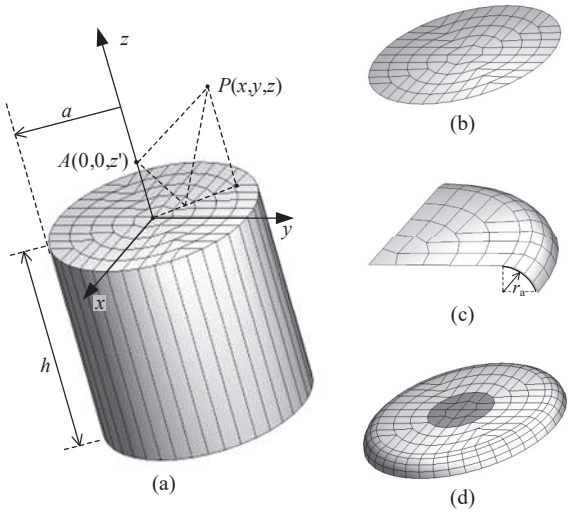

Fig. 2. Different realizations of truncated ground clump. (a) Cylindrical clump. (b) Circular disk. (c) Enlarged part of disk with additional curved rim for diffraction mitigation. (d) Entire disk with a curved rim and a colored central disk, denoting part of the clump surface with local settings.

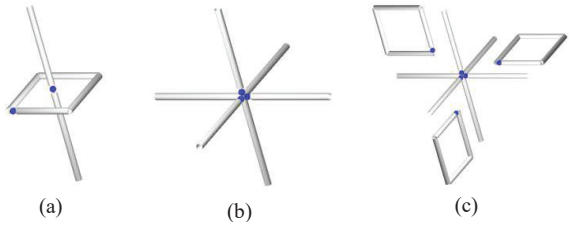

Fig. 3. Examples of excitations that consist of elementary electric- and magnetic-current sources, realized as wire models. Electric-current sources are short dipoles, whereas magnetic-current sources are simulated as short square wire loops. (a) A pair of collinear electric-current and magnetic-current sources. (b) Three orthogonal electric-current sources. (c) Six coexisting sources.

To speed up the verification process, a number of equivalent wire antennas can be combined into an antenna system, as a single project, by exciting one-generator-at-a-time (OGAT) operation mode. Namely, the most consuming part in MoM/SIE simulation is the evaluation of the MoM matrix and its LU decomposition. Once the LU decomposition is performed, the solution of the matrix equations can be quickly obtained for various excitations columns by forward and backward substitution. This is exactly how the OGAT mode operates: one-by-one voltage generator is turned on, while all other generators are turned off, giving each time the corresponding excitation columns. For each excitation column, the solution is found for overall currents and electric and magnetic fields are evaluated in a grid of points of interest. If the coupling between antennas is negligible, the results obtained for each excitation column will correspond to those of a stand-alone antenna. For example, there will be no coupling at all if we combine wire antennas equivalent to vertical Hertzian electric and magnetic dipoles, as shown in Fig. 3 (a), or wire antennas equivalent to x, y, and z-directed Hertzian electric dipole, as shown in Fig. 3 (b). Also, there is a practically negligible coupling between three orthogonal loop antennas, even if they are combined with the system of electric dipoles, resulting in configuration shown in Fig. 3 (c).

Once placed above the ground clump, all antennas will be additionally coupled. However, if the antenna system is not too close to the ground clump, this coupling remains negligible.

IV. NUMERICAL EXAMPLES

In order to analyze the proposed verification procedure, we perform numerical simulations, in which SI solutions, obtained by applying the approach from [13] to equations elaborated in [30], are tested against the reference TGC MoM-based solutions. We assume an arbitrary real ground with relative permittivity $\varepsilon_r = 10 - j5$ and relative permeability $\mu_r = 1$, above which unit current sources, Hertzian dipoles, are placed and operating at frequency $f = 1$ GHz. All examples consider only the reflected field from the real ground due to the Hertzian dipoles, as well as their wire equivalents, excited by $I^e \Delta l = 1\,\text{Am}$ and $I^m \Delta l = 1\,\text{Vm}$. The presented results are calculated in single precision. Specific to each example is the type of excitation antenna system, the type of TGC, the radius of TGC, the heights of the source z' and of the observation point z, and the range of x- and y-coordinates for observation points.

A. Six-antenna scenario: Rapid verification

In the first example, the fast verification method is demonstrated. The radius of the ground clump, shown in Fig. 2 (c), and the maximum patch size are adjusted to $a = 2.5\lambda$ and $d_{\max} = 0.8\lambda$, respectively. The full set of dipoles, shown in Fig. 3 (c), is placed at height $z' = 0.1\lambda$. The reflected electric and magnetic fields are evaluated in yOz-plane at height of $z = z'$, in a range of y-coordinates, $y \in [0.01\lambda, a]$. The field magnitudes are shown in Fig. 4. Generally, excellent agreement between TGC and SI solutions is observed. The only exception are the results for magnetic field due to equivalent y-directed Hertzian electric dipole in a short range of y-coordinates, around $y = 0.5\lambda$, marked by a black circle in Fig. 4 (b). In this range, the magnetic field due to equivalent y-directed Hertzian electric dipole is extremely small, so that mutual coupling to equivalent Hertzian magnetic dipole antennas is not negligible. Namely, if magnetic dipoles are omitted from the scenario, which correspond to the set of dipoles shown in Fig. 3 (b), this deviation vanishes.

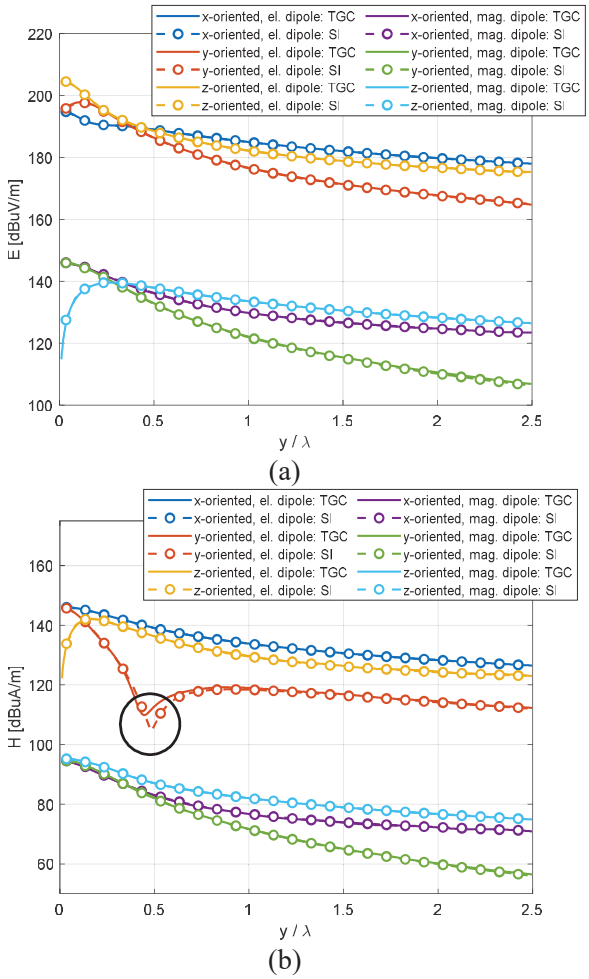

Fig. 4. Magnitude of electric and magnetic field due to Hertzian dipoles, versus y-coordinate ($z' = z = 0.1\lambda, a = 2.5\lambda$). TGC and SI solution are compared. (a) Electric field. (b) Magnetic field.

B. Single-antenna scenarios

In the following examples, single-antenna sources are applied, i.e. short electric dipoles (Fig. 1 (b)). The antennas are placed above the ground-clump model from Fig. 2 (d). The objective is to demonstrate the level of accuracy that can be achieved with the TGC solution. The relative error evaluated by TGC method is defined as:

$$\delta_X = \frac{|\mathbf{X}_{\mathrm{TGC}} - \mathbf{X}_{\mathrm{SI}}|}{|\mathbf{X}_{\mathrm{TGC}}|}, \tag{5}$$

where $\mathbf{X}_{\mathrm{TGC}}$ and $\mathbf{X}_{\mathrm{SI}}$ are electric or magnetic complex vector fields obtained from the TGC and SI solutions, respectively. The plots for the relative error of the magnetic field are omitted whenever they are similar to those for the electric field.

The relative error of the electric field versus x- and y-coordinates, for an x-directed Hertzian electric dipole ($z = 0.1\lambda$, $a = 5\lambda$) is shown in Fig. 5. The error slowly increases as we approach the rim and then rises sharply beyond it. Obviously, the error is lower in the direction that is orthogonal to the dipole axis.

In Figs. 6 (a) and 6 (b), the relative errors of the electric field due to vertical (z-oriented) and horizontal (x-directed) Hertzian electric dipole for various radii of the ground clump are presented. By increasing the radius of TGC from $a = 2.5\lambda$ to $a = 10\lambda$ the general level or the relative error for vertical dipole decreases from 10^{-2} to 10^{-3}, while in the vicinity of $y = 0$, this level is even lower by an order of magnitude. In the case of the horizontal dipole, the general level or relative error decreases from $3 \cdot 10^{-4}$ to $3 \cdot 10^{-5}$. By further increase of the radius, the relative error can be lowered only if the number of unknowns is also increased and the simulation is performed in double precision.

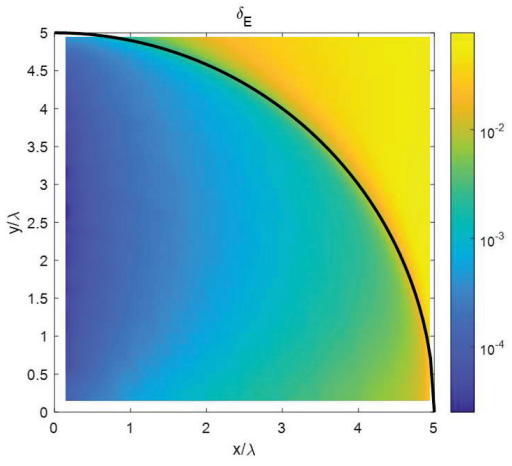

Fig. 5. Relative error of electric field due to horizontal (x-directed) Hertzian electric dipole versus x- and y-coordinates in plane $z = 0.1\lambda$ ($z' = 0.1\lambda, a = 5\lambda$).

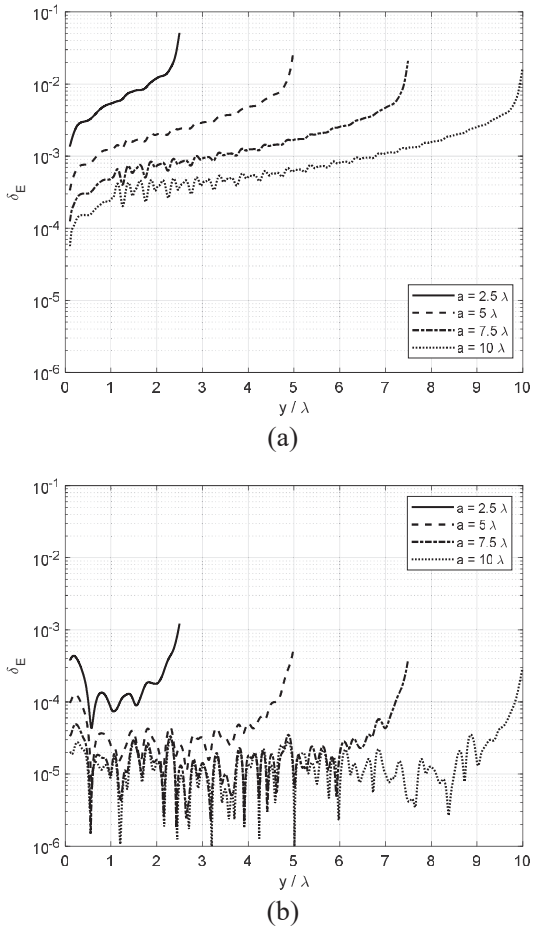

Fig. 6. Relative error of electric field due to Hertzian electric dipole versus y-coordinate, for various radii, a, of the ground clump ($z' = z = 0.1\lambda, x = 0$). (a) Vertical dipole ($z$-directed). (b) Horizontal dipole (x-directed).

An analysis of the same scenario with the Hertzian magnetic dipoles shows that the general level of the relative error remains around 10^{-2}, independently of the value of the TGC radius (first four curves in Figs. 7 (a) and 7 (b)). Obviously, an electrically small square current loop does not model the infinitesimal magnetic Hertzian dipole as well as an electrically short wire dipole models infinitesimal electric Hertzian dipole. However, by taking advantage of the duality of the expressions for fields resulting from electric and magnetic current moment above magnetic and electric grounds, respectively [30], an alternative simulation is conducted. Namely, electric dipoles are placed above lossy *magnetic* TGC, with converse parameters, i.e. $\varepsilon_{\mathrm{r}} = 1$ and $\mu_{\mathrm{r}} = 10 - \mathrm{j}5$. The obtained electric field corresponds to the magnetic field of the original problem and vice versa. The error resulting from such dual simulation is evidently lower, as denoted by $\delta_{H\mathrm{m}}$ and given by last four curves in Figs. 7 (a) and 7 (b).

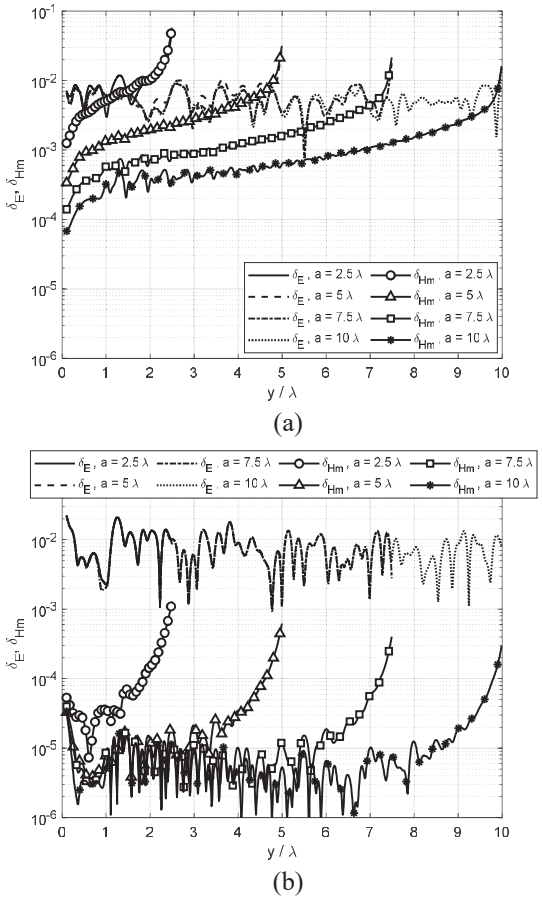

Fig. 7. Relative error of electric field due to Hertzian magnetic dipole versus y-coordinates, for various radii, a, of the lossy dielectric ground clump. For comparison, results are shown for a dual problem, relative error of magnetic field due to Hertzian electric dipole above lossy magnetic ground clump $(z = 0.1\lambda, x = 0, a = 5\lambda)$. (a) Vertical dipole ($z$-directed). (b) Horizontal dipole (x-directed).

C. Elevation analysis in single-antenna scenarios

Besides the size of the TGC, also the impact of the heights of the source and observation points are of interest. In that sense, a set of simulations is performed where we fix the height of the observation point and vary the height of the dipole up to 100λ, and vice versa. The relative error of the electric field due to horizontal (x-directed) Hertzian electric dipole is shown in Fig. 8.

We observe that by increasing the height of the dipole, the general level of relative error rises from $3 \cdot 10^{-5}$ to 10^{-2}, except in the vicinity of $y = 0$, where this level is higher for half an order of magnitude (Fig. 8 (a)). In the converse case (Fig. 8 (b)), we can see that for heights of observation point up to $z = 1\lambda$, the general level of the relative error is between $3 \cdot 10^{-5}$ and $3 \cdot 10^{-4}$, while by increasing this height up to $z = 100\lambda$, this level rises up to 10^{-2}. This result is expected, since the high elevation above TGC reduces the model adequacy for half-space scenarios.

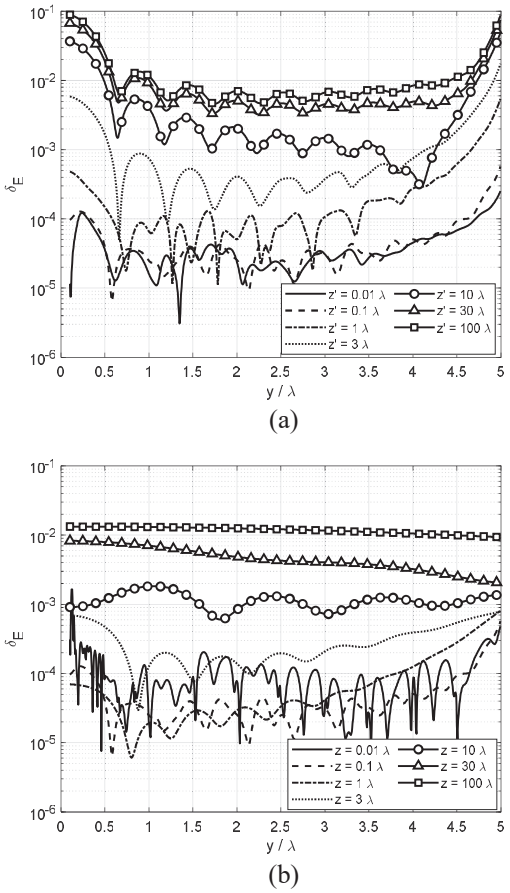

Fig. 8. Relative error of electric field due to horizontal (x-directed) Hertzian electric dipole versus y-coordinate, for various heights of source and observation points. (a) Height variation of the source point, z' $(z = 0.1\lambda, x = 0, a = 5\lambda)$. (b) Height variation of the observation point, z $(z' = 0.1\lambda, x = 0, a = 5\lambda)$.

V. CONCLUSION

In this work, an alternative approach to verification of a family of Green's functions, namely the homogenous half-space dyadic Green's matrices, is presented. The elements of these matrices are typically linear combinations of numerically demanding Sommerfeld integrals and represent field responses to unit excitations, such as magnetic- or electric-current moments, i.e. elementary Hertzian dipoles.

Due to the diversity of practical half-space problems, it is often more tedious and less efficient to program a published algorithm as a reference solution for each of the possible scenarios, than to assemble a

3-D model in a proven EM tool, using basic primitives like wires, plates, and cylinders. However, testing a half-space computational procedure against complete and complex EM scenarios, e.g. by observing parameters of installed antenna, like impedance or radiation field, conceals the accuracy information on the actual algorithm that computes the elements of the Green's matrices. Therefore, we propose verification of that numerical algorithm through simulations of fundamental scenarios that consist of elementary dipoles carefully designed as electrically small antennas, and of a model of infinite ground plane that is adjustable and thoughtfully constructed as finite-sized piece of ground, i.e. the ground clump. The procedure is easy to implement using any general-purpose 3-D EM solver in frequency domain and is applicable for all combinations of source and observation points directly above the clump, up to the height equal to the transversal dimension of the clump. With increase of the distance between the points, their heights, and the required accuracy, the resources required for the simulation also increase (e.g. number of unknowns, memory, CPU time). In order to reduce the simulation resources, the full ground-clump model is replaced by the upper boundary surface with a rounded rim (i.e. the TGC), and the number of rules is set for adjusting the simulation parameters, as well as the size and shape of antennas.

For fast and coarse verification of the DGMs, a multi-antenna scenario, based on simultaneous excitation of a set of three orthogonal electric dipoles together with a set of three orthogonal magnetic dipoles is recommended. The single-antenna scenarios allow us to attain more accurate results, where the relative error ranges from 10^{-2} to 10^{-5}. This is successfully demonstrated for ground clumps up to 20λ in transversal dimension. Further refinement of the finite 3-D model and of the basis functions may allow for lower error levels.

The proposed method is convenient for quick and simple verification of new algorithms that compute the elements of the half-space DGMs with somewhat limited, but controlled, accuracy. The analysis illuminates the potentials and provides guidelines for accurate verification in any 3-D EM analysis tool. Even though the given examples consider only the reflected fields, the proposed approach can also be extended to the transmitted fields, since the associated SIs are of similar nature. Naturally, care must be taken in the design of the elementary dipoles that are submerged in the ground clump.

The specific design of the TGC as open surface-of-rotation is currently limited to homogenous half-space scenarios. In future work, a multilayered TGC will be investigated and compared to the corresponding SI-based solutions.

REFERENCES

[1] A. Sommerfeld, "Über die Ausbreitung der Wellen in der drahtlosen Telegraphie," *Ann. Physik*, vol. 28, pp. 665–736, 1909.

[2] H. Weyl, "Ausbreitung elektromagnetischer Wellen über einem ebenen Leiter," *Ann. Physik*, vol. 60, pp. 481–500, 1919.

[3] B. Van der Pol and K. Niessen, "Über die Ausbreitung von elektromagnetischer Wellen über eine ebene Erde," *Ann. Physik*, vol. 398, pp. 273–294, 1930.

[4] X. F. Li, Y. J. Xie, R. Yang, and Y. Y. Wang, "High-frequency analysis of scattering from complex targets in half space," *Applied Computational Electromagnetics Society (ACES) Journal*, vol. 25, no. 5, pp. 433–443, June 2022.

[5] M. García-Fernández, G. Álvarez-Narciandi, Y. Álvarez López, and F. Las-Heras, "Array-based ground penetrating synthetic aperture radar on board an unmanned aerial vehicle for enhanced buried threats detection," *IEEE Transactions on Geoscience and Remote Sensing*, vol. 61, pp. 1–18, May 2023.

[6] M. F. Pantoja, A. R. Bretones, and A. G. Yarovoy, "On the direct computation of the time-domain plane-wave reflection coefficients," *Applied Computational Electromagnetics Society (ACES) Journal*, vol. 24, no. 3, pp. 294–299, June 2022.

[7] F. Rodriguez-Morales, D. Braaten, H. T. Mai, J. Paden, P. Gogineni, and J.-B. Yan, "A mobile, multichannel, UWB radar for potential ice core drill site identification in East Antarctica: Development and first results," *IEEE Journal of Selected Topics in Applied Earth Observations and Remote Sensing*, vol. 13, pp. 4836–4847, Aug. 2020.

[8] B. Li, W. Ke, H. Lu, S. Zhang, and W. Tang, "Far field reconstruction based on compressive sensing with prior knowledge," *Applied Computational Electromagnetics Society (ACES) Journal*, vol. 33, no. 12, pp. 1383–1389, July 2021.

[9] T. J. Cui and W. C. Chew, "Fast algorithm for electromagnetic scattering by buried 3-D dielectric objects of large size," *IEEE Transactions on Geoscience and Remote Sensing*, vol. 37, no. 5, pp. 2597–2608, Sep. 1999.

[10] D. Koufogiannis, A. G. Polimeridis, M. Mattes, and J. R. Mosig, "Real axis integration of Sommerfeld integrals with error estimation," in *2012 6th European Conference on Antennas and Propagation (EUCAP)*, Prague, pp. 719–723, Mar. 2012.

[11] K. Yang and A. E. Yilmaz, "A three-dimensional adaptive integral method for scattering from structures embedded in layered media," *IEEE Transactions on Geoscience and Remote Sensing*, vol. 50, no. 4, pp. 1130–1139, Apr. 2012.

[12] K. A. Michalski and J. Mosig, "The Sommerfeld half-space problem revisited: From radio frequencies and Zenneck waves to visible light and fano

modes," *Journal of Electromagnetic Waves and Applications*, vol. 30, no. 1, pp. 1–42, 2016.

[13] N. Basta and B. Kolundžija, "Efficient evaluation of the finite part of pole-free Sommerfeld integrals in half-space problems with predefined accuracy," *IEEE Transactions on Antennas and Propagation*, vol. 67, no. 7, pp. 4930–4935, July 2019.

[14] Automotive Antenna Test Solutions [Online]. Available: https://www.nsi-mi.com/applications/automotive.

[15] K. A. Michalski and J. R. Mosig, "Efficient computation of Sommerfeld integral tails – methods and algorithms," *Journal of Electromagnetic Waves and Applications*, vol. 30, no. 3, pp. 281–317, 2016.

[16] V. V. Petroviæ and A. R. Djordjević, "General singularity extraction technique for reflected Sommerfeld integrals," *AEU – International Journal of Electronics and Communications*, vol. 61, no. 8, pp. 504–508, 2007.

[17] M. Yuan and T. K. Sarkar, "Computation of the Sommerfeld integral tails using the matrix pencil method," *IEEE Transactions on Antennas and Propagation*, vol. 54, no. 4, pp. 1358–1362, Apr. 2006.

[18] C.-P. Chang and C.-F. Yang, "A moment method solution for the shielding properties of three-dimensional objects above a lossy half space," *IEEE Transactions on Electromagnetic Compatibility*, vol. 47, no. 4, pp. 723–730, Nov. 2005.

[19] W. Luo, Z. Nie, and Y. P. Chen, "Fast analysis of electromagnetic scattering from three-dimensional objects straddling the interface of a half space," *IEEE Geoscience and Remote Sensing Letters*, vol. 11, no. 7, pp. 1205–1209, July 2014.

[20] X. Qi, Z. Nie, X. Que, Y. Wang, and Y. Yang, "An efficient method for analysis of EM scattering from objects straddling the interface of a half-space," *IEEE Geoscience and Remote Sensing Letters*, vol. 13, no. 12, pp. 2014–2018, Dec. 2016.

[21] K. A. Michalski and J. R. Mosig, "On the complete radiation pattern of a vertical hertzian dipole above a low-loss ground," *IEEE Journal of Microwaves*, vol. 1, no. 3, pp. 747–762, July 2021.

[22] J. Zhuo, F. Han, N. Liu, L. Ye, H. Liu, and Q. H. Liu, "Derivation and fast computation of dyadic Green's functions of magnetic vector potential for unbounded uniaxial anisotropic media," *Applied Computational Electromagnetics Society (ACES) Journal*, vol. 32, no. 10, pp. 862–871, July 2021.

[23] M. Kolundžija, A. R. Đorđević, and V. V. Petrović, "A new approach for accurate analysis of antennas above real ground," in *IEEE Antennas and Propagation Society International Symposium*, Orlando, FL, USA, 11–16 July 1999.

[24] Ansys HFSS [Online]. Available: https://www.ansys.com/products/electronics/ansys-hfss.

[25] Altair Feko [Online]. Available: https://altair.com/feko.

[26] WIPL-D [Online]. Available: https://wipl-d.com/.

[27] J. M. Mosig and F. E. Gardiol, "Analytical and numerical techniques in the Green's function treatment of microstrip antennas and scatterers," *IEE Proceedings H Microwaves, Optics and Antennas*, vol. 130, no. 2, pp. 175–182, 1983.

[28] J. R. Mosig and A. A. Melcon, "Green's functions in lossy layered media: integration along the imaginary axis and asymptotic behavior," *IEEE Transactions on Antennas and Propagation*, vol. 51, no. 12, pp. 3200–3208, Dec. 2003.

[29] B. M. Kolundzija and N. Basta, "Method for evaluating the accuracy of Sommerfeld integrals calculations in half-space problems," in *2023 International Conference on Electromagnetics in Advanced Applications (ICEAA)*, Venice, Italy, p. 435, Oct. 2023.

[30] N. Basta and B. Kolundžija, "Application of Sommerfeld-integral expressions in dielectric and magnetic half-space problems," in *2024 11th International Conference on Electrical, Electronic and Computing Engineering (IcETRAN)*, Niš, Serbia, 2024.

Nikola Basta was born in 1983 in Belgrade, Serbia. In 2008 he received the Dipl. Ing. degree from the School of Electrical Engineering, University of Belgrade, with a major in tele-communications. After graduation, he joined the Antenna Group at the Institute of Communications and Navigation of the German Aerospace Center (DLR), where he worked until 2014 on design and characterization of smart antennas and RF systems for GNSS application, as well as on time-domain analysis of wideband pulsed antenna arrays. Since 2014 he has been working at the School of Electrical Engineering, University of Belgrade, from which he received his Ph.D. degree in the area of computational electromagnetics. Currently, he works as assistant professor at the same school and his main interests are microwaves, applied electromagnetics, antenna systems, array signal processing and circuit theory.

Branko Kolundžija (Fellow, IEEE) was born in Zenica, Bosnia and Herzegovina, in 1958. He received the B.Sc., M.Sc., and D.Sc. degrees from the University of Belgrade, Belgrade, Serbia, in 1981, 1986, and 1990, respectively. He joined the Faculty of Electrical Engineering, University of Belgrade, in 1981, where he is currently a Full Professor in electromagnetics and

antennas and propagation. He has held lectures and short courses in Ottawa, Lisbon, Urbana, Albuquerque, Syracuse, Monterrey, Stuttgart, New York, Copenhagen, Helsinki, Calgary, Zurich, Long Island, Calcutta, Tokyo, Washington, Yokohama, and Okinawa. He is the main architect of the WIPL-D software suite. He is the author or coauthor of two monographs, a chapter in a monograph, three software packages, one textbook, 32 journal articles, and 160 papers at international conferences. His research interests are numerical problems in electromagnetics, especially those applied to antennas and microwave components.

A Broadband Metasurface for Effective Control of Transmission Phase by Applied Voltage

Zhen Wang[1], Ajay K. Poddar[2], Ulrich L. Rohde[2], and Mei Song Tong[1]

[1]Department of Electronic Science and Technology, Tongji University
Shanghai 201804, China
2210232@tongji.edu.cn; mstong@tongji.edu.cn

[2]Synergy Microwave Corporation, 201 McLean Boulevard, Paterson, NJ 07504, USA
akpoddar@ieee.org; u.l.rohde@ieee.org

Abstract – This paper presents a reconfigurable transmissive metasurface operating at 8.5 GHz. The metasurface consists of a four-layer stacked structure of circular radiating patches, with varactor diodes integrated into the patches to achieve 360° continuous transmission phase control. The structure exhibits a transmission loss of less than 2 dB and a relative bandwidth of approximately 12%. By tuning the capacitance of the varactor diodes, the transmission phase can be precisely and continuously adjusted. Compared to switch-diode-based metasurfaces, this approach offers a simpler design and enables dynamic continuous phase modulation. Both simulation and measurement results, including the relationship between transmission magnitude and phase shift versus bias voltage, show strong agreement. The metasurface demonstrates excellent bandwidth characteristics. This work provides a valuable strategy for designing dynamically tunable broadband metasurfaces and holds significant potential for applications in high-gain phased array antennas and efficient beamforming systems.

Index Terms – Active metasurface, transmission phase, varactor tuning.

I. INTRODUCTION

Metamaterials are novel synthetic materials engineered to achieve specific properties not normally found in nature [1]. However, large volume and inflexibility of normal metamaterials make them impractical in many applications. Based on the generalized Snell's law, metasurface, a kind of metamaterial with a planar structure, was proposed [2]. Since then, the study of phase gradient metasurfaces (PGMS) has attracted the interest of many researchers. PGMS is capable of providing predefined in-plane wave vectors to manipulate the directions of the refracting/reflecting waves [3]. The wave beam can be controlled by introducing sudden phase changes at different positions on the plane and making its distribution meet certain rules.

In [4], a multilayer square-ring metallic structure was employed to design a phase metasurface, where transmission phase variation was achieved by adjusting the perimeter of the square rings. In addition, the design procedure of some metasurfaces is to change the size of unit cell firstly, then combine them properly to achieve electromagnetic wave control [5–10].

Another way to adjust the phase of the unit is to rotate the metasurface unit. A new type of metasurface design is used to generate vortex beams [11], the proposed metasurface units are rotated at different angles and then distributed regularly. In [12], a transmission–reflection-integrated metasurface is proposed, which enables full-space amplitude and phase control of circularly polarized (CP) waves. By rotating the receiving and transmitting patches of each meta-atom around their respective feed points, the transmission and reflection phases can be independently tailored. Also, a similar principle is used to adjust the phase of the unit in [13–16].

The above two methods to change the phase of the unit are realized by changing the shape of the unit structure under the passive condition. Changing the shape of the unit structure compromises the dynamic control of the phase. In order to dynamically control the transmission phase, a multilayer metasurface unit is proposed, and the PIN diodes are attached to each unit [17]. However, since the PIN diode only has two states, on and off, it is complicated for this kind of metasurface to realize continuous controlling of phase. Another type of active metasurface for vortex beam generation is designed in [18]. The method is to divide the entire metasurface into several regions and then control capacitance in different regions. But this active metasurface only allows full phase adjustment within the

Submitted On: March 18, 2025
Accepted On: September 23, 2025

https://doi.org/10.13052/2025.ACES.J.401004

limited bandwidth. Reference [19] presents a metasurface capable of both transmission and reflection functionalities, where the switching between transmission and reflection modes is achieved using only a single PIN diode. However, the phase control of the unit cells in this design relies solely on geometric dimension variations, making dynamic phase tuning unattainable. Moreover, the integration of varactor diodes into metasurfaces enables dynamic phase tuning. In [20], a varactor-based metasurface was developed to achieve continuous phase modulation. Under different bias voltages, the unit cell demonstrated a transmission phase shift of 245° and a reflection phase shift of 300°. However, the design exhibited an insertion loss of approximately 3 dB. In [21], a novel metasurface incorporating varactor diodes was proposed, capable of simultaneously controlling both amplitude and phase, and achieving 360° phase tuning. Nevertheless, the operational bandwidth was relatively narrow, limited to only 6%.

In this paper, an active metasurface which can dynamically adjust the transmission phase over a broad bandwidth is proposed and its prototype has been simulated in [22]. Each unit of the metasurface consists of a circular patch and two strip patches, with two varactor diodes placed in the gap between the two types of patches. By changing the capacitance of the varactor diodes, the transmission phase can be changed efficiently. The two ends of the varactor diode are fed by the strip patch and the circular patch respectively to avoid the influence of the re-designed feed structure on the metasurface performance. The simulation and measurement results show that the metasurface can reach a bandwidth of 12% and a tunability of transmission phase over $0^\circ - 360^\circ$ with a transmission magnitude more than 0.8.

II. TUNABLE METASURFACE DESIGN AND ANALYSIS

A. Metasurface unit cell design

The perspective structure of the proposed active transmissive metasurface is shown in Fig. 1 (a). Its metasurface structure can produce different electromagnetic responses with continuously adjustable phases to incident waves. Figure 1 (b) presents the geometrical model of the unit cell of the active metasurface. The structure primarily consists of three dielectric substrate layers and four metallic patch layers. The substrates are square-shaped and made of Rogers AD260A material, with a thickness of 1.4 mm, a relative permittivity of 2.65, and a loss tangent of 0.0017. The first and fourth metallic layers employ circular patches with a radius of r_1, while the second and third metallic layers use circular patches with a radius of r_2. The significant difference in patch radii between the two groups results in distinct

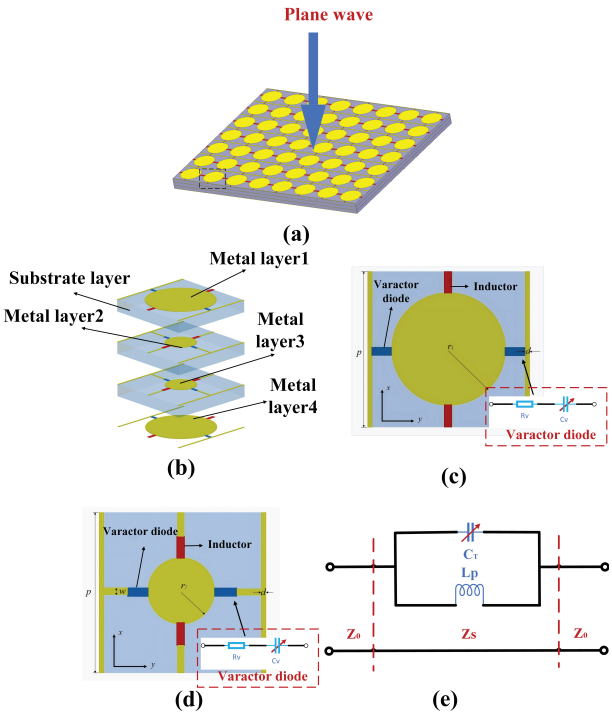

Fig. 1. Structure of the proposed metasurface. (a) Schematic diagram of the overall metasurface structure. (b) Cross-section view. (c) Circular patch layer structure with radius r_1. (d) Circular patch layer structure with radius r_2. (e) Single-layer radiating patch resonant circuit model structure.

frequency responses. For a circular patch with radius R, the approximate value of the resonant frequency is given by the following equation [23]

$$f_r = \frac{1.841 \cdot c}{2\pi R\sqrt{\varepsilon_{reff}}}, \tag{1}$$

where f_r is the resonant frequency of the metasurface unit, c is the speed of light, R is the radius of the circular patch, and ε_{reff} is the effective dielectric constant.

Two varactor diodes are placed symmetrically on both sides of the circular patch. Each diode has one terminal connected to the circular patch and the other terminal connected to a bias line etched on the bottom layer of the substrate. The equivalent resonant circuit of a single layer is illustrated in Fig. 1 (e). The incident electromagnetic wave can be modeled as a parallel LC resonant circuit comprising an inductance L_p and a capacitance C_T [24]. where, C_T represents the equivalent capacitance between the metallic bias line and the circular patch, while L_p corresponds to the equivalent inductance of the metallic patch. Consequently, the circular patch no longer behaves as a pure resonant cavity but forms an LC-tunable resonator, with its resonant

frequency determined by

$$f_r = \frac{1}{2\pi\sqrt{L_T \cdot C_T}}, \tag{2}$$

$$C_T = C_{patch} + C_v, \tag{3}$$

where C_{patch} denotes the capacitance between the metallic patches, and C_v represents the variable capacitance of the varactor diode. The values of L_T and C_{patch} are determined by the geometry of the patches and the corresponding current paths. Therefore, its equivalent resonant structure is not only determined by the geometric dimensions, but also affected by the variable capacitance C_v. The configurations of the two types of circular patches are shown in Figs. 1 (b) and (c). The components marked in blue represent varactor diodes, specifically the MAVR-000120-14110, with a capacitance range of $0.14 - 1.1$ pF, which ensures adequate tunability to meet the capacitance requirements of the metasurface. The components marked in red are inductors with an inductance value of 3.3 nH, used to isolate AC signals. The geometric parameters are defined as follows: $p = 10$ mm, $w = 0.2$ mm, $r_1 = 4$ mm, $r_2 = 1.8$ mm. The unit cell is simulated using the finite element method (FEM), with periodic boundary conditions applied to all four sidewalls. The simulated transmission characteristics of a single-layer metallic patch on a single dielectric substrate are presented in Figs. 2 and 3. The simulation results show that when the patch area of the unit cell is larger, the transmission magnitude is easier to be stabilized in a certain range. When the patch area of the unit cell is smaller, the adjustment range of transmission phase can be larger. At the same time, it is found that for a transmission metasurface, it is difficult to achieve a phase adjustment of 360° by using the structure of single patch and substrate, but such a phase adjustment can be easily achieved by simply adding a phase offset in a multi-layer structure.

B. Transmission phase principle analysis

As shown in Fig. 1 (e), the impedance of the parallel resonant circuit of a single-layer metal patch is $Z_s = \frac{1}{j\left(\frac{1}{\omega L_p} - \omega C_T\right)}$, which is put into the transmission model, and the electromagnetic transmission matrix [24] can be expressed as

$$\begin{aligned}\begin{bmatrix} A & B \\ C & D \end{bmatrix} &= \begin{bmatrix} 1 & Z_0 \\ 0 & 1 \end{bmatrix} \begin{bmatrix} 1 & 0 \\ 1/Z_s & 1 \end{bmatrix} \begin{bmatrix} 1 & Z_0 \\ 0 & 1 \end{bmatrix} \\ &= \begin{bmatrix} 1 + Z_0/Z_s & 2Z_0 + Z_0^2/Z_s \\ 1/Z_s & Z_0/Z_s + 1 \end{bmatrix},\end{aligned} \tag{4}$$

where $Z_0 = 377\Omega$ is the wave impedance in free space. The transmission coefficient of a single-layer metal patch can be expressed as

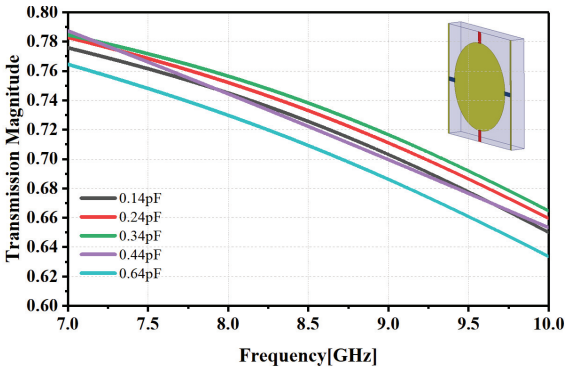

(a)

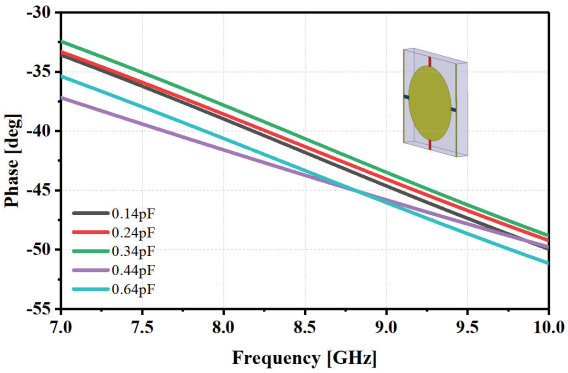

(b)

Fig. 2. Simulation of transmission characteristics for a single-layer circular radiating patch with a radius of r_1. (a) Transmission magnitude. (b) Transmission phase.

$$S_{21} = \frac{2}{A + B/Z_0 + CZ_0 + D}. \tag{5}$$

According to the above analysis, the transmission amplitude and phase of the artificial electromagnetic structure are related to the equivalent electrical parameters. By changing the electromagnetic structure to affect the corresponding electrical parameters, the amplitude and phase of the incident electromagnetic wave can be controlled. The overall matrix transmission parameters can be described as [25].

$$\begin{aligned}S_{21}^{To} &= \frac{S_{21}^1 \cdot S_{21}^2 \cdot S_{21}^3}{\left(1 - S_{11}^2 \cdot S_{22}^1\right)\left[1 - S_{11}^3 \cdot \left(\frac{S_{22}^1 \cdot S_{22}^2 \cdot S_{12}^2}{1 - S_{11}^2 \cdot S_{22}^2} + S_{22}^2\right)\right]} \\ &= \frac{S_{21}^1 \cdot S_{21}^2 \cdot S_{21}^3}{1 - S_{11}^1 \cdot S_{11}^2 - S_{11}^2 \cdot S_{11}^3 - S_{11}^1 \cdot S_{11}^3 \cdot T},\end{aligned} \tag{6}$$

where S^1, S^2, S^3, and S^{To} represent the first matrix, second matrix, third matrix, and overall cascaded matrix, respectively, and $T = (S_{21}^2)^2 - (S_{11}^2)^2$. When the characteristics of the selected substrate remain constant, the

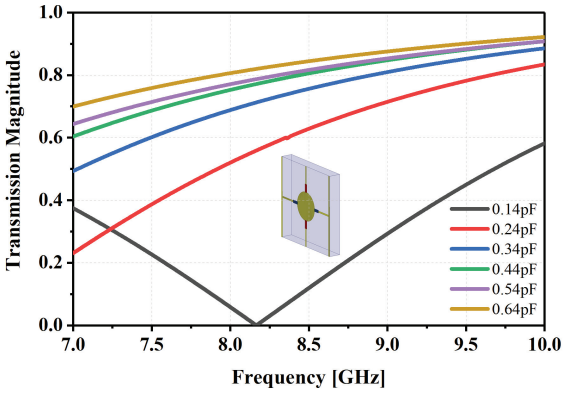

(a)

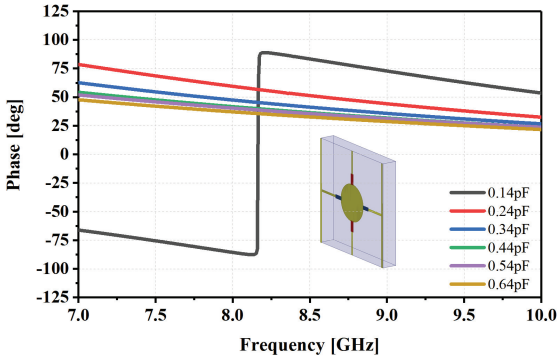

(b)

Fig. 3. Simulation of transmission characteristics for a single-layer circular radiating patch with a radius of r_2. (a) Transmission magnitude. (b) Transmission phase.

main factors affecting the transmission characteristics are the matrices of the two conductive layers, so equation (6) can be simply written as

$$S_{21}^{To} = \text{Am} \cdot e^{j\,\text{Phase}} = f(\angle S_{21}^{1}, \angle S_{21}^{3}). \qquad (7)$$

As the number of layers increases, the transmission phase can be equivalent to the phase superposition of each conductive layer unit. Therefore, using multilayer conductive patches can enhance the transmission phase of the metasurface unit.

C. Metasurface design

As shown in Fig. 1 (a), the overall structure of the proposed metasurface consists of 8×7 unit cells. The dimension of the whole structure is 100.0 mm $\times$ 90.0 mm. Since each unit cell of the metasurface has no need to be fed independently, experimental measurements are facilitated. In order to avoid the tedious design of additional feeding structure, the strip patch of every unit cell can directly function as the feeding structure to feed one end of the varactor diode [26] while the circular patch can be used to feed the other end of the varactor diode. Also, the inductors are added for blocking alternating current to reduce the influence of the feeding structure on the performance of the metasurface [27]. When the direct current (DC) power supply is used to feed the metasurface, the positive pole of the power supply is connected with the circular patch while the negative pole is connected with the strip patch. The width of all the bias lines is 0.2 mm.

III. SIMULATION AND MEASUREMENT RESULTS

In order to ensure that the transmission metasurface can achieve a phase shift of 360°, the varactor diode values in the range of $0.14 - 0.7$ pF are determined. From the simulation results as shown in Fig. 4, the phase and magnitude of the transmission metasurface at different capacitance values can be intuitively obtained respectively. The simulation results show that within the range of 1.01 GHz from 8.05 GHz to 9.06 GHz, the transmission phase can be adjusted 360° by adjusting the capacitance value of the varactor diode. Meanwhile,

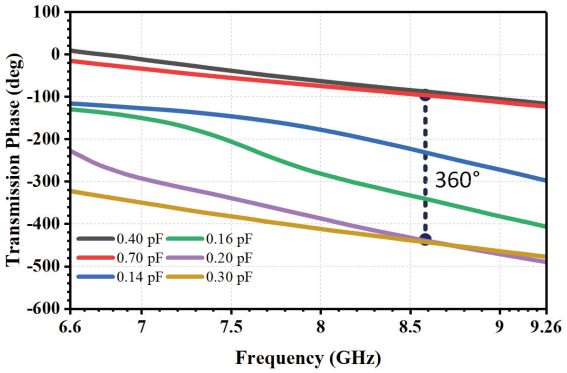

(a)

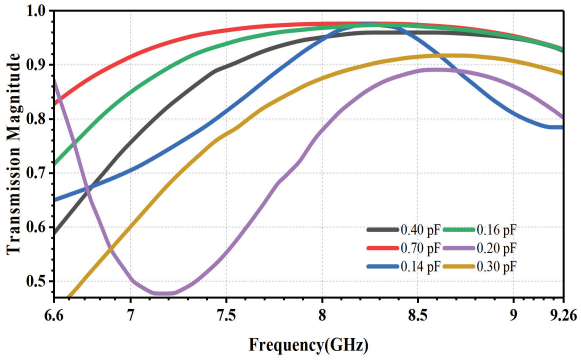

(b)

Fig. 4. Simulated results of the proposed transmission metasurface consisting of the unit cell with different capacitance values. (a) Transmission phase. (b) Transmission magnitude.

the transmission magnitude can be stabilized above 0.8, indicating the transmission loss remains within -2 dB across the operating frequency band. This means that the transmission phase can be continuously and dynamically adjusted by 360° at each frequency point in the frequency band, while the transmission amplitude is also well controlled. It is noted that, due to the resonance in the metasurface with the capacitance of 0.2 pF, the transmission magnitude is decreased significantly near 7.32 GHz, resulting in the maximum bandwidth limitation of the proposed metasurface.

An 8×7 metasurface as shown in Fig. 5 was fabricated by using a printed circuit board to verify the performance of the metasurface proposed in this paper. The metasurface was measured in a microwave anechoic chamber as shown in Fig. 6, and the different layers of the metasurface are fixed with plastic screws. The wires connect the metasurface and the DC power supply ZF-303D to feed the two ends of the varactor diode. A PNA network analyzer of KEYSIGHT N5227A and two horn antennas were selected to measure the fabricated metasurface. The end face dimensions of the two horn antennas ($7.05 - 10.0$ GHz) are 57.0 mm $\times$ 42.0 mm,

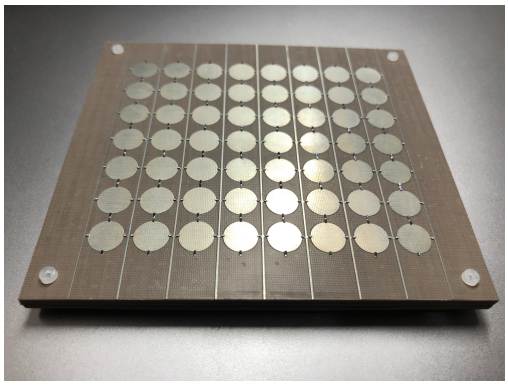

Fig. 5. Photograph of the fabricated metasurface sample.

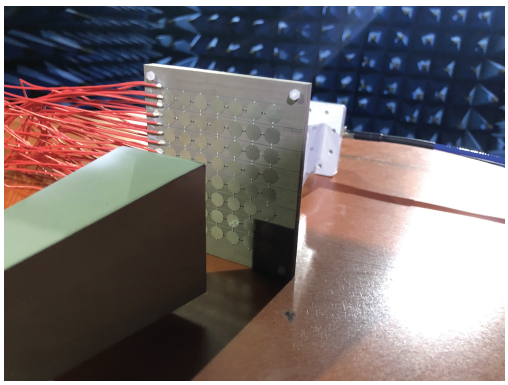

Fig. 6. Measurement setup.

which is smaller than that of the metasurface. To accurately characterize the transmission amplitude and phase response of the metasurface under various bias conditions, a near-field measurement setup was employed, with a fixed test distance of 47 mm between the horn antennas and the metasurface.

The transmission magnitude and phase of the metasurface controlled by different uniform bias voltages at 8.05 GHz, 8.5 GHz and 9.06 GHz are shown in Figs. 7–9, respectively. By adjusting the voltage at both ends of varactor diode from 1.0 V to 10.0 V,

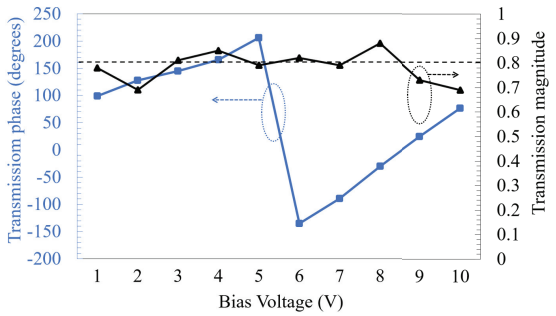

Fig. 7. Measurement results of transmission phase and transmission magnitude at different bias voltages at 8.05 GHz.

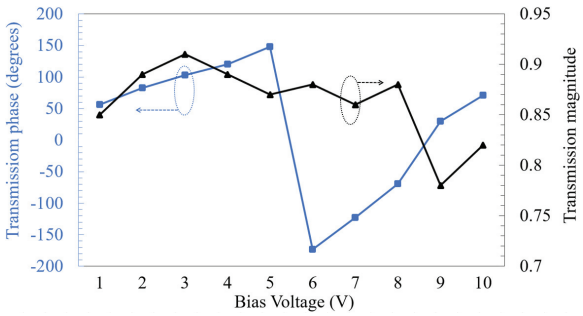

Fig. 8. Measurement results of transmission phase and transmission magnitude at different bias voltages at 8.5 GHz.

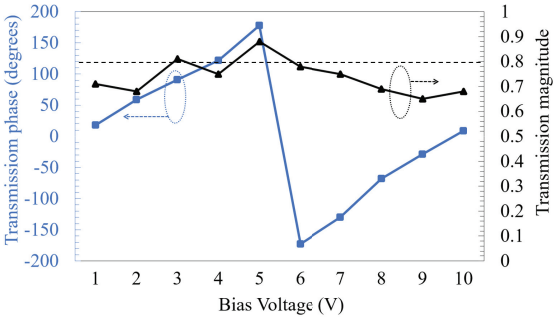

Fig. 9. Measurement results of transmission phase and transmission magnitude at different bias voltages at 9.06 GHz.

the fabricated metasurface realizes full phase adjustment of transmission phase. However, at 8.05 GHz and 9.06 GHz, the transmission amplitude is measured below 0.8 at some bias voltages. One reason for the differences between the measurement results and the simulation results is that the size of the varactor diode is very small and there is a size error in production, that is, the length and width of all varactors are not exactly the same. Another reason is the limited measurement conditions. In addition, the phase shows a good linearity with the biased voltage.

Table 1: Comparison between proposed design and others

Source	Transmission Phase	Tunability	Bandwidth
[18]	360°	Yes	3.7%
[20]	245°	Yes	7%
[21]	360°	Yes	6%
[28]	2bit	Yes	5.89%
[29]	360°	Yes	4.1%
This Work	360°	Yes	12%

For a comparison, Table 1 lists the transmission phase tunability, and relative bandwidth of other designs and this work. It should be noted that the operating bandwidth is determined on the basis that 360° transmission phase control can be achieved at all frequencies and the transmission amplitude is above 0.8. Reference [18] uses a single-layer dielectric substrate design. While it uses a varactor diode to achieve 360° phase tuning, its operating bandwidth is only 3.7%. Compared with [20, 21], and [29], all of which use a three-layer dielectric substrate and add a varactor diode, this design has a wider operating bandwidth while achieving a dynamic phase tuning of 360°. Reference [28] uses a double-layer substrate design, but it only achieves a 2-bit tuning phase. This shows that this design is superior to other designs in terms of relative bandwidth and, more importantly, the transmission phase can be dynamically and continuously controlled.

IV. CONCLUSION

A broadband transmission metasurface with a dynamic phase adjustment is proposed. Through the analysis of the equivalent circuit of the transmission model, a new optimization method to stabilize the transmission amplitude of the metasurface is adopted. Simulation results show that the proposed transmission metasurface can achieve an adjustment of 360° for the transmission phase in the working frequency band of about 1.01 GHz, while maintaining the transmission magnitude above 0.8. In order to verify the performance of the proposed metasurface, a sample including 8×7 unit cells is fabricated, and the measurement results are consistent with the simulation results. This work will benefit significantly the development of wave manipulation technology used for beamforming in high-gain phased antennas.

REFERENCES

[1] C. L. Holloway, E. F. Kuester, J. A. Gordon, J. O'Hara, J. Booth, and D. R. Smith, "An overview of the theory and applications of metasurfaces: The two-dimensional equivalents of metamaterials," *IEEE Antennas Propag. Mag.*, vol. 54, no. 2, pp. 10–35, Apr. 2012.

[2] N. Yu, P. Genevet, M. A. Kats, F. Aieta, J.-P. Tetienne, F. Capasso, and Z. Gaburro, "Light propagation with phase discontinuities: Generalized laws of reflection and refraction," *Science*, vol. 334, no. 6054, pp. 333–337, Oct. 2011.

[3] H. Li, G. Wang, H. Xu, T. Cai, and J. Liang, "X-band phase-gradient metasurface for high-gain lens antenna application," *IEEE Trans. Antennas Propag.*, vol. 63, no. 11, pp. 5144–5149, Nov. 2015.

[4] H. Hao, S. Zheng, Y. Tang, and X. Ran, "Broadband transmissive amplitude-and-phase metasurface for vortex beam generation and hologram," *Phys. Lett. A*, vol. 434, p. 128036, 2022.

[5] Y. Lv, X. Ding, B. Wang, and D. E. Anagnostou, "Scanning range expansion of planar phased arrays using metasurfaces," *IEEE Trans. Antennas Propag.*, vol. 68, no. 3, pp. 1402–1410, Mar. 2020.

[6] H. Ali, M. U. Afzal, K. P. Esselle, and R. M. Hashmi, "Integration of geometrically different elements to design thin near-field metasurfaces," *IEEE Access*, vol. 8, pp. 225336–225346, 2020.

[7] S. Tiwari, A. K. Singh, and A. Dubey, "Millimeter-wave wide-angle beamsteerable transmission-type metasurface lens antenna," *Proc. IEEE Microwaves, Antennas, and Propagation Conf. (MAPCON)*, Bangalore, India, Dec. 2022.

[8] F. Qin, L. Wan, L. Li, H. Zhang, G. Wei, and S. Gao, "A transmission metasurface for generating OAM beams," *IEEE Antennas Wireless Propag. Lett.*, vol. 17, no. 10, pp. 1793–1796, Oct. 2018.

[9] J. Liang, G. Huang, J. Zhao, Z. Gao, and T. Yuan, "Wideband phase-gradient metasurface antenna with focused beams," *IEEE Access*, vol. 7, pp. 20767–20772, 2019.

[10] T. Huang, Z. Wu, S. Huang, Z. Wen, W. Jiang, J. Xu, J. Wang, and Y. Luo, "Broadband transreflective metasurface for multifunctional dual-band OAM engineering," *IEEE Trans. Antennas Propag.*, vol. 72, no. 9, pp. 7041–7047, Sep. 2024.

[11] Y. Yuan, X. Ding, K. Zhang, and Q. Wu, "Planar efficient metasurface for vortex beam generating

and converging in microwave region," *IEEE Trans. Magn.*, vol. 53, no. 6, pp. 1–4, June 2017.

[12] J-Y. Yin, Z. Wu, F. Li, and J.-Y. Deng, "Transmission-type 2-bit coding polarization conversion metasurface with radiation characteristic," *Optics Express*, vol. 33, pp. 85–97, 2025.

[13] B. Lin, J. Guo, L. Lv, Z. Liu, X. Ji, and J. Wu, "An ultra-wideband reflective phase gradient metasurface using Pancharatnam-Berry phase," *IEEE Access*, vol. 7, pp. 13317–13325, 2019.

[14] C. Fang, C. Wu, Z. J. Gong, S. Zhao, A. Q. Sun, Z. Y. Wei, and H. Q. Li, "Broadband and high-efficiency vortex beam generator based on a hybrid helix array," *Opt. Lett.*, vol. 43, no. 7, pp. 1538–1541, Apr. 2018.

[15] Y. Ran, J. Liang, H. Li, and T. Cai, "High-performance broadband vortex beam generator using reflective Pancharatnam–Berry metasurface," *Opt. Commun.*, vol. 427, pp. 101–106, Nov. 2018.

[16] H. Wang, Y. F. Li, H. Y. Chen, Y. J. Han, S. Sui, Y. Fan, Z. T. Yang, J. F. Wang, J. Q. Zhang, S. B. Qu, and Q. Cheng, "Multi-beam metasurface antenna by combining phase gradients and coding sequences," *IEEE Access*, vol. 7, pp. 62087-62094, 2019.

[17] C. Zhang, J. Gao, X. Cao, S. Li, H. Yang, and T. Li, "Multifunction tunable metasurface for entire-space electromagnetic wave manipulation," *IEEE Trans. Antennas and Propag.*, vol. 68, no. 4, pp. 3301-3306, Apr. 2020.

[18] H. Y. Shi, L. Y. Wang, G. T. Peng, X. M. Chen, J. X. Li, S. T. Zhu, A. X. Zhang, and Z. Xu, "Generation of multiple modes microwave vortex beams using active metasurface," *IEEE Antennas Wireless Propag. Lett.*, vol. 18, no. 1, pp. 59-63, Jan. 2019.

[19] C. Zhang, Y. Luo, N. Yan, X. Guo, Y. Guo, and K. Ma, "A reconfigurable metasurface with precise phase distribution for both transmission and reflection functions," *IEEE Trans. Antennas Propag.*, vol. 72, no. 9, pp. 7154–7163, Sep. 2024.

[20] D. Y. Lau and S. V. Hum, "A planar reconfigurable aperture with lens and reflectarray modes of operation," *IEEE Trans. Microw. Theory Techn.*, vol. 58, no. 12, pp. 3547–3555, Dec. 2010.

[21] B. W. Zheng, H. Ren, S. S. An, H. Tang, H. Li, M. Haerinia, Y. X. Dong, C. Fowler, and H. L. Zhang, "Tunable metasurface with dynamic amplitude and phase control," *IEEE Access*, vol. 9, pp. 104522–104529, 2021.

[22] J. R. Wang, Y. J. Zhang, and M. S. Tong, "A broadband metasurface with voltage-controlled transmission phase," *2021 IEEE Int. Symp. Antennas Propag. and USNC/URSI Radio Sci. Meeting*, Singapore, Dec. 2021.

[23] J. Howell, "Microstrip antennas," *IEEE Trans. Antennas Propag.*, vol. 23, no. 1, pp. 90–93, Jan. 1975.

[24] T. Yuan, J. Xie, and X. Yang, "A high-gain, polarization-universal metasurface lens antenna for millimeter-wave communication," *AEU - Int. J. Electron. Commun.*, vol. 193, no. 155727, 2025.

[25] Z. Qu, J. R. Kelly, and Y. Gao, "Analysis of the transmission performance limits for a multilayer transmitarray unit cell," *IEEE Trans. Antennas Propag.*, vol. 70, no. 3, pp. 2334–2339, Mar. 2022.

[26] D. M. Pozar, *Microwave Engineering*. New York, NY, USA: John Wiley, 2008.

[27] W. R. Smythe, *Static and Dynamic Electricity*. New York, NY, USA: McGraw-Hill, 1968.

[28] H. Liu, H. Zhang, and L. Deng, "Design and implementation of a reconfigurable transmitarray employing varactor-tuned Huygens elements for dynamic beam shaping," *IEEE Antennas Wireless Propag. Lett.*, vol. 24, no. 6, pp. 1542–1546, June 2025.

[29] W. S. Hu, Y. H. Liu, C. Y. Gong, S. Y. Wang, and Y. B. Li, "Dual-frequency co-aperture control of beam scanning by programmable metasurface," *IEEE Antennas Wireless Propag. Lett.*, vol. 22, no. 12, pp. 3013–3017, Dec. 2023.

Zhen Wang received the B.S. degree in Communications and Information Engineering from Qingdao University, Qingdao, China, in 2017, and the M.S. degree in Electronic and Information Engineering from the University of Electronic Science and Technology of China (UESTC), Chengdu, China, in 2020. He is currently pursuing the Ph.D. degree in Electronic and Information Engineering at Tongji University, Shanghai, China. His research interests include phased arrays, metasurfaces, millimeter-wave antennas, and computational electromagnetics.

Ajay K. Poddar is an IEEE Fellow and a member of IEEE Eta Kappa Nu, recognized worldwide for his pioneering contributions to electrical engineering, electronics, and communications. He earned his graduate degree from the Indian Institute of Technology (IIT) Delhi, India, followed by a Doctorate (Dr.-Ing.) from the Technical University of Berlin, Germany, and a Post-Doctorate (Dr.-Ing. habil.) from Brandenburg Technical University Cottbus, Germany. Dr. Poddar currently serves as Chief Scientist at Synergy Microwave Corporation, New Jersey, USA, where he leads cutting-edge research in signal generation and processing electronics, RF-MEMS, antennas, and metamaterial-based

resonators and sensors for present and future communication and electronic systems. His innovations have enabled advancements in industrial, medical, and aerospace applications, integrating AI-inspired electronic architectures to enhance system performance, efficiency, and reliability. Earlier in his career, Dr. Poddar served as a Senior Scientist and Program Director at India's Defense Research and Development Organization (DRDO) under the Ministry of Defense (1991–2001). During that tenure, he also held the position of Visiting Professor at the University of Pune, contributing to advanced research and technology development in defense electronics. Beyond industry, Dr. Poddar is deeply involved in academia. He serves as a Visiting Professor at the University of Oradea (UO), Romania, and the Indian Institute of Technology (IIT) Jammu, India, as well as a Guest Lecturer at the Technical University of Munich (TUM), Germany. Through his teaching and mentorship, he continues to inspire students and researchers worldwide to pursue innovation in the service of humanity. Dr. Poddar's exceptional career has been recognized with numerous prestigious awards, including the 2025 IEEE Antennas and Propagation Society Outstanding Service Award, the 2023 RCA Armstrong Medal Award, the 2018 IEEE MGA Innovation Award, the 2015 IEEE IFCS W.G. Cady Award, the 2015 IEEE Region 1 Scientific Innovation Award, and the 2009 IEEE Region 1 Scientific Contributions Award. He is the author or co-author of over 400 research publications in international journals, magazines, and conference proceedings, and has contributed to six technical books and book chapters. He holds more than 50 patents for his scientific and technological innovations and has supervised numerous graduate and Ph.D. students across the globe. Additionally, he has served as editor and reviewer for several leading technical journals. Dr. Poddar is actively engaged in professional societies and global initiatives addressing key technological challenges in green and renewable energy, decarbonization, metamaterial-based environmental sensors, and solid-state high-current density batteries. His portrait was featured on the cover of *Microwave Journal* (November 2011), where he was profiled as one of the "Divine Innovators" in the article "Divine Innovation: 10 Technologies Changing the Future of Passive and Control Components."

Ulrich L. Rohde is a Partner of Rohde & Schwarz, Munich Germany; Chairman of Synergy Microwave Corp., Paterson, New Jersey; President of Communications Consulting Corporation; serving as an honorary member of the Senate of the University of the Armed Forces Munich, Germany honorary member of the Senate of the Brandenburg University of Technology Cottbus–Senftenberg, Germany.

Dr. Rohde is serving as a full Professor of Radio and Microwave Theory and Techniques at the University of Oradea and several other universities worldwide, to name a few: Honorary Professor IIT-Delhi, Honorary Chair Professor IIT-Jammu, Professor at the University of Oradea for microwave technology, an honorary professor at the BTU Cottbus-Senftenberg University of Technology, and professor at the German Armed Forces University Munich (Technical Informatics).

Rohde has published 400+ scientific papers, coauthored over dozen books, with John Wiley and Springer, and holds 50 plus patents; received several awards, to name a few recent awards: recipient of 2023 IEEE Communications Society Distinguished Industry Leader Award, 2023 IEEE Antennas and Propagation Society Distinguished Industry Leader Award, 2022 IEEE Photonics Society Engineering Achievement Award, 2021 Cross of Merit of the Federal Republic of Germany, 2020 IEEE Region 1 Technological Innovation Award, 2019 IETE Fellow Award, 2019 IEEE CAS Industrial Pioneer Award; 2017 RCA Lifetime achievement award, 2017 IEEE-Cady Award, 2017 IEEE APS Distinguish achievement award, 2017 Wireless Innovation Forum Leadership Award, 2016 IEEE MTT-S Applications Award, 2015 IEEE-Rabi Award, 2015 IEEE Region-1 Award, and 2014 IEEE-Sawyer Award.

Dr. Ulrich Rohde is the recipient of the 2021 Cross of Merit of the Federal Republic of Germany. The Order of Merit of the Federal Republic of Germany, also known as the Federal Cross of Merit, the highest tribute the Federal Republic of Germany can pay to individuals for services to the nation. In December 2022, The Indian National Academy of Engineering (INAE) inducted Dr. Ulrich Rohde as a fellow during ceremonies for

"outstanding contributions to engineering and also your dynamic leadership in the engineering domain, which has immensely contributed to the faster development of the country." Dr. Rohde is only the third foreign fellow elected by the INAE, preceded by Dr. Jeffrey Wineland, who won a Nobel Prize in Physics.

Mei Song Tong received the B.S. and M.S. degrees from Huazhong University of Science and Technology, Wuhan, China, respectively, and Ph.D. degree from Arizona State University, Tempe, Arizona, USA, all in electrical engineering. He is currently a Humboldt Awardee Professor in the Chair of High-Frequency Engineering, Technical University of Munich, Munich, Germany, and is on leave from the Distinguished/Permanent Professor and Head of Department of Electronic Science and Technology, and Vice Dean of College of Microelectronics, Tongji University, Shanghai, China. He has also held an adjunct professorship at the University of Illinois at Urbana-Champaign, Urbana, Illinois, USA, and an honorary professorship at the University of Hong Kong, China. He has published more than 700 papers in refereed journals and conference proceedings and co-authored eight books or book chapters. His research interests include electromagnetic field theory, antenna theory and technique, modeling and simulation of RF/microwave circuits and devices, interconnect and packaging analysis, inverse electromagnetic scattering for imaging, and computational electromagnetics.

Prof. Tong is a Fellow of the Electromagnetics Academy, Fellow of the Japan Society for the Promotion of Science (JSPS), and Senior Member (Commission B) of the USNC/URSI. He has been the chair of Shanghai Chapter since 2014 and the chair of SIGHT committee in 2018, respectively, in IEEE Antennas and Propagation Society. He has served as an associate editor or guest editor for several well-known international journals, including IEEE Antennas and Propagation Magazine, IEEE Transactions on Antennas and Propagation, *IEEE Transactions on Components, Packaging and Manufacturing Technology, International Journal of Numerical Modeling: Electronic Networks, Devices and Fields, Progress in Electromagnetics Research*, and *Journal of Electromagnetic Waves and Applications*. He also frequently served as a session organizer/chair, technical program committee member/chair, and general chair for some prestigious international conferences. He was the recipient of a Visiting Professorship Award from Kyoto University, Japan, in 2012, and from University of Hong Kong, China, 2013. He advised and coauthored 15 papers that received the Best Student Paper Award from different international conferences. He was the recipient of the Travel Fellowship Award of USNC/URSI for the 31th General Assembly and Scientific Symposium (GASS) in 2014, Advance Award of Science and Technology of Shanghai Municipal Government in 2015, Fellowship Award of JSPS in 2016, Innovation Award of Universities' Achievements of Ministry of Education of China in 2017, Innovation Achievement Award of Industry-Academia-Research Collaboration of China in 2019, "Jinqiao" Award of Technology Market Association of China in 2020, Baosteel Education Award of China in 2021, Carl Friedrich von Siemens Research Award of the Alexander von Humboldt Foundation of Germany in 2023, and Technical Achievement Award of Applied Computational Electromagnetic Society (ACES) of USA in 2024. In 2018, he was selected as the Distinguished Lecturer (DL) of IEEE Antennas and Propagation Society for 2019-2022, and in 2025, he was selected to the Top 2% Scientists List for both Career-Long Impact and Single-Year Impact by ELSEVIER and Stanford University.

Ultra-Wideband Frequency Selective Surface With Metal Gratings for Polarization Conversion Under Arbitrary Polarized Angles

Xueyan Song, Hua Lu, Shaochen Yang, XuPing Li, Chao Xiong, YunQi Zhang, and Xin Wang

School of Electronic Engineering
Xi'an University of Posts & Telecommunications, Xi'an 710121, China
xysong6597@126.com, 1690998220@qq.com, 1625804505@qq.com,
lixuping@163.com, 2096712375@qq.com, johnny_5@126.com, wang.xin@xupt.edu.cn

Abstract – A frequency selective surface (FSS) with metal gratings (FSSMGs) is proposed for insensitive cross polarization conversion in an ultra-wide bandwidth. To obtain the ultra-wide bandwidth, a multiple-resonance structure of metal gratings are selected as the sub-units. The unit of FSSMGs is composed of four grating-via-grating (GVG) modules. Each GVG module is made up of two layers of vertically arranged metal grids, quasi-wave-guiding structures (metalized vias), and shielded floors. To ensure the FSSMGs convert waves in arbitrary polarization directions, the four GVG modules in the unit are rotationally symmetric arranged. Simulated results show that the cross-polarization transmission coefficient is greater than -1 dB in an ultra-wide band of 8.17–18.5 GHz (77.5%), in which the PCR (polarization conversion ratio) and the ECR (energy conversion ratio) are greater than 90%. Meanwhile, the designed FSSMGs is insensitive for arbitrary polarized angles. In addition, the proposed FSSMGs can operate in the band 8.17–12 GHz (38.0%) and 15–18.5 GHz (20.9%) when the incident angle is less than 45°. To verify the simulated results, the proposed FSSMGs was fabricated and measured, and the measured results are in good agreement with the simulated ones.

Index Terms – Grating-via-grating (GVG) module, incidence stability, polarization converter, polarization insensitivity, ultra-wideband.

I. INTRODUCTION

A frequency selective surface (FSS) is a type of spatially selective filter composed of a periodic array of metallic resonant elements arranged in a two-dimensional plane. It exhibits a transmission/reflection response that is highly dependent on the frequency of the incident electromagnetic wave, thereby enabling the spatial filtering of electromagnetic radiation [1, 2]. Polarization converters, a type of FSS, have been found important applications in reducing radar cross-sections [3], wireless communication [4], chiral sensing [5], among other fields. In practical applications, the polarization converter is typically placed between transmitter and receiver antennas to facilitate polarization conversion. In general, polarization converters can be categorized into transmission type [3, 4, 6–10] and reflection type [11–13] according to their transmission mode. They can also be classified into line-to-line polarization conversion [6–13], line-to-circular polarization conversion [14, 15], and circular-to-circular polarization conversion [16] in accordance with their polarizing category. Polarization converters have been researched for over a decade. Heretofore, extensive studies have been conducted on performances of polarization converters such as low profile [17], multi-functionality [18], wide bandwidth [19], oblique incidence stability [12], and reconfigurability [20]. However, the majority of traditional polarization converters can merely receive waves in a single polarization direction [6–13], which restricts their applications.

In recent years, a new type of polarization-insensitive cross polarization converter (PICPC) has been designed. Unlike traditional polarization converters, PICPCs can receive arbitrary polarized waves and convert them into cross-polarized waves, which have strong angle stability [8–10]. In [8], an insensitive polarization converter was proposed. The unit of the polarization converter consists of four monopole-via-monopole (MVM) modules, which can receive waves in four polarization directions and it exhibits a 3.0-dB transmission bandwidth ranging from 5.5 to 6.18 GHz (12%). In [10], a bi-isotropic Huygens' metasurface (BIHMS) is proposed for polarization-insensitive cross-polarization conversion in the bandwidth from 8.4 to 11.2 GHz (27.7%). Though there have been numerous papers on PICPCs, bandwidth limits their potential applications. To obtain ultra-wide bandwidth, several novel converters [21–23] according to the theory of multiple resonances

Submitted On: June 20, 2025
Accepted On: October 07, 2025

https://doi.org/10.13052/2025.ACES.J.401005

have been presented. In [21], an ultra-wideband tri-layer transmissive linear polarization converter is designed for terahertz waves. It achieves a conversion efficiency of more than 80% in the band from 0.2 to 1.0 THz (133%). In 2023, a polarization converter with collective coupling was proposed in [13]. The converter consists of two layers of strip-shaped grids and serrated grids, which can convert linearly polarized waves into cross-polarized ones in an ultra-wide band, and the conversion efficiency is above 80%. How to achieve an ultra-wide bandwidth with a conversion efficiency of more than 90% is still a challenge.

To obtain a conversion efficiency of over 90% in an ultra-wide bandwidth for arbitrary polarization angles, an FSSMGs is proposed in this paper. The unit of proposed FSSMGs consists of four grating-via-grating (GVG) modules, with a size of 0.16 (8.25 GHz) and a section thickness of 0.13. The four GVG modules are placed vertically in such a way that the proposed FSSMGs can achieve polarization insensitivity and incidence stability. Simulations show that the proposed converter is capable of transforming linearly polarized waves into cross-polarized waves (90° polarization rotation) in the band from 8.17 GHz to 18.5 GHz (77.5%), in which the polarization conversion ratio (PCR) is above 90% on average. The presented FSSMGs is polarization-insensitive under arbitrary polarized angles. In addition, the proposed FSSMGs can obtain oblique incidence stability in the band 8.17–12 GHz (38.0%) and 15–18.5 GHz (20.9%) when the incident angle is less than 45°.

II. DESIGN PROCESS AND OPERATION PRINCIPLE

A. Design process

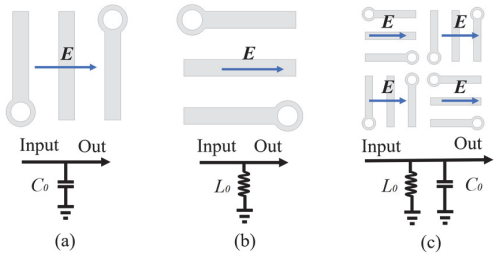

Fig. 1. Grid structures in different directions and their equivalent circuit models.

To achieve the required frequency band, gratings are selected as the sub-units of FSSMGs, and the corresponding equivalent resonance circuit can be manifested as depicted in Fig. 1. When perpendicular to the electric field direction, gratings behave as capacitance (C_0) [23], and thus the structure possesses low-pass filtering characteristics in Fig. 1 (a). When parallel to the electric field direction, gratings behave as inductance (L_0) and thus the structure exhibits high-pass filtering characteristics [24] as shown in Fig. 1 (b). Therefore, to obtain a band-pass response, the unit of FSSMGs are designed as in Fig. 1 (c), which consists of gratings in two vertical directions, and the grids behave as a parallel resonance circuit of inductance and capacitance.

Bandwidth depends mainly on the number of metals in each grating. Gratings made up of 3, 4, or 5 metals in the proposed unit were designed and the co-polar reflection coefficient R_{uu} of the FSSMGs in the three situations is simulated in HFSS, as depicted in Fig. 2. It can be observed that, as the number of metals increases, the number of resonances increases, as does the bandwidth of the FSSMGs. Considering the actual processing precision, the optimum number of metals in each grating is determined to be 5, as shown in Fig. 3.

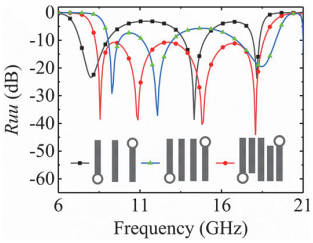

Fig. 2. Simulated R_{uu} of the FSSGMs with 3, 4, or 5 metals in each grating.

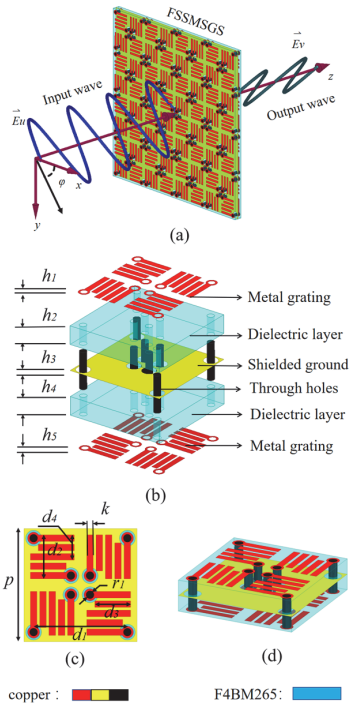

Fig. 3. (a) Configuration of the proposed FSSMGs, (b) exploded view, (c) top view, (d) 3D view.

Figure 3 shows the final configuration of the proposed FSSMGs. The unit consists of four GVG modules. In each GVG structure, the receiving metal grating and the transmitting metal grating are etched on a dielectric substrate (F4BM265, $\varepsilon_r = 2.65$, $\tan\delta = 0.003$) and connected by a metalized via, which contributes a unit. The four GVG modules are placed with a fourfold rotationally symmetric method, thus can effectively convert waves in arbitrary polarization direction, resulting in polarization insensitivity and incidence stability. The dimensions of the parameters in Fig. 1 are $h_1 = h_3 = h_5 = 0.035$ mm, $h_2 = h_4 = 2.5$ mm, $r_1 = 1$ mm, $d_1 = 9.42$ mm, $d_2 = 4.5$ mm, $d_3 = 3.6$ mm, $d_4 = 2.52$ mm, $p = 11.3$ mm, and $k = 0.65$ mm.

B. Operation principle

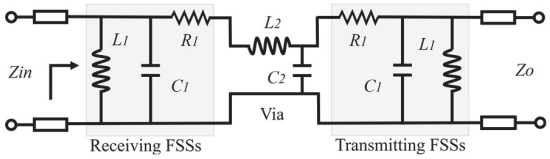

Fig. 4. Equivalent circuit model of a transmission-type polarization converter.

The sub-unit of FSSMGs consists of a receiving grid on the top layer, metalized vias, and an emitting grid on the bottom layer. The receiving and the emitting grid structure can be equivalent to parallel resonant circuits (C_1, L_1), and the metalized vias (waveguide structures) can be represented by a series resonant circuit (L_2,C_2 and R_1 are related to electric energy storage, magnetic energy storage and medium loss), as shown in Fig. 4.

The frequency response of FSSMGs can be illustrated by S-parameters, which can be defined as [25]:

$$S_{11} = \frac{A_{11} + A_{12}/Z_0 - A_{21}\cdot Z_0 - A_{22}}{A_{11} + A_{12}/Z_0 + A_{21}\cdot Z_0 + A_{22}}, \tag{1}$$

$$S_{21} = \frac{2}{A_{11} + A_{12}/Z_0 + A_{21}\cdot Z_0 + A_{22}}, \tag{2}$$

where A_{11},A_{12},A_{21}, and A_{22} are the elements of the two-port network transmission matrix. According to transmission line theory, the transmission matrix of the FSSMGs can be represented as:

$$T = \begin{pmatrix} A_{11} & A_{12} \\ A_{21} & A_{22} \end{pmatrix} = \begin{pmatrix} 1 & 0 \\ j\omega C_1 + \dfrac{1}{j\omega L_1} & 1 \end{pmatrix} \times \begin{pmatrix} cos(\beta d) & jZ_2 sin(\beta d) \\ \dfrac{jsin(\beta d)}{\left(\frac{L_2}{C_2}\right)^{\frac{1}{2}}} & cos(\beta d) \end{pmatrix}, \tag{3}$$

$$\beta = 2\pi f\sqrt{L_2 C_2}. \tag{4}$$

During transmission, the phase is delayed and caused by the metalized vias in FSSMGs. Equation (4) represents the phase constant of the metalized vias, where f is the operation frequency, L_2 and C_2 are the inductance and capacitance per unit length of the metalized vias, respectively, and Z_2 is the characteristic impedance. The values of the inductance and capacitance of the polarization converter in the form of an infinite array can be optimally designed through the following equation [16]:

$$L_1 = \frac{W_m}{|I_L|^2}, \quad C_1 = \frac{|I_c|^2}{2\omega^2 W_e}, \tag{5}$$

where W_m and W_e represent for the magnetic and electric energies stored around the grid cell, I_L and I_c denotes the currents associated with the inductance and capacitance of the grid, respectively.

To verify the analyzed results, the equivalent circuit simulator is utilized to simulate the transmission and reflection coefficients. The extracted current parameters used in the equivalent circuit are: $L_1 = 6.612$ nH, $C_1 = 0.049$ pF, $L_2 = 3.211$ nH, $C_2 = 0.002$ pF, $R_1 = 10.8\ \Omega$. The simulated R_{uu} results by the equivalent circuit simulator are shown in Fig. 5, which are compared with results simulated by ANSYS HFSS at the polarization angle of 0°. From analysis of the equivalent circuit in Fig. 1, it can be obtained that the width of the grating metal k has a significant impact on S-parameters. Therefore, Fig. 5 demonstrates the compared R_{uu} results of different parameter k. It can be illustrated from

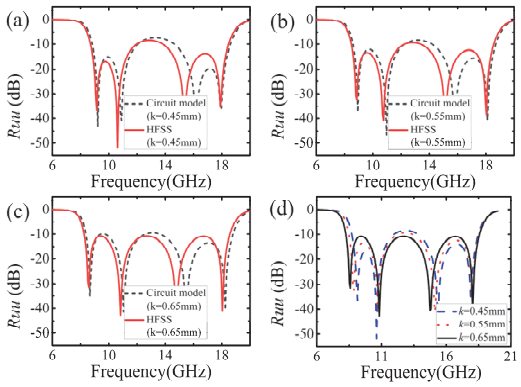

Fig. 5. R_{uu} at $\varphi = 0°$ calculated by equivalent circuit models and HFSS when (a) $k = 0.45$ mm, (b) $k = 0.55$ mm, (c) $k = 0.65$ mm, and (d) R_{uu} simulated by HFSS at different k values.

Figs. 5 (a–c) that the results by equivalent circuit simulator are in good agreement with those by HFSS. Moreover, it can be obtained from Fig. 5 (d) that the widest bandwidth of the proposed FSSMGs is observed at a k value of 0.65 mm.

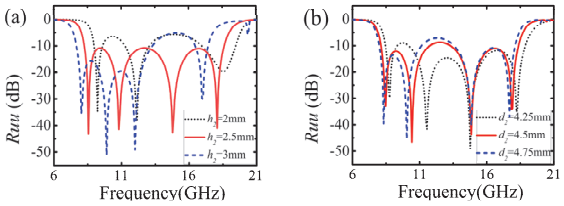

Fig. 6. Simulated R_{uu} of proposed FSSMGs with different values of main parameters, including d_2 and h_2.

Full wave simulation based on Floquet mode is conducted in ANSYS HFSS. All parameters, except k, d_2 (dimension of the sub-unit) and h_2 (thickness of the dielectric substrates), have significant impact on the simulation results. Figure 6 depicts the simulated R_{uu} of the proposed FSSMGs with different values of d_2 and h_2. It can be seen from Fig. 6 (a) that, when h_2 increases, the resonant frequencies move to the low frequency band, and the bandwidth of R_{uu} is wider when $h_2 = 2.5$ mm. Therefore, parameter h_2 is chosen as 2.5 mm, which is also beneficial for processing. In Fig. 6 (a), when d_2 increases, the resonant frequencies moves to the low frequency band. Moreover, the dimension of d_2 has an effect on the two lower resonant frequencies. To ensure the R_{uu} value to be lower than -10 dB, d_2 is selected as 4.5 mm.

In order to visually validate the polarization insensitivity of FSSMGs, the electric field vector distributions at the receiving and radiating ends were analyzed at 8.56 GHz. The receiving and radiating ports of the FSSMGs unit were placed on two mutually perpendicular planes, with the angle between the receiving plane and the x-axis set as φ. Figure 7 depicts the electric field vector distribution on the receiving and radiating planes of FSSMGs at polarization angles of $\varphi = 0°$, 15°, 30°, and 45°. It can be observed that the electric field direction of incident and transmitted waves are perpendicular to each other, which demonstrates the cross-polarization conversion of the proposed converter. The energy levels of transmitted waves at the four polarization angles are almost identical, which verifies the polarization-insensitivity of the designed FSSMGs.

III. ANALYSIS OF SIMULATION RESULTS

FSSMGs can be considered as a dual-port device, and its transmission characteristics can be demonstrated using S-parameters. When the polarization angle of electromagnetic wave φ is not equal to 0 or 90 deg,

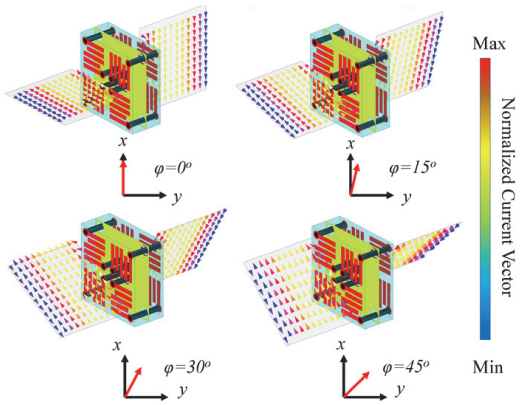

Fig. 7. Electric field vector distribution at input and output ports of the FSSMGs for an incident LP wave in (a) $\varphi = 0°$, (b) $\varphi = 15°$, (c) $\varphi = 30°$, and (d) $\varphi = 45°$.

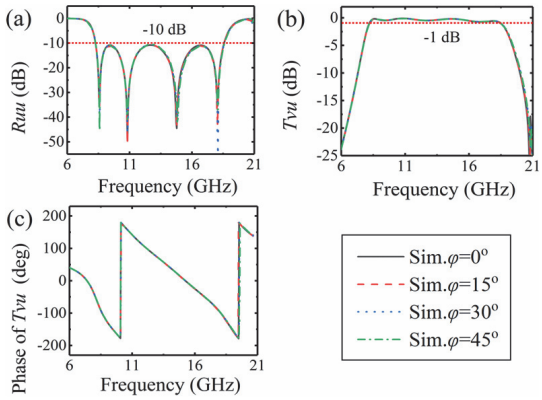

Fig. 8. Simulated (a) R_{uu}, (b) T_{vu}, and (c) phase of T_{vu} of FSSMGs when φ is equal to 0°, 15°, 30°, 45°, respectively.

the performance of the polarization converter can be demonstrated by the co-polarized reflection coefficient (R_{uu}) and cross-polarized transmission coefficient (T_{vu}). The proposed polarization converter is stable for any angle of polarization. Due to the rotational symmetry of the structure, the results at the polarization angle of 0–45° are taken as examples to analyze the performance of the polarization converter. Full wave simulation based on Floquet mode is conducted in ANSYS HFSS, and the 3D frequency-domain solver is used to obtain the propagation characteristic of the FSSMGs at copolar- and cross-polarized incidence within the required frequency band.

Figure 8 shows the simulated amplitude of R_{uu}, T_{vu}, and the phase of T_{vu} at polarization angles from 0° to 45°. It can be found that the R_{uu} at different polarization angles are approximately consistent, which demonstrates the polarization insensitivity of the proposed converter. The frequency bandwidth in Fig. 8 (a) at

the R_{uu} of less than -10 dB is from 8.25 GHz to 18.7 GHz, which is consistent with the bandwidth from 8.17 GHz to 18.5 GHz at T_{vu} of more than -1 dB in Fig. 8 (b). Therefore, the polarization converter can realize polarization conversion in the band from 8.17 GHz to 18.5 GHz.

$$PCR = \frac{T_{vu}^2}{T_{vu}^2 + T_{uu}^2}, \tag{6}$$

$$ECR = \frac{T_{vu}^2}{T_{vu}^2 + T_{uu}^2 + R_{vu}^2 + R_{uu}^2}. \tag{7}$$

For the purpose of evaluating the polarization conversion efficiency, the PCR and energy conversion ratio (ECR) [13] of are defined and expressed in equations (6) and (7).

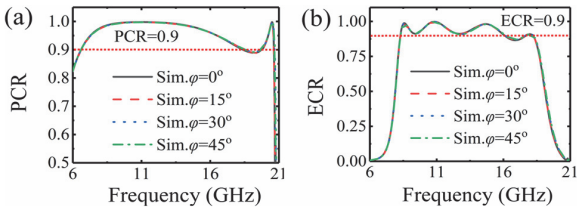

Fig. 9. Simulation results at $\varphi = 0°$, 15°, 30°, and 45°. (a) PCR. (b) ECR.

Figure 9 depicts the PCR and ECR of the proposed converter at different polarization angles. It can be seen that the PCR value is more than 90% in the frequency range of 6.72–19.1 GHz, and the maximum PCR value reaches 97% at 11 GHz. Figure 8 (b) shows that the ECR value in the band of 8.28–18.14 GHz is averagely more than 90%. Moreover, the simulated results at different polarization angles in Fig. 8 are completely consistent. In conclusion, the proposed FSSMGs exhibits high polarization conversion efficiency and high polarization insensitivity.

Furthermore, the amplitude and phase of T_{vu} under oblique incidence were simulated under the oblique incidence θ from 0° to 45°, as depicted in Figs. 10 (a) and (b), respectively. Due to polarization-insensitive characteristic, φ was defined as 0° in Fig. 9. It can be illustrated that, the proposed FSSMGs has excellent oblique incidence stability in the frequency band of 8.17–12 GHz (38.0%) and 15–18.5 GHz (20.9%) when the incident angle is less than 45°.

IV. EXPERIMENTAL VERIFICATION

To verify simulations, a prototype of the polarization converter with 21×21 units was made, as shown in Fig. 11. The part inside the dashed rectangle is enlarged. The prototype has a size of 238×238 mm. The transmission characteristic parameters of the FSSMGs

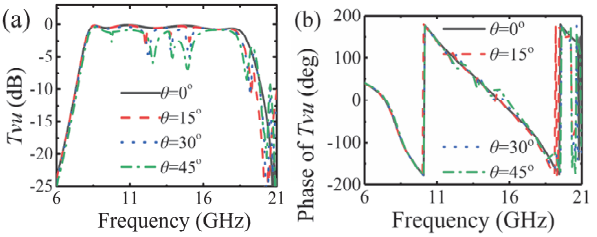

Fig. 10. The (a) amplitude and (b) phases of T_{vu} at the incident angle-θ of 0°, 15°, 30°, and 45°.

were measured using two standard horn antennas in a microwave anechoic chamber, and the distance between horn antennas and the fabricated converter is 100 cm. The installation diagram and the measured environment is shown in Fig. 12.

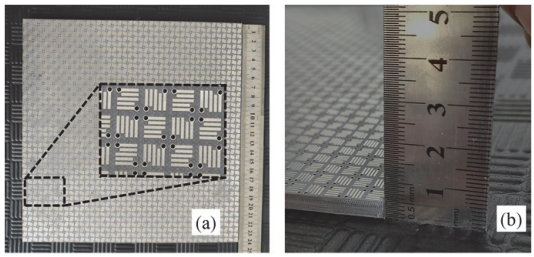

Fig. 11. Fabrication of the proposed FSSMGs.

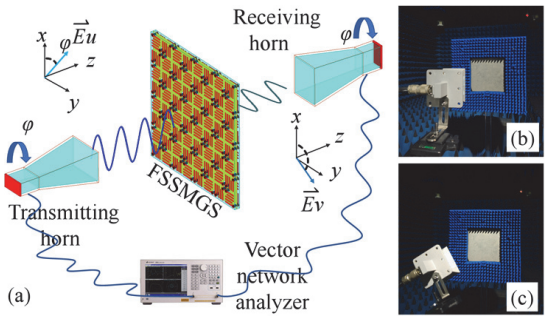

Fig. 12. Experimental setup.

Figure 13 illustrates the measured amplitude of R_{uu} and T_{uv} at $\varphi = 0°$, 15°, 30°, and 45°. It is evident that the curves at different φ are almost coincident, which validates the polarized insensitivity of the proposed converter. The bandwidth of the measured T_{vu} ranges from 8.21 GHz to 18.62 GHz (77.6%), closely aligning with simulated ones.

Finally, to emphasize the benefits of the proposed FSSMGs, a comparison with several related PICPCs is provided in Table 1. Compared with existing PICPCs, the FSSMGs introduced in this letter demonstrates a broader transmission bandwidth along with higher polarization conversion efficiency.

Table 1: Data comparison of the most advanced polarization-insensitive polarization converters

Ref.	Unit Cell Dimension	Num. of Layer	Bandwidth (GHz)	PCR	ECR
[8]	$0.23\lambda_0$	2	9.14-9.5 (4%),10.9-11.4 (5.1%)	/	>79%
[9]	$0.31\lambda_0$	3	5.5-6.18 (12%)	>90%	>50%
[10]	$1.13\lambda_0$	3	9.5-10.9 (13.7%)	>99%	>95%
[11]	$0.35\lambda_0$	7	26-32 (21%)	/	>50%
[12]	$0.33\lambda_0$	2	8.4-11.2 (27.2%)	>92%	>60%
This work	**$0.16\lambda_0$ (8.21 GHz)**	**3**	**8.21–18.62 (77.6%)**	**>94%**	**>92%**

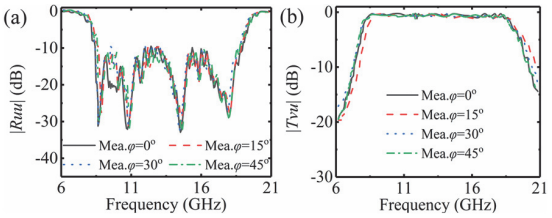

Fig. 13. Measured and simulation results: (a) R_{uu} and (b) T_{uv} with polarization angles at $\varphi = 0°$, 15°, 30°, and 45°.

V. CONCLUSION

A novel FSSMGs is proposed to achieve insensitive polarization conversion in an ultra-wide bandwidth. The unit is made up of four rotationally symmetric GVG modules. Compared to existing PICPCs, the proposed FSSMGs demonstrates an ultra-wide bandwidth by designing innovative multiple-resonance unit. Polarization conversion occurs within the band 8.21–18.62 GHz (77.6%), during which the polarization conversion efficiency is higher than 90% and the proposed converter can achieve polarization conversion in arbitrary polarized angles. The high polarization conversion efficiency and ultra-wide bandwidth suggest potential prospects in applications such as X/Ku communication for military unmanned aerial vehicles and multi-band polarization multiplexing in satellite communications.

ACKNOWLEDGMENT

This work was supported by Technology Innovation Leading Program of Shaanxi (Program No. 2024ZC-YYDP-33).

REFERENCES

[1] J. Huang, T. K. Wu, and S. W. Lee, "Tri-band frequency selective surface with circular ring elements," *IEEE Trans. Antennas Propag.*, vol. 42, no. 2, pp. 166–175, 1994.

[2] R. Panwar and J. R. Lee, "Progress in frequency selective surface based smart electromagnetic structure: A critical review," *Aerosp. Sci. Technol.*, vol. 66, pp. 216–234, 2017.

[3] H. A. Zebker and J. J. Van Zyl, "Imaging radar polarimetry: A review," *Proc. IEEE*, vol. 79, no. 11, pp. 1583–1606, Nov. 1991.

[4] W. Li, S. Gao, Y. Cai, Q. Luo, M. Sobhy, G. Wei, P. Xu, J. Li, C. Wu, and Z. Cheng, "Polarization-reconfigurable circularly polarized planar antenna using switchable polarizer," *IEEE Trans. Antennas Propag.*, vol. 65, no. 9, pp. 4470–4477, Sep. 2017.

[5] R. Singh, E. Plum, C. Menzel, C. Rockstuhl, A. K. Azad, R. A. Cheville, F. Lederer, W. Zhang, and N. I. Zheludev, "Terahertz metamaterial with asymmetric transmission," *Phys. Rev. B, Condens. Matter*, vol. 80, no. 15, Oct. 2009.

[6] G. Cheng, L. Si, P. Tang, Q. Zhang, and X. Lv, "Study of symmetries of chiral metasurfaces for azimuth-rotation-independent cross polarization conversion," *Opt. Exp.*, vol. 30, no. 4, p. 5722, 2022.

[7] S. Y. Wang, J.-D. Bi, W. Liu, W. Geyi, and S. Gao, "Polarization insensitive cross-polarization converter," *IEEE Trans. Antennas Propag.*, vol. 69, no. 8, pp. 4670–4680, Aug. 2021.

[8] W. Liu, L. Zhang, J. Ke, J. Liang, C. Xiao, Q. Cheng, and T. Cui, "Metasurface-based broadband polarization-insensitive polarization rotator," *Opt. Exp.*, vol. 30, no. 19, p. 34645, Sep. 2022.

[9] J. Zhu, Y. Yang, J. Lai, and J. Nulman, "Additively manufactured polarization insensitive broadband transmissive metasurfaces for arbitrary polarization conversion and wavefront shaping," *Adv. Opt. Mater.*, vol. 10, no. 21, Nov. 2022.

[10] J. Li, Y. Yuan, Q. Wu, and K. Zhang, "Bi-isotropic Huygens' metasurface for polarization-insensitive cross-polarization conversion and wavefront manipulation," *IEEE Transactions on Antennas and Propagation*, vol. 72, no. 3, pp. 2445–2454, Mar. 2024.

[11] K. Li, Y. Liu, Y. Jia, and Y. J. Guo, "A circularly polarized high-gain antenna with low RCS over a wideband using chessboard polarization conversion metasurfaces," *IEEE Trans. Antennas Propag*, vol. 65, no. 8, pp. 4288–4292, Aug. 2017.

[12] M. Anh Nguyen and G. Byun, "Anisotropic metagratings with a polarization-selective layer for anomalous wide-angle reflection and polarization conversion," *IEEE Trans. Antennas Propag*, vol. 72, no. 10, pp. 7961–7969, Oct. 2024.

[13] M. Yang, F. Lan, Y. Zhang, L. Qi, G. He, Y. Pan, T. Song, L. Wang, P. Mazumder, H. Zeng, and Z. Yang, "Collective-coupling enhanced

ultrabroadband linear polarization conversion on zigzag-split metasurfaces," *IEEE Trans. Antennas Propag*, vol. 71, no. 6, pp. 5001–5013, June 2023.

[14] E. Arnieri, F. Greco, L. Boccia, and G. Amendola, "A SIW-based polarization rotator with an application to linear-to-circular dual-band polarizers at K-/Ka-band," *IEEE Trans. Antennas Propag.*, vol. 68, no. 5, pp. 3730–3738, May 2020.

[15] H. B. Wang and Y. J. Cheng, "Single-layer dual-band linear to-circular polarization converter with wide axial ratio bandwidth and different polarization modes," *IEEE Trans. Antennas Propag*., vol. 67, no. 6, pp. 4296–4301, June 2019.

[16] P. Xu, W. X. Jiang, S. Y. Wang, and T. J. Cui, "An ultrathin cross-polarization converter with near unity efficiency for transmitted waves," *IEEE Trans. Antennas Propag*, vol. 66, no. 8, pp. 4370–4373, Aug. 2018.

[17] V. Singh, S. Bhattacharyya, and R. Agrahari, "A low-profile tri-functional metasurface toward polarization conversions and absorption," *IEEE Antennas and Wireless Propagation Letters*, vol. 23, no. 9, pp. 2593–2597, Sep. 2024.

[18] P. Naseri, S. A. Matos, J. R. Costa, C. A. Fernandes, and N. J. G. Fonseca, "Dual-band dual-linear-to-circular polarization converter in transmission mode application to K/K a-band satellite communications," *IEEE Trans. Antennas Propag.*, vol. 66, no. 12, pp. 7128–7137, Dec. 2018.

[19] A. A. Omar, Z. Shen, and S. Y. Ho, "Multiband and wideband 90° polarization rotators," *IEEE Antennas Wireless Propag. Lett.*, vol. 17, no. 10, pp. 1822–1826, Oct. 2018.

[20] W. Fu, Y. Cai, P. Mei, G. Frølund Pedersen, and S. Zhang, "Electronically reconfigurable filtering reflectarray antenna using polarization conversion elements with controllable conversion zeros," *IEEE Trans. Antennas Propag.*, vol. 72, no. 9, pp. 7359–7364, Sep. 2024.

[21] R. T. Ako, W. S. L. Lee, S. Atakaramians, M. Bhaskaran, S. Sriram, and W. Withayachumnankul, "Ultra-wideband tri-layer transmissive linearpolarization converter for terahertz waves," *APL Photon.*, vol. 5, no. 4, Apr. 2020.

[22] M. Yang, F. Lan , Y. Zhang, L. Qi, G. He, Y. Pan, T. Song, L. Wang, P. Mazumder, H. Zeng, and Z. Yang, "Collective-coupling enhanced ultrabroadband linear polarization conversion on zigzag-split metasurfaces," *IEEE Trans. Antennas Propag*, vol. 71, no. 6, pp. 5001–5013, June 2023.

[23] D. Feng, "A new equivalent circuit of miniaturized frequency selective surface," in *Proceedings of 2014 3rd Asia-Pacific Conference on Antennas and Propagation*, Harbin, China, pp. 1363–1365, 2014.

[24] P. Xu, W. X. Jiang, S. Y. Wang, and T. J. Cui, "An ultrathin cross-polarization converter with near unity efficiency for transmitted waves," *IEEE Trans. Antennas Propag*, vol. 66, no. 8, pp. 4370–4373, Aug. 2018.

[25] S. Y. Wang, J. D. Bi, W. Liu, W. Geyi, and S. Gao, "Polarization insensitive cross-polarization converter," *IEEE Trans. Antennas Propag.*, vol. 69, no. 8, pp. 4670–4680, Aug. 2021.

Xueyan Song was born in Henan Province, China, in 1989. She received the B.E. degree in 2012 and the Ph.D. degree in 2018 from Xidian University. She joined Xi'an University of Posts and Telecommunications in 2018. Her research interests include metasurface, antennas, and reflector antennas.

Hua Lu was born in Shaanxi, China, in 1998. He holds the Master of Engineering degree from the School of Electronic Engineering, Xi'an University of Posts and Telecommunications. His current research interests include metasurface and polarization converter.

Shaochen Yang was born in Shaanxi, China, in 2002. He is currently pursuing a Master of Engineering degree in the School of Electronic Engineering, Xi'an University of Posts and Telecommunications.

XuPing Li was born in Xi'an, Shanxi, China, in 1981. He received the Ph.D. degree in electromagnetic fields and microwaves from Xidian University, Xi'an, in 2015. In January 2019, he was transferred to Xi'an University of Posts and Telecommunications as leader of the phased array antenna technology research team. His research programs focus on phased array antennas.

Chao Xiong was born in Jiangxi, China, in 2004. He is currently pursuing B.E. degree in the school of Electronic Engineering, Xian University of Posts and Telecommunications.

YunQi Zhang was born in BaoTou, Inner Mongolia, China, in 1986. He received the Ph.D. degree from Xidian University in 2015. He is currently working in Xi'an University of Posts & Telecommunications. His research interests include GPS antenna, CP antenna, omnidirectional antenna and antenna array designs.

Xin Wang received his master's degree in 2015 from Xidian University, China. Subsequently, he worked at several major communication equipment manufacturers. In 2024, he received his Ph.D. from Xidian University. He is currently employed at Xi'an University of Posts & Telecommunications, with research interests in reconfigurable metasurfaces for active power amplifiers, power amplifiers, and phased array antennas.

A Novel GaN Power Amplifier Based on Quasi-Monolithic Microwave Integrated Circuits

Letian Guo[1], Shunli Ma[1], Hou Yi Ding[2], and Mei Song Tong[2]

[1]State Key Laboratory of ASIC and System, Fudan University, Shanghai 200438, China
19112020081@fudan.edu.cn, shunlima@fudan.edu.cn

Department of Electronic Science and Technology
Tongji University, Shanghai 201804, China
mstong@tongji.edu.cn

Abstract – In this paper, we propose a compact quasi-monolithic microwave integrated circuit (MMIC) ultra-wideband gallium nitride (GaN) power amplifier (PA), highlighting its innovative design approach and the associated fabrication techniques aimed at enhancing integration and performance. The discrete transistor is manufactured by a 0.35-μm GaN high electron mobility transistor (HEMT) process. The input matching network employs a GaAs passive device process for compact and wideband flexible design. The output matching network employs a ceramic technology for high power and low insertion loss design. The discrete transistor is connected to the input and output network with gold bonding wires. The PA exhibited a gain of 11 dB, a saturation power of 48 dBm, and a peak power-added efficiency of 32.8%.

Index Terms – Gallium nitride (GaN), matching network, monolithic microwave integrated circuit (MMIC), power amplifier (PA), ultra-wideband.

I. INTRODUCTION

Broadband power amplifier (PA) monolithic microwave integrated circuits (MMICs) are extensively studied and applied in electronic systems such as electronic countermeasure and multifunction platforms [1–4]. The key performance metrics, including the output power (P_{out}) and power-added efficiency (PAE), can critically impact the overall effectiveness of these systems [5–8]. The gallium nitride high electron mobility transistors (GaN HEMTs) on silicon carbide (SiC) substrates can offer notable advantages in radio-frequency (RF) applications, including the high breakdown voltage, superior current handling capability, and elevated power density [9]. Consequently, numerous high-power and high-efficiency GaN-based PAs have been proposed [10, 11]. To enhance their performance, a variety of advanced techniques have been developed, such as stacked field effect transistor (FET) technology [12], reactive filter synthesis, and asymmetric magnetically coupled resonator (MCR) technology [13].

Distributed amplifiers (DAs) have attracted considerable interest due to their excellent return loss and wide bandwidth characteristics [14]. By incorporating the parasitic capacitance of multiple transistors into artificial transmission lines, the DAs can achieve a broadband operation, which can theoretically extend from the zero frequency to the cutoff frequency of the artificial line. Despite these advantages, the DAs still encounter several limitations [15], including low gain [16], poor efficiency [17], large chip area [18], and restricted output power [19]. To address these challenges, reactive matching power amplifiers have been proposed, albeit at the expense of increased design complexity.

In this paper, we propose a novel two-stage GaN PA based on the quasi-MMICs and the analysis, design, and implementation for it with a reactive matching network are presented. The high-pass and low-pass filter matching techniques are employed to achieve effective impedance transformation. Resistors are incorporated into the input-stage matching network to improve the circuit stability and enhance gain flatness across the operating band. Based on the proposed design methodology, the amplifier can operate over the frequency range of 2–6 GHz and deliver an output power (P_{out}) of exceeding 60 W with a PAE ranging from 27% to 40% and an averaged small-signal gain of 26 dB. Simulation and experimental results demonstrate the excellent performance of the proposed PA through a comparison with other PAs available in literature.

II. TRANSISTOR MODELING METHODOLOGY

Transistor modeling is a crucial step in amplifier circuit design optimization, and building accurate transistor

Submitted On: April 07, 2025
Accepted On: August 21, 2025

https://doi.org/10.13052/2025.ACES.J.401006

models plays a vital role in optimizing circuit performance [20]. There are two transistor modeling methods: linear small-signal [21] and nonlinear large-signal modeling [22]. Linear small-signal modeling extracts linear parameters through the *S*-parameters in each bias state to establish small-signal models. Large-signal modeling extracts nonlinear parameters based on current-voltage (I-V) test data to establish a large-signal model. By integrating and optimizing the extracted linear and nonlinear parameters, a complete model of the transistor that satisfies both S parameters and IV characteristics is established.

The transistor used in this paper is a GaN high electron mobility transistor (HEMT), which is modeled as a small-signal equivalent circuit using the 15 elements field-effect transistor model, with the structure shown in Fig. 1.

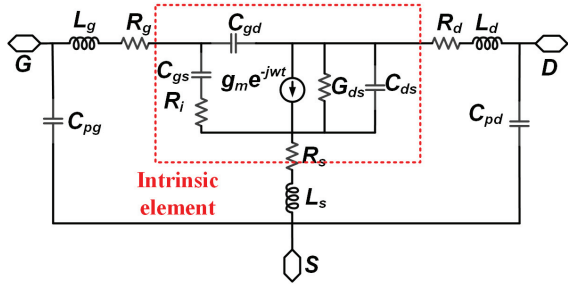

Fig. 1. Small-signal equivalent circuit model.

The parasitic capacitance C_{pg} and C_{pd} are extracted by the Dambrine method [23], the parasitic resistance R_s is extracted by the Yang-Long method [24], and the rest of the parasitic parameters are extracted by the ColdFET method [25]. After extracting the parasitic component parameters, the *S*-parameters can be converted to *Z*-parameters, and the influence of parasitic components can be removed from the *Z*-parameters, i.e., "de-embedding" [26], and the de-embedded *Z*-parameters can be converted to *Y*-parameters to extract the corresponding parameter values of the intrinsic components. The corresponding equivalent circuits of the intrinsic components are shown in Fig. 2.

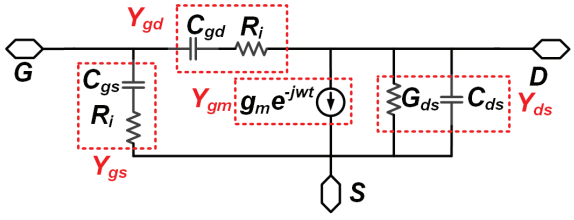

Fig. 2. Intrinsic components equivalent circuit.

While the small-signal model is effective for simulating the linear behavior of the device, accurate prediction of nonlinear characteristics, including DC performance and output power behavior, necessitates the use of a large-signal model. The large-signal model of the traditional HEMT is shown in Fig. 3, in which I_{ds} ("IDS" in Fig. 4), C_{ds}, and C_{gd} are three important nonlinear parameters, each of which has a corresponding nonlinear equation.

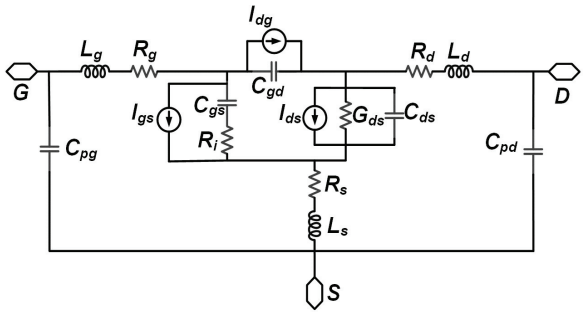

Fig. 3. Conventional HEMT large-signal model.

III. AMPLIFIER ARCHITECTURE

Based on the proposed transistor model, a DC bias scan is applied to the transistor and the results are shown in Fig. 4. Considering the output power and efficiency, the base bias voltage is selected to be −2.4 V and the emitter stage bias voltage is 28 V. At the given bias voltages, the transistor operates in the A and B bias states.

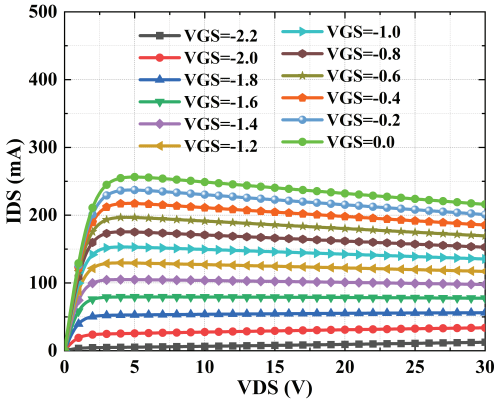

Fig. 4. Load-pull results for the model at 4 GHz.

The core is an eight-cell transistor with a single cell which has the gate width $10 \times 150\ \mu m^2$, transistor capacitance density of 0.45 pF/mm, single cell transistor resistance of 80 Ω, the structure shown in Fig. 5. After extracting the impedance parameters of the power tube core model, the output matching circuit design, if the eight cells are matched separately and then combined to

the RF output and input ports, the branch will become more, increasing the path loss, and the circuit size is too large. To ensure the simplicity and feasibility of the circuit structure design, in the output matching circuit, the eight cells are divided into two four-cell cores, and then the combined design. In the input matching circuit, the octet is divided into four two-cell cores and then combined.

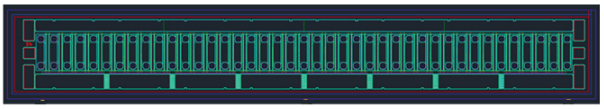

Fig. 5. Octal transistor core.

For the passive components in this circuit, the isolation capacitor and the bypass capacitor adopt the general-purpose non-remaining edge type microwave chip capacitor of Tianji Company, whose upper and lower surfaces are gold electrodes, and the middle ceramic dielectric layer is suitable for the bonding and mounting of gold wires and ribbons, and the structure is shown in Fig. 6. A microwave chip capacitor is a single-layer parallel plate capacitor structure, the capacitance depends on the dielectric constant of the dielectric material (K), the thickness of the dielectric material (T) and the size of the electrode $L \times W$.

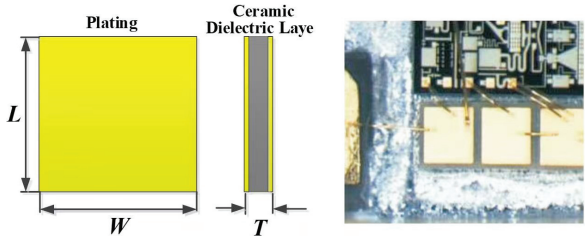

Fig. 6. Schematic and physical drawings of general-purpose no-edge-type microwave chip capacitors.

The designed quasi-monolithic PA consists of a tube core, an output matching circuit and an input matching circuit, and the tube core is connected to the matching circuit by a bonding alloy wire. The length of a single gold wire is 500 μm and the diameter is 25 μm. To realize the high power performance of the amplifier, the output matching circuit is made of alumina substrate, with the dielectric constant of 9.6, thickness of 380 μm, and copper thickness of 35 μm. The input matching circuit is made of a GaAs integrated circuit, with the dielectric constant of 12.9, board thickness of 100 μm, and metal layer thickness of 3 μm.The input matching circuit, the core and the output matching circuit are connected in cascade to obtain the overall structure of the amplifier, which is shown in Fig. 7.

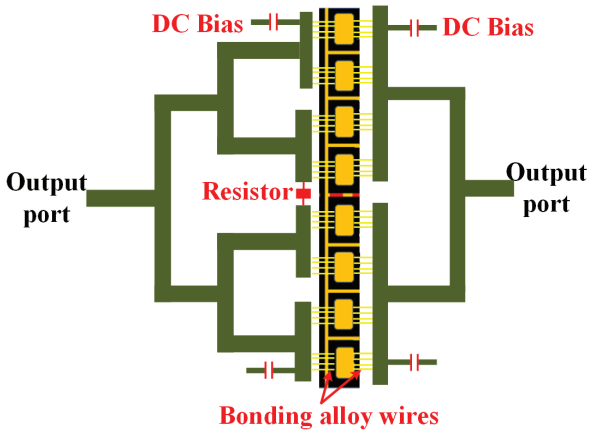

Fig. 7. Schematic diagram of quasi-monolithic amplifier structure.

IV. OVERALL CIRCUIT DESIGN APPROACH

A. Output matching circuit

In power amplifiers, output matching circuits are used to match the optimum output impedance obtained from the transistor by load traction to 50 ohms for maximum output power. The matching circuit is usually realized by using passive devices such as capacitors and inductors as well as microstrip lines, and L-type and ϕ-type structures are commonly used for the structure. When designing the output matching circuit, the octal cell is divided into two four-cell cores, and then the combined design is carried out, the structure is shown in Fig. 8.

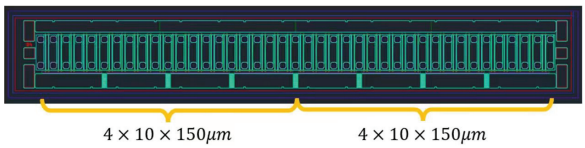

Fig. 8. Schematic diagram of an eight-cell transistor core divided into two equal paths.

The parallel equivalent resistance of a single four-cell core is $80/4 = 20\ \Omega$, and the parallel equivalent capacitance is 0.45 pF/mm$\times$10$\times$150μm$\times$4=2.7 pF. The transistor cores are bonded to the output matching circuit by a total of 36 gold wires, and each 4-cell core is connected in parallel using 18 gold wires, with a total of 36, spaced 130 μm single wires measuring 500 μm in diameter length and 25 μm in diameter. The inductance of a single gold wire is about 1.4 nF.

The constructed output circuit structure is shown in Fig. 9, and it can be seen that the output matching circuit consists of the parallel RC structure corresponding to the core impedance, the imaginary part compensation

network constructed by the bonding alloy wire and the bias feed circuit, the two-order L-type impedance transformation network, and the two-path power synthesis network. Among them, R_o and C_o are equivalent to the optimal output impedance of the four-cell core, L_a is the equivalent inductance introduced by the bonding alloy filament, and the parallel inductor L_b is used to offset the capacitance of the imaginary part of the core impedance, C_o and, at the same time, it plays the role of the drain bias supply. To improve the matching bandwidth, a two-stage low-pass L-type impedance conversion network is used, and the microstrip lines TL1 and TL2 play the roles of impedance conversion and power synthesis.

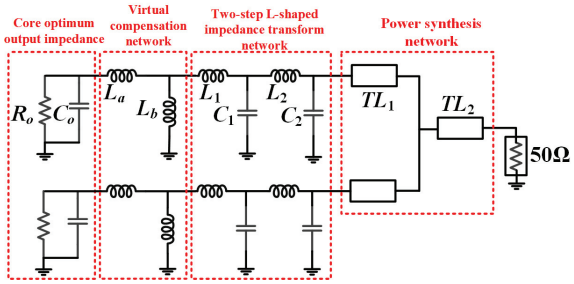

Fig. 9. Output matching network circuit.

Based on the above circuit diagram, an output circuit layout is constructed where the inductors L_b, L_1, and L_2 are in series microstrip line equivalents and the capacitors C_1 and C_2 are in parallel open microstrip line equivalents. A ceramic with a dielectric constant of 9.6 and thickness of 380 μm is used as the substrate for the output matching circuit, and the dimensions of each microstrip line are shown in Table 1. To accurately process the prepared samples, the high frequency structure simulator (HFSS) is used for modeling and simulation regarding the above simulation layout configuration and data based on the advanced design system (ADS). The HFSS model of the output circuit is shown in Fig. 10. The overall size of the structure is about 7.6×11.6 mm^2, and the widths of the microstrip lines are all greater than 100 μm, which can satisfy the maximum current and will not be fused due to overheating.

Table 1: Dimensions of microstrip lines in the output matching circuit

Microstrip Line	Dimension (μm)	Microstrip Line	Dimension (μm)
TL_1	350×1200	TL_2	900×1000
TL_3	2050×3700	TL_4	800×1700
TL_5	700×1000	TL_6	400×700
TL_7	700×1400	TL_8	1200×2000

The overall simulation results of the output matching circuit are shown in Fig. 11, which shows that the

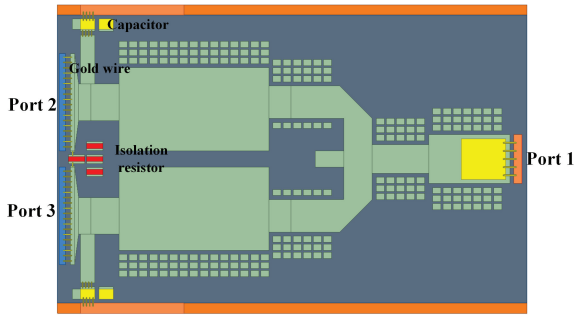

Fig. 10. HFSS modeling of output circuits.

RF output S_{11} is better than -10 dB in the band from 2 to 6.22 GHz, the drain output S_{22} is better than -7 dB in the band from 2 to 6 GHz, and the insertion loss S_{21} is better than -3.8 dB in the band range from 2 to 6.2 GHz. Taking into account that the actual loss conditions will produce a frequency-shift phenomenon, it would be better to extend the extended to about 6.2 GHz at high frequencies.

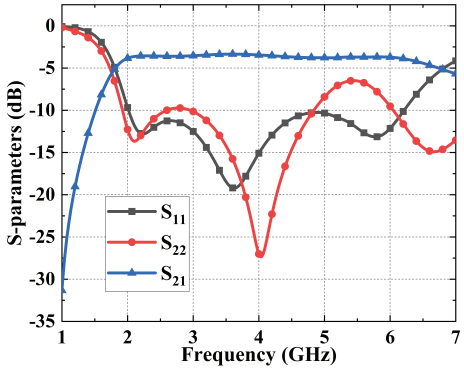

Fig. 11. Simulation result of S parameters for the output matching circuit.

B. Input matching circuit

In terms of the input matching circuit, the matching circuit is constructed by equalizing four two-cell merge circuits for the tube core, and the structure is shown in Fig. 12. The input circuit is realized using a 0.35 μm GaAs monolithic process to equalize the input signal into four two-cell transistor ports, with the output impedance of each circuit set to 40 Ω, and the output impedance of the four parallel combined circuits is 10 Ω.

The input matching circuit construction method is similar to the output matching circuit, in order to ensure a wide bandwidth of low insertion loss and the overall gain of the amplifier within the bandwidth, the use of type microstrip line structure, loading capacitors and other passive components to build matching network,

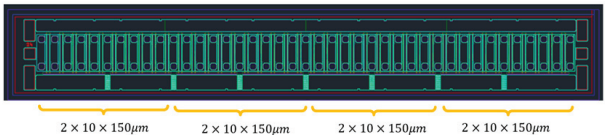

Fig. 12. Schematic diagram of an eight-cell transistor core divided into four equal paths.

the circuit is shown in Fig. 13. It can be seen that the input matching circuit consists of a series RC structure corresponding to the impedance of the core, the imaginary part of the compensation network constructed by the bonding alloy wire and the bias feed circuit, the third-order L-type impedance transformation network and the power synthesis network. Among them, R_o and C_o are equivalent to the input impedance of the double-cell core, L_a is the equivalent inductance introduced by the bonding alloy wire, and the parallel inductance L_b plays the role of gate bias power supply while it is used to offset the imaginary part of the core impedance capacitance C_o. To improve the matching bandwidth, a three-stage low-pass impedance conversion network is used, and the microstrip lines TL1 and TL2 play the role of impedance conversion and power synthesis at the same time.

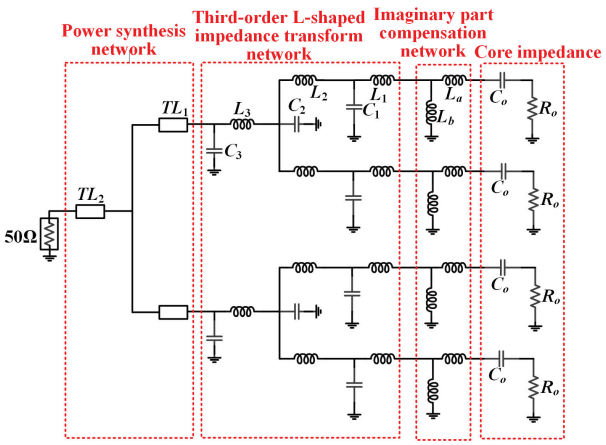

Fig. 13. Input matching circuit structure.

The structure of the input matching circuit is shown in Fig. 14, and the dimensions of each microstrip line are shown in Table 2.

The above input matching, tube core and output matching modules are cascaded to construct the overall circuit structure of the amplifier, and the circuit structure is shown in Fig. 15. Based on the transistor small-signal model and the S-parameters extracted from the output matching circuit, the S-small-signal simulation circuit of the amplifier is constructed. The impedance of input port 1 is 50 Ω. The small-signal simulation results of the

Table 2: Dimensions of microstrip lines in the input matching circuit

Microstrip Line	Dimension (μm)	Microstrip Line	Dimension (μm)
TL_1	806×67	TL_2	135×50
TL_3	820×50	TL_4	1790×50
TL_5	870×50	TL_6	260×50
TL_7	548×50	TL_8	1286×2000
TL_9	289×50	TL_{10}	463×50
TL_{11}	602×65	TL_{12}	202×65
TL_{13}	347×65	TL_{14}	187×65
TL_{15}	582×65	TL_{16}	141×65
TL_{17}	300×100	TL_{18}	1000×100
TL_{19}	1000×100		

amplifier are shown in Fig. 16, and the output port S_{22} is better than -12 dB in the range of $2-6$ GHz, the input S_{11} is better than about -5.6 dB in the band range of $2-6$ GHz, and the gain S_{12} is better than 10 dB in the range of $2-6$ GHz.

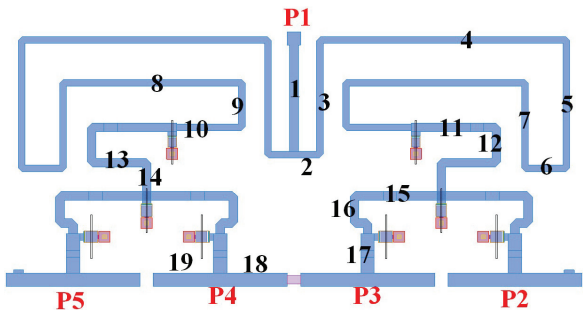

Fig. 14. Structure and layout of input matching circuit.

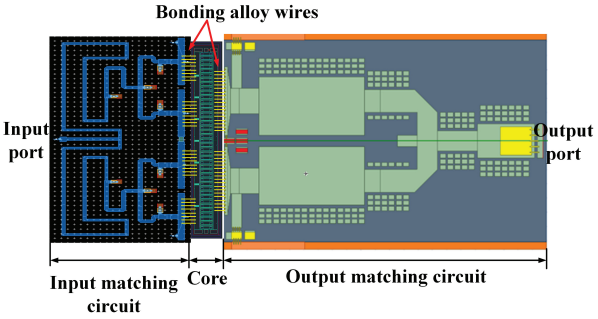

Fig. 15. Circuit structure of the $2-6$ GHz quasi-monolithic amplifier.

V. AMPLIFIER CIRCUIT SIMULATION AND TEST RESULTS

Based on the above amplifier structure, a physical sample is prepared as shown in Figs. 17 and 18, in which

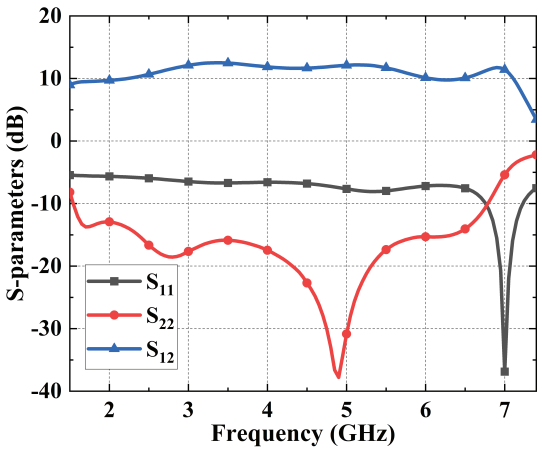

Fig. 16. Simulation results of S_{11}, S_{22}, and S_{12} parameters with a small-signal for the $2-6$ GHz quasi-monolithic amplifier.

the bias voltage is set to -2 V and 28 V. The amplifier is subjected to small-signal testing of S-parameters, gain, and other small-signal performances in the range of $2-6$ GHz, and the small-signal performances are obtained by on-chip testing using a vector network analyzer and so on. The small-signal test and simulation results of the amplifier are shown in Fig. 19, and the measured results show that the amplifier fluctuates between $12-15$ dB in the $2-6$ GHz range.

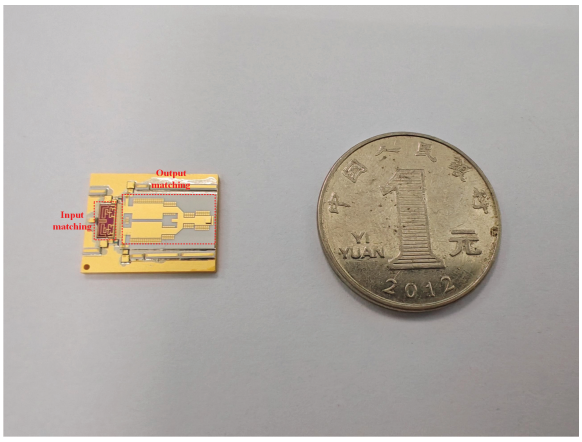

Fig. 17. A sample of matching circuit.

The large-signal test of the amplifier is conducted to measure the output power and saturated power added efficiency of the amplifier at the $2-6$ GHz band. The block diagram of the large-signal test connection and the test results are shown in Fig. 20. From the test results, it can be seen that the saturated output power of the amplifier is in the range of $48-50$ dBm in the $2-6$ GHz range, and the gain additive efficiency PAE is $34\sim46\%$.

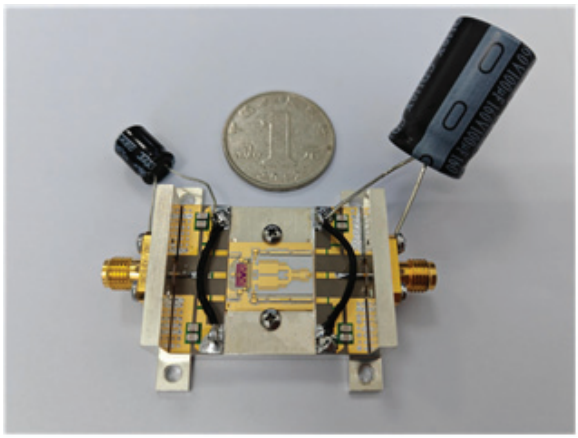

Fig. 18. A sample of the $2-6$ GHz quasi-monolithic amplifier.

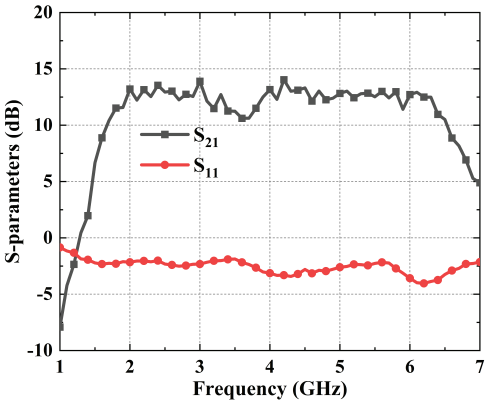

Fig. 19. Simulation results of S_{21} and S_{11} parameters with a small-signal for the $2-6$ GHz quasi-monolithic amplifier.

The performances of this PA is compared with other quasi-monolithic microwave integrated circuit (MMIC) ultra-wideband GaN PAs available in literature [21–26] and the result is shown in Table 3. The proposed PA can achieve an excellent performance with a bandwidth of $2.0\sim6.0$ GHz, a gain of 11.0 dB, a saturated output power (P_{sat}) of 48.0 dBm, and a maximum PAE of 34.0%. Compared with the performance indexes of those PAs from the references, the proposed PA has the highest value of figure of merit (FoM) which is defined by $FoM_{PA}=P_{sat}+10\log[PAE_{max}(\%)]+Gain+10\log[BW_{3dB}/f_0]$, where f_0 is the central frequency of the frequency band.

For the thermal effect of the amplifier, we have conducted a test and the results are shown in Fig. 21. From Fig. 21, we can see that the heat of the amplifier mainly concentrates in the input matching circuit and the maximum temperature is 106°.

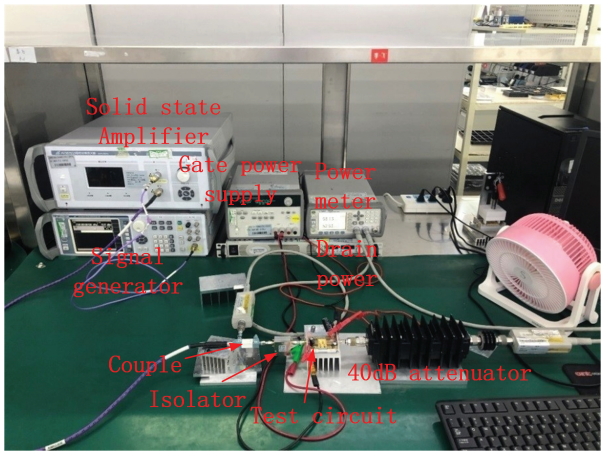

(a)

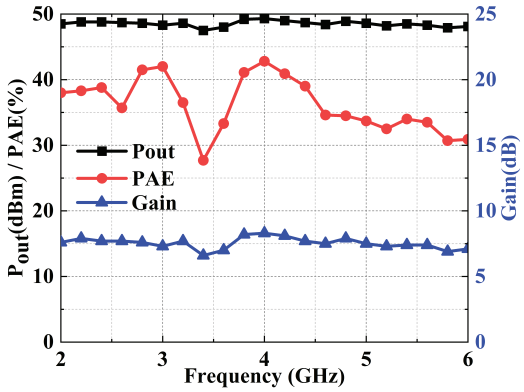

(b)

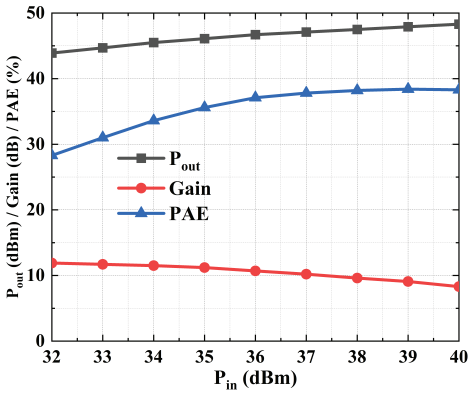

(c)

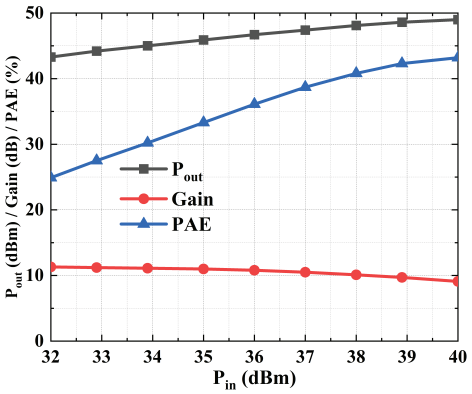

(d)

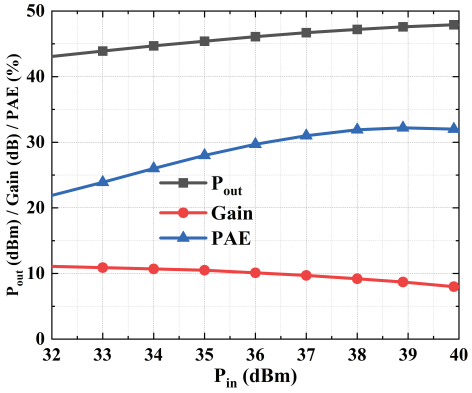

(e)

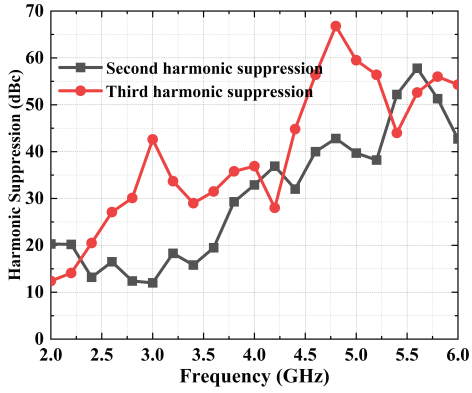

(f)

Fig. 20. Test results for the performance of the proposed PA. (a) Test setup. (b) Changes of P_{out}, gain, and PAE as a function of frequency. (c) Changes of P_{out}, gain, and PAE in terms of P_{in} at 2.0 GHz. (d) Changes of P_{out}, gain, and PAE in terms of P_{in} at 4.0 GHz. (e) Changes of P_{out}, gain, and PAE in terms of P_{in} at 6.0 GHz. (f) Suppression effect of harmonic waves.

Table 3: Performance summary and comparison of different distributed amplifiers

Reference	Frequency (GHz)	Gain (dB)	P_{sat} (dBm)	PAE$_{max}$ (%)	Bandwidth (%)	FoM	Technology
[27]	1.8-3.2	9.0	41.4	36.0	56.0	83.4	250-nm GaN
[28]	8.4-9.8	7.4	50.4	36.0	15.4	85.2	250-nm GaN
[29]	1.0-1.6	10.5	47.0	27.0	46.0	88.4	GaN HEMT
[30]	5.5-6.5	12.5	44.0	40.0	16.7	84.7	250-nm GaN
[31]	8.4-8.6	5.0	35.0	45.0	2.3	60.1	GaN HEMT
[32]	2.0-4.0	9.8	46.5	38.0	33.3	87.3	500-nm GaN
This Work	2.0-6.0	11.0	48.0	34.0	100.0	94.3	350-nm GaN

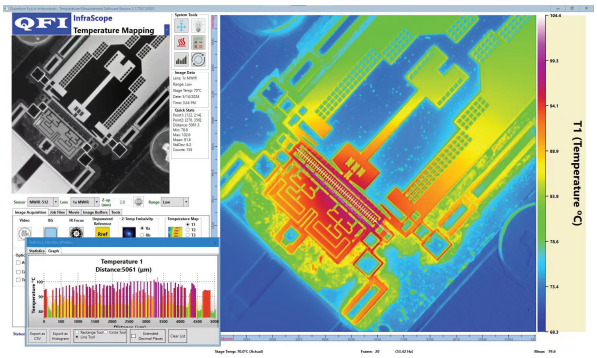

Fig. 21. Test result of thermal distribution for the 2-6 GHz quasi-monolithic amplifier.

VI. CONCLUSION

In this paper, a $2-6$ GHz broadband quasi-monolithic amplifier design method is proposed, with the GaN HEMT structure for the tube core, GaAs monolithic microwave integrated circuits for the input matching circuit of the amplifier, and high dielectric constant ceramic substrate for the output matching circuit. The core is a single-cell size gate width of the eight-cell transistor, the output matching circuit will be divided into eight-cell equal to two four-cell core, the input matching circuit will be divided into eight-cell equal to four two-cell core, through the multi-order L-type impedance transformation structure to achieve impedance matching after the design of the combined circuit. The test results show that the amplifier saturates the output power P_{out} in the range of $2.0-6.0$ GHz band at $48-50$ dBm, and the gain added efficiency PAE is $34-46\%$.

REFERENCES

[1] M. Garven and J. P. Calame, "Simulation and optimization of gate temperatures in GaN-on-SiC monolithic microwave integrated circuits," *IEEE Transactions on Components and Packaging Technologies*, vol. 32, no. 1, pp. 63–72, Mar. 2009.

[2] L. T. Guo, G. J. Deng, S. Y. Xie, H. Shao, W. H. Huang, Y. C. Zhang, Y. J. Zhang, and M. S. Tong, "A miniaturized high-power integrated passive frontend for high-power active array antenna," *IEEE Transactions on Components, Packaging and Manufacturing Technology*, vol. 13, no. 11, pp. 1770–1777, Nov. 2023.

[3] Q. Y. Liang and M. S. Tong, "A compensation amplifier with automatic zeroing and stable chopping," in *2022 IEEE Electrical Design of Advanced Packaging and Systems Symposium*, Urbana, Illinois, USA, Dec. 2022.

[4] S. Q. Wang, Y. Y. Hu, and M. S. Tong, "A low-power design of common-mode feedback circuit for fully-differential operational amplifiers," in *2024 Progress in Electromagnetics Research Symposium*, Chengdu, China, Apr. 2024.

[5] H. Kim, I.-J. Yoon, and Y. J. Yoon, "A novel fully integrated transmitter front-end with high power-added efficiency," *IEEE Transactions on Microwave Theory and Techniques*, vol. 53, no. 10, pp. 3206–3214, Oct. 2005.

[6] Z. G. Zhou, X. J. Huang, and M. S. Tong, "A 3D circuit model for power distribution networks in complex package structures," in *2016 IEEE Electrical Design of Advanced Packaging and Systems Symposium*, Honolulu, Hawaii, USA, Dec. 2016.

[7] S. C. Wang, M. J. Li, and M. S. Tong, "A miniaturized high-efficiency rectifier with extended input power range for wireless power harvesting," *IEEE Microwave and Wireless Components Letters*, vol. 30, no. 6, pp. 617–620, June 2020.

[8] S. C. Wang, M. J. Li, and M. S. Tong, "Wireless power transfer for CubeSats by using a novel high-performance rectenna," *IEEE Antennas and Wireless Propagation Letters*, vol. 19, no. 12, pp. 2197–2200, Dec. 2020.

[9] G. Meneghesso, M. Meneghini, A. Tazzoli, N. Ronchi, A. Stocco, A. Chini, and E. Zanoni, "Reliability issues of gallium nitride high electron mobility transistors," *International Journal of Microwave and Wireless Technologies*, vol. 2, no. 1, pp. 39–50, Feb. 2010.

[10] R. Sun, J. Lai, W. Chen, and B. Zhang, "GaN power integration for high frequency and high efficiency power applications: A review," *IEEE Access*, vol. 8, pp. 15529–15542, 2020.

[11] J. S. Moon, H. Moyer, P. Macdonald, D. Wong, M. Antcliffe, M. Hu, P. Willadsen, P. Hashimoto, C. McGuire, M. Micovic, M. Wetzel, and D. Chow, "High efficiency X-band class-E GaN MMIC high-power amplifiers," in *2012 IEEE Topical Conference on Power Amplifiers for Wireless and Radio Applications*, Santa Clara, CA, USA, Apr. 2012.

[12] S. Pornpromlikit, J. Jeong, C. D. Presti, A. Scuderi, and P. M. Asbeck, "A Watt-level stacked-FET linear power amplifier in silicon-on-insulator CMOS," *IEEE Transactions on Microwave Theory and Techniques*, vol. 58, no. 1, pp. 57–64, Jan. 2010.

[13] G. Lee, B. H. Waters, C. Shi, W. S. Park, and J. R. Smith, "Design considerations for asymmetric magnetically coupled resonators used in wireless power transfer applications," in *2013 IEEE Radio and Wireless Symposium*, Austin, TX, USA, Mar. 2013.

[14] M.-D. Tsai, H. Wang, J.-F. Kuan, and C.-S. Chang, "A 70GHz cascaded multi-stage distributed amplifier in 90nm CMOS technology," *2005 IEEE International Digest of Technical Papers. Solid-State Circuits Conference*, San Francisco, CA, USA, Aug. 2005.

[15] G. Nikandish and A. Medi, "Unilateralization of MMIC distributed amplifiers," *IEEE Transactions on Microwave Theory and Techniques*, vol. 62, no. 12, pp. 3041–3052, Dec. 2014.

[16] J. C. Chien and L. H. Lu, "40-Gb/s high-gain distributed amplifiers with cascaded gain stages in 0.18-μm CMOS," *IEEE Journal of Solid-State Circuits*, vol. 42, no. 12, pp. 2715–2725, Dec. 2007.

[17] K. Fang, C. S. Levy, and J. F. Buckwalter, "Supply-scaling for efficiency enhancement in distributed power amplifiers," *IEEE Journal of Solid-State Circuits*, vol. 51, no. 9, pp. 1994–2005, Sep. 2016.

[18] J. Kim, H. Park, S. Lee, and Y. Kwon, "6–18 GHz, 8.1 W size-efficient GaN distributed amplifier MMIC," *Electron. Lett.*, vol. 52, pp. 622–624, 2016.

[19] J. C. Kao, P. Chen, P. C. Huang, and H. Wang, "A novel distributed amplifier with high gain, low noise, and high output power in 0.18-μm CMOS technology," *IEEE Transactions on Microwave Theory and Techniques*, vol. 61, no. 4, pp. 1533–1542, Apr. 2013.

[20] C. Enz and Y. Cheng, "MOS transistor modeling for RF IC design," *IEEE Journal of Solid-State Circuits*, vol. 35, no. 2, pp. 186–201, Feb. 2000.

[21] R. Menozzi, A. Piazzi, and F. Contini, "Small-signal modeling for microwave FET linear circuits based on a genetic algorithm," *IEEE Transactions on Circuits and Systems I: Fundamental Theory and Applications*, vol. 43, no. 10, pp. 839–847, Oct. 1996.

[22] L. Zhang, Q.-J. Zhang, and J. Wood, "Statistical neuro-space mapping technique for large-signal modeling of nonlinear devices," *IEEE Transactions on Microwave Theory and Techniques*, vol. 56, no. 11, pp. 2453–2467, Nov. 2008.

[23] G. Dambrine, A. Cappy, F. Heliodore, and E. Playez, "A new method for determining the FET small-signal equivalent circuit," *IEEE Transactions on Microwave Theory and Techniques*, vol. 36, no. 7, pp. 1151–1159, July 1988.

[24] L. Yang and S. I. Long, "New method to measure the source and drain resistance of the GaAs MESFET," *IEEE Electron Device Letters*, vol. 7, no. 2, pp. 75–77, Feb. 1986.

[25] R. Anholt and S. Swirhun, "Equivalent-circuit parameter extraction for cold GaAs MESFET's," *IEEE Transactions on Microwave Theory and Techniques*, vol. 39, no. 7, pp. 1243–1247, July 1991.

[26] A. M. Mangan, S. P. Voinigescu, M.-T. Yang, and M. Tazlauanu, "De-embedding transmission line measurements for accurate modeling of IC designs," *IEEE Transactions on Electron Devices*, vol. 53, no. 2, pp. 235–241, Feb. 2006.

[27] R. Quaglia, M. D. Greene, M. J. Poulton, and S. C. Cripps, "A 1.8-3.2-GHz Doherty power amplifier in quasi-MMIC technology," *IEEE Microw. Wireless Compon. Lett.*, vol. 29, no. 5, pp. 345–347, 2019.

[28] D. Resca and F. Scappaviva, "A minature 70 W quasi-MMIC PA block suitable for highly integrated X-band pulsed SSPA schemes," in *Proceedings of the 11th European Microwave Integrated Circuits Conference*, London, UK, Oct. 2016.

[29] D. Bouw, P. Sin, M. Camiade, and J. P. Viaud, "High performance plastic packaged 100 W L-band quasi-MMIC HPA," in *Proceedings of the 46th European Microwave Conference*, London, UK, Oct. 2016.

[30] M. Ayad, E. Byk, G. Neveux, M. Camiade, and D. Barataud, "Single and dual input packaged 5.5-6.5 GHz, 20 W, quasi-MMIC GaN-HEMT Doherty power amplifier," in *2017 IEEE MTT-S International Microwave Symposium*, Honolulu, HI, USA, June 2017.

[31] J. Jeong, P. Kim, P. Pech, Y. Jeong, and S. Lee, "Quasi-MMIC high power amplifier with silicon IPD matching network," in *Proceedings of the 48th European Microwave Conference*, Madrid, Spain, Sep. 2018.

[32] C. Berrached, D. Bouw, M. Camiade, and D. Barataud, "Wideband high efficiency high power GaN amplifiers using MIC and quasi-MMIC technologies," in *Proceedings of the 43rd European Microwave Conference*, Nuremberg, Germany, Oct. 2013.

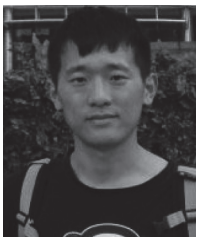

Letian Guo received the B.S. degree in electrical engineering from Xi'an Jiaotong University, Xi'an, China, in 2012, the M.S. degree in electromagnetic field and microwave technology from the Northwest Institute of Nuclear Technology, Xi'an, China, in 2015, and the Ph.D. degree in microelectronics and solid-state electronics from Fudan University, Shanghai, China, in 2024, respectively. He has been with the Northwest Institute of Nuclear Technology since 2012. His current research interests include the microwave passive devices and phased array radar technology.

Shunli Ma received the B.S. degree in microelectronics engineering from Shanghai Jiao Tong University, Shanghai, China, in 2011, and the Ph.D. degree in microelectronics engineering from Fudan University, Shanghai, China, in 2016, respectively. From 2012 to 2014, he was a Project Officer with Nanyang Technological University, Singapore. From 2016 to 2017, he worked in industry and designed 77-GHz FMCW PLL for automotive radar sensors. He received the title of Distinguished Designer for millimeter-wave (mm-wave) PLL design for automotive radars. He is currently an Assistant Professor with the State Key Laboratory of ASIC and System, Fudan University, Shanghai, China. He has published many papers related to high-performance mm-wave circuits on top conferences, including ESSCIRC, CICC,RFIC, ASSCC, and IMS. His research interests include 2D MoS2 chip design and mm-wave integrated-circuit design, including mm-wave imaging sensing, mm-wave PLL and high-speed sampler in ADC, and biomedical RF circuits for cancer detection. He received the 2015 ISSCC Student Research Preview and the ISSCC STGA Award.

Hou Yi Ding received the B.S. degree and M.S. degree in microelectronic science and engineering from Tongji University, Shanghai, China, in 2022 and 2025, respectively. He is currently pursuing the Ph.D. degree in Tokyo University, Tokyo, Japan. His current research interests include the development of novel microwave devices and antennas.

Mei Song Tong received the B.S. and M.S. degrees from Huazhong University of Science and Technology, Wuhan, China, and Ph.D. degree from Arizona State University, Tempe, Arizona, USA, all in electrical engineering. He is currently a Humboldt Awardee Professor in the Chair of High-Frequency Engineering, Technical University of Munich, Munich, Germany, and is on leave from the Distinguished/Permanent Professor and Head of Department of Electronic Science and Technology, and Vice Dean of College of Microelectronics, Tongji University, Shanghai, China. He has also held an adjunct professorship at the University of Illinois at Urbana-Champaign, Urbana, Illinois, USA, and an honorary professorship at the University of Hong Kong, China. He has published more than 700 papers in refereed journals and conference proceedings and co-authored eight books or book chapters. His research interests include electromagnetic field theory, antenna theory and technique, modeling and simulation of RF/microwave circuits and devices, interconnect and packaging analysis, inverse electromagnetic scattering for imaging, and computational electromagnetics.

Prof. Tong is a Fellow of the Electromagnetics Academy, Fellow of the Japan Society for the Promotion of Science (JSPS), and Senior Member (Commission B) of the USNC/URSI. He has been the chair of Shanghai Chapter since 2014 and the chair of SIGHT committee in 2018, respectively, in IEEE Antennas and Propagation Society. He has served as an associate editor or guest editor for several well-known international journals, including *IEEE Antennas and Propagation Magazine, IEEE Transactions on Antennas and Propagation, IEEE Transactions on Components, Packaging and Manufacturing Technology, International Journal of Numerical Modeling: Electronic Networks, Devices and Fields, Progress in Electromagnetics Research, and Journal of Electromagnetic Waves and Applications*. He also frequently served as a session organizer/chair, technical program committee member/chair, and general chair for some prestigious international conferences. He was the recipient of a Visiting Professorship Award from Kyoto University, Japan, in 2012, and from University of Hong Kong, China, 2013. He advised and coauthored 15 papers that received the Best Student Paper Award from different international conferences. He was the recipient of the Travel Fellowship Award of USNC/URSI for the 31th General Assembly and Scientific Symposium (GASS) in 2014, Advance Award of Science and Technology of Shanghai Municipal Government in 2015, Fellowship Award of JSPS in 2016, Innovation

Award of Universities' Achievements of Ministry of Education of China in 2017, Innovation Achievement Award of Industry-Academia-Research Collaboration of China in 2019, "Jinqiao" Award of Technology Market Association of China in 2020, Baosteel Education Award of China in 2021, Carl Friedrich von Siemens Research Award of the Alexander von Humboldt Foundation of Germany in 2023, and Technical Achievement Award of Applied Computational Electromagnetic Society (ACES) of USA in 2024. In 2018, he was selected as the Distinguished Lecturer (DL) of IEEE Antennas and Propagation Society for 2019–2022, and in 2025, he was selected to the Top 2% Scientists List for both Career-Long Impact and Single-Year Impact by ELSEVIER and Stanford University.

Dual-Polarized, Low-RCS Wideband Fabry-Pérot Antenna Utilizing a 3D-Printed Stepped Absorbing Structure

Zhixin Lei[1], Zhiming Liu[1], Hao Xu[1], Huilin Zhou[1], Fei Wang[2], and Yuxuan Huang[1]

[1]School of Information Engineering
Nanchang University, Nanchang 330031, China
zhixinlei2001@163.com, zhimingliu@ncu.edu.cn, xuhao_0805@163.com,
zhouhuilin@ncu.edu.cn, yuxuanhuang2002@163.com

[2]Fujian Key Laboratory of Special Energy Manufacturing
Huaqiao University, Xiamen 361021, China
wangfei@hqu.edu.cn

Abstract – A dual-polarized Fabry-Pérot (FP) antenna with ultra-wideband radar cross section (RCS) reduction using 3D printing technology is proposed. The proposed antenna consists of a dual-polarized primary antenna and a partially reflective surface (PRS) loaded with reflective surface (RS) and 3D-printed stepped absorbing structure (3D-PSAS). The combination of the RS and the 3D-PSAS effectively reduces the RCS of the FP antenna and maintains the gain of the antenna. Meanwhile, the proposed antenna can be used in the construction of stealth systems. Both the simulated results and the measured results verify the reliability of the design. The FP antenna owns 10-dB RCS reduction bands cover 3.0∼3.8 GHz and 6∼15 GHz, with a peak RCS reduction of 27 dB at 12.5 GHz. In the radiation, it owns a 10-dB return-loss bandwidth of 4.64–5.64 GHz (19.4%) and 4.76–5.61 GHz (16.3%) respectively in X polarization and Y polarization modes, with a maximum realized gain of 12.4 dBi at 4.9 GHz.

Index Terms – 3D printing technology, Fabry-Pérot antenna, partially reflective surface, radar cross section.

I. INTRODUCTION

Fabry-Perot (FP) antennas are widely used in satellite communications, radar, stealth platforms, wireless communications and other fields due to their high gain, strong directivity, planar structure, compactness and light weight [1–5]. Its flexible design optimizes wideband performance, circular polarization, high gain, and low radar scattering area (RCS). Low-RCS is crucial for enhancing the stealth capabilities of military equipment and improving the performance of communication systems. It plays a significant role in reducing signal leakage and interference, ensuring the stability and reliability of communication systems. However, in the process of reducing RCS using a radome or metasurface, the commonly employed structure involves a combination of metal and dielectric substrate, which limits the bandwidth of RCS reduction. Moreover, FP antennas can be reconfigured for various purposes such as frequency reconfiguration [6, 7], polarization reconfiguration [8], radiation pattern reconfiguration [9], and RCS reduction reconfiguration [10].

In recent years, an increasing number of researchers have turned their attention to the study of antennas with reduced RCS. In order to reduce the RCS of the antenna and improve its deployment capability on stealth platforms, various design methods have been proposed, including polarization conversion metasurfaces (PCMs) [11–13], hybrid reflection methods [14], coding metasurfaces [15], artificial magnetic conductors (AMCs) and absorbing surfaces (ASs) [16–19]. The PCM effectively realizes the in-band RCS reduction of the FP antenna through phase cancellation, which improves the gain bandwidth while maintaining good RCS rejection performance. However, the RCS reduction effect of this method in broadband is still not ideal, which limits its application in stealth antennas. Moreover, AMCs and ASs provide effective absorption of incident waves and reduce RCS in a broader frequency range [16]. However, they absorb a large amount of radiation energy of antennas. Consequently, simultaneously achieving both broadband RCS reduction and antenna gain improvement in an antenna remains a challenging task.

Meanwhile, 3D printing technology, owing to its capability of fabricating complex structures, is increasingly applied in the design of multifunctional antennas. Many researchers are using 3D printing technology to design different kinds of antennas, such as circularly polarized antennas [20, 21], dual-polarized antennas,

Submitted On: April 24, 2025
Accepted On: August 21, 2025

https://doi.org/10.13052/2025.ACES.J.401007

array antennas [22], Yagi-Uda antennas [23], resonant cavity antennas [24], and lens antennas [25]. It has also been employed in designing complex electromagnetic structures like circuits [26], frequency selective surfaces [27], and absorbers [28]. This application of 3D printing has broadened the possibilities for developing innovative antenna systems and electromagnetic devices [29].

A low-RCS dual-polarized FP antenna based on a partially reflective surface (PRS) using 3D printed technology is proposed here. The PRS of the proposed antenna combines a 3D-printed stepped absorbing structure (3D-PSAS) with a reflective surface (RS). Firstly, the RS is positioned above a dual-polarized primary antenna at an appropriate height. By utilizing the reflection characteristic of the RS, a simple FP resonant cavity between PRS and ground is formed, which concentrates the radiation energy of the antenna. The 3D-PSAS utilizes 3D printing technology to process absorbing materials into stepped gradient structures that help to reduce RCS. A dual-polarized slot patch antenna is used as the primary antenna, which switches the polarization mode by regulating the voltage at both ends of the PIN diode. According to the simulation and measured results, the proposed antenna not only significantly reduces the RCS and covers the ultra-wide band but also enhances the realized gain. RCS peak reduction is 27 dB.

II. DESIGN OF FABRY-PÉROT ANTENNA

A FP antenna possesses the characteristics of high gain and concentrated radiation energy. Its main performance indicators include operating frequency, gain, radiation pattern, and bandwidth, which depend on the reflection phase of PRS and the height of the resonator cavity of the FP antenna. The above performance indicators meet the following formula [30]:

$$f = \frac{c}{4\pi h_c}(\varphi_{PRS} + \varphi_{GND} - 2N\pi), \quad N = 0, 1, 2\ldots, \tag{1}$$

where φ_{PRS} and φ_{GND} are the reflection phases of PRS and ground, respectively, c is the speed of light, h_c is the cavity height of the FP antenna resonator, f is the resonance frequency of the FP antenna, N is the number of times that the electromagnetic waves excited by the antenna are reflected between PRS and ground. In this design, $\varphi_{GND} = -\pi$. The electromagnetic waves emitted by the main antenna oscillate several times in the resonator. When the reflection phase of the PRS satisfies Equation (1), a standing wave pattern is formed, which excites the FP resonance to enhance the directivity and gain of the antenna.

A. Partially reflective surface

In the proposed antenna, the PRS is composed of a RS and 3D-PSAS, as shown in Fig. 1. The RS adopts a double-layer structure design, with a square metal patch with a length of b_1 on one side and a circular square ring structure with an inner diameter of b_2 at the bottom. These patches are printed on either side of the F_4BM265 ($\varepsilon_r = 2.65$, $\tan\delta = 0.0007$) dielectric substrate. It is used to form a FP resonant cavity between PRS and ground. In addition, 3D-PSAS is a metamaterial structure that sits on top of the RS and is designed with three layers of stepped square holes, each with layer height of H_1, H_2, and H_3 to achieve a gradient electromagnetic absorption characteristic. In order to achieve better absorption performance, the metamaterial is composed of 4% carbon black and 250% carbonyl iron powder, which can comprehensively utilize their respective advantages and enhance the dielectric properties and magnetic properties of the material, absorb electromagnetic waves transmitted from RS and reduce RCS. Adjusting the stepped gradient structure of 3D-PSAS can change the selective transmittance of PRS and flexibly adjust the frequency band of RCS reduction. Therefore, the simulation results of the reflection coefficient of 3D-PASA with three different height parameter changes are given. This is shown in Fig. 2. At the same time, this adjustment decreases the extent to which electromagnetic waves emitted by the primary antenna are absorbed. The parameters of the optimized PRS unit structure are shown in Table 1.

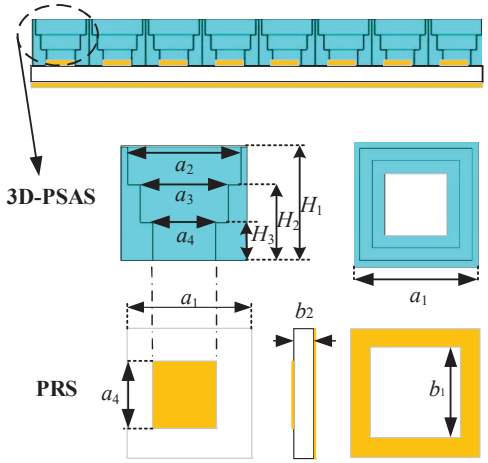

Fig. 1. Schematic of the PRS.

Table 1: Design parameters of the PRS

Parameter	H_1	H_2	H_3	a_1	a_2
Value (mm)	9	6	3	10	9
Parameter	a_3	a_4	b_1	b_2	
Value (mm)	7	5	7	1.5	

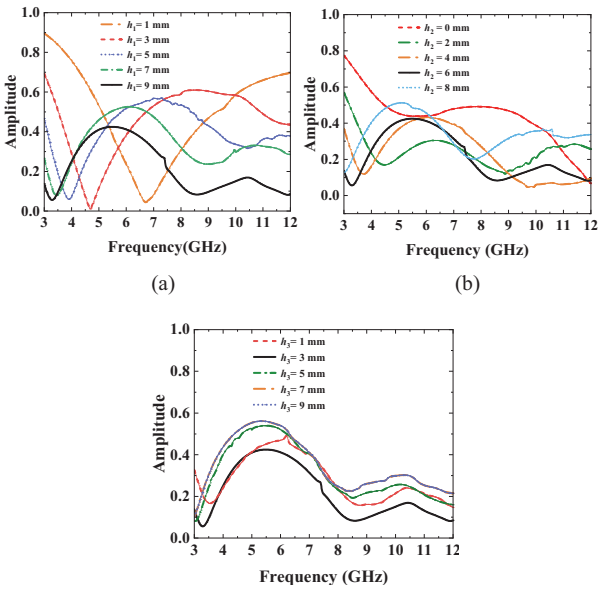

Fig. 2. Effect of each parameter on the Port 1 reflection coefficient of 3D-PSAS. (a) h_1, (b) h_2, (c) h_3.

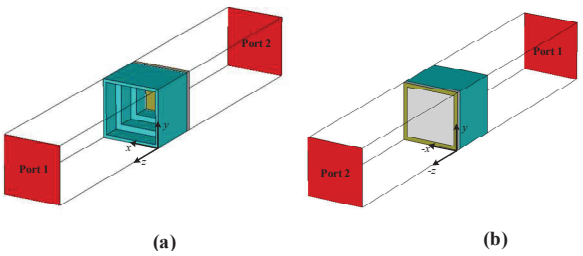

Fig. 3. Simulated model of the PRS unit: (a) top and (b) bottom.

In this design, the model was simulated using CST Microwave Studio 2022 version, using a time-domain solver and global meshing, with a maximum grid element size of 1 mm and an S-parameter convergence accuracy of −40 dB. The PRS model design and simulation settings are as follows. In Fig. 3, Port 1 and Port 2 are located at fixed distances on either side of the PRS unit. To simulate the PRS unit structure, the $\pm x$ directions are set as electric wall boundary conditions, while the $\pm y$ directions are set as magnetic wall boundary conditions.

Figure 4 depicts the simulated results of the PRS unit. The diagram illustrates the reflection coefficient (S_{11}) and transmission coefficient (S_{12}) of the PRS and depicts the absorption characteristics of the PRS for electromagnetic waves using the absorptivity. A is the absorptivity of the PRS, which can be calculated by:

$$A = 1 - |S_{11}|^2 - |S_{12}|^2. \quad (2)$$

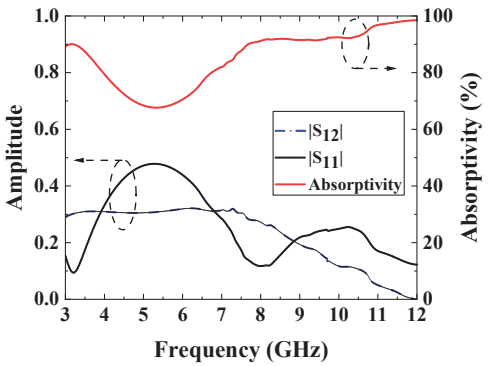

Fig. 4. S_{11}, S_{12}, and absorptivity of the PRS.

As shown in Fig. 4, the PRS has an absorptivity of greater than 67% but lower than 80% within the frequency range 3.90–6.50 GHz. It indicates that the absorption ability of 3D-PSAS has a relatively small impact on the antenna radiation within the operating band of the antenna. However, outside this frequency band, the PRS shows excellent wave absorption performance, with the absorptivity higher than 80%. which effectively attenuates the energy of the incident wave and reduces the RCS.

B. Primary antenna

As shown in Fig. 5, a dual-polarized slot antenna with parasitic patch acts as the primary antenna. The antenna is fed through a microstrip line that is patterned on the underside of the substrate. The parasitic patch is an F4BM265 dielectric substrate printed with a square metal length l_1, which can expand the bandwidth of the primary antenna. It is placed above the primary antenna at H_{air}. On the surface of the dual-polarized antenna, a metal ground plane is etched. Two H-shaped coupling slots are formed on this plane to achieve the dual-polarization characteristics of the antenna. The specifications for the primary antenna's design are provided in Table 2.

The polarization mode of the primary antenna is determined by the states of the Pin 1 and Pin 2 diodes. These diodes can be controlled by changing the voltage levels at both ends of the diode using wires. The antenna radiates y-polarization (YP) waves as the Pin 1 diode is turned on and the Pin 2 diode is turned off. The antenna radiates x-polarization (XP) waves as the Pin 2 diode is turned on and the Pin 1 diode is turned off. By switching between these two states, the electromagnetic waves radiated by antennas can be converted between XP and YP, allowing for adaptable communication and reception capabilities.

The simulated results for the primary antenna are presented in Fig. 6. These results demonstrate

that when the antenna radiates YP waves, its 10-dB impedance bandwidth ranges from 4.83 to 5.70 GHz, which corresponds to a relative bandwidth of 16.5%. The primary antenna achieves a maximum realized gain of 8.70 dBi at a frequency of 5.50 GHz. Comparison of simulated results of YP and XP show similar operating bandwidths and realized gains, except for differences in polarization states. The primary antenna works within the frequency band of 4.83 to 5.70 GHz, during which the 3D-PSAS exhibits lower absorptivity, minimizing the effect of the 3D-PSAS on the FP antenna's radiation performance.

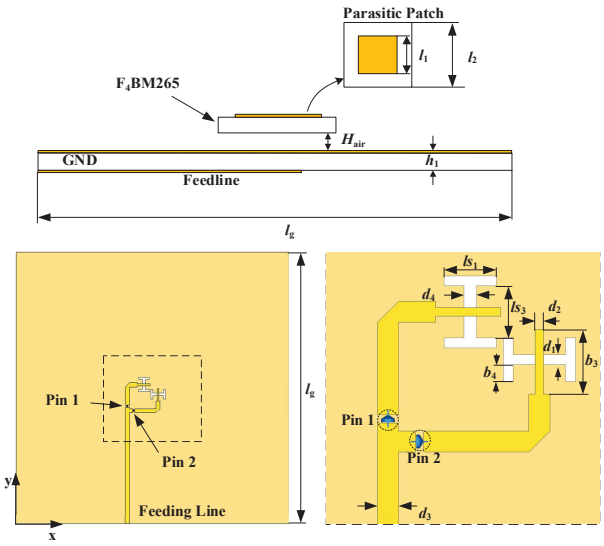

Fig. 5. Schematic of the primary antenna.

Table 2: Design parameters of the primary antenna

Parameter	l_1	l_2	d_1	d_2	d_3
Value (mm)	30	17.7	1.2	1	2.5
Parameter	ls_1	ls_2	b_3	b_4	d_4
Value (mm)	5.2	6.2	7.7	2	1.4

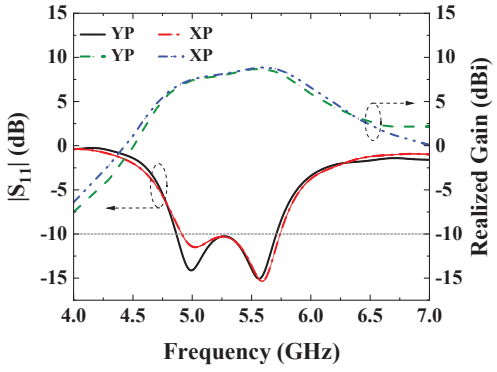

Fig. 6. S_{11} and realized gain of primary antenna.

III. FABRY-PÉROT ANTENNA USING 3D-PRINTED STEPPED ABSORBING STRUCTURE

After analyzing the unit of the PRS and the primary antenna, a unit structure with a length and width of 10 mm is designed. The structure of the 3D-PASA is originally designed as a 16×16 array, with specific RS having dimensions of l_g. In addition, the four corners of the 3D-PSAS are adjusted to a rectangular shape with a height of 5 mm. Cylindrical holes are incorporated in these modified corners to facilitate fixation using nylon screws. The simulated results indicate that this modification has minimal impact on the antenna performance. As depicted in Fig. 7, the 3D-PSAS is installed at a fixed elevation H_c above the primary antenna.

The key to FP resonant excitation lies in the reasonable design of the height of the antenna resonator. Based on Equation (1), the initial reference height is calculated, and the parameter sweep and performance analysis are carried out in its neighborhood, and the optimal cavity height is determined to be $H_c = 31.7$ mm by considering the 10 dB impedance bandwidth and antenna gain holistically.

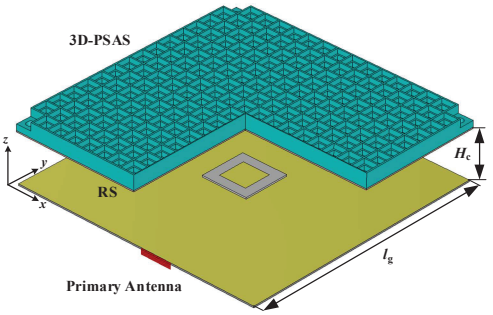

Fig. 7. Proposed FP antenna with 3D-PSAS.

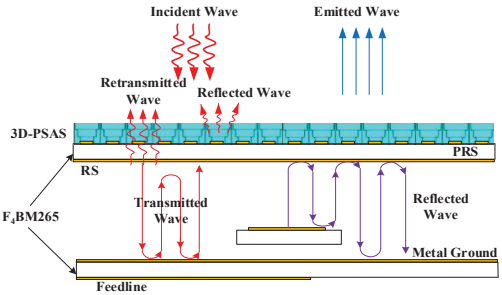

Fig. 8. RCS-reduced FP antenna working schematic.

In Fig. 8, the mechanism for decreasing RCS and improving gain of the FP antenna is depicted. When the incident waves enter the cavity through PRS, a portion of the energy of the incident wave is absorbed

by 3D-PSAS, while another portion passes through 3D-PSAS and becomes transmitted waves. These transmitted waves experience repeated reflections between the metallic ground plane and the PRS. Part of the transmitted waves are transmitted out of the antenna through the bottom of the PRS and becomes the retransmitted waves. The others continue to reflect and transmit within the cavity. The proposed antenna achieves ultra-wideband RCS reduction by absorbing incident waves through the 3D-PSAS layer.

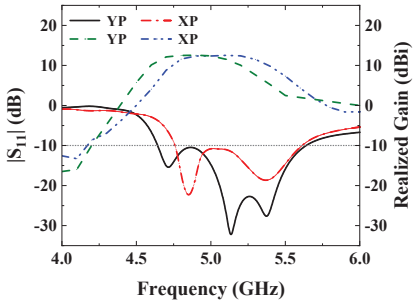

Fig. 9. S_{11} and realized gain of FP antenna.

Figure 9 displays the simulated S_{11} and the realized gain of the proposed FP antenna under YP and XP. The proposed antenna, when operating under YP, exhibits a 10-dB impedance bandwidth ranging from 4.64 GHz to 5.64 GHz (19.4%) and a peak realized gain of 12.40 dBi at 4.90 GHz. Comparing the proposed FP antenna with the primary antenna, the 10-dB impedance bandwidth is slightly reduced and the maximum realized gain is increased from 8.7 dBi to 12.4 dBi. The proposed antenna under XP has a 10-dB impedance bandwidth of 4.76–5.61 GHz (16.3%) and a maximum realized gain of 12.4 dBi at 5.2 GHz. The 10-dB impedance bandwidth and gains of the proposed FP antenna varies between YP and XP. This difference is due to the inconsistent widths of the H-shaped slots designed for each polarization. Compared with the primary antenna, the performance comparison shows that the polarization characteristics have not changed significantly.

In addition, in terms of antenna efficiency, the analog efficiency of the antenna at the operating frequency center (5.14 GHz) is 64% after the PRS is added above the feed. It is 59% after loading the absorbing structure, which is due to its effect on the absorption of electromagnetic waves. In addition, the antenna has an aperture efficiency of 45.1% at 5.14 GHz.

IV. EXPERIMENTAL RESULTS

Figure 10 shows a physical image of the antenna using 3D printing technology. The measurement scene is shown in Fig. 11.

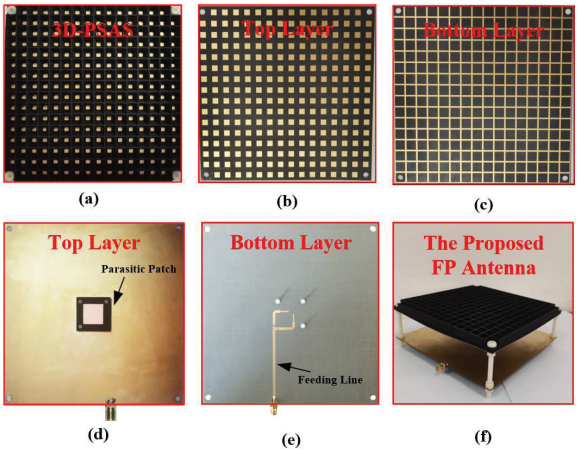

Fig. 10. FP antenna using 3D printing technology: (a) top layer of 3D-PSAS, (b) top layer of RS, (c) bottom layer of RS, (d) top layer of primary antenna, (e) bottom layer of primary antenna, (f) FP antenna.

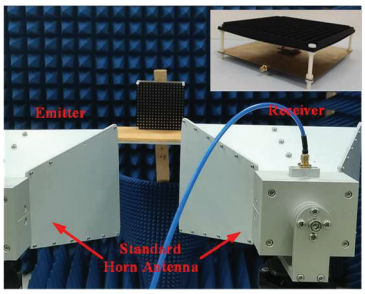

Fig. 11. Measurement scene of the FP antenna.

Figure 12 presents a comparison between the simulated and measured results of the primary antenna in both YP and XP states. It indicates that the primary antenna exhibits measured 10-dB impedance bandwidths ranging from 4.83–5.70 GHz for YP and 4.91–5.70 GHz for XP. Additionally, the maximum realized gain achieved is 8.71 dBi at 5.5 GHz under YP, and 8.80 dBi at 5.6 GHz under XP. Under YP, the measured results of resonant frequency are generally shifted to higher frequencies compared to the simulated results. This phenomenon is primarily due to the error when installing the antenna, and the error causes the height of the parasitic patch to change. When the height of the parasitic patch is decreased, the resonant frequency of the primary antenna shifts towards higher frequencies.

From Fig. 13, it can be seen that the measured results of the FP antenna loaded with 3D-PSAS generally conforms to the simulated results. Under YP, it shows that the FP antenna has a measured 10-dB impedance bandwidth of 4.60 to 5.63 GHz (20.1%), a measured 3-dB gain bandwidth of 4.60 to 5.30 GHz (14%), and a measured maximum realized gain of

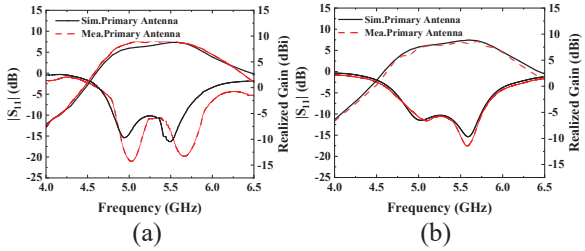

Fig. 12. Comparison of measured and simulated results of the primary antenna: (a) YP, (b) XP.

12.5 dBi at 4.9 GHz. Shown in Figs. 13 (c,d), under XP, the proposed FP antenna possesses a measured 10-dB impedance bandwidth of 4.70–5.60 GHz (17.4%) and a measured maximum realized gain of 12.6 dBi at 5.0 GHz.

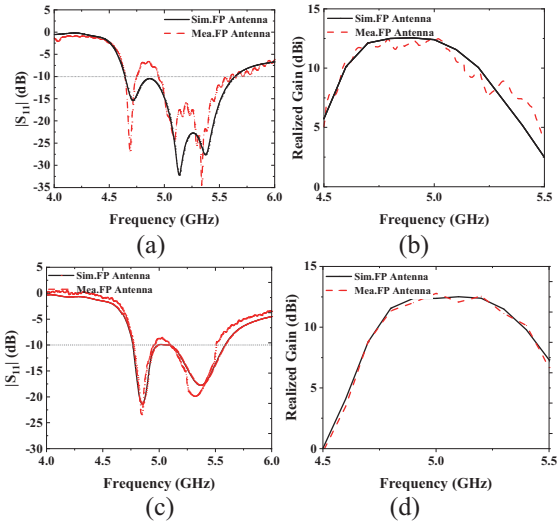

Fig. 13. Comparison of the measured and simulated results of the FP antenna: (a) $|S_{11}|$-YP, (b) realized gain-YP, (c) $|S_{11}|$-XP, (d) realized gain-XP.

Figure 14 presents the E-plane radiation patterns, both simulated and measured, at frequencies of 4.7 GHz and 5.0 GHz for YP and XP. As can be seen from Fig. 14, the sidelobe level decreases significantly relative to the direction of the main beam and is basically below 0 dB. This result fully shows that the proposed antenna exhibits excellent radiation performance in the whole operating frequency band.

Figure 15 shows the measured results and simulated results of the monostatic RCS curves for the designed antenna. It can be observed that the measured RCS of the FP antenna decreases within the range of 3–18 GHz, with a peak reduction of 27 dB at 12.5 GHz. In addition, it can be seen from the measured results that the proposed antenna exhibits bandpass filter characteristics.

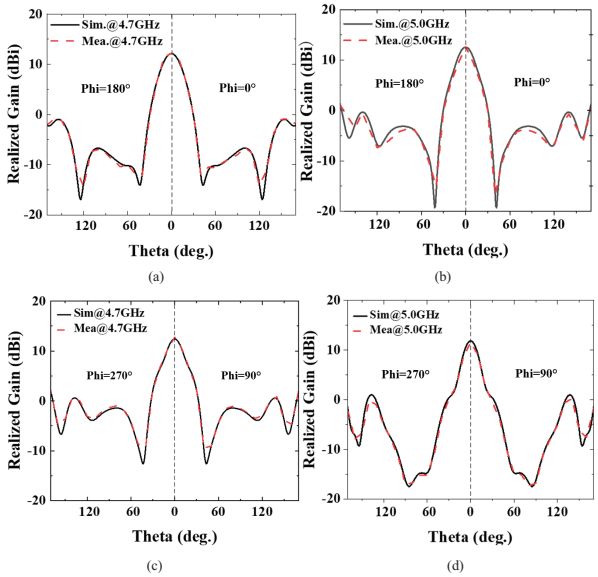

Fig. 14. Radiation patterns of the proposed antenna: (a) 4.7 GHz-YP, (b) 5.0 GHz-YP, (c) 4.7 GHz-XP, (d) 5.0 GHz-XP.

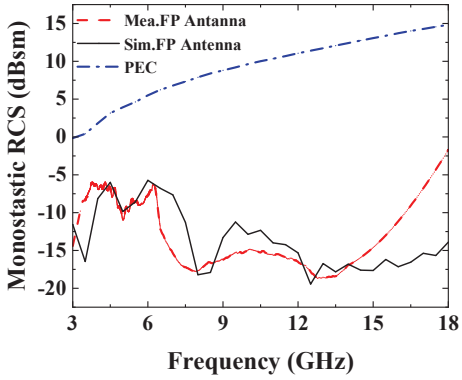

Fig. 15. Simulated RCS reduction and measured RCS reduction of the proposed antenna.

In the frequency range of 4.6–6.4 GHz, the monostatic RCS of the proposed antenna is higher than −10 dB, so that more electromagnetic waves can radiate out of the antenna through 3D-PSAS. The proposed antenna is capable of achieving higher realized gain. Due to the lack of test environment, the aging of the performance of the test device and the error of antenna processing, the measurement results and the simulation results have changed slightly, but the trend is basically the same.

Table 3 lists other works that have used AMC, ASs, and other methods to reduce RCS. Comparison shows that this work has a wide 10-dB RCS reduction band and good radiation performance. The test results closely match the simulation results, thereby validating the feasibility and effectiveness of this work.

Table 3: Comparison between the proposed antenna and existing works

Ref.	Method	Feed Type	10-dB Impedance Bandwidth (GHz)	Max Realized Gain (dBi)	10-dB RCS Reduction Band (GHz)	Max RCS Reduction Value (dB)	Area (λ_0^2)
[15]	Coding Metasurface	Horn antenna	N.A.	N.A.	9.26–12.87 14.84–19.35	19	N.A.
[17]	AMC	Whip antenna	N.A.	N.A.	8.0–12.0	22	0.5, 0.67, 0.83
[18]	AMC-FSS	MAs-loading antenna	4.25–5.42 (24%)	11.13	8.2–18.0	35	2.6×2.6
[19]	AS	Circularly polarized patch antenna	10.50–10.78 (2.6%)	10.2	8.0–12.0	27.6	2.7×2.7
This Work	3D-PSAS	Dual-polarized slot antenna	4.60–5.40 (16%)	12.40	3.0–3.86.0–18.0	27	2.7×2.7

Note: λ_0 denotes the wavelength of the center frequency of the effective bandwidth in free space.

V. CONCLUSION

A low-RCS dual-polarized FP antenna based on 3D-PSAS is proposed. By comparing the simulated and measured results, it has been demonstrated that the 3D-PSAS can effectively achieve ultra-wideband RCS reduction for the FP antenna. The PRS of the proposed antenna consists of the RS and the 3D-PSAS which was produced using 3D printing technology. The reflection performance and absorption performance of the antenna are optimized through analysis. The antenna has a maximum gain of 12.4 dBi at 4.9 GHz and a maximum RCS reduction of 27 dB at 12.5 GHz. The measured results show that the 10-dB impedance matching bandwidths of the proposed FP antenna are 19.7% and 16.2% in YP and XP, and RCS reduction bandwidth of 3.0–3.8 GHz and 7.3–18 GHz under different polarization modes. The antenna can be useful in the construction of stealth communication systems.

ACKNOWLEDGMENT

This research was supported in part by the National Natural Science Foundation of China (Grant No. 62201240, 62161027, 71961017), in part by Jiangxi Provincial Natural Science Foundation (Grant No. 20224BAB212005), in part by open research project of the science and technology innovation platform (Huaqiao University) of Fujian Key Laboratory of Special Energy Manufacturing (No. FKLSEM-2022-04), in part by Jiangxi Provincial Key Laboratory of Intelligent Systems and Human-Machine Interaction (2024SSY03121).

REFERENCES

[1] Y. Sun, Z. N. Chen, Y. Zhang, H. Chen, and T. S. P. See, "Subwavelength substrate-integrated Fabry-Pérot cavity antennas using artificial magnetic conductor," *IEEE Trans. Antennas Propag.*, vol. 60, no. 1, pp. 30–35, 2012.

[2] Y. Zheng, J. Gao, Y. Zhou, X. Cao, H. Yang, and S. Li, "Wideband gain enhancement and RCS reduction of Fabry-Perot resonator antenna with chessboard arranged metamaterial superstrate," *IEEE Trans. Antennas Propag.*, vol. 66, no. 2, pp. 590–599, 2018.

[3] M. W. Niaz, Y. Yin, R. A. Bhatti, Y.-M. Cai, and J. Chen, "Wideband Fabry-Perot resonator antenna employing multilayer partially reflective surface," *IEEE Trans. Antennas Propag.*, vol. 69, no. 4, pp. 2404–2409, 2021.

[4] W. Wang and Y. Zheng, "Wideband gain enhancement of high-isolation Fabry-Pérot antenna array with tandem circular parasitic patches and radial gradient PRS," *IEEE Trans. Antennas Propag.*, vol. 69, no. 11, pp. 7959–7964, 2021.

[5] Z. Liu, J. Bornemann, D. F. Mamedes, S. Liu, X. Kong, and X. Zhao, "A wideband Fabry-Pérot antenna with enhanced gain in the high-frequency operating band by adopting a truncated field correcting structure," *IEEE Trans. Antennas Propag.*, vol. 69, no. 12, pp. 8221–8228, 2021.

[6] C. J. You, S. H. Liu, J. H. Zhang, X. Wang, Q. Y. Li, and G. Q. Yin, "Frequency- and pattern-reconfigurable antenna array with broadband tuning and wide scanning angles," *IEEE Trans. Antennas Propag.*, vol. 71, no. 6, pp. 5398–5403, 2023.

[7] C. Huang, W. Pan, X. Ma, and X. Luo, "A frequency reconfigurable directive antenna with wideband low-RCS property," *IEEE Trans. Antennas Propag.*, vol. 64, no. 3, pp. 1173–1178, 2016.

[8] J. Yang, S.-S. Qi, W. Wu, and D.-G. Fang, "A Fabry-Perot conical beam antenna with multi-polarization reconfigurable capability," *IEEE Trans. Antennas Propag.*, vol. 70, no. 11, pp. 11091–11096, 2022.

[9] X. Yang, Y. Liu, H. Lei, Y. Jia, P. Zhu, and Z. Zhou, "A radiation pattern reconfigurable Fabry-Pérot antenna based on liquid metal," *IEEE Trans. Antennas Propag.*, vol. 68, no. 11, pp. 7658–7663, 2020.

[10] Y. Wang, Z. Liu, H. Zhou, J. Bornemann, Y. Wang, and X. Kong, "A high-gain wideband Fabry-Pérot antenna employing a water-based frequency selective surface for polarization- and RCS-reconfigurability," *Int. J. RF Microw. Comput. Aided Eng.*, vol. 2024, no. 1, p. 1804375, 2024.

[11] K. Li, Y. Liu, Y. Jia, and Y. J. Guo, "A circularly polarized high-gain antenna with low-RCS over a wideband using chessboard polarization conversion metasurfaces," *IEEE Trans. Antennas Propag.*, vol. 65, no. 8, pp. 4288–4292, 2017.

[12] J. Liu, J.-Y. Li, and Z. N. Chen, "Broadband polarization conversion metasurface for antenna RCS reduction," *IEEE Trans. Antennas Propag.*, vol. 70, no. 5, pp. 3834–3839, 2022.

[13] H. Dai, Y. Zhao, and C. Yu, "A multi-elements chessboard random coded metasurface structure for ultra-wideband radar cross section reduction," *IEEE Access*, vol. 8, pp. 56462–56468, 2020.

[14] Z. Liu, S. Liu, X. Zhao, X. Kong, Z. Huang, and B. Bian, "Wideband gain enhancement and RCS reduction of Fabry-Perot antenna using hybrid reflection method," *IEEE Trans. Antennas Propag.*, vol. 68, no. 9, pp. 6497–6505, 2020.

[15] C. Fu, L. Han, C. Liu, X. Lu, and Z. Sun, "Combining Pancharatnam-Berry Phase and conformal coding metasurface for dual-band RCS reduction," *IEEE Trans. Antennas Propag.*, vol. 70, no. 3, pp. 2352–2357, 2022.

[16] M. Paquay, J.-C. Iriarte, I. Ederra, R. Gonzalo, and P. de Maagt, "Thin AMC structure for radar cross-section reduction," *IEEE Trans. Antennas Propag.*, vol. 55, no. 12, pp. 3630–3638, 2007.

[17] Y. Tian, H. Gao, W. Yao, X. Huang, F. Peng, and L. Yu, "Out-of-band RCS reduction of HF/VHF whip antenna using curved AMC structures," *IEEE Trans. Antennas Propag.*, vol. 70, no. 11, pp. 10086–10094, 2022.

[18] Z. Xing, F. Yang, P. Yang, and J. Yang, "A low-RCS and wideband circularly polarized array antenna co-designed with a high-performance AMC-FSS radome," *IEEE Antennas Wirel. Propag. Lett.*, vol. 21, no. 8, pp. 1659–1663, 2022.

[19] J. Ren, W. Jiang, K. Zhang, and S. Gong, "A high-gain circularly polarized Fabry-Perot antenna with wideband low-RCS property," *IEEE Antennas Wirel. Propag. Lett.*, vol. 17, no. 5, pp. 853–856, 2018.

[20] K. X. Wang and H. Wong, "A wideband millimeter-wave circularly polarized antenna with 3-D printed polarizer," *IEEE Trans. Antennas Propag*, vol. 65, no. 3, pp. 1038–1046, Mar. 2017.

[21] Y. Al-Alem, S. M. Sifat, Y. M. M. Antar, and A. A. Kishk, "Circularly polarized Ka-band high-gain antenna using printed ridge gap waveguide and 3-D-printing technology," *IEEE Trans. Antennas Propag.*, vol. 71, no. 9, pp. 7644–7649, 2023.

[22] Z. Zheng, L. Zhang, Q. Luo, C. Mao, Y. He, and S. Gao, "Wideband 3-D-printed transmit-reflect-array antenna with independent beam control," *IEEE Trans. Antennas Propag.*, vol. 71, no. 7, pp. 6196–6201, 2023.

[23] D. Kim, M. Hwang, G. Kim, and S. Kim, "Self-deployable circularly polarized phased Yagi-Uda antenna array using 3-D printing technology for CubeSat applications," *IEEE Antennas Wirel. Propag. Lett.*, vol. 21, no. 11, pp. 2249–2253, 2022.

[24] Z.-X. Xia and K. W. Leung, "3-D-printed wideband circularly polarized dielectric resonator antenna with two printing materials," *IEEE Trans. Antennas Propag.*, vol. 70, no. 7, pp. 5971–5976, 2022.

[25] K. Liu, C. Zhao, S.-W. Qu, Y. Chen, J. Hu, and S. Yang, "A 3-D-printed multibeam spherical lens antenna with ultrawide-angle coverage," *IEEE Antennas Wirel. Propag. Lett.*, vol. 20, no. 3, pp. 411–415, 2021.

[26] I. Piekarz, J. Sorocki, M. T. Craton, K. Wincza, S. Gruszczynski, and J. Papapolymerou, "Application of aerosol jet 3-D printing with conductive and nonconductive inks for manufacturing mm-Wave circuits," *IEEE Trans. Compon., Packag., Manuf. Technol.*, vol. 9, no. 3, pp. 586–595, 2019.

[27] D. Z. Zhu, M. D. Gregory, P. L. Werner, and D. H. Werner, "Fabrication and characterization of multiband polarization independent 3-D-printed frequency selective structures with ultrawide fields of view," *IEEE Trans. Antennas Propag.*, vol. 66, no. 11, pp. 6096–6105, Nov. 2018.

[28] J. Su, Y. Li, M. Qu, H. Yu, Q. Guo, and Z. Li, "A 3-D-printed ultrawideband and ultralow-scattering water-based metasurface," *IEEE Trans. Antennas Propag.*, vol. 71, no. 3, pp. 2885–2890, 2023.

[29] K. Alhassoon, Y. Malallah, and A. S. Daryoush, "RF characterization of 3-D-printed material for antenna applications," *IEEE Trans. Antennas Propag.*, vol. 71, no. 9, pp. 7073–7080, Sep. 2023.

[30] Q. Guo, Z. Li, J. Su, L. Y. Yang, and J. Song, "Dual-polarization absorptive/transmissive frequency selective surface based on tripole elements," *IEEE Antennas Wirel. Propag. Lett.*, vol. 18, no. 5, pp. 961–965, 2019.

Zhixin Lei received a B.S. degree from Nanchang University, China, in 2023. He is currently pursuing the M.S. degree at Nanchang University. His current research interests include lens antennas based on phase gradient metasurfaces and RCS reduction.

Zhiming Liu, born in 1989, received a B.S degree from East China University of Technology, China, in 2012, a M.S. degree from Nanchang University in 2015, and a Ph.D. degree from Nanjing University of Aeronautics and Astronautics in 2019. His current research interests include electromagnetic metamaterial device design and application, microwave component and system design, and antenna design.

Hao Xu received a B.S. degree from East China Jiaotong University, China, in 2022. He is currently pursuing a M.S. degree at Nanchang University. His current research interests include Fabry-Perot antenna and RCS reduction.

Huilin Zhou was born in Jiangxi in 1979. He received M.S. degree and Ph.D. degrees from Wuhan University, China, in 2002 and 2006. His current research interests include artificial intelligence medical image processing and ultra-wideband radar signal processing.

Fei Wang was born in 1979. He received the Ph.D. degree from Huaqiao University, Quanzhou, China, in 2010. His research interests include special energy field assisted 3D printing and preparation of integrated structural and functional metamaterials based on 3D printing.

Yuxuan Huang received the B.S. degree in Communication Engineering from Nanchang University, China, in 2024. She is currently pursuing a M.S. degree at Nanchang University. Her research interests include antenna design for wireless communication systems.

A Wideband Single-Fed Circularly Polarized Eight-Arm Archimedean-Spiral Image-Dielectric Antenna

Dong Chen[1,2], Guanghui Xu[1,2,3], Yanbin Luo[3], Wei Wang[3], Dawei Ding[1,2], Luyu Zhao[1,2], Yingsong Li[1,2], Zhixiang Huang[1,2], and Xianliang Wu[1,2]

[1]School of Electronics and Information Engineering
Anhui University, Hefei 230039, China
dchen86@163.com, ghxu86@ahu.edu.cn, 19119@ahu.edu.cn,
lyzhao@ahu.edu.cn, yingsong.li@aliyun.com, zxhuang@ahu.edu.cn

[2]Information Materials and Intelligent Sensing Laboratory of Anhui Province
Anhui University, Hefei 230039, China
ghxu86@ahu.edu.cn

[3]East China Research Institute of Electronic Engineering
Hefei 230088, China
luoyanb001@163.com, shu00ww@163.com

Abstract – A wideband single-fed circularly polarized (CP) eight-arm Archimedean-spiral image-dielectric antenna (ASIDA) is proposed in this paper. The ASIDA consists of eight Archimedean-spiral dielectric arms with equal angular spacing. The eight Archimedean-spiral image-dielectric arms are excited by the unequal-length cross-slot and microstrip. The unequal-length cross-slot can generate the CP electric field to excite the dielectric arms for the wideband CP radiation. The image-dielectric waveguide line is employed to achieve a low-profile structure. The measured results show that the proposed ASIDA has an impedance bandwidth of 40.8% (1.54–2.33 GHz) and an axial ratio (AR) bandwidth of 39.8% (1.55–2.32 GHz), with a maximum realized gain of 12.2 dBic. This work will provide a new insight into the CP dielectric antenna.

Index Terms – Archimedean spiral, circularly polarized, image-dielectric antenna, wideband antenna.

I. INTRODUCTION

Circular polarized (CP) antennas have been extensively studied due to their anti-multipath fading characteristics, strong anti-interference capabilities, resistance to rain and fog interference, and reliable free-space propagation performance [1]. Wideband CP antennas are extensively used in wireless communication, global positioning, and navigation systems [2–4]. To achieve the wideband CP operations, various antenna types have been adopted, including patch antennas [5], dielectric resonator antennas (DRAs) [6], magnetoelectric (ME) dipole antennas [7], and helix/spiral antennas [8].

Among these types, DRAs possess advantages such as no conductor loss, low dielectric loss, high design flexibility, and ease of mode excitation, which facilitate achieving broadband CP operation. To achieve broadband CP, dual-feed techniques have been widely adopted, such as in [9], which achieved a 3% axial ratio (AR) bandwidth and 6.2 dBic gain. Reconfigurable DRAs using PIN-diode networks achieve >30% bandwidth but involve complex biasing circuits [10]. Mode-merging strategies enhance bandwidth up to 21% AR with moderate gain [11–13], but require multilayer or high-permittivity structures. Dielectric-via designs [12] offer 26.7% AR bandwidth in a compact form yet introduce fabrication complexity. Dual-band or substrate-integrated DRAs [14, 15] can reach 30% bandwidth but often rely on cavity structures or nearly degenerate mode excitation. Stacking dielectric slabs can also extend AR bandwidth [16, 17]. Overall, most existing designs face trade-offs between bandwidth, profile, and fabrication complexity. Achieving a low-profile and wideband CP antenna with a simple structure remains a significant challenge.

Recently, spiral dielectric antennas have been proposed to generate wideband CP waves [18, 19]. Compared to metal spiral antennas, dielectric waveguide lines, due to their ability to flexibly select different dielectric materials for design freedom, are more conducive to achieving miniaturization and high performances. Two reported works adopted dielectric waveguide lines to replace spiral metal lines for realizing

Submitted On: May 09, 2025
Accepted On: September 17, 2025

https://doi.org/10.13052/2025.ACES.J.401008

wideband CP radiation. In [18], a dual-feed dielectric Archimedean-spiral dielectric antenna achieves an AR bandwidth of 28%. Literature [19] proposes the single-feed Archimedean-spiral dielectric antenna with an AR bandwidth of 9.7%. Due to the required distance between the dielectric waveguide line and the ground plane, both antennas exhibit a high profile. In our study, an image-dielectric waveguide line is adopted to achieve a low-profile design, and the eight Archimedean-spiral image-dielectric arms with the unequal-length cross-slot feeding achieves a wider AR bandwidth of 39.8% in the compact size.

In this paper, a wideband single-fed CP eight-arm Archimedean-spiral image-dielectric antenna (ASIDA) is presented. This paper is organized as follows. Section II describes the structure design and analysis process of the ASIDA. Section III compares and discusses the simulated and measured results of the ASIDA. The final conclusion is summarized in Section IV.

II. DESIGN OF THE PROPOSED ANTENNA

A. Antenna configuration

Fig. 1 illustrates the configuration of the proposed ASIDA. The ASIDA employs two-layer dielectric substrates. The upper layer, substrate1, is TLY-5 ($\varepsilon_r = 2.2$, $\tan\delta = 0.0009$), while the lower layer, substrate2, is F4BM220 ($\varepsilon_r = 2.2$, $\tan\delta = 0.0007$). The thickness of substrate1 is $h_1 = 0.787$ mm and the thickness of substrate2 is $h_2 = 1.575$ mm. Alignment holes with a radius of 1 mm were machined at the substrate edges and the gaps between spiral arms was secured using insulating screws. To highlight the key radiating structures, the via details were intentionally omitted from the schematic diagram in Fig. 1.

As shown in Fig. 1 (b), the ground plane, with dimensions g_x length and g_y width, is positioned on the upper surface of substrate1. The eight Archimedean-spiral dielectric arms with the equal angular spacing of α are located on the ground with an asymmetrical cross-slot coupler featuring unequal arm lengths ($l_{s1} \neq l_{s2}$) but uniform width, which is concentrically positioned beneath the eight spiral arms. The cross-slot is oriented at an angle of $\theta_1 = 30^\circ$ relative to the microstrip feed line. Arm material is Al_2O_3 ceramic with a dielectric constant of 9.8. Microwave signal is transmitted through the microstrip line at the bottom to the slot forming a CP electric field [20] which excites the ASIDA to radiate CP waves.

As shown in Fig. 1, r_0 represents the starting radius of the spiral, a denotes the growth rate of the spiral, and β is the angle on the spiral arm. The equation for the inner edge of a single Archimedean dielectric arm is

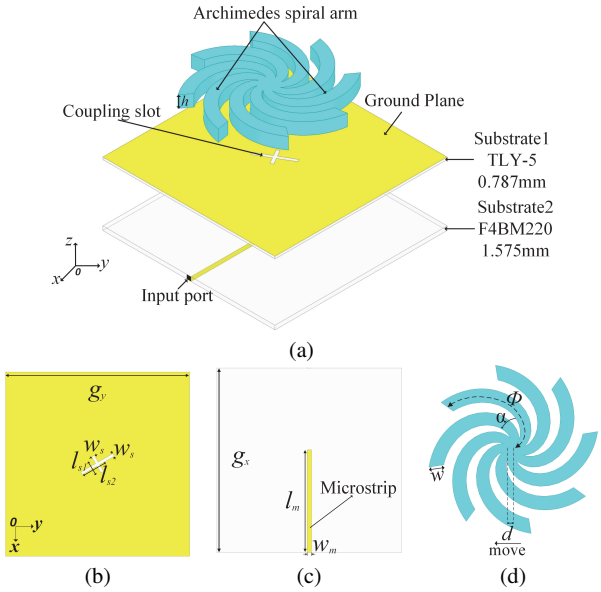

Fig. 1. Geometries and dimensions of (a) the proposed ASIDA, (b) top view of substrate1, (c) bottom view of substrate2 and (d) top view.

Table 1: Key parameters of ASIDA (unit: mm)

g_x	g_y	l_{s1}	l_{s2}	w_s	w
250	250	28	50	4.9	20
l_m	w_m	h	h_1	h_2	d
142	7	20.5	0.787	1.575	8

given by:

$$\begin{cases} x_1 = (r_0 + a\beta)\cos\beta \\ y_1 = (r_0 + a\beta)\sin\beta \end{cases}. \tag{1}$$

The outer edge curve equation of the single Archimedean dielectric arm is given by:

$$\begin{cases} x_2 = (r_1 + a\beta)\cos\beta \\ y_2 = (r_1 + a\beta)\sin\beta \end{cases}, \tag{2}$$

where the angle of Archimedes' spiral is $\Phi = 0.8\pi$, the spiral growth rate a is 34.5 mm/rad, the arm width is w, and its height is h. The inner and outer radius of the single arm are defined by:

$$r_1 = r_0 + w. \tag{3}$$

The other spiral arms are generated by rotating a single arm in sequence at the angular spacing $\alpha = \pi/4$, thus forming eight arms in total. Detailed dimensions of the ASIDA are listed in Table 1. Based on the geometrical parameters of the dielectric spiral arms and the unequal-length cross-slot feed, the proposed antenna is ultimately designed to operate over the frequency range of 1.5–2.4 GHz.

B. Design flow of the proposed ASIDA

The design process of the proposed antenna is shown in Fig. 2. Figure 3 gives the surface current distributions on the ground plane without the radiator at 1.8 GHz for four characteristic phase angles (0°, 90°, 180°, 270°), where the current vectors exhibit periodic rotational behavior with orthogonal directional switching at T/4 intervals, confirming the CP generation mechanism. The corresponding simulated $|S_{11}|$ and AR results are shown in Fig. 4. The three antenna types all exhibit wide impedance bandwidths, consistent with the wideband characteristics of spiral antennas; however, their 3 dB AR bandwidths differ significantly. As the number of arms increases, both the impedance and AR bandwidths widen. Specifically, the AR bandwidths range from 7% to 39.1%.

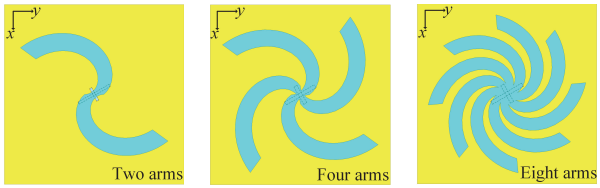

Fig. 2. Design process of the proposed antenna: (a) Type I, (b) Type II, and (c) Type III.

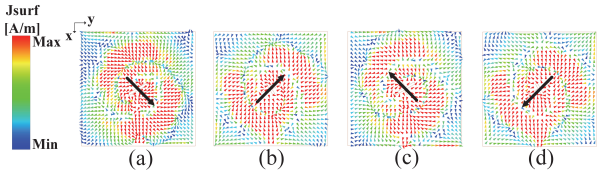

Fig. 3. Surface current distribution in the ground plane at 1.8 GHz (a) 0°, (b) 90°, (c) 180°, (d) 270°.

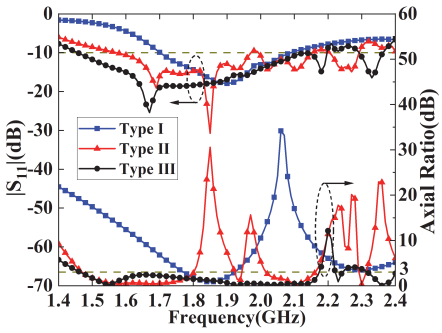

Fig. 4. Simulated $|S_{11}|$ and AR results of the three types.

Figure 5 (a) presents a comparison of the realized gains for the three antenna types. Compared to Type I and Type II, the Type III antenna demonstrates more stable gain and higher values across the entire operating frequency band. The simulated realized right-hand circular polarization (RHCP) and left-hand circular polarization (LHCP) gains of Type III is shown in Fig. 5 (b). It is observed that Type III achieves the peak RHCP gain of 12.3 dBic at 2.04 GHz.

To further explain the AR change trend, the electric field distributions of the three antenna types at 1.8 and 2.1 GHz are shown in Fig. 6. All three types exhibit gradual outward leakage of electromagnetic waves along the spiral arms. In other words, the electric fields radiate the CP waves as they propagate. However, compared with Types I and II, the surface electric field of Type III exhibits a good right-hand rotation performance along the spiral arm, resulting in efficient RHCP wave radiation. Since these eight arms are involved in radiation, Type III achieves a higher gain. The radiation patterns of Type III at the sideband frequency points of 1.5 and 2.05 GHz are given in Fig. 7. Type III has good radiation performance and low back lobe within the frequency band.

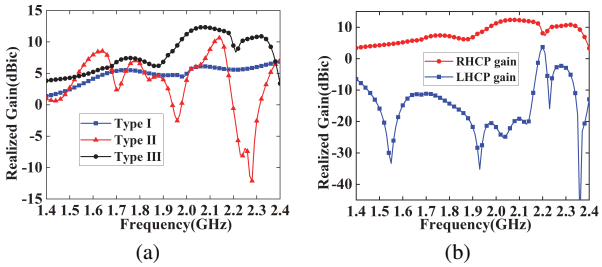

Fig. 5. (a) Simulated realized gains of Type I (2-arms), Type II (4-arms), and Type III (8-arms) antennas. (b) Simulated RHCP and LHCP realized gains of Type III antenna.

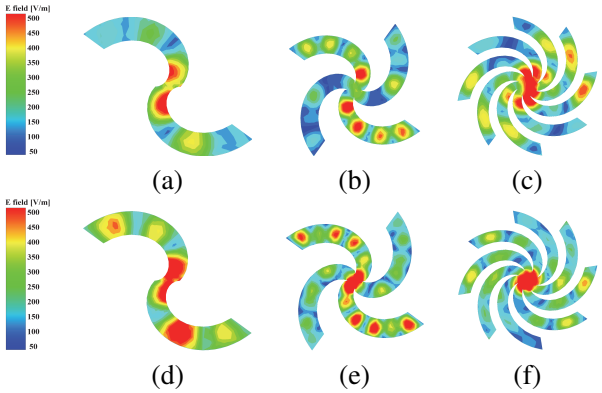

Fig. 6. Simulated electric field distributions at 1.8 GHz for (a) Type I, (b) Type II, (c) Type III, and at 2.1 GHz for (d) Type I, (e) Type II, (f) Type III.

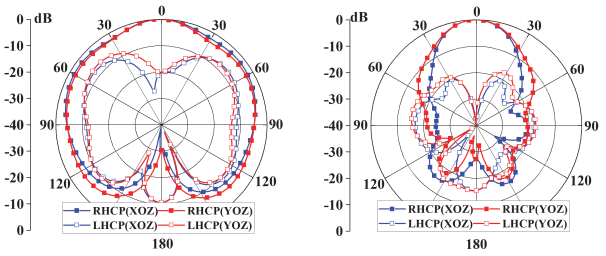

(a) (b)

Fig. 7. Normalized radiation patterns of the Type III at (a) 1.5 and (b) 2.05 GHz.

C. Parameter optimization of the proposed ASIDA

For Type III, the parameter optimization of the proposed ASIDA is performed in this part. Figure 8 illustrates the effects of the spiral growth rate a and the height h on the AR and $|S_{11}|$. When the spiral growth rate a increases, both AR and impedance bandwidth decrease. As the height h increases, the impedance bandwidth decreases, while the AR initially shifts toward lower frequencies. At $h = 22.5$ mm, the low-frequency AR performance remains unchanged, but significant degradation occurs in the high-frequency AR characteristics. To achieve optimal impedance matching and AR performance simultaneously, the values of $a =$ 34.5 mm/rad and $h = 20.5$ mm are selected as the compromise.

Figure 9 presents the parametric analysis of the dielectric arm width w and cross-slot rotation angle θ_1. As illustrated in Fig. 9 (a), w significantly influences the frequency-dependent characteristics of the AR bandwidth, where excessive width values degrade the high-frequency radiation performance. Figure 9 (b) experimentally validates that θ_1 governs the orthogonal phase difference, consistent with the theoretical analysis in section IIA. The optimized design configuration with $w = 20$ mm and $\theta_1 = 30°$ demonstrates an optimal balance between impedance matching and AR bandwidth performance.

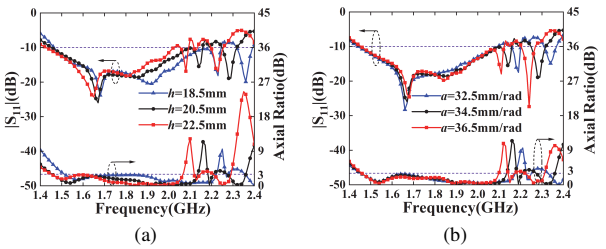

(a) (b)

Fig. 8. Parametric effects of (a) spiral growth rate a and (b) dielectric height h on simulated $|S_{11}|$ and AR.

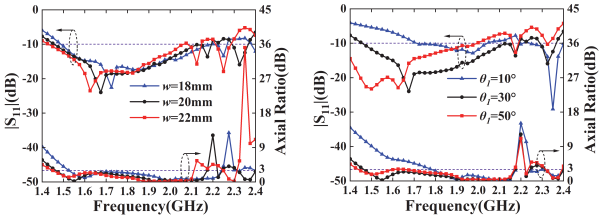

(a) (b)

Fig. 9. Simulated results of $|S_{11}|$ and AR with the different (a) spiral arm width w and (b) unequal-length cross-slot angle θ_1.

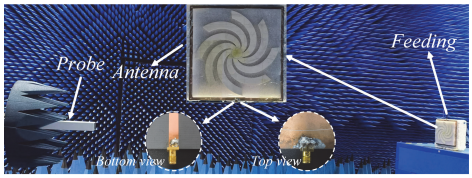

Fig. 10. Photographs of the proposed antenna and testing anechoic chamber.

III. EXPERIMENTAL RESULTS AND DISCUSSION

In this section, the proposed ASIDA is fabricated, measured, and its simulated and measured results are compared and analyzed. To ensure fabrication accuracy, a modular strategy is adopted by dividing the overall spiral structure into eight individual spiral arms and a central octagonal support, which are fabricated separately and assembled using a foam jig for precise alignment and fixation.

Photographs of the proposed ASIDA and testing anechoic chamber are shown in Fig. 10. The simulated and measured $|S_{11}|$ and efficiency results are presented in Fig. 11. Due to no conductor loss and low-loss materials Al_2O_3 ($\tan\delta = 0.0004$), the ASIDA maintains a radiation efficiency exceeding 87% at the operation band. The simulated impedance bandwidth is 40.4% (1.46–2.20 GHz), while the measured bandwidth is 40.8% (1.54–2.33 GHz).

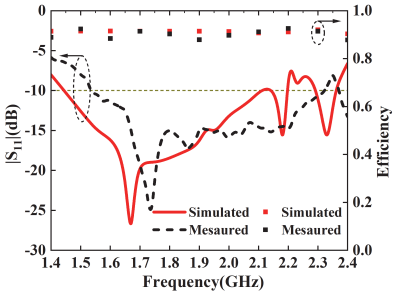

Fig. 11. Comparisons for $|S_{11}|$ and efficiency of the proposed ASIDA.

Table 2: Comparison of the proposed antenna and the previous wideband DRAs

Ref.	−10 dB Imp-BW	3-dB AR.BW	Overlapping BW	Peak Gain (dBic or dBi)	Size (λ_e^3)	Dielectric ε_r	Radiating Type
[10]	34.3%/36.6%	30.4%/32.9%	30.4%/32.9%	6.18/6.58	NA	9.9	DRA
[12]	41.2%	26.7%	26.7%	4.75	$3.19 \times 3.19 \times 0.51$	10.2	DRA
[17]	36%	26%	26%	8.7	$6.6 \times 6.6 \times 0.9$	36	DRA
[18]	29%	24.9%	24.9%	9	$11.26 \times 11.26 \times 0.96$	32	DW
[19]	22.2%	9.7%	9.7%	25	$34.7 \times 34.7 \times 0.76$	10	DW
This Work	**40.8%**	**39.8%**	**39.8%**	**12.2**	$5.04 \times 5.04 \times 0.47$	**9.8**	**IDW**

Imp-BW is the frequency range over which the reflection coefficient ($|S_{11}|$) remains below −10 dB.
Overlapping BW is the frequency range where impedance bandwidth and AR bandwidth overlap.
AR BW is the frequency range over which the axial ratio (AR) remains below 3 dB.
λ_e is the wavelength of an electromagnetic wave propagating inside a dielectric material with relative permittivity ε_r.
NA: Not Available; DW: dielectric waveguide; IDW: Image-dielectric waveguide.

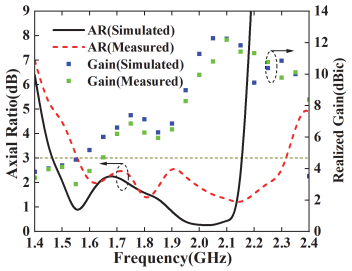

Fig. 12. Comparisons for AR and realized gain of the proposed ASIDA.

Figure 12 compares the simulated and measured results of AR and realized gain. The simulated and measured AR bandwidths are 39.1% (1.46–2.17 GHz) and 39.8% (1.55–2.32 GHz), respectively. ASIDA achieves a maximum measured realized gain of 12.2 dBic. Figure 13 shows the simulated and measured normalized radiation patterns of the ASIDA. The differences between simulated and measured results may arise from discrepancies in ASIDA fabrication, assembly, and dielectric constant tolerances.

Finally, comparison results of the proposed ASIDA and other wideband CP dielectric antennas are summarized in Table 2. The proposed ASIDA exhibits a wider impedance and AR bandwidth than those reported in [18, 19] and a higher gain than that in [18]. The image-dielectric waveguide line is implemented to achieve a lower profile compared to [18, 19]. With its advantages in wide impedance and AR bandwidth, low profile, and high gain, the proposed ASIDA shows strong potential as a candidate for future wireless communication and navigation applications.

In addition, several other designs listed in Table 2 are also considered for comparison. The antennas in [10, 12, 17] employ dual-feed structures, reconfigurable circuits, or multilayered geometries to achieve wideband CP operations. These designs have the structure complexity or larger size. In contrast, the proposed single-fed ASIDA achieves wideband CP with a structurally simple and compact design, highlighting its practical advantages in integration and implementation.

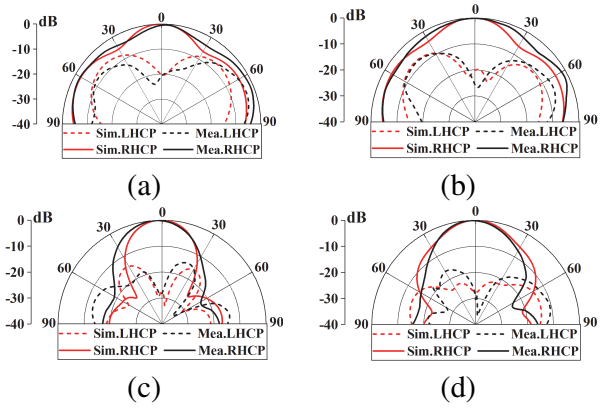

Fig. 13. Simulated and measured radiation patterns of the ASIDA: (a) *xoz* plane at 1.6 GHz, (b) *yoz* plane at 1.6 GHz, (c) *xoz* plane at 2.15 GHz, and (d) *yoz* plane at 2.15 GHz.

IV. CONCLUSION

In this paper, a wideband CP ASIDA with the eight arms is proposed. The image-dielectric waveguide line is adopted to achieve a low profile, and the eight Archimedean-spiral image-dielectric arms with the unequal-length cross-slot feed achieves wider AR bandwidth of 39.8% in a compact size. The measured results show that the proposed ASIDA has a wide impedance bandwidth of 40.8% (1.54–2.33 GHz) and a wide AR bandwidth of 39.8% (1.55–2.32 GHz), with a maximum realized gain of 12.2 dBic. The proposed ASIDA design demonstrates good performance in terms of impedance bandwidth, AR bandwidth, and gain, offering valuable insights for the design of wideband CP antennas. The ASIDA exhibits potential applications in wireless communication systems and satellite navigation systems.

REFERENCES

[1] C. Zhu, G. Xu, A. Ren, W. Wang, Z. Huang, and X. Wu, "A compact dual-band dual-circularly polarized SIW cavity-backed antenna array for millimeter-wave applications," *IEEE Antennas and Wireless Propag. Lett.*, vol. 21, no. 8, pp. 1572–1576, Aug. 2022.

[2] Q. Wu, J. Hirokawa, J. Yin, C. Yu, H. Wang, and W. Hong, "Millimeter wave planar broadband circularly polarized antenna array using stacked curl elements," *IEEE Trans. Antennas Propag.*, vol. 65, no. 12, pp. 7052–7062, Dec. 2017.

[3] H. Xue, L. Wu, Z.-L. Xiao, and T.-Y. Hu, "A low-profile broadband circularly polarized patch antenna with wide axial-ratio beamwidth," *IEEE Antennas Wireless Propag. Lett*., vol. 22, no. 9, pp. 2115–2119, Sep. 2023.

[4] Y. Cheng and Y. Dong, "Wideband circularly polarized split patch antenna loaded with suspended rods," *IEEE Antennas Wireless Propag. Lett*., vol. 20, no. 2, pp. 229–233, Feb. 2021.

[5] W. Tan, X. Shan, and Z. Shen, "Ultrawideband circularly polarized antenna with shared semicircular patches," *IEEE Trans. Antennas Propag*., vol. 69, no. 6, pp. 3555–3559, June 2021.

[6] P. Mallick, M. Ameen, R. Chowdhury, A. K. Ray, and R. K. Chaudhary, "Wideband circularly polarized cavity-backed dielectric resonator antenna with low RCS for aerial vehicle communications," *IEEE Antennas Wireless Propag. Lett*., vol. 21, no. 7, pp. 1418-1422, July 2022.

[7] X. Ruan and C. H. Chan, "A circularly polarized differentially fed transmission-line-excited magnetoelectric dipole antenna array for 5G applications," *IEEE Trans. Antennas Propag*., vol. 67, no. 3, pp. 2002-2007, Mar. 2019.

[8] Y.-W. Zhong, G.-M. Yang, J.-Y. Mo, and L.-R. Zheng, "Compact circularly polarized Archimedean spiral antenna for ultrawideband communication applications," *IEEE Antennas Wireless Propag. Lett*., vol. 16, pp. 129-132, 2017.

[9] S. Ranjit, S. Chakrabarti, and S. K. Parui, "A dual circularly polarized substrate integrated waveguide antenna for X-band application," in *Proc. IEEE Microw., Antennas, Propagat. Conf. (MAPCON)*, pp 1308-1312, 2022.

[10] B.-J. Liu, J.-H. Qiu, C.-H. Wang, W. Li, and G.-Q. Li, "Polarization-reconfigurable cylindrical dielectric resonator antenna excited by dual probe with tunable feed network," *IEEE Access*, vol. 7, pp. 60111-60119, 2019.

[11] J.-E. Zhang, Q. Zhang, W. Kong, W.-W. Yang, and J.-X. Chen, "Compact and low-profile linear-/circular-polarization dielectric resonator antennas with extended bandwidths," *IEEE Open J. Antennas Propag*., vol. 3, pp. 391–397, 2022.

[12] C. Tong, H. I. Kremer, N. Yang, and K. W. Leung, "Compact wideband circularly polarized dielectric resonator antenna with dielectric vias," *IEEE Antennas Wireless Propag. Lett*., vol. 21, no. 6, pp. 1100–1104, June 2022.

[13] A. A. Abdulmajid, Y. Khalil, and S. Khamas, "Higher-order-mode circularly polarized two-layer rectangular dielectric resonator antenna," *IEEE Antennas Wireless Propag. Lett*., vol. 17, no. 6, pp. 1114–1117, June 2018.

[14] X. C. Wang, L. Sun, X. L. Lu, S. Liang, and W.-Z. Lu, "Single-feed dual-band circularly polarized dielectric resonator antenna for CNSS applications," *IEEE Trans. Antennas Propag*., vol. 65, no. 8, pp. 4283–4287, Aug. 2017.

[15] M.-D. Yang, Y.-M. Pan, Y.-X. Sun, and K.-W. Leung, "Wideband circularly polarized substrate-integrated embedded dielectric resonator antenna for millimeter-wave applications," *IEEE Trans. Antennas Propag*., vol. 68, no. 2, pp. 1145–1150, Feb. 2020.

[16] T.-W. Chen, W.-W. Yang, Y.-H. Ke, and J.-X. Chen, "A circularly polarized hybrid dielectric resonator antenna with wide bandwidth and compact size," *IEEE Antennas Wireless Propag. Lett*., vol. 22, no. 3, pp. 591–595, Mar. 2023.

[17] W.-J. Sun, W.-W. Yang, L. Guo, W. Qin, and J.-X. Chen, "A circularly polarized dielectric resonator antenna and its reconfigurable design," *IEEE Antennas Wireless Propag. Lett*., vol. 19, pp. 1088–1092, July 2020.

[18] S. Wang, F. Fan, Y. Xu, Z.-C. Guo, W. Zheng, Y.-T. Liu, and Y. Li, "3-D printed zirconia ceramic Archimedean spiral antenna: Theory and performance in comparison with its metal counterpart," *IEEE Antennas Wireless Propag. Lett*., vol. 21, no. 6, pp. 1173–1177, June 2022.

[19] T. Lira-Valdés, E. Rajo-Iglesias, and F. Pizarro, "3-D-printed spiral leaky wave antenna with circular polarization," *IEEE Open J. Antennas Propag*., vol. 4, pp. 427–433, 2023.

[20] C.-Y. Huang, J.-Y. Wu, and K.-L. Wong, "Cross-slot-coupled microstrip antenna and dielectric resonator antenna for circular polarization," *IEEE Trans. Antennas Propag*., vol. 47, no. 4, pp. 605–609, Apr. 1999.

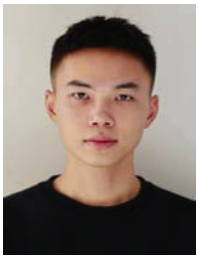

Dong Chen was born in 2001. He received his B.S. degree from Chongqing Jiaotong University, Chongqing, China, in 2023. He is currently pursuing his M.S. degree, in Anhui University. His current research interests include dielectric resonator antenna and millimeter-wave antenna.

Guanghui Xu was born in 1986. He received the B.E. degree from Anhui Jianzhu University, Hefei, China, in 2009, the M.E. degree from Shenzhen University, Shenzhen, China, in 2012, and the Ph.D. degree from the Department of Electronic Engineering, Shanghai Jiao Tong University, Shanghai, China, in 2019. His research interests include millimeter-wave (mm-wave) antenna and reconfigurable antennas.

Yanbin Luo received the B.S. degree from the China University of Mining and Technology, Xuzhou, China, in 2015. He is currently pursuing the Ph.D. degree with Beijing University of Posts and Telecommunications, Beijing. His research interests include graphene/GaAs nanowire photodetectors, graphene reconfigurable antennas, wideband antennas, and miniaturized antennas.

Wei Wang received the Ph.D. degree in navigation, guidance, and control from Harbin Engineering University (HEU), Harbin, China, in 2005. He was a Post-Doctoral Research Associate at Harbin Institute of Technology, Harbin, from July 2006 to April 2009. His current research interests include location, mapping, and image processing.

Dawei Ding received the B.E. degree from Jiangsu University, Zhenjiang, China, in 2009, and the Ph.D. degree from the University of Science and Technology of China, Hefei, in 2015. He is currently an Associate Professor with the School of Electronic Engineering, Anhui University, Hefei. His research interests include antenna theory and design, multiobjective optimization methods, and microwave circuit design.

Luyu Zhao was born in Xi'an, China, in 1984. He received the B.Eng. degree from Xidian University, Xi'an, in 2007, and the Ph.D. degree from The Chinese University of Hong Kong, Hong Kong, in 2014. His current research interests include design and application of multiple antenna systems for next generation mobile communication systems, innovative passive RF and microwave components and systems, millimeter wave and terahertz antenna array, and meta-material-based or inspired antenna arrays.

Yingsong Li received the B.S. degree in electrical and information engineering and the M.S. degree in electromagnetic field and microwave technology from Harbin Engineering University (HEU), Harbin, China, in 2006 and 2011, respectively, and the Ph.D. degree from the Kochi University of Technology (KUT), Kochi, Japan, and Harbin Engineering University (HEU) in 2014. His research interests include remote sensing, underwater communications, signal processing, adaptive filters, metasurface designs, and microwave antennas.

Zhixiang Huang was born in 1979. He received the B.S. and Ph.D. degrees from Anhui University, Hefei, China, in 2002 and 2007. His research interests include theoretical and computational research in electromagnetics and imaging, focusing on multiphysics and interdisciplinary research, and fundamental and applied aspects in metamaterials and active metamaterials.

Xianliang Wu was born in Bozhou, Anhui, China, in 1955. He is a Second-Level Professor, a Ph.D. Supervisor, and the Academic and Technological Leader of Anhui. He has been engaged in teaching and scientific research in electromagnetic field theory, mobile communications, electromagnetic scattering theory of complex targets, and electromagnetic field numerical calculation. His research interests include theoretical and computational research in electromagnetics and imaging, focusing on multiphysics and interdisciplinary research, and fundamental and applied aspects in metamaterials and active metamaterials.

A Low Cost, Wideband, Microstrip Patch Antenna Array With Improved Gain for Millimeter-Wave Applications

Zakir Khan[1,2], Ce Zhang[2], Saeed Ur Rahman[3], Xiao-Chuan Wang[1,2], Lei Wen[1,2], and Wen-Zhong Lu[1,2]

[1]School of Optical and Electronic Information and Key Lab of Functional Materials for Electronic Information
Huazhong University of Science and Technology, Wuhan 430074, China
zakirkhan@mail.ustc.edu.cn, wxc@hust.edu.cn, wenlei@mail.hust.edu.cn, lwz@hust.edu.cn

[2]Advanced Manufacturing Institute
Huazhong University of Science and Technology, Wenzhou 325035, China
zhangce@wzhust.com,

[3]School of Electronic Engineering
Xidian University, China
saeed@xidian.edu.cn

Abstract – In this paper the design and analysis of a low cost, wideband and high gain 2×2 elements patch antenna array for millimeter-wave (mmWave) applications is presented. The proposed antenna array has been designed and fabricated using the cost-effective F4B substrate which is an economical and a suitable option for high frequency communication applications. The final geometry of the unit cell contains a slotted octagonal ring on the outside and a small parasitic octagonal ring on the inner side, connected by crossed-shape strip lines. A prototype of the proposed antenna element and array has been fabricated, which demonstrates a good agreement between the simulated and measured results. According to −10 dB matching bandwidth criteria, the proposed antenna array operates at frequency range 23.8–29.0 GHz, achieving a maximum gain of approximately 13.5 dBi and efficiency range 83–91% at its operating frequencies. The high performance of the proposed antenna array compared to the existing designs along with its simple design and cost-effectiveness demonstrate its potential for high data rate mmWave wireless communication applications.

Index Terms – Bandwidth, efficiency, fifth-generation, millimeter-wave, parasitic patch, wideband.

I. INTRODUCTION

In recent years, the lifestyle of the world has been significantly changing due to the development of wireless communication systems, most specifically in the past two decades. The increased demands for high data rates have demonstrated that ubiquitous communication systems are required to support the rising demand for high data rates. In response, substantial work has been done in the development of next generations, specifically fifth-generation (5G) communication standards. In 5G and upcoming wireless communication, the role of the millimeter-wave (mmWave) band is really important due to providing gigabit per second (Gbps) data throughput capability, enhanced user capacity and unprecedented bandwidth [1–3]. This technology offers various important features that can improve connectivity and performance of communication systems including high data rates in ultra-HD video streaming, low latency in real time applications such as self-driving cars and robotic surgeries, and the ability to support a large number of devices for Internet of Things (IoT) applications in smart cities. Limited bandwidth of the sub-6 GHz band, which is already crowded by current wireless standards, motivated researchers to utilize the spectrum in mmWave bands [4, 5]. Along with various advantages of mmWave communication, there are some disadvantages, i.e., multipath fading and attenuation are very eminent due to poor refraction and diffraction effects [6, 7], which is exacerbated by environmental factors such as rain and foliage. Therefore, along with a wide impedance bandwidth, a high gain directive antenna system is required for both mobile terminals and base stations to overcome high path losses and support potential wireless applications.

The deployment of high-performance antenna arrays is a promising solution to deliver high data rate and maintain reliable connectivity for future wireless communication. Various types of antenna arrays can be used for mmWave applications, which includes

Submitted On: June 26, 2025
Accepted On: October 14, 2025

https://doi.org/10.13052/2025.ACES.J.401009

multi-layered printed circuit board (PCB) antennas such as magnetoelectric (ME) dipoles by [8], tightly coupled dipole antenna (TCDA) by [9, 10] and tapered slot Vivaldi antennas by [11]. However, these antennas have complex profiles, multilayers and expensive fabrication processes. Therefore, microstrip patch antennas are the widely used solution due to its compact form and simple design geometry which makes them perfectly suited for modern wireless applications.

Few mmWave antennas have been designed [12–17], however, these designs face limitations such as narrow bandwidth, bulky size, low efficiency or high cost due to complex design and fabrication process. In [12], a 6×5 element array having a size of 101×96.5 mm^2 fed by proximity couple has been designed. While this antenna achieves a high gain of 21 dBi, the operating bandwidth is narrow at 27.5–28.5 GHz, and it has a larger size and complex design geometry. In [13], a mmWave antenna array measuring 70×63.5×2.2 mm^3 utilizing substrate integrated waveguide (SIW) feeding has been designed. The antenna operates over a frequency range 27.4–28.94 GHz, providing a bandwidth of 1.54 GHz and a gain of approximately 13.5 dBi. However, the design has a bulky size and complex geometry with four layers, and SIW feeding is used making it difficult and costly to fabricate. Similarly, a dual band patch antenna array for 5G applications has been designed in [14, 15]. The designed antennas have compact sizes and achieve gain of 13.5 dBi; however, it exhibits limitations in achieving a broad bandwidth and utilizes Rogers RT5880, which is costly for fabrication.

A planar antenna array having a dimension of 66×15×0.3 mm^3 for 5G communication has been designed in [16]. The antenna array operates at 24–29.5 GHz and achieves a gain of 12 dBi, while it consists of a complex design geometry having substrate integrated cavity (SIC) which makes the fabrication difficult and costly. The authors in [17] proposed an inset feed antenna array having size of 100×17.45 mm^2 for 5G communication. The design operates at frequency range 24.35–31.13 GHz, provides a broadband of 6.7 GHz and a gain of 19.88 dBi, however, the design geometry consists of multiple layers of substrate which make the fabrication difficult and increases the cost for desired applications.

To address these challenges, a high-performance mmWave antenna array is required, characterized by low cost, broad bandwidth, compact size, better integration capability and high gain, which aims to overcome the limitations of existing state-of-the-art designs and minimize issues related to attenuation and potential path loss in the mmWave band. Therefore, this work proposes an octagonal ring patch antenna array, which is mainly focused on the enhancement of bandwidth for high data rates applications, high directivity and efficiency to overcome the losses in mmWave communication and simplifying the design complexity and cost-effectiveness by utilizing a low-cost substrate F4B, which is economical and efficient when compared to expensive Rogers RT5880, and using a single layer to minimize fabrication cost, with future plans to advance beamforming and beam scanning functionalities.

The rest of the paper is organized as follows. Section II presents the detailed methodology and geometry of the proposed antenna array. Section III presents various results. Section IV provides a comparison with related works, and section V concludes the paper.

II. MATERIALS AND METHODS

In this section the theoretical detail, methodology and evolution of the proposed antenna array from a circular disc will be discussed in detail.

A. Proposed antenna element

The proposed antenna element is shown in Fig. 1 (a) and its prototype in Fig. 1 (b). The overall size of the proposed antenna is 22×20 mm^2 and its thickness is 0.25 mm. The proposed antenna is single layer and its geometry consists of a patch which is its main radiating element, a substrate and a ground plane. The proposed antenna is printed on one side of a cost-effective substrate., i.e., F4B which has a dielectric constant of $\varepsilon_r = 2.2$ and loss tangent tan $\delta = 0.002$. The radiating element of the antenna comprises of two octagonal rings coupled through a crossed strip line, with a full ground plane at its bottom layer. The radiating element is fed by a 50 Ω microstrip line, where the inner part of the SubMiniature version-A (SMA) connector is used to feed the microstrip line and the outer part is soldiered to the ground plane. The designing, simulation and mathematical analysis of the proposed antenna has been carried out in a commercially available computer simulation technology (CST) Microwave studio software [18].

B. Design evolution

The primary design of the proposed antenna is an octagonal shaped patch extracted from a circular disc having 8 mm radius as shown in Figs. 2 (a) and 2 (b). The resonating frequency of a circular patch can be calculated by (1) [19] as:

$$f_r = \frac{\mathrm{Xmn}}{2\pi \mathrm{ae}\sqrt{\varepsilon \mathrm{r}}}\mathrm{C}, \tag{1}$$

where f_r is resonating frequency, $\mathrm{X_{mn}} = 1.8411$ for $\mathrm{TM_{11}}$ dominant mode, $\mathrm{a_e}$ = effective radius of the

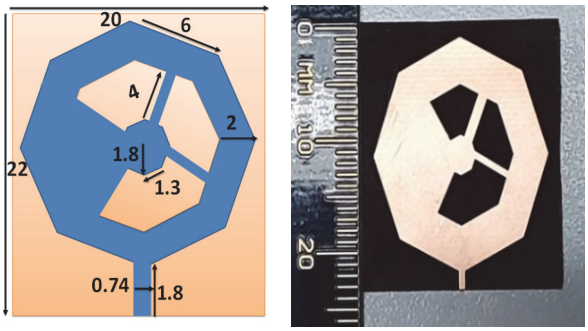

(a) (b)

Fig. 1. Proposed designed antenna: (a) geometry and (b) prototype.

circular patch, C = free space light speed and ε_r is substrate relative permittivity.

To calculate a_e of the circular patch, (2) is used [19]:

$$a_e = a\sqrt{1-\frac{2h}{\pi ae\varepsilon r}\left(ln\frac{\pi a}{2h}+1.7726\right)}. \quad (2)$$

Equation (2) is used to design an octagonal patch by relating the area of octagonal and circular patch given in (3):

$$\pi a_e^2 = 2(1+\sqrt{2})s^2. \quad (3)$$

The side length of the octagonal patch is found to be 6 mm. The primary design gives us a very narrow bandwidth. Therefore, various types of techniques in the form of etching a slot, inserting a parasitic patch, and direct-coupled strip-lines, shown in Figs. 3 (a) and 3 (b), will be applied to obtain a wide impedance bandwidth.

Etching a slot in the conductive patch causes a significant change in current distribution and introduces multiple resonant modes that are overlapped with the fundamental resonance and results in the broadening of the impedance bandwidth. In the next step, a parasitic patch is inserted which is placed inside the main patch that shift the characteristic modes to the desired resonant frequencies by capacitive loading of the parasitic patch which facilitate coupling effects that further optimize the bandwidth [20]. Finally, the direct coupled strip lines connecting the two patches result in better impedance matching and broad bandwidth. These techniques couple the parasitic patch to the main radiating element which produces double resonance by the driven patch and parasitic patch which results in bandwidth enhancement of the proposed antenna element [21]. Using these techniques has enhanced bandwidth in the state-of-the-art designs [22, 23]. Furthermore, a parametric study of antenna dimensions was also performed to optimize antenna dimensions. The wide bandwidth was improved by analyzing the current distribution and precise positions of the parasitic patch, slots length and cross-shaped strip line. S_{11} comparison of the various designs is illustrated in Fig. 3 (c).

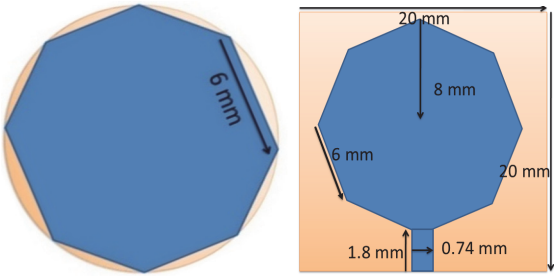

(a) (b)

Fig. 2. Extracting octagonal patch: (a) octagonal patch and (b) primary octagonal patch antenna.

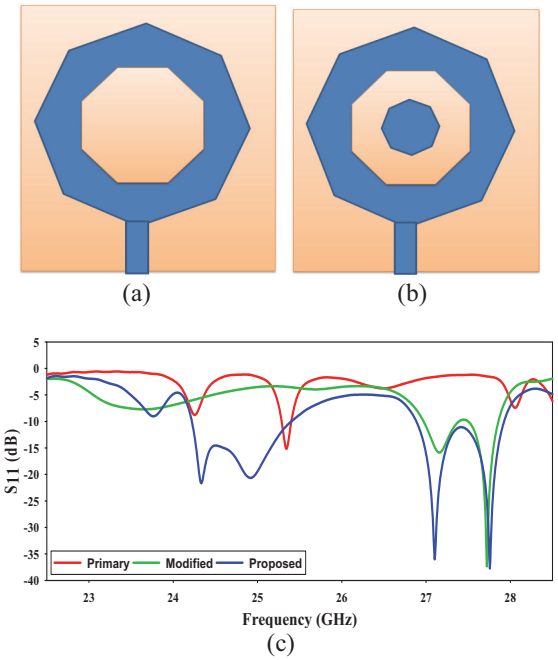

(a) (b) (c)

Fig. 3. Antenna design evolution: (a) primary design, (b) modified design, and (c) S_{11} comparison.

C. Detailed geometry of the antenna array

Multipath fading and attenuation at mmWave band is very eminent due to poor refraction and diffraction effects. Therefore, a high gain advanced antenna system is required for both mobile terminals and base station to overcome these high path losses and to support potential wireless applications. Before designing an array, we need to design a proper feeding network that works as a power splitter to excite each element of the array.

A series-parallel sequential feeding power splitter has been designed and simulated without the attachment

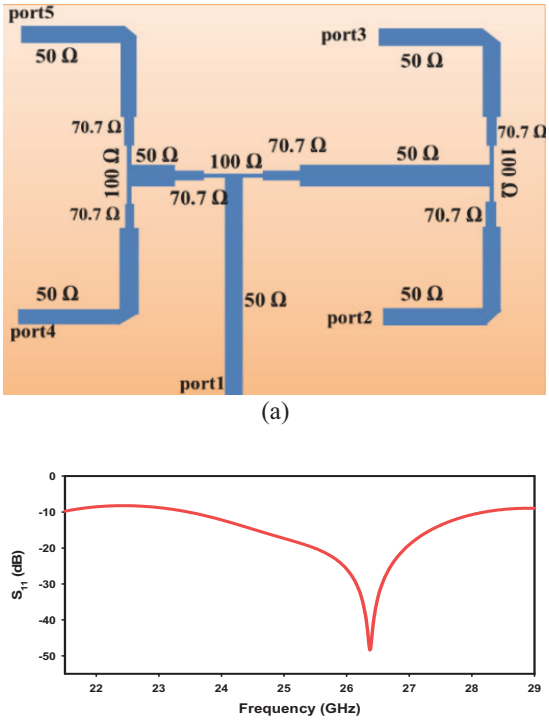

Fig. 4. Feeding network of proposed antenna array: (a) geometry of feed-line and (b) S_{11} of feed-line.

of the antenna elements. To connect the antenna element with each terminal of the feedline, a three-step quarter-wave impedance matching transmission line has been used. For matching to a 50 Ω (port 1) feed line, we need to match the other branching strips of the feeding network to the input impedance by equations (4) and (5) [24]:

$$Z = \sqrt[Z0]{N}, \tag{4}$$

where N = number of branching points, Z_0 = initial input impedance:

$$W_{Z0} = \left[\frac{377}{Z_0\sqrt{\varepsilon_r}} - 2\right] \times hs. \tag{5}$$

As shown in Fig. 4 (a), the 50 Ω feed line is given in the start as an input to port 1 which is connected to 100 Ω two parallel lines. These 100 Ω are further matched to another 100 Ω with the help of a 70.71 Ω quarter wave impedance transformer and, further, they are connected to ports 2 to 5. The performance of the feedline is analyzed. From the S_{11} graph, it is perceived that the feeding network is well matched and, according to −10 dB impedance matching, the feeding network is resonating at frequency range 23.0 to 29.0 GHz. The return loss graph of the feeding network is illustrated in Fig. 4 (b), where maximum matching is around −50 dB at 26.5 GHz.

The detailed geometry and prototype of the proposed 2×2 elements array is illustrated in Figs. 5 (a) and 5 (b). The total dimensions of the antenna array is 50×50×0.25 mm^3. The separation distance between the elements of antenna array can be usually kept as (0.5λ − 0.8λ) to decrease mutual coupling and prevent grating lobes [19]. The overall geometry of the array comprises of (2×2) elements, which have element spacing of 0.6λ between the two elements along horizontal direction D_x, and 0.55λ spacing along the vertical direction D_y.

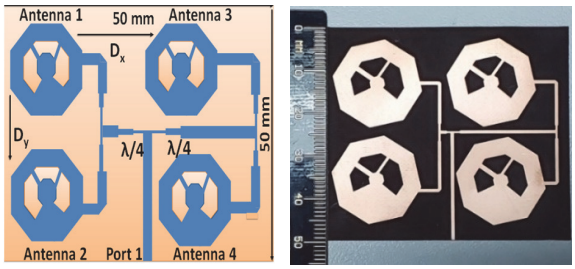

Fig. 5. Proposed antenna array: (a) geometry and (b) prototype front.

III. RESULTS AND DISCUSSION

Various results of the proposed final antenna array are discussed in this section.

A. Return loss

The ratio of the incident power to the power reflected is termed as the return loss and is expressed in dB, which is used to observe how much energy is transmitted to the radiator by the input power through the transmission line. The S_{11} value should be less than −10 dB for an efficient antenna to perform well. A 2.92 (D360B50H01-118) SMA was used at the input feeding port of the proposed antenna to measure S_{11}. First, calibration of the VNA is performed with different types of open, short and load connectors and then measurement of the return loss over a specific frequency is performed. From the measurement results, the proposed antenna element is dual-band operating at frequency range 23.8–25.1 GHz and 26.75–27.9 GHz. Similarly, it is observed that the array bandwidth is further enhanced as compared to a single element due to the phenomena of a mutual coupling [25] feeding network. Measured results show that the antenna array is operating in the frequency range 23.8–29.0 GHz. The simulated and measured results of S_{11} are illustrated in Figs. 6 (a) and 6 (b), which demonstrate good agreement, however the small deviation might be due to environmental

factors, measurement setup and manually soldering of the SMA connector. The measurement setup is shown in Fig. 6 (c).

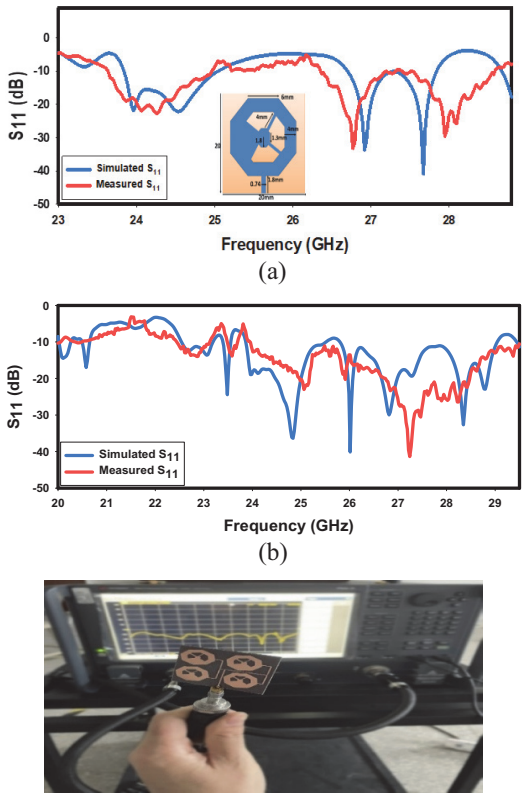

Fig. 6. S_{11} parameter of antenna: (a) return loss of single antenna, (b) return loss of array and (c) measurement setup.

B. Radiation pattern

The measure of the maximum energy of the antenna in a specified direction is its radiation pattern. The radiation pattern of the proposed array has been analyzed and measured in an anechoic chamber at 25 GHz and 27.5 GHz which is shown in the two-dimensional (2D) pattern in Figs. 7 (a) and 7 (b) and in the three-dimensional (3D) pattern in Figs. 7 (c) and 7 (d). It can be seen that the simulated and measured results agree with each other, however there is a minor discrepancy which might be due to factors such as measurement setup limitations, environmental factors and manually soldiering of the SMA connector. The array gives a broadside pattern with main lobe direction at around 0–10 degree. Moreover, the array pattern is directive, giving a high directivity of about 14 dBi at 25 GHz and 13.5 dBi at 27.5 GHz, which can be used for numerous mmWave wireless communication applications.

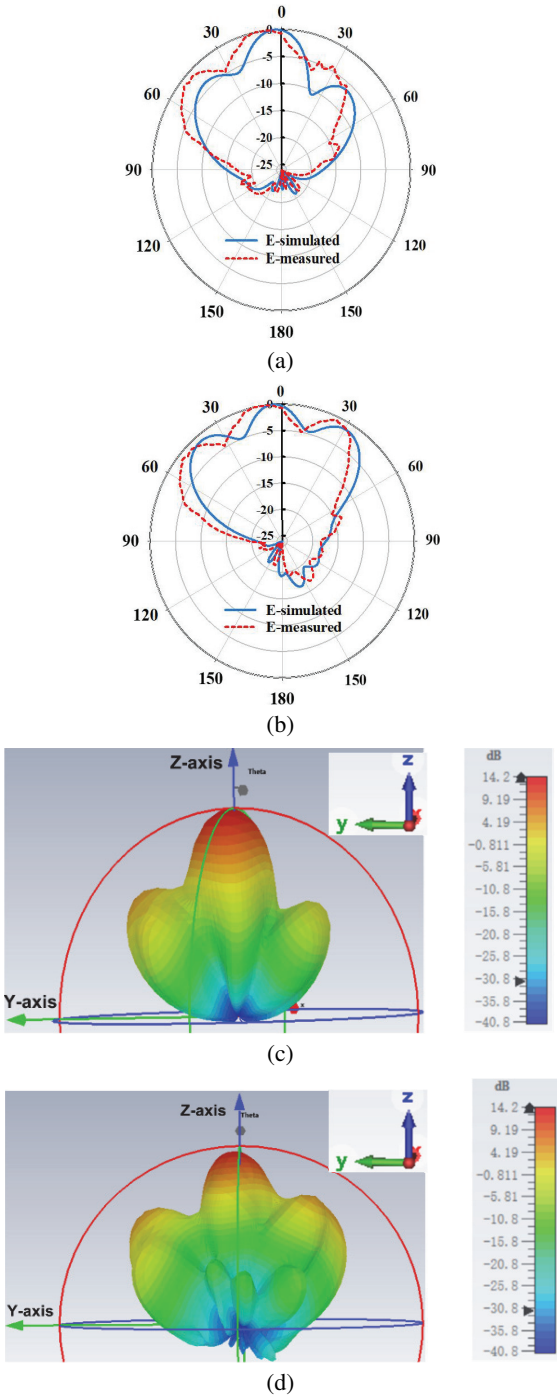

Fig. 7. Simulated and measured radiation pattern: (a) 2D pattern at 25 GHz, (b) 2D pattern at 27.5 GHz, (c) 3D pattern at 25 GHz and (d) 3D pattern at 27.5 GHz.

C. Gain

The simulated and measured gain versus frequency of the proposed antenna array is represented in Fig. 8. The antenna gain has been measured in an anechoic chamber where a calibrated horn antenna is used at a

Table 1: Comparison of proposed antenna array with state-of-the-art

S	NL	Size (λ^3)	Eff (%)	BW	G	Sub	Ref
1	2	8.91×8.49×0.04	–	1	21	Taconic TLY-5	[12]
2	4	6.42× 5.83× 0.20	60–78	1.5	13	Rogers 4350	[13]
4	1	2.93× 0.67× 0.065	85.6	1.3	13.5	Rogers 5880	[14]
5	1	2.38× 1.59×0.04	92	0.4	12	Rogers 5880	[15]
6	2	5.28× 1.2×.03	90	5.5	11.5	–	[16]
3	2	8.13× 1.42 ×0.11	75–86	6.7	18	Rogers 5880	[17]
7	1	3.97 ×3.97 ×0.02	83–91	5.2	13.5	F4B	This Work

S = serial number, NL = number of layers, Eff = efficiency, BW = bandwidth, G = gain, Sub = substrate.

specific distance as a reference antenna, the proposed antenna is antenna under test (AUT) and the gain is calculated by a specific formula. The array gain has been improved due to high numbers of antenna elements. The proposed antenna array gives high gain of 13.5 dBi at 26 GHz and 12.5 dBi at 28 GHz.

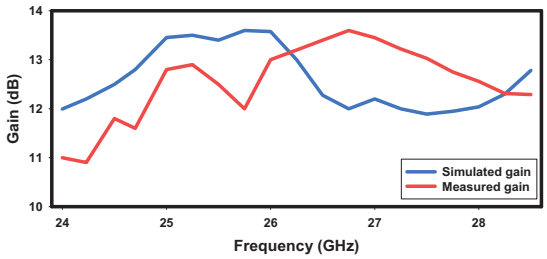

Fig. 8. Gain versus frequency plot of the proposed antenna.

D. Efficiency

A graph of total and radiated efficiency versus frequency of the proposed antenna array is illustrated in Fig. 9. The array gives a very high efficiency and its radiated and total efficiency is 83–91% at its operating frequencies.

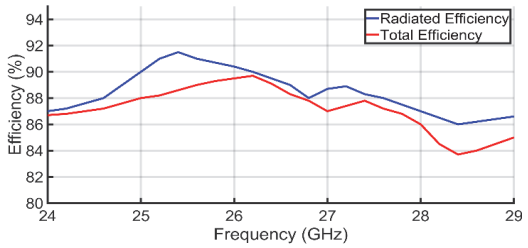

Fig. 9. Total and radiated efficiency of the antenna array.

IV. COMPARISON WITH STATE-OF-THE-ART

The proposed antenna array has been compared with existing designs in Table 1. Notably, the proposed antenna array demonstrates better performance as compared to the existing designs mentioned in the state-of-the-art. The proposed array has a more compact size than the designs in [12, 13, 16, 17]. Additionally, the impedance bandwidth of the proposed antenna array is better than [12–15]. While the designs in [16, 17] exhibit better broad bandwidth, they contain a more complex geometry design containing multiple layers. The gain of the proposed antenna array is better than [14, 16–18]. Furthermore, the proposed array is single layer and fabrication cost is minimized by utilizing a cost-effective substrate and standard PCB fabrication technique compared to more complex multi-layer and high-cost designs. Based on performance, the proposed antenna array is a good option which can be used for numerous mmWave wireless communication applications.

V. CONCLUSION

In this paper, a single layer, low cost, wideband, high gain antenna element and antenna array operating at 28 GHz have been proposed for mmWave applications. The innovative techniques of the proposed design have resulted in a significant improvement in high-performance results over the existing designs in the state-of-the-art, without requiring a complex design and multilayer configuration. The proposed array has been fabricated and the measured results show close resemblance with the simulated results. The high-performance results of the proposed antenna, resonating at frequency range 23.8–29 GHz achieving a wide bandwidth up to 5.2 GHz, a high gain of about 13.5 dBi and efficiency 83–91% make it an ideal candidate for numerous mmWave wireless communication applications.

ACKNOWLEDGMENT

This research work was supported by Wenzhou City Key Technology Development Funding ZG2023033.

REFERENCES

[1] J. Qiao, X. S. Shen, J. W. Mark, Q. Shen, Y. He, and L. Lei, "Enabling device-to-device communications in millimeter-wave 5G cellular networks," *IEEE Communications Magazine*, vol. 53, no. 1, pp. 209–215, 2015.

[2] M. Stanley, Y. Huang, T. Loh, Q. Xu, H. Wang, and H. Zhou, "A high gain steerable millimeter-wave antenna array for 5G smartphone applications," in *11th European Conference on Antennas and Propagation (EUCAP)*, pp. 1311–1314, 2017.

[3] T. S. Rappaport, Y. Xing, G. R. MacCartney, A. F. Molisch, E. Mellios, and J. Zhang, "Overview of millimeter-wave communications for fifth-generation wireless networks: With a focus on propagation models," *IEEE Transactions on Antennas and Propagation*, vol. 65, no. 12, pp. 6213–6230, 2017.

[4] R. M. Nelson, D. A. Rogers, and A. G. D'Assuncao, "Resonant frequency of a rectangular microstrip patch on several uniaxial substrates," *IEEE Transactions on Antennas and Propagation*, vol. 38, no. 7, pp. 973–981, 1990.

[5] H. Gutton and G. Baissinot, "Flat aerial for ultra-high frequencies," *French Patent*, vol. 703113, 1955.

[6] W. Hong, K.-H. Baek, Y. Lee, Y. Kim, and S.-T. Ko, "Study and prototyping of practically large-scale mmWave antenna systems for 5G cellular devices," *IEEE Communications Magazine*, vol. 52, no. 9, pp. 63–69, 2014.

[7] H. Zhou, "Phased array for millimeter-wave mobile handset," in *2014 IEEE Antennas and Propagation Society International Symposium (APSURSI)*, pp. 933–934, 2014.

[8] Y. Li and K.-M. Luk, "A 60-GHz wideband circularly polarized aperture coupled magneto-electric dipole antenna array," *IEEE Trans. Antennas Propag*., vol. 64, no. 4, pp. 1325–1333, Apr. 2016.

[9] J. A. Kasemodel, C.-C. Chen, and J. L. Volakis, "Broadband planar widescan array employing tightly coupled elements & integrated balun," in *Proc. IEEE Int. Symp. Phased Array Syst*., pp. 467–472, Oct. 2010.

[10] Z. Khan, C. Zhang, M. Zhang, X. Wang, W. Lu, and W. Lei, "An integrated feed ultrawideband Tightly-Coupled Dipole Antenna (TCDA) array for mmWave 5G communication systems," in *IEEE 12th Asia-Pacific Conference on Antennas and Propagation (APCAP)*, pp. 1–2, 2024.

[11] T. Logan, R. W. Kindt, and M. N. Vouvakis, "Low cross-polarization Vivaldi arrays," *IEEE Transactions on Antennas and Propagation*, vol. 66, no. 4, pp. 1827–1837, 2018.

[12] H. A. Diawuo and Y.-B. Jung, "Broadband proximity-coupled microstrip planar antenna array for 5G cellular applications," *IEEE Antennas and Wireless Propagation Letters*, vol. 17, no. 7, pp. 1286–1290, 2018.

[13] S.-J. Park and S.-O. Park, "LHCP and RHCP substrate integrated waveguide antenna arrays for millimeter-wave applications," *IEEE Antennas and Wireless Propagation Letters*, vol. 16, pp. 601–604, 2016.

[14] M. I. Khattak, A. Sohail, U. Khan, Z. Barki, and G. Witjaksono, "Elliptical slot circular patch antenna array with dual band behaviour for future 5G mobile communication networks," *Progress in Electromagnetics Research C*, vol. 89, pp. 133–147, 2019.

[15] J. Khan, D. A. Sehrai, and U. Ali, "Design of dual band 5G antenna array with SAR analysis for future mobile handsets," *Journal of Electrical Engineering & Technology*, vol. 14, no. 2, pp. 809–816, 2019.

[16] C.-X. Mao, M. Khalily, P. Xiao, T. W. Brown, and S. Gao, "Planar sub-millimeter-wave array antenna with enhanced gain and reduced sidelobes for 5G broadcast applications," *IEEE Transactions on Antennas and Propagation*, vol. 67, no. 1, pp. 160–168, 2018

[17] M. Khalily, R. Tafazolli, P. Xiao, and A. A. Kishk, "Broadband mmWave microstrip array antenna with improved radiation characteristics for different 5G applications," *IEEE Transactions on Antennas and Propagation*, vol. 66, no. 9, pp. 4641–4647, 2018.

[18] SIMULIA. *CST Studio Suite* ® [Online]. Available: https://www.cst.com.

[19] K. F. Lee, K. M. Luk, and H. W. Lai, *Microstrip Patch Antennas*. Singapore: World Scientific, 2017.

[20] G. Kim and S. Kim, "Design and analysis of dual polarized broadband microstrip patch antenna for 5G mmWave antenna module on FR4 substrate," *IEEE Access*, vol. 9, pp. 64306–64316, 2021.

[21] G. Kumar and K. P. Ray, *Broadband Microstrip Antennas*. Norwood, MA: Artech House, 2003.

[22] N.-W. Liu, L. Zhu, W.-W. Choi, and X. Zhang, "A low-profile aperture-coupled microstrip antenna with enhanced bandwidth under dual resonance," *IEEE Transactions on Antennas and Propagation*, vol. 65, no. 3, pp. 1055–1062, 2017.

[23] Z. Khan, M. H. Memon, S. U. Rahman, M. Sajjad, F. Lin, and L. Sun, "A single-fed multiband antenna for WLAN and 5G applications," *Sensors*, vol. 20, no. 21, p. 6332, 2020.

[24] J. D. Kraus and R. J. Marhefka, *Antennas: For All Applications*. New Delhi: Tata McGraw-Hill Publishing Company Ltd., 2001.

[25] W. Yang, K. Ma, K. S. Yeo, and W. M. Lim, "A compact high-performance patch antenna array for 60-GHz applications," *IEEE Antennas and Wireless Propagation Letters*, vol. 15, pp. 313–316, 2015.

Zakir Khan received the B.Sc. Engineering degree in Telecommunication Engineering from the University of Engineering and Technology (UET), Peshawar, Pakistan, in 2013, the master's degree in Electrical Engineering from COMSATS University, Abbottabad, in 2016, and the Ph.D. (Engineering) degree from the University of Science and Technology of China (USTC) in 2022 in Electronic Science and Technology. He was with the University of Naples, Parthenope, Italy, 2022–2024. Currently, he is a postdoctoral researcher at Advanced Manufacturing Institute of HUST in Wenzhou, China. His major research interests include microwave/mmWave antenna design and microwave remote sensing.

Ce Zhang (S'11–M'16) received the B.E. degree in electronic communication engineering from the City University of Hong Kong, Hong Kong, in 2011, and the Ph.D. degree in electrical engineering from the University of Washington, Seattle, WA, USA, in 2016. He worked at Tubis Technology (now Kyocera) from 2016 to 2017, Amazon Inc. from 2017 to 2019 and Facebook (now Meta) from 2019 to 2023. From 2023 to now, he works at Huazhong University Advanced Manufacturing Research Institute. His current research interests include antenna design, phased array system, and signal processing and electromagnetic theory in wireless power transfer and radar imaging system.

Saeed ur Rahman completed his B.S. degree from COMSATS University Abbottabad, Pakistan, and his master's degree from Capital University of Science and Technology (CUST), with a major in Electronic Engineering. He completed his Ph.D. degree from Nanjing University of Aeronautics and Astronautics, Nanjing, China, majoring in Information and Communication Engineering. He worked as a postdoctoral fellow from 2020 to 2022 at Nanjing University of Aeronautics and Astronautics, Nanjing. He has been working as an associate professor at Xidian University, Xi'an, since 2022. His major research includes electromagnetic and microwave technology, especially in meta surfaces, antennas, and intelligent reflective surfaces (RIS).

Xiao-Chuan Wang (M' 14) received the B.E. degree in electronic science and technology and the Ph.D. degree in microelectronics and solid-state electronics from the Huazhong University of Science and Technology, Wuhan, China, in 2005 and 2010, respectively. From 2010 to 2015, he served as a Lecturer with the Department of Electronic Science and Technology, Huazhong University of Science and Technology, where he was promoted to Professor within the School of Optical and Electronic Information in 2023. His current research interests include microwave and millimeter-wave components.

Lei Wen is a Professor and Ph.D. supervisor at the School of Optical and Electronic Information in Huazhong University of Science and Technology (HUST), and vice dean of Advanced Manufacturing Institute of HUST, Wenzhou, China. He obtained his Ph.D. degree in Materials Science at HUST in 2008. His research activities are mainly concerned with microwave dielectric materials and components for microwave communication. He has undertaken more than 30 research projects supported by the National Natural Science Funds, the National Key Research and Development Program of China, and about 200 academic papers have been published and several research productions have been applied successfully for antennas, resonators and LTCC modules.

Wen-Zhong Lu received the Ph.D. degree in electronic materials and components from Huazhong University of Science and Technology, Wuhan, China, in 1994. From 1997 to 1998, he was a Research Scholar with the Department of Physics, Moscow University, Moscow, Russia. In 2002, he was a Senior Research Scholar in Material Research Center. Manchester University, Manchester, UK. He is currently a Professor and Dean of Advanced Manufacturing Institute of Huazhong University of Science and Technology in Wenzhou. He has authored or coauthored more than 300 journal and conference papers. His current research interests include microwave functional materials and components.

Dual-Beam Series-Fed MIMO Antenna With Metasurface Loading for 5G Sub-6 GHz Access Point Applications

R. Anandan[1], V. Vinoth Kumar[2], M. Pandi Maharajan[3], and G. Jothi[4]

[1]Department of Electronics and Communication Engineering,
Dhanalakshmi Srinivasan College of Engineering and Technology
Mamallapuram, Chennai, Tamil Nadu, India
anandandscet@gmail.com

[2]Department of Electronics and Communication Engineering,
Vel Tech Rangarajan Dr.Sagunthala R&D Institute of Science and Technology
Chennai-600062, Tamil Nadu, India
icevinoth@gmail.com

[3]Dept. of ECE, Saveetha School of Engineering,
Saveetha Institute of Medical and Technical Sciences
Saveetha University, Chennai-602105, Tamil Nadu, India
pandimaha.net@gmail.com

[4]Saveetha School of Engineering,
Saveetha Institute of Medical and Technical Sciences
Saveetha University, Chennai-602105, Tamil Nadu, India
jothigopal1006@gmail.com

Abstract – This article presents a compact series-fed MIMO antenna integrated with metamaterial structures, designed for 5G sub-6 GHz applications. The design employs a Substrate Integrated Waveguide (SIW)-based power divider operating at 3 GHz, offering a wide bandwidth from 3 to 5 GHz. A series-fed dipole structure is realized by connecting four dipoles of varying lengths and spacing using a microstrip line, arranged symmetrically on both sides of the SIW divider. A square-ring metamaterial array is placed along the y-axis in front of the radiating elements to enhance performance. This configuration boosts the gain significantly, achieving values between 5 and 11 dB across 2.4 to 6.5 GHz, without increasing the antenna size or compromising efficiency. The metamaterial also improves polarization characteristics, reducing cross-polarization over the entire band. MIMO capability is achieved by placing two metamaterial-loaded radiators side by side, with an Electromagnetic Band Gap (EBG) structure on the ground plane to suppress mutual coupling. The proposed design is evaluated using key MIMO performance metrics, including mutual coupling, diversity gain (DG), envelope correlation coefficient (ECC), mean effective gain (MEG), and total active reflection coefficient (TARC), demonstrating its suitability for next-generation wireless systems.

Index Terms – 5G antenna sub-6 GHz, dual-beam, metasurface, MIMO antenna, series-fed.

I. INTRODUCTION

The rapid evolution of wireless communication technologies has brought forth unprecedented demands on system performance, particularly in terms of data rate, coverage, and reliability [1]. Future technologies, such as augmented reality, video games, and smart cities, have a huge need for high-speed data rates [2]. In order to attain the gigabit-per-second data rate, multi-network connectivity is required [2]. In order to achieve extraordinarily high throughput, on the order of several gigabits per second, 5G communication technology has made excellent use of the cm and mm wave spectrum, which spans 3–300 GHz. Another advantage of focusing on this frequency is that other communication applications, like WLAN and Bluetooth, are able to use a smaller portion of the spectrum simultaneously [3]. The sub-6 GHz range of the 5G spectrum has garnered

Submitted On: xxxx xx, 2025
Accepted On: xxxx xx, 2025

https://doi.org/10.13052/2025.ACES.J.401010

significant attention from researchers and professionals due to its capacity to provide highly precise and fast communication across extensive distances. The Federal Communications Commission(FCC) has allocated the frequency range of 2–6 GHz for the 5G sub-6 GHz bands inside the 5G spectrum. MIMO antennas must possess the capability to ensure minimal mutual interference between antenna elements [4]. Minimizing inter-element mutual coupling in MIMO antennas poses a significant design obstacle for antenna engineers, particularly in densely packed device environments [5–7]. In addition, a high-gain antenna lessens the impacts of multipath fading and path loss [7, 8]. A lot of recent research has focused on microstrip line and Substrate-Integrated Waveguide (SIW)-based high-gain antenna [9–11]. It operates within the frequency band of 24.5-28.4 GHz and has a gain of 7-11.4 dBi. The dipole array antenna implemented in [10, 11]. Additionally, the series-fed method has been mentioned in more recent publications as a way to improve the performance of antenna gain [12–16]. A challenge in enhancing gain is the increasing desire for smaller gadgets that occupy less physical space. In the last decade, metamaterials have emerged as a practical and affordable way to boost gain without significantly expanding the antenna's physical dimensions. These composite structures can greatly enhance the gain performance of various antennas when integrated into them [16, 17]. In [16] the metamaterial is positioned in front of the series-fed antenna on the front side of the substrate to enhance the antenna's gain. Similarly, the metamaterial is placed just above the SIW radiator, and gain is improved in [18]. In recent years, numerous MIMO antennas have been developed for sub-6GHz applications, as reported in the literature [19–22]. The mutual coupling between the radiators in the MIMO antenna was reduced through a variety of decoupling structures and methods, including a defected ground, a stub-based decoupling structure, a parasitic element, and an electromagnetic band gap (EBG) [19–22]. Recent advancements in high-gain antenna systems have rarely explored the integration of metamaterials within series-fed MIMO architectures, particularly for 5G sub-6 GHz applications. Addressing this gap, the present work introduces a compact metamaterial-loaded series-fed MIMO antenna capable of delivering both wide impedance bandwidth and enhanced gain. The antenna configuration utilizes a SIW-based power divider designed to operate at 3 GHz with a bandwidth extending from 3 to 5 GHz, ensuring compact and efficient signal distribution. Four dipole elements, each with tailored lengths and spacing, are symmetrically arranged along both sides of the SIW. These elements are interconnected in series using microstrip lines, forming a continuous feed network that supports wideband radiation. A metamaterial superstrate is positioned above the radiators, effectively enhancing gain without increasing the antenna's physical dimensions. This arrangement achieves a compact, high-gain MIMO solution optimized for 5G sub-6 GHz applications.

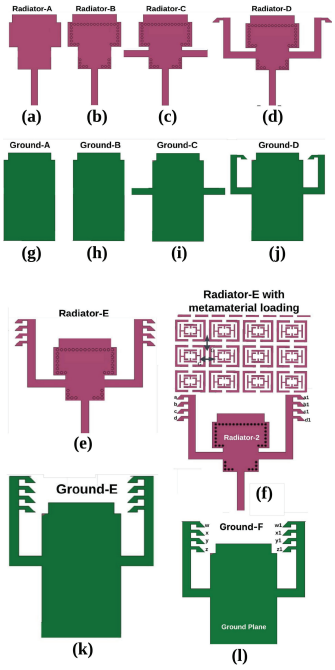

Fig. 1. Development of the proposed SIW-based series-fed dipole radiator.

II. SIW-BASED SERIES-FED DIPOLE MIMO ANTENNA DESIGN

A. SIW-based series-fed dipole unit cell

The design of the unit cell for the series-fed dipole radiator is the starting point for the proposed series-fed dipole MIMO antenna. Initially, the rectangular radiator (Radiator-A) is fed by a single line (P1-Input) in the antenna design, as depicted in Fig. 1 (a). The reflection coefficient of the initial design (Radiator-A) is depicted in Fig. 2. As depicted in Fig. 2, the initial design is resonating at 2.8 GHz. Further, as shown in Fig. 1 (b), in Radiator (B), a metallic via (M-Via) is used to connect the top side conductor and bottom side conductor through a 0.8 mm FR4 substrate in order to construct a SIW-based power divider in the radiator. Equations (1) and (2) can be used to calculate the resonant frequency of the proposed SIW. This enables efficient power transfer from the line to the SIW. Further, two lines (P2, P3-Output ports) are connected along with the SIW-based power divider in Radiator-C as depicted in Fig. 1 (c). Because of its y-axis symmetry, the power divider can evenly divide the input power (P1) into two

output port lines (P2 and P3).

$$f_{\text{SIW}} = \frac{c}{2\sqrt{\varepsilon_r}}\sqrt{\left(\frac{1}{L_{\text{eff}}}\right)^2 + \left(\frac{1}{W_{\text{eff}}}\right)^2}, \quad (1)$$

$$L_{\text{eff}} = L_{\text{s}} - \frac{d^2}{0.95s}, \quad W_{\text{eff}} = W_{\text{s}} - \frac{d^2}{0.95s}. \quad (2)$$

The modification is also done in the ground plane of Radiator-C by connecting two lines on the ground parallel to the front side (output ports P1 and P2) along with the x-axis. Hence, Radiator-C consists of the lines (P2 and P3) on both the top and bottom sides as depicted in Fig. 1 (g). Figure 2 depicts the reflection coefficient of Radiator-C. Due to the first-order resonance, the designed power divider operates at 3.8 GHz and has an impedance bandwidth of 4– 6 GHz, as can be illustrated.

Further, in order to improve the impedance bandwidth of the proposed radiator, Radiator-D is designed as depicted in Fig. 1 (d). Radiator-C is designed by connecting the rectangular-shaped arm along with power divider output ports P2 and P3 on the front and back sides of the substrate in the y-axis (perpendicular to the output ports P2 and P3) to connect the dipole elements. Initially, the single dipole is connected top and bottom sides along with the output port P2 and outport P3 arm. The dipole 'a' is connected to the left arm, whereas the dipole 'b' is connected to the right arm, together with P2 and P3 on the front side (radiator) of the substrate (Fig. 1 (c)). Similarly, the dipole 'a1' is connected to the left arm, whereas the dipole 'b1' is connected to the right arm, together with P2 and P3 on the backside (ground) of the substrate, as depicted in Fig. 1 (d).

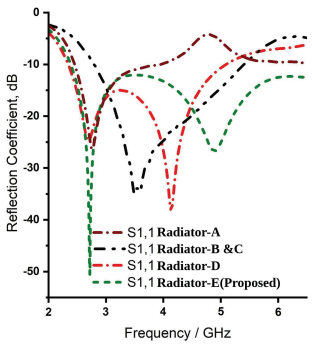

Fig. 2. Reflection coefficient of the proposed series-fed dipole radiator.

A second-order resonance is introduced at the input as a consequence of this modification, which leads to an extended impedance bandwidth for the dipole antenna. Figure 2 illustrates Radiator-C's reflection coefficient. It can be seen that the impedance bandwidth has been improved, and it operates over 2.3-5.2 GHz by Radiator-D.

Radiator-D currently does not cover the complete sub-6 GHz 5G range, thus necessitating an enhancement in the impedance bandwidth of Radiator-D. In order to further enhance the impedance bandwidth of the proposed radiator, Radiator-E is designed as shown in Fig. 1 (e). In addition, the four dipoles are interconnected on the top (radiator) and bottom sides (ground), as well as on the left and right sides, together with the output port P2 and output port P3 arm. The dipoles 'b', 'c', and 'd' are connected to the left arm, while the dipoles 'a1', 'b1', 'c1', and 'd1' are connected to the right arm, along with P2 and P2 located on the front side (radiator) of the substrate, as illustrated in Fig. 1 (e). Similarly, the dipoles 'w', 'x', 'y', and 'z' are connected to the left arm, whereas the dipoles 'w1', 'x1', 'y1', and 'z1' are connected to the right arm, together with P2 and P2 positioned on the bottom side (ground) of the substrate, as shown in Fig. 1 (j). In addition, the dipoles are connected with a periodic spacing of 2 mm in order to enhance the bandwidth and radiation properties. As a result of including four dipoles, the impedance of Radiator-E has experienced a significant improvement, resulting in a bandwidth of 2.3–6 GHz. Therefore, Radiator-E encompasses the complete operational range of the sub-6GHz band for 5G applications.

III. GAIN IMPROVEMENT OF THE PROPOSED SERIES-FED DIPOLE

The suggested series-fed dipole sub-6 GHz 5G antenna is designed for deployment in environments with a high degree of scattering, such as industrial factories. Due to these harsh conditions, the proposed antenna must exhibit both polarization diversity and high gain. The gain performance of the radiator is shown in Fig. 4, demonstrating values ranging from 2.5–4 dB across the 2.3–6 GHz band. Although this gain is acceptable for general environments, it is inadequate for industrial settings, where signal loss is more significant. Therefore, a gain enhancement strategy is necessary for the proposed series-fed dipole antenna. To achieve this, an SSRR-shaped metamaterial array is positioned along the y-axis in front of the radiator, as illustrated in Fig. 1 (f), enabling improved gain without increasing the antenna's size.

A. Metamaterial characterization

The metamaterial unit cell that is being suggested is shown in Fig. 3 (a). The proposed metamaterial consists of an outer Rectangular Split Ring Resonator (RSRR) with a split located at the top and bottom of the RSRR. The RSRR contains two T-shaped stubs and a modified H-shaped stub, which are positioned as shown in Fig. 3 (a). Both 'T' and modified C-shaped stubs have a uniform thickness of 0.5 mm. Additionally, the

two T-shaped stubs are positioned with a vertical axis spacing of 1 mm, while the two modified C-shaped stubs are positioned with a y-axis separation of 1 mm. The entire structure is printed on a substrate made of FR4 with a thickness of 0.8 mm, and a dielectric constant of 4.3. The characterization of metamaterial is achieved by positioning the unit cell along the x- and z-axis between two waveguide ports in CST Studio software, as shown in the Fig. 3 (a). In addition, the perfect electric conductor (PEC) and perfect magnetic conductor (PMC) boundary conditions are applied to the x-z axis for the characterization of metamaterial. The PEC boundary lies in the x-axis, and the ideal PMC boundary lies along the z-axis. It has been determined that the y-axis will propagate an electromagnetic wave that is incident normally. Transmission of the electromagnetic wave that is ordinarily incident occurs along the y-axis. In the process of establishing resonance in the transmitted and reflected waves, the resonator structure is excited by the incident waves, and electromagnetic interaction takes place within the multi-ring metamaterial unit cell. As the SIW cavity-backed antenna functions as the primary source of electromagnetic radiation propagating through the unit cells along the y-direction, the selection of the y-axis as the excitation axis for the multi-ring metamaterial unit cell is both appropriate and physically justified

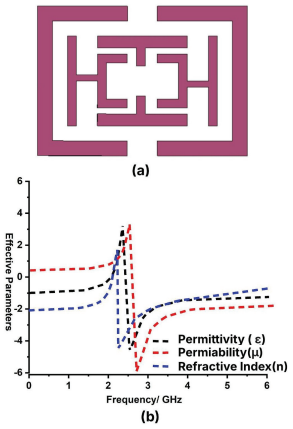

Fig. 3. (a) Proposed RSRR unit cell. (b) Effective parameters of the proposed metamaterial unit cell.

The permeability, refractive index, and impedance characteristics of the proposed metamaterial unit cell is important criteria for successfully evaluating their performance characteristics. Figure 3 (b) depicts the effective parameter of the proposed RSRR metamaterial unit cell. Figure 3 (b) demonstrates that the proposed metamaterial has a negative permeability, permititivity and negative refractive index over 2.2–6 GHz. It is evident from the results that the proposed metamaterial exhibits substantial negative real non-zero Refractive Index(NZRI) and Epsilon-negative (ENG) properties over 2.2–6 GHz frequency range. Therefore, this specific frequency resonance range may be used to improve the proposed antenna gain array with dimensions of 4×8 unit cells is positioned on the upper surface of the substrate in the y-direction, as shown in Fig. 1 (f). The metamaterial array maintained a gap of 1 mm between two unit cells in both the x- and y-axis.

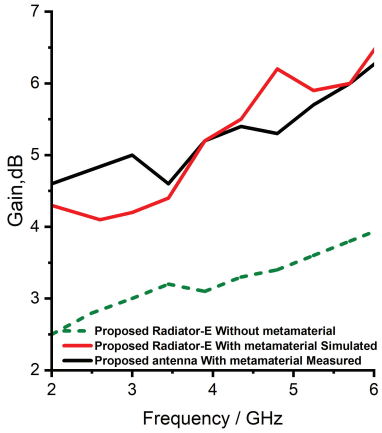

Fig. 4. Gain of the proposed antenna with and without metamaterial.

Table 1: Dimensions of the proposed antenna (mm)

Parameter	Value	Parameter	Value	Parameter	Value	Parameter	Value
L	45	LG2	1.9	W2	1	WG1	3
L1	12.1	LG3	12.1	W3	2.3	WG2	1.5
L2	5.5	LG4	1	W4	7.3	WG3	5
L3	1.8	LG5	1.2	W5	7.5	WG4	3.5
L5	5	LG6	18	W6	3	WG7	12
L6	8.3	LG7	2	W7	1	WG8	20
L7	1.5	LG8	2	W8	1.5	WG10	1
L8	1.4	LG9	1	W9	1.5	G	1
LG	24.5	W	35	W10	1.5	R	0.4
LG1	1.4	W1	10	WG	44	D1	2
D3	1.2	D4	0.5	D5	1.2	D6	1
D7	0.5	D8	0.5	D9	0.5	D10	0.5
D11	3	E1	2.1	E2	2.1	E3	0.6
E4	0.6	E5	0.5	E6	0.5	E7	0.3

B. Impact of metamaterial

The presence of the metamaterial array has a considerable impact on the gain of the proposed antenna, but it does not have any effect on the bandwidth. The gain of the suggested antenna has been enhanced by placing the metamaterial on the y-axis, resulting in an improvement of gain from 2.5–4 dB to 4.8–7.2 dB over the frequency range of 2.3–6 GHz. Further, the simulated and measured gain of the Radiator-E with metamaterial is depicted in Fig. 4. It can be observed the proposed antenna has a measured gain of 4.3–7 dB over 2.3–6 GHz. Hence, the proposed antenna has good agreement between simulated and measured gain.

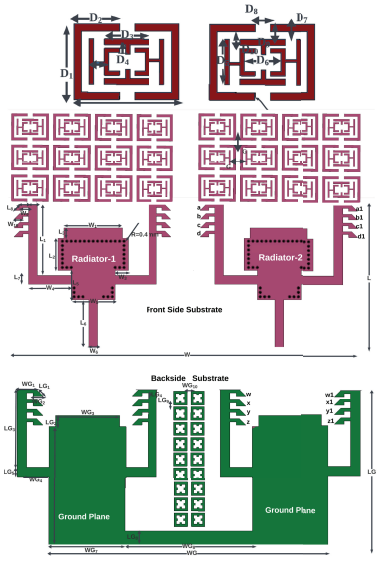

Fig. 5. Proposed series-fed MIMO antenna.

IV. DUAL-BEAM SERIES-FED MIMO ANTENNA DESIGN

In order to achieve link reliability and increased channel capacity in an environment with a high degree of scattering, a two-element MIMO antenna is designed with a suggested dual-beam high-gain series-fed radiator. The MIMO antenna is constructed by positioning two series-fed radiators side by side, with a common ground plane, as shown in Fig. 5. Additionally, the front side of the substrate is comprised of two series-fed radiators, while the rear side consists of a common ground and parallel running dipoles for both radiators, as depicted in Fig. 5. Further, in a series-fed radiator, the input signal is evenly divided between the two branches of the antenna, which are connected in series. The proposed antenna demonstrates a uniform distribution in the E-plane, leading to the generation of radiation with a dual-beam characteristic. Moreover, the employment of dual-beam radiation at both the transmitter and receiver significantly enhances the reliability of the link, even in the presence of obstacles that may hinder the communication. The proposed antenna demonstrates exceptional link reliability due to the utilization of MIMO technology and dual-beam characteristics. The dimensions of the proposed MIMO antenna is presented in Table 1.

A. EBG unit cell design

This section describes the design method for the proposed EBG unit cells. The EBG structure may suppress and allow electromagnetic propagation in a certain frequency band (Band gap), or allowed frequency band, which is determined by the structural capacitance and inductance variations of the EBG structure. Figure 6 (a) illustrates the proposed square-shaped stub EBG structure. The proposed EBG unit cell consists of a square stub and four rectangular-shaped stubs that are connected at the four sides of the square-shaped stub as depicted in Fig. 6 (a). The square stub and rectangular stub have an inductance effect. At the same time, the distance between adjacent stubs creates a capacitance effect.

$$L = 0.2h\left[\ln\left(\frac{2h}{r}\right) - 0.75\right], \tag{3}$$

$$C = \varepsilon_0\varepsilon_r\frac{w^2}{h}, \tag{4}$$

$$\omega_0 = \frac{1}{\sqrt{LC}}, \tag{5}$$

$$BW = \frac{1}{\eta}\sqrt{\frac{L}{C}} = \frac{\Delta\omega}{\omega_0}. \tag{6}$$

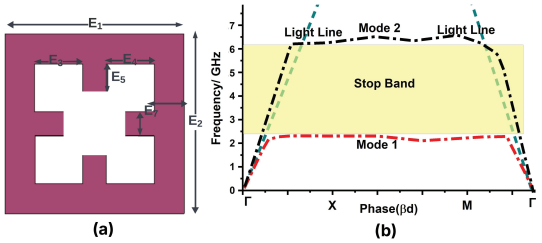

Fig. 6. (a) Proposed EBG unit cell. (b) Dispersion diagram of the proposed unit cell.

As a result, the suggested square-shaped EBG unit cell performs equivalently to a stop-band LC filter. The passband may be estimated using the approximate LC values. Equations (3) and (4) are used to calculate the estimated LC values, whereas equations (5) and (6) are employed to determine the bandwidth of the proposed EBG. Furthermore, the EBG can be characterized using the dispersion diagram for a better understanding of the function. Figure 6 (b) displays the proposed unit cell's dispersion diagram. It can be observed that the proposed EBG structure has a stop band from 2.4 to 6.4 GHz. According to the dispersion diagram, the suggested unit cell suppresses the electromagnetic wave across the frequency range 2.3–6 GHz. As a result, the suggested EBG structure may serve as a band-stop filter.

B. Mutual coupling reduction using EBG

The side-by-side arrangement decreased mutual coupling between radiators but not sufficient for MIMO functioning. To eliminate mutual coupling between the series-fed radiators in the proposed MIMO antenna, the proposed square-shaped 2×9 element EBG decoupling structure is installed on the back side of the substrate as

depicted in Fig. 5. Further, the distance between EBG elements in the x- and y-axes is 1 mm, as depicted in Fig. 5. Due to the placement of the EBG element decoupling structure, the surface current is suppressed since EBG behaves as a stop-band filter at the operating band.

V. RESULTS AND DISCUSSIONS

The photograph of the fabricated proposed MIMO antenna is depicted in Fig. 7 (a). Figure 8 (a) illustrates the simulated and measured reflection coefficient of the proposed MIMO antenna. The figure reveals that the proposed MIMO antenna exhibits a reflection coefficient of less than −10 dB between 2.2 and 6 GHz.

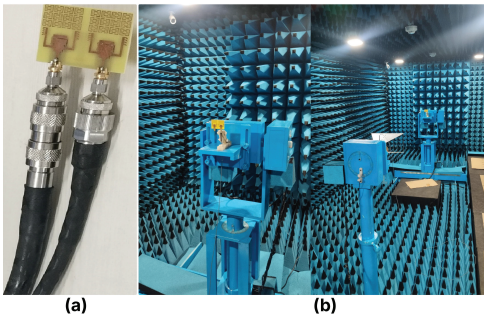

Fig. 7. Photograph of the fabricated antenna and radiation pattern measurement setup of the proposed antenna in anechoic chamber.

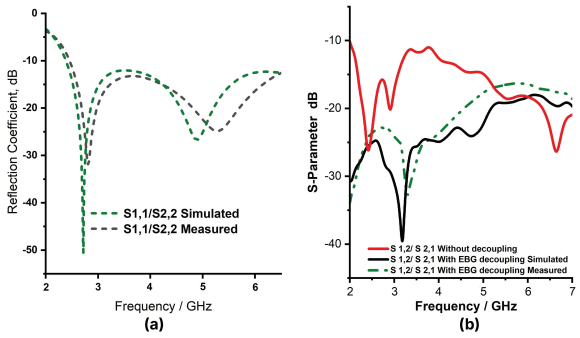

Fig. 8. (a) Simulated and measured reflection coefficient comparison, (b) mutual coupling comparison.

Furthermore, Fig. 8 (b) illustrates the simulated and measured mutual coupling between the series-fed radiator in the proposed MIMO antenna. Figure 8 (b) clearly demonstrates that the proposed MIMO antenna has less than −15 dB over an operating band of 2.2–6 GHz in both simulated and measured scenarios due to EBG decoupling structure.

Figure 7 (b) illustrates the radiation pattern measurement setup within the anachoic chamber. Figures 9 (a)–(d) depicts the E- and H-plane radiation

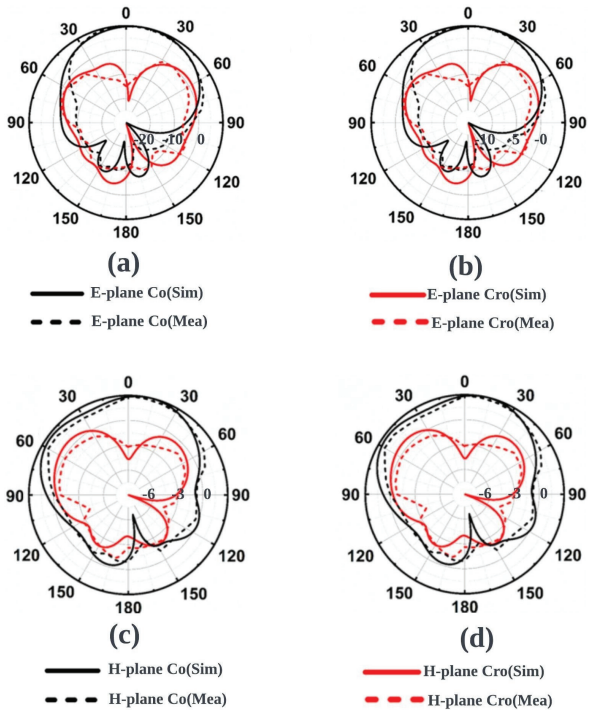

Fig. 9. Radiation pattern of the proposed antenna, (a) E-plane at 2.8 GHz, (b) 5 GHz and (c) H-plane at 2.8 GHz, (d) 5 GHz.

patterns of the series-fed dipole MIMO antenna at 2.8 and 5 GHz. Further, the metamaterial array is placed in front of the two radiators in y-axis. The proposed metamaterial array exhibits a polarization-altering ability that effectively suppresses cross polarization in both the E-plane and H-plane within the operational band. Due to this, the suggested antenna enhances its radiation performance. Furthermore, the series-fed dipole antenna, as shown in Figs. 9 (a)–(d), achieves suppressed cross-polarization in the E-plane. In addition to that it can be observed that the proposed MIMO antenna has an omnidirectional radiation pattern in the E- and H-plane at the operating bands.

Figure 10 illustrates the measured and simulated efficiency of the proposed MIMO antenna. The proposed MIMO antenna exhibits an efficiency of over 85% throughout the entire operating band.

A. MIMO parameters

A.1. Envelope Correlation Coefficient (ECC) and Diversity Gain(DG)

The ECC is a method used to quantify the level of coupling between various antenna elements in a MIMO antenna system. A lower ECC value, preferably less than 0.5, is associated with improved performance in diversity gain. Through the examination of far-field

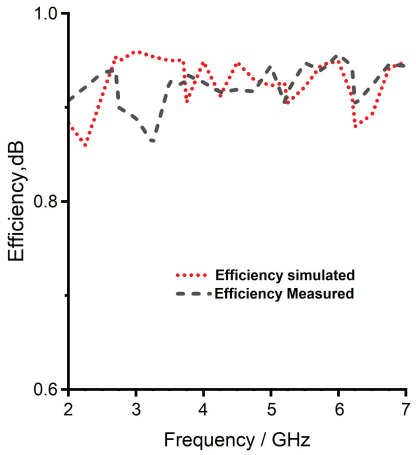

Fig. 10. Efficiency of the proposed antenna.

patterns, it is possible to ascertain the ECC performance of a MIMO antenna. In order to determine the ECC using far-field, equation (7) is employed.

$$\rho_{ij} = \frac{\left|\iint_{4\pi} E_i(\theta,\varphi) * E_j(\theta,\varphi) d\Omega\right|^2}{\iint_{4\pi} \left|E_i(\theta,\varphi)\right|^2 d\Omega \iint_{4\pi} \left|E_j(\theta,\varphi)\right|^2 d\Omega}. \quad (7)$$

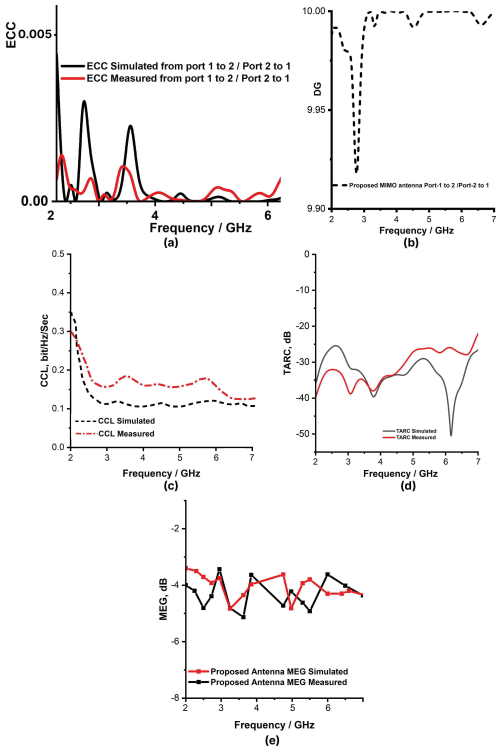

Fig. 11. (a) ECC, (b) DG of the proposed MIMO antenna, (c) CCL, (d) TARC, (e) MEG of the proposed MIMO antenna.

Figure 11 (a) shows that the suggested antenna has an ECC range of less than 0.0005 over the 2.2–6 GHz frequency range, which is lower than the optimum range. It is evident from the result that the proposed MIMO antenna has less coupling between the adjacent elements due to the EBG decoupling structure.

A.2. Diversity gain

Diversity gain is a metric that quantifies the reduction in transmission capacity that can be achieved by employing a diversity technique while maintaining efficiency. DG can be calculated using equation (8). In order to achieve optimal MIMO performance, it is recommended that the DG for the MIMO antenna in practical scenarios be close to 10. Figure 11 (b) illustrates the DG of the proposed series-fed MIMO antenna. The suggested MIMO antenna exhibits a DG of around 10 over the whole operating frequency range.

$$DG = \sqrt{1 - ECC^2}. \quad (8)$$

A.3. Channel Capacity Loss (CCL)

CCL is a term that refers to a variety of parameters that influence the performance of the MIMO system. It specifies the reduction in the maximum attainable data rate of the communication channel. Channel capacity of a MIMO system significantly impacts its data rate. Consequently, the channel capacity of MIMO antenna systems can be improved by minimizing the reduction in channel capacity. Channel capacity increases in a proportional manner as the number of antenna elements increases. Equation (9) can be employed to calculate CCL. In order to achieve optimal performance in MIMO systems, it is recommended that the CCL be maintained below 0.5 bits/Hz/Sec.

$$CCL = -\log_2 \det(\Psi^R). \quad (9)$$

CCL of the proposed series-fed dipole MIMO antenna is illustrated in Fig. 11 (c). The suggested MIMO antenna exhibits a CCL of less than 0.3 bits/Hz/Sec across the frequency range of 2.2 to 6 GHz. Therefore, it is appropriate for achieving superior MIMO performance.

A.4. Total Active Reflection Coefficient (TARC)

The presence of interference among the radiators in a system with many elements deteriorates the performance of the MIMO system. The MIMO system is based on precise determination of the degree of interference. TARC can accurately measure interference between radiators. The TRAC of a two-element antenna system is determined using equation (10). In order for a MIMO

Table 2: Performance comparison

Ref.	Antenna Structure (Size mm^3)	Frequency (GHz)	Method
[16]	Dipole single antenna ($112 \times 50 \times 3$)	18	1×8 array
[17]	Dipole single antenna ($66 \times 15 \times 0.3$)	26	1×8 array
[19]	DRA single antenna ($20.7 \times 21.2 \times 1.5$)	28	2×2 array with three layers
[20]	Dipole single antenna ($10 \times 36.5 \times 0.2032$)	28	Series-fed dipole and 8-element
[21]	Dipole single antenna ($25 \times 67 \times 0.5$)	28.5	Series-fed dipole and 6-element
[22]	Dipole single antenna ($10 \times 59 \times 0.203$)	28	Series-fed dipole and 8-element
[23]	Dipole single antenna ($31.5 \times 18.7 \times 0.508$)	30.5	Series-fed + Placing metameterial in front of the antenna
This Work	Dipole MIMO ($45 \times 35 \times 0.8$)	2.2-6	Series-fed + Placing metameterial in front of the antenna + MIMO antenna + EBG decoupling

system to operate effectively, it is essential to keep the TARC value below 0 dB.

$$TARC = \frac{\sum_{n=1}^{N} |b_i|^2}{\sum_{n=1}^{N} |a_i|^2} = \sqrt{\frac{(S_{ii}+S_{ij})^2 + (S_{jj}+S_{ji})^2}{n}}. \quad (10)$$

The TARC of the proposed series-fed MIMO antenna is depicted in Fig. 11 (d). It can be observed from the proposed MIMO antenna that it has less than -20 dB over the 2.2–6 GHz operating band.

A.5. Mean Effective Gain (MEG)

A theoretical definition of MEG that takes into account all potential spatial propagation scenarios is the ratio of the average received signal strength to the average transmitted signal power.

$$\mathrm{MEG_i} = 0.5\left[1 - \sum_{\mathrm{i}=1}^{\mathrm{N}} \left|\, \mathrm{S_{ij}}\right|^2\right]. \quad (11)$$

The MEG of the MIMO antenna can be computed using equation (11). The MEG of the proposed series-fed MIMO antenna is depicted in Fig. 11 (e). It can be observed from Fig. 11 (e) proposed MIMO antenna has less than -3 dB over the 2.2–6 GHz operating band.

B. Performance comparison

Performance comparison of the proposed MIMO antenna is presented in Table 2. From Table 2 it can be observed that many series-fed antennas are implemented, but this is the first dual-beam compact metamaterial-loaded high-gain series-fed dipole MIMO antenna for sub-6 GHz 5G applications. It has a compact size of 45×35 mm, high gain 2.2–6 dBi in sub-6 GHz band, and dual beam characteristics. Therefore, the suggested MIMO antenna is a superior choice compared to the current antennas.

VI. CONCLUSION

This work presents a compact series-fed MIMO antenna integrated with metamaterial structures, targeting high-gain, wideband performance in the 5G sub-6 GHz range. The antenna employs a Substrate Integrated Waveguide (SIW)-based power divider operating at 3 GHz with a 3–5 GHz bandwidth. Four dipoles of varying lengths are connected in series via microstrip lines to achieve an impedance bandwidth of 2.2–6.5 GHz. To enhance radiation characteristics without increasing antenna size, a square-ring metamaterial array is placed along the y-axis, resulting in a gain improvement from 5 to 11 dB and reduced cross-polarization. MIMO functionality is achieved by arranging two such radiators side by side, while an Electromagnetic Band Gap (EBG) structure on the ground suppresses mutual coupling. The antenna's MIMO performance is comprehensively evaluated. ECC remains below 0.005, DG is consistently near 10 dB, and CCL is maintained below 0.4 bits/s/Hz. TARC remains under -10 dB across the band, reaching -40 dB at 3.5 GHz. MEG values range between -2.5 dB and -7 dB, indicating balanced reception. These results confirm that the proposed metamaterial-loaded MIMO antenna

offers an effective, compact, and robust solution for next-generation sub-6 GHz wireless systems.

REFERENCES

[1] V. Dala-Pegorara-Souto, "Emerging MIMO technologies for 6G networks," *Sensors*, vol. 23, p. 1921, 2023.

[2] R. Bajracharya, R. Shrestha, and H. Jung, "Future is unlicensed: Private 5G unlicensed network for connecting industries of future," *Sens. Switzerl*, vol. 20, 2020.

[3] B. K. Ng and C. T. Lam, "Single-carrier rotation-interleaved space-time code for frequency-selective fading channels," *Appl. Sci*, vol. 12(24), p. 12803, 2022.

[4] Z. Xu and C. Deng, "High-isolated MIMO antenna design based on pattern diversity for 5G mobile terminals," *IEEE Antennas Wirel. Propag. Lett*, vol. 19, pp. 467–471, 2020.

[5] T. Upadhyaya, "Aperture-fed quad-port dual-band dielectric resonator-MIMO antenna for sub-6 GHz 5G and WLAN application," *Int. J. Antennas Propag*, vol. 1, pp. 1–13, 2022.

[6] P. R. Girjashankar, T. Upadhyaya, and A. Desai, "Multiband hybrid MIMO DRA for Sub-6 GHz 5G and WiFi-6 applications," *Int. J.RF Microw. Comput. Eng*, vol. 32, 2022.

[7] J. C. Martínez-Quintero, E. P. Estupiñán-Cuesta, and G. L. Escobar-Quiroga, "Design, analysis, and simulation of 60 GHz Millimeter Wave MIMO microstrip antennas," *J. Sens. Actuator Netw*, vol. 11, 2022.

[8] K. Ding, D. M. Leenaerts, and H. Gao, "A 28/38 GHz dual-band power amplifier for 5G communication," *IEEE Trans. Microw. Theory Tech*, vol. 70, pp. 4177–4186, 2022.

[9] A. Desai, Y. F. Tsao, and H. T. Hsu, "High gain substrate integrated waveguide antenna with enhanced bandwidth for millimeter-wave wireless network applications," *Wirel. Netw*, vol. 29, pp. 2251–2260, 2023.

[10] J. Wang, X. Zhao, Y. Ye, and S. Liu, "A millimeter-Wave ultrawideband tightly coupled dipole array antenna for vehicle communication," *IEEE Antennas Wirel. Propag. Lett*, vol. 21(10), pp. 2135–2139, 2022.

[11] S. Kadiyam and A. J. Rani, "Design and analysis of a high gain millimeter-mave antenna array for dual purpose applications," *Wirel. Pers. Commun*, vol. 130, pp. 593–607, 2023.

[12] H. Wang, K. E. Kedze, and I. Park, "A high-gain and wideband series-fed angled printed dipole array antenna," *IEEE Trans. Antennas Propag*, vol. 68, pp. 5708–5713, 2020.

[13] N. K. Maurya, M. J. Ammann, and P. Mcevoy, "Series-fed omnidirectional mm-wave dipole array," *IEEE Trans. Antennas Propag*, vol. 71, no. 2, p. 1330, 2023.

[14] S. K. Duddu and J. Kumar, "High-gain series-fed-planar millimetre-wave Franklin antenna array," *Arab. J. Sci. Eng.*, vol. 49, pp. 6331–6341, 2024.

[15] T. Ma, J. Ai, M. Shen, and W. T. Joines, "Design of novel broadband endfire dipole array antennas," *IEEE Antennas Wirel. Propag. Lett*, vol. 16, pp. 2935–2938, 2017.

[16] B. A. F. Esmail, S. Koziel, and A. Pietrenko-Dabrowska, "Wideband high-gain low-profile series-fed antenna integrated with optimized metamaterials for 5G millimeter wave applications," *Sci Rep*, vol. 14, pp. 185–192, 2024.

[17] Z. Wani, M. P. Abegaonkar, and S. K. Koul, "High-low-epsilon biaxial anisotropic lens for enhanced gain and aperture efficiency of a linearly polarized antenna," *IEEE Trans. Antennas Propag*, vol. 68, pp. 8133–8138, 2020.

[18] A. Gorai, A. Deb, and J. R. Panda, "Millimeter wave/5G multiband SIW antenna with metasurface loading for circular polarization and bandwidth enhancement," *J Infrared Milli Terahz Waves*, vol. 43, pp. 366–383, 2022.

[19] R. Khan, W. T. Sethi, and W. A. Malik, "Enhancing gain and isolation of a quad-element MIMO antenna array design for 5G sub-6 GHz applications assisted with characteristic mode analysis," *Sci Rep*, vol. 11111(14), pp. 1–20, 2024.

[20] H. Ahmed, X. Zeng, H. Bello, Y. Wang, and N. Iqbal, "Sub-6 GHz MIMO antenna design for 5G smartphones: A deep learning approach," *AEU - International Journal of Electronics and Communications*, vol. 168, p. 154716, 2023.

[21] N. P. Kulkarni, N. B. Bahadure, P. D. Patil, and J. S. Kulkarni, "Flexible interconnected 4-port MIMO antenna for sub-6 GHz 5G and X band applications," *AEU - International Journal of Electronics and Communications*, vol. 152, p. 154243, 2022.

[22] A. Desai, M. Palandoken, I. Elfergani, I. Akdag, C. Zebiri, J. Bastos, J. Rodriguez, and A. Raed, "Transparent 2-element 5G MIMO antenna for sub-6 GHz applications," *Electronics*, vol. 11, no. 2, pp. 251–251.

R. Anandan, Associate Professor and Head, Department of Electronics and Communication Engineering, Dhanalakshmi Srinivasan College of Engineering and Technology, India, completed his Ph.D. in the Faculty of Information and Communication Engineering from Anna University Chennai in May 2023. His interest includes antenna, optical communication, satellite communication, digital electronics, and wireless communication. He has published seven papers in international

conferences and national conferences and four papers in international journals with good impact factors.

V. Vinoth Kumar, Assistant Professor, Department of Electronics and Communications, Vel Tech High Tech Dr Rangarajan Dr Sakuntala Engineering College, India. He completed his Ph.D. at the Faculty of Information and Communication Engineering from Anna University Chennai in May 2022.

M. Pandi Maharajan, Associate Professor, Department of ECE, Saveetha School of Engineering, Saveetha Institute of Medical and Technical Sciences, India. He completed his Ph.D. in the Faculty of Information and Communication Engineering from Anna University Chennai in May 2020.

G. Jothi received the B.E. and M.E. degrees in Computer Science Engineering from the Anna University Chennai, India. She is adjunct professor in ECE at Saveetha School of Engineering, Saveetha Institute of Medical and Technical Sciences, Chennai.